UC Irvine
UC Irvine Electronic Theses and Dissertations

Title

Exploring Non-Traditional Solid-Liquid Interfaces Under Nanoconfinement

Permalink

Author

Polster, Jake Wyatt

Publication Date

2022

Peer reviewed|Thesis/dissertation

UNIVERSITY OF CALIFORNIA,
IRVINE

Exploring Non-Traditional Solid-Liquid Interfaces Under Nanoconfinement

DISSERTATION

submitted in partial satisfaction of the requirements
for the degree of

DOCTOR OF PHILOSOPHY

in Chemistry

by

Jake Wyatt Polster

Dissertation Committee:
Professor Zuzanna S. Siwy, Chair
Associate Professor Shane A. Ardo
Professor Matthew D. Law

2022

DEDICATION

To my family and friends for their love and support

TABLE OF CONTENTS

Page

LIST OF FIGURES

Page

ACKNOWLEDGEMENTS

I want to first thank Dr. Zuzanna Siwy. From the moment I asked to rotate in her lab she was kind, welcoming, and enthusiastic. She set aside time to meet with me one-on-one to discuss potential rotation projects and had a current student mentor me. After my first meeting with her and talking with her students it was clear she is a great advisor. Joining her lab was one of the easiest decisions in graduate school and I have enjoyed every moment. Zuzanna is an exceptional advisor and treats all her students with kindness and respect. Being in her research group is like joining a team – Zuzanna sees us as her colleagues and treats us as equals. She has realistic expectations of her students and strongly values work-life balance. As my research advisor, Zuzanna has made my graduate school experience rewarding and enjoyable, and for that I am truly grateful.

I am also grateful for the support of my dissertation committee, Dr. Shane Ardo and Dr. Matt Law. Shane and Matt provided support and thoughtful comments throughout my graduate experience. I reached out to Shane before even applying to UCI and he provided enthusiastic support and encouraged me to apply to the program. Shane also nominated me for two internal fellowships, which made my decision to come to UCI extremely easy. Shane also ran a summer materials research experience that I had the opportunity to join during the summer prior to my first year at UCI. This summer experience gave me a great opportunity to meet more faculty, adjust to the new location, and create great friendships that have lasted my entire graduate school experience. I am truly thankful for the support Shane showed to me even before I joined UCI. Matt has also been a strong supporter of mine throughout my graduate school experience, with heading my advancement committee and teaching the materials chemistry course that I learned so much in (even though it was at 8 AM!). I am grateful for the support of Shane and Matt.

I next want to thank the amazing coworkers, labmates, and friends that supported me and helped me excel in graduate school. Crystal Yang, James Boyd, Joseph Martinez, Elif Türker-Acar, Rachel Lucas, Cody Combs, Scottie Lin, Wilfred Russell, Kabin Lin, Jin Zhang, Taylor Frey, Dan Seith, Ethan Cao, Savannah Silva, and DaVante Cain are all amazing labmates from the Siwy lab that have helped me excel in my research while keeping me laughing and smiling. Their support has helped me grow as a researcher and critical thinker. It was truly an honor to meet and work alongside each of you all. Ilektra Andoni, Eric Choi, Mackenzie Field, Deanna Myers, Josh Ziegler, Gaurav Jha, Vivian Chen, Alex Abelson, Caroline Qian, Shane Flynn, Bridgett Kohno, Carly Brennan, Shane Coffield, and Ethan Licon are all amazing coworkers and friends I got to meet at UCI. You all have helped me grow as a person, both inside and outside the lab. You all made my time at UCI very enjoyable, and I truly cherish the bonds we have formed.

I also want to acknowledge my CENT collaborators, Dr. Tuan Anh Pham and Dr. Fikret Aydin. I collaborated with Anh and Fikret for two of my projects, and their work helped elevate my projects. I also gained some great friendships through CENT, including Cody Ritt, Stevie Bush, Kyle Sendgikoski, and Pedro de Souza. It was great to connect with you all at our CENT meetings and I am thankful for your support and friendship.

Finally, I am the most grateful for the love, support, and encouragement I have received from my family and loved ones. My parents are my biggest supporters and are always there to talk through any issue I encountered. I am truly thankful for their love and support and am very lucky to have them. I am also very appreciative of my brother and my sister-in-law for always be there to talk about the latest episode of our favorite show or share jokes with each other. It is great to have such a strong support group that also knows how to make me laugh. My extended family has also been a great support system both in graduate school and prior. Finally, I want to thank my close friends from high school and college. Kristen Amaddio is one of my dearest friends and has been one of my biggest cheerleaders since high school. Her dedication and passion to her profession are contagious, and she always inspires me to be a better person. Lindsay Robinson and Katrina Piemonte are both amazing scholars I met in college. Lindsay is one of the kindest and smartest people I know, and her support throughout college and graduate school has enhanced my journey immensely. Katrina is a brilliant scientist, and she always makes time to visit me when I am home. Her support and friendship have been valuable during my graduate school experience. I am truly grateful and honored for my family and loved ones' support on this journey.

A portion of the text and all figures in Chapter 4 and Appendix A are reprints of the materials as it appears in *Natural Sciences*. The co-authors Z. S. Siwy, N. R. Aluru, and J. T. Fourkas listed in this publication directed and supervised research which forms the basis for these chapters.

A portion of the text and all figures in Chapter 5 and Appendix B are reprints of the materials as it appears in *ACS Nano*. The co-authors Z. S. Siwy and T. A. Pham listed in this publication directed and supervised research which forms the basis for these chapters.

VITA

Jake Wyatt Polster

Education

University of California, Irvine, Irvine, CA   6/2022

   Doctor of Philosophy in Chemistry; GPA: 3.99/4.0

College of Wooster, Wooster, OH   5/2017

   Bachelor of Arts in Chemistry, Minor in Mathematics; **GPA:** 3.94/4.0

Skills

- **Laboratory**: Nanopore fabrication (track-etch, dielectric breakdown, TEM and FIB drilling); Electron microscopy (TEM, SEM); Electrochemical analysis (Keithley Picoammeter, Axopatch, potentiostat); Wet chemistry; Surface chemistry modifications (silane and EDC coupling, electrostatic attachment, PVD, sputtering); Contact angle measurements; Spectroscopy (UV, FT-IR, NMR); Chromatography (HPLC-UV); N_2 glovebox use

- **Computer**: Microsoft Word, PowerPoint, Excel; Social media (LinkedIn, Twitter, YouTube); OriginLab; Clampfit; ImageJ; Gatan DigitalMicrograph

- **Scientific Communication**: Interdisciplinary research and frequent collaborations with biologists, physicists, material scientists, and organic and computational chemists. Attended and presented (oral, poster) at international scientific conferences (ACS, BPS). Interviewed for funding agency and department recruitment videos. Participated in a multi-institution collaboration center with weekly webinars and semiannual in-person meetings and presentations.

Research Experience

Graduate Research (Professor Zuzanna S. Siwy Group, UC Irvine)   2/2018 – 6/2022

Dissertation Title: Exploring Non-Traditional Solid-Liquid Interfaces Under Nanoconfinement

- **Project 1: The Electrical Double-Layer Revisited**
  - Investigated surface charge modulation of glass nanopipettes in acetonitrile for a series of inorganic salts. Recorded ion-current measurements with a self-designed experimental setup in a nitrogen glovebox. Determined surface charge sign from ion-current anisotropy.
  - Discovered that the surface charge for an acetonitrile-silica interface is ion concentration dependent. At low salt concentrations the surface is negatively charged, whereas the surface charge flips to positive at higher salt concentrations. The solvent's nitrile group orientation at the solid-liquid interface induces the negative charge, which is overcome by high concentrations of small cations (Li^+, Na^+) accumulating at the interface.

- **Project 2: Gating of Hydrophobic Nanopores with Large Anions**
  - Studied ion transport gating of hybrid, hydrophobic-hydrophilic nanopores with solutions of varying ionic size using current-voltage measurements. Nanopores were fabricated using dielectric breakdown and

surface properties were modified with electrostatic attachment and silane coupling. Modification was tracked with current-voltage measurements and confirmed with contact angle measurements.

- o In the absence of electric field, the hybrid nanopores were filled with water vapor, stopping all transport across the device. The hybrid devices displayed voltage-dependent ionic gating for solutions with small anions (NaCl, KCl, LiCl), while solutions with large, polarizable anions (KBr, KI) showed current flow for both voltage polarities. The enhanced wetting seen for large, polarizable anions was due to their more flexible solvation shell and accumulation near hydrophobic surfaces.

- **Project 3: Rectified and Salt Concentration Dependent Wetting of Hydrophobic Nanopores**
  - o Probed role of ion concentration and electric field on the gating of hybrid, hydrophobic-hydrophilic nanopores. Nanopores were fabricated using TEM drilling and modified with silane coupling.
  - o Hybrid devices displayed voltage- and ion concentration-dependent transport gating. As in Project 2, KI solutions more easily wet the pore than KCl solutions. Higher ionic strength solutions also enhanced pore wetting probability. This finding is on contrast to bulk surface tension trends, which would predict higher ionic strength solutions would have higher surface tension and thus decrease wetting probability.
  - o As with Project 2, devices were voltage-sensitive, such that negative electric fields had enhanced pore wetting probability than positive fields. Nanopore diameter also played a critical role in wettability, as the smallest nanopores ($\sim$4 nm) did not wet for any examined parameters.

Senior Independent Study (Professor Karl Feierabend Group, College of Wooster)   1/2016 – 5/2017

Investigated the effect of matrix composition on the photodegradation of acetaminophen (APAP)

- o Prepared and irradiated buffered (control) and wastewater solutions of trace APAP. Analyzed degradation kinetics, photoproduct formation, and quantum yield using HPLC-UV.
- o For direct photolysis, APAP degraded faster in wastewater than in the control matrix due to radical-forming pollutants. For indirect photolysis, wastewater matrix slowed down APAP degradation due to pollutant interaction with hydroxide radicals.

WAVE Fellow (Professor Michael Hoffmann Group, Caltech)   Summer 2016

Researched electrochemical wastewater treatment technologies using TiO_2/IrO_2 catalysts

- o Tested atomically thin TiO_2 coated IrO_2 catalysts for their chlorine evolution reaction (CER) current and CER selectivity. Assessed wastewater treatment efficiency using ion chromatography and changes to total organic carbon (TOC) and chemical oxygen demand (COD) in wastewater solutions.
- o IrO_2 catalysts with 3 monolayers of TiO_2 showed best performance, demonstrating the catalyst's active site is sensitive to the metal-oxygen bond strength and follows the Sabatier principle.

Polymer Engineering REU Student (Professor Bryan Vogt Group, University of Akron)   Summer 2015

Studied electrospinning of metal oxide fibers for battery anodes

- o Prepared electrospinning dope with zinc and cobalt nitrate and poly(ethylene oxide) (PEO). Performed thermogravimetric analysis on precursor solutions to reveal carbonate and oxide formation temperatures.

o Stable Taylor cone formation only occurred for spinning solutions with 0.85% PEO; electrospinning failed at high humidity levels.

Teaching/Mentoring Experience

Chemistry Teaching Assistant, UC Irvine   2017-2018, 2021

- Taught general chemistry classes in person and online (5 discussion sections and 2 office hours per week)

Chemistry Laboratory Assistant, College of Wooster   2015-2017

- Taught inorganic and organic chemistry laboratory techniques to 20 undergraduate students
- Performed nuclear magnetic resonance spectroscopy for students

Awards

Nature Nanotechnology Poster Prize   Ein Gedi, Israel, 2019

UC Irvine ChaMP Outstanding Poster Award   Irvine, CA, 2019

Provost Ph.D. Fellowship   Irvine, CA, 2017

Graduate Dean's Recruitment Fellowship   Irvine, CA, 2017

Publications

1. **Polster, J. W.**; Aydin, F; de Souza, P.; Bazant, M. Z.; Pham, T. A.; Siwy, Z. S. Rectified and Salt Concentration Dependent Wetting of Hydrophobic Nanopores. *Manuscript in preparation*.

2. **Polster, J. W.**; Souna, A. J.; Motevaselian, M. H.; Lucas, R. A; Tran, J. D.; Siwy, Z. S.; Aluru, N.R.; Fourkas, J. T. The Electrical Double-Layer Revisited. Natural Sciences 2022, e20210099.

3. Frey, T. L.; Fruehauf, K. R.; Lucas, R. A.; **Polster, J. W.**; Shea, K. J.; Siwy, Z. S. Electrochemical Probing of Steric, Electrostatic and Hydrophobic Interactions of Large Cations in Polymers of Intrinsic Microporosity. J. Electrochem. Soc. 2022, 169 (2), 020566.

4. **Polster, J. W.**; Acar, E. T.; Aydin, F.; Zhan, C; Pham, T. A.; Siwy, Z. S. Gating of Hydrophobic Nanopores with Large Anions. ACS Nano 2020, 14 (4), 4306-4315.

5. Lin, K.; Lin, C.-Y.; **Polster, J. W.**; Chen, Y.; Siwy, Z. S. Charge Inversion and Calcium Gating in Mixtures of Ions in Nanopores. J. Am. Chem. Soc. 2020, 142 (6), 2925-2934.

6. Lin, C.-Y.; Turker Acar, E.; **Polster, J. W.**; Lin, K.; Hsu, J.-P.; Siwy, Z. S. Modulation of Charge Density and Charge Polarity of Nanopore Wall by Salt Gradient and Voltage. ACS Nano 2019, 13 (9), 9868–9879.

ABSTRACT OF THE DISSERTATION

Exploring Non-Traditional Solid-Liquid Interfaces Under Nanoconfinement

by

Jake Wyatt Polster

Doctor of Philosophy in Chemistry

University of California, Irvine, 2022

Professor Zuzanna S. Siwy, Chair

Studying ion transport in nanoporous materials is crucial to a wide range of energy and environmental technologies, including ion-selective membranes, drug delivery systems, and supercapacitors. Many of these applications rely on non-aqueous solvents or non-traditional interfaces, such as hydrophobic surfaces. However, classical descriptions of solid-liquid interfaces fail to adequately describe ion and electrical potential distributions in these non-traditional systems. This dissertation examines what consequences occur when these non-traditional solid-liquid interfaces are placed under nanoconfinement. Specifically, ion transport measurements were performed in a variety of nanodevices, including nanopipettes and nanopores, which acted as model systems for probing non-traditional solid-liquid interfaces.

My first project details the breakdown in classical electrical double-layer models when moving from water to an organic solvent. This project demonstrates that in a model system, acetonitrile at a silica interface, the solvent molecules organize in a well-defined lipid-bilayer-like structure. This solvent organization in turn dictates the ionic distribution at the interface, which stands in stark contrast to traditional models, where ion distribution

is determined by native surface charge. A combined approach of ion-transport measurements in nanopipettes, surface-selective spectroscopy, and molecular dynamics simulations were used to probe the acetonitrile-silica interface in a variety of salts, including $LiClO_4$, $NaClO_4$, $LiBF_4$, and $LiPF_6$. These findings emphasize the importance of including solvent molecules and ions explicitly in descriptions of solid/liquid interfaces.

My second and third project examine hydrophobic interfaces in nanopores. Single hydrophobic nanopores are ideal model systems for studying nanoconstricted hydrophobic surfaces and wetting/dewetting transitions at the nanoscale. In these projects, ion current measurements in single silicon nitride nanopores containing a hydrophobic-hydrophilic junction were performed in a variety of salt types and concentrations. The results show that transport properties in these devices are highly dependent on the size, hydration strength, and concentration of the solvated ions. Large, polarizable anions, such as bromide and iodide, facilitate pore wetting, with an unusual dependence on electrolyte concentration – higher concentrated solutions more easily wet the devices, in contrast to bulk surface tension trends. Experimental results were supplemented with molecular dynamic simulations that revealed key characteristics of the asymmetric nanopore system. These results are essential for designing nanoporous systems that are selective for ions of the same charge as well as understanding the fundamental role of ion hydration on the properties of solid-liquid interfaces.

Chapter 1: Introduction

Nanopores Are All Around Us

Despite all the chemistry and physics terms I will introduce in this thesis, the term "nanopore", the key research system I used in my graduate research, is as straightforward as its name. Nanopores are pores (holes) with diameters ranging from $<1-100$ nanometers (nm). Nanopores can have varying lengths, but their diameters must remain on the nanoscale. One billion (10^9) nanometers fit into one meter; to put this into prospective, the distance to the moon is ~ 0.3 billion meters, so comparing the size of a meter stick to one and a half round trips to the moon is a fair comparison for meters to nanometers. Nanopores are even so small that they cannot be seen with an optical microscope–one must employ use of an electron microscope (detailed in chapter 2) to examine these tiny holes. One might question why, if we cannot even see these tiny holes with our eyes, would I study nanopores. And the reasons for studying nanopores mirrors those for this hesitation: in the small size dimensions of nanopores, surface chemistry and electrostatics have much more pronounced influence on transport through these pores. Being a water molecule entering a nanopore would be like walking in a group of ~ 4000 people in an area the size of California and then being forced into a Boeing 737 plane. Suddenly the entire group (despite being extremely uncomfortable, no doubt) will see and interact with the "walls" of this area – if there is something on the wall that attracts a subgroup of people, say a TV broadcasting a sports event, those individuals will get "stuck" and travel slower through the "pore". In this hyper-confined space, nearly every ion/water molecule/dissolved species/person will interact with the "walls" – making the wall's chemical properties extremely important. If the properties of these "walls" are strong enough to prevent a group of ions/people from entering the pore/airplane, exquisite

selectivity can be achieved that would not be possible with larger areas (say, a football field instead of the airplane example). In this way, nanopore research is fascinating to me due to growing number of applications of the technology, including water desalination, chemical separations, and energy storage, as well as fundamental science to be learned through nanoconfined species.

Biological Nanopores

Nanopores occur in naturally in biological systems and can be synthetically fabricated in a laboratory setting. Biological nanopores are essential structures for living organisms; primarily located in cell membranes, nanopores help preserve homeostasis in the cell by regulating ion and water transport. One example of a biological nanopore is the water channel, aquaporin (AQP1, Figure 1.1A, left). Aquaporin is located in the cell membrane and regulates osmotic water transport between the cytoplasm of the cell with the extracellular environment. Aquaporin can transport 3×10^9 water molecules per second per channel, with the transport activation energy being only slightly larger than the bulk water self-diffusion rate.[1] Aquaporin has an hourglass shape with an opening diameter of 1.5 nm and narrowing to 2.8 Angstroms (Å, 10^{-10} m) at the thinnest section.[2] This narrow section, called the selectivity filter, is the key to achieving such selective transport. The selectivity filter repels both positively charged ions (cations) and negatively charged ions (anions); only allowing water molecules to pass through. Cations are rejected because the selectivity filter is dominated by positively charged amino acids that electrostatically repel positively charged species. You can think of this like the positive pole of a magnet repelling the positive pole of another magnet. Anions are rejected because they cannot effectively shed their waters of hydration and are too large to enter

the pore. You can think of this like not being able to find a babysitter for your young children and thus cannot attend the movies. Water molecules, on the other hand, are swiftly transported through the pore in a single-file line; their transport being stabilized by the same factors that repel all ions.

In a similar way to the water channel, which selectively transports only water molecules, other biological nanopores are structurally tailored to transport only specific ions. One of the most ion-selective biological nanopores is the potassium channel, KcsA (Figure 1.1A, right). The potassium channel is located in the cell membrane and transports potassium ions (K^+) close to the diffusion-limited rate (10^7 ions per channel per second).[3] In addition to fast K^+ transport, KcsA has over 10,000 times selectivity for K^+ over sodium ions (Na^+), an ion with the same charge and a smaller radius.[4] The key to KcsA's exquisite selectivity resides in its selectivity filter: a 12 Å long segment decorated in carbonyl groups with an average diameter of 3.4 Å.[5] The small size requires that any species diffusing through the pore must shed its waters of hydration, requiring significant energy input. This energy input can be compensated for by replacing the shed water with favorable interactions from pore wall groups. In KcsA, the selectivity filter's carbonyl groups have lone pairs of electrons that create a coordination environment akin to a hydration shell. The selectivity filter's geometry is such that a dehydrated K^+ ion will fit perfectly, but a Na^+ ion would be too small.[4] The energy for shedding Na^+ hydration shell is not off-set by the carbonyl groups in KcsA's selectivity filter, making the pore highly selective for K^+ ions. Research on the structure of AQP1 and KcsA was awarded the Nobel Prize in Chemistry in 2003, emphasizing the importance of understanding the structure and function of biological nanopores.
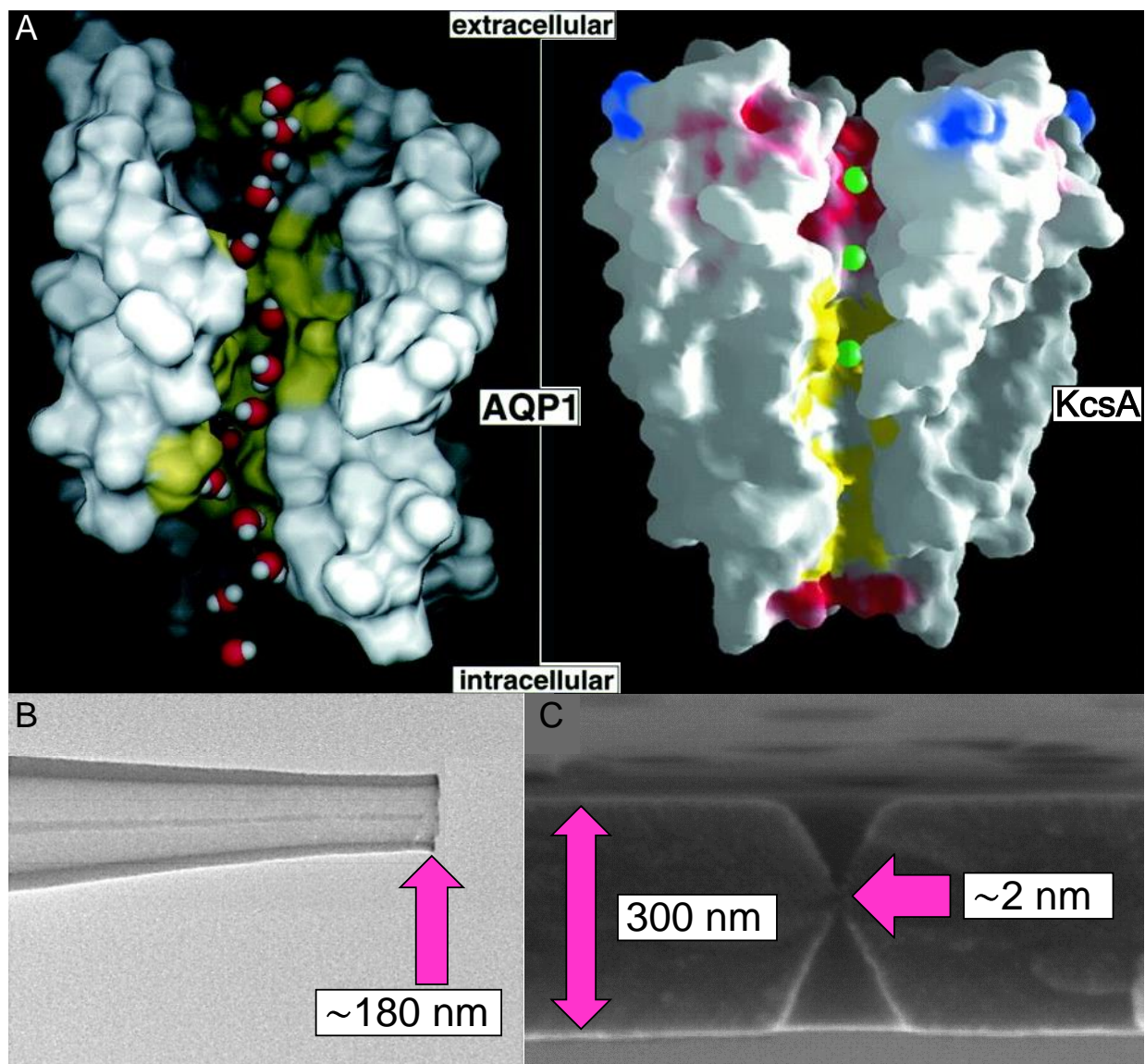
Figure 1.1: Examples of biological and synthetic nanopores. (A) Left: Surface representation of AQP1 structure. The selectivity filter is located near the center of the pore, at its thinnest region. Figure from de Groot, B. L.; Grubmüller, H. Water Permeation Across Biological Membranes: Mechanism and Dynamics of Aquaporin-1 and GlpF. *Science* **2001**, *294* (5550), 2353.[1] Reprinted with permission from AAAS. (A) Right: Surface representation of KcsA. Green spheres represent K^+ ion positions. The selectivity filter is located in the red, electron dense region at the extracellular end of the pore. Figure from Doyle, D. A.; Cabral, J. M.; Pfuetzner, R. A.; Kuo, A.; Gulbis, J. M.; Cohen, S. L.; Chait, B. T.; MacKinnon, R. The Structure of the Potassium Channel: Molecular Basis of K^+ Conduction and Selectivity. *Science* **1998**, *280* (5360), 69.[4] Reprinted with permission from AAAS. (B) Transmission electron microscopy image of a glass nanopipette. Glass nanopipettes are pulled to various sizes by modulating the pulling force and time. Figure adapted with permission from Perry, D.; Momotenko, D.; Lazenby, R. A.; Kang, M.; Unwin, P. R. Characterization of Nanopipettes. Anal. Chem. 2016, 88 (10), 5523–5530.[6] Copyright 2016 American Chemical Society. (C) Scanning electron microscopy image of

a track-etched silicon nitride nanopore. The double conical geometry was achieved by etching from both sides of the film. Figure adapted from Vlassiouk, I.; Apel, P. Y.; Dmitriev, S. N.; Healy, K.; Siwy, Z. S. Versatile Ultrathin Nanoporous Silicon Nitride Membranes. *PNAS* **2009**, *106* (50), 21039–21044.[7]

Controllable transport is key for many biological nanopores

An interesting aspect about biological nanopores is that they can be gated. Gated simply means that the nanopore can be opened and closed for transport because of external stimuli. The most common stimuli are voltage changes, ligand binding, and mechanical stress.[8] Cells will naturally have an electric potential due to the unequal concentrations of ions inside and outside of their membranes. When this potential is disturbed, voltage-gated ion channels can change their conformation and allow specific ions to transport across the cell membrane. Examples of voltage-gated channels are the various sodium channel ($Na_v1.1$ through $Na_v1.9$).[9] Sodium channels are often found in parts of the nervous system and skeletal and muscle cells.[9] For this reason, local anesthetics target sodium channels to block them from transmitting action potentials (electrical signals) to the brain.[10]

Ligand-gated ion channels undergo conformational changes when a ligand, or messenger molecule, binds to their structure. Examples of ligand-gated ion channels are γ-aminobutyric acid type A ($GABA_A$) receptors. $GABA_A$ receptors are anion-selective channels crucial to the central nervous system.[11] When two GABA molecules bind to a $GABA_A$ receptor, the central ion channel in the receptor opens up and allows permeation of Cl^- and HCO_3^-.[11] These ions establish a new equilibrium membrane potential that makes it harder to form action potentials, thus inhibiting communication between nerve cells.[11,12] Drugs in the benzodiazepine class are positive allosteric agonists to $GABA_A$;

increasing the opening frequency for the channel, thus reducing the chance of firing an action potential and leading to inhibited neuron activity.[12]

Mechanical stress or pressure gated ion channels create electrical signals when physically displaced. Ion channels gated by stress are called mechanotransducer (MT) channels. The most straightforward example of this type of gating occurs in hair cell transducer channels.[13,14] When sound waves enter the ear, small pointed tubes on top of hair cells are slightly displaced, causing physical strain and gating MT channels, which are cation channels particularly permeable to calcium ions.[13,14] The change in membrane potential releases a neurotransmitter that then carries the signal to the central nervous system.[15]

Properties of biological nanopores are of high research interest

Biological nanopores, both gated and not, serve as inspirations for nanoscale device development. Scientists create synthetic nanopores that mimic biological channel properties, such as surface charge, geometry, and hydrophobic character, with the aim to design devices boasting the same superb selectivity and ion transport seen in biological channels. Nanopore experts have also found new ways to utilize synthetic nanopores, including chemical and biological sensors and DNA sequencing. Nanopore technology has also made its way into commercial products, such as portable DNA sequencing (Oxford Nanopore product SmidgION), waterproof breathable technology (Gore-Tex),[16] molecular sieves/desiccants, and breathable surgical tape (3M product Micropore Surgical Tape),[17] to name a few. All these products incorporate some form of nanopores in their usage—including tiny pores in single-atom thick graphene that allow DNA to pass through and provide distinguishing signals between base-pairs, hydrophobic nanopores

that allow for water vapor to pass but not liquid water, pores that are small enough to trap water but too small to trap organic solvents, and pores that can draw moisture away from wounds using capillary action. Synthetic nanopores offer extreme control over pore size and surface charge, making them an ideal medium to research fundamental and applied sciences.

Lab-Made Nanopores

Synthetic nanopores are made from polymers or solid-state materials and provide notable advantages in stability compared to biological ones. Synthetic nanopores can be studied and operated in varying temperatures, pH levels, salinity, and solvents. Conversely, biological nanopores, although boasting extreme levels of selectivity and structure controlled with atomistic precision, do not survive well outside of physiological conditions. I have dedicated chapter 4 to discuss my work on organic solvents under nanoconfinement, which would be exceptionally difficult to investigate in biological nanopores. Another advantage of synthetic nanopores is the tunability of their dimensions, both pore opening and length, although preparation of nanopores with opening diameters less than 1 nm remains difficult.

Synthetic nanopores can be fabricated in a variety of materials. Research in the Siwy lab focuses on nanopores created in polymer membranes, such as polyethylene terephthalate (PET), polycarbonate (PC), or poly(4,4'-oxydiphenylene-pyromellitimide) (Kapton), and solid-state films, such as silicon nitride (SiN_x) and silicon dioxide (SiO_2, or glass). We fabricate nanopores in these materials using a variety of techniques that I will detail in chapter 2.

Single nanopores in polymer films are prepared by the track-etch technique. Briefly, each polymer film is irradiated with a single heavy ion having total kinetic energy ~10^9 electronvolts (eV) followed by wet chemical etching. This irradiation step is performed at the Institute for Heavy Ions Research in Darmstadt, Germany. Chemical etching, which determines pore shape and diameter, is performed at UC Irvine. Track-etched polymer pores (PET, PC, and Kapton) have carboxyl groups on the surface and pore walls, making the pores negatively charged in neutral and basic solutions. Additionally, the carboxyl group allows the pore to be chemically modified through amide bond formation with an amino group of a target molecule, detailed in chapter 2.

As an alternative to polymer films, solid-state films are another system for nanopore research. Nanopores can be made in solid-state films by the track-etch method, like polymer films, but there are additional techniques made available to solid-state films (detailed in chapter 2), such as drilling by focused ion beam or electron-beam in a transmission electron microscope. Solid-state films are stable in all organic solvents of interest, making them very attractive options for researching ion transport in non-aqueous systems. Silicon nitride and silicon dioxide nanopores are terminated in silanol groups, which results in reported isoelectric points (pH when the surface has no net charge) ranging from 4-8.[18–26] Silanol groups also allow the SiN_x and SiO_2 nanopores to be chemically modified with silane coupling, opening the pores up to many potential surface properties (described in chapter 2). Images of solid-state nanopores can be found in Figure 1.1B (glass micropipette) and 1.1C (SiN_x film).

Other nanopore systems, although not directly discussed in this thesis, are ever expanding and exciting. Some notable systems and relevant references include: carbon nanotubes (CNT);[27] molybdenum disulfide (MoS_2);[28] and graphene.[29,30]

Although nanopore research is very diverse, not all nanopores are created equal. There has been a great scientific interest in preparing nanopores with diameters not only below 10 nm but even below 1 nm, making these structures comparable in size to biological nanochannels. These nanopores are often made in pursuit of new physicochemical phenomena that accompany ion and solvent transport. One example of an effect induced by nanoconfinement is ion selectivity. Ion selectivity will be detailed more in chapter 3, but briefly, a negatively charged nanopore, when in contact with an electrolyte solution, will be predominantly filled with positively charged ions. The ratio of positive to negative ions in a negative nanopore roughly correlates to its selectivity, with smaller diameter nanopores having the highest selectivity. To this end, much research is being done on extremely small nanopores. In fact, the Siwy lab is part of a Department of Energy (DOE) Energy Frontier Research Center (EFRC) called the Center for Enhanced Nanofluidic Transport (CENT), dedicated to investigating new scientific phenomena in single digit nanopores (SDN), or nanopores with diameters <10 nm. The EFRC is centered around investigating seven critical knowledge gaps in SDN systems, two being enhanced ion selectivity and nanoscale solvation seen in SDNs. I will be discussing my work in these knowledge gaps in chapters 4, 5, and 6. Details about CENT and the other critical knowledge gaps are found in Ref. [31].

Within the nanopore field, we are often inspired by the previously described biological nanochannels. We design our nanopore devices to mimic their surface

properties to try and achieve similar levels of selective transport, or design similar interfaces to better understand the fundamentals of nanoscale ion transport. These ideas inspired my PhD research and lead me on a scientific journey at the interface of physical chemistry, biophysics, and material science. My dissertation focuses on nanopore devices, and in particular investigating non-traditional interfaces under nanoconfinement. The term non-traditional simply means interfaces that are not well described by our fundamental models of surfaces, described more in chapter 3. The fundamental models of charged interfaces are typically modeled in aqueous solutions, however many disciplines (energy storage, chemical purifications and separations, to name a few) utilize non-aqueous solvents for their nanoscale experiments. To that end, my first project investigated acetonitrile, a non-aqueous solvent, in a silicon nanopipette. Another missing component to our traditional models of charged interfaces is the importance of ion size and polarizability. Ions of the same charge are treated exactly the same, regardless of their size. However, my second and third project look at hydrophobic interfaces, where the charge *and* size of an ion actually dictates its distribution near the surface. Although non-traditional, the nanoconfined interfaces I explore in this dissertation are crucial to many aspects of science, including understanding the fundamentals of nanoscale ion transport, designing next-generation chemical separation devices, creating nanoscale drug delivery devices, and more.

Chapter 2: Fabrication and Modification Techniques for Nanopore Devices

Nanopore Material Synthesis

Before we can fabricate nanopores, the pore material must be synthesized. Although we do not typically synthesize the pore material in the Siwy lab, it is important to understand the fabrication details. Information crucial to nanopore research, such as available chemical functional groups, charged surface species, and material stability, can be uncovered by understanding the fabrication process.

Glass micropipettes are formed by pulling a heated glass tube symmetrically from both ends with varying force and pulling time.[32] Different tip diameters are made by varying the force and pull time. Glass pipettes can be prepared easily and inexpensively, making them a common tool in nanopore research. An image of a glass pipette puller is shown in Figure 2.1. Glass pipette diameters I used in my research ranged from 400 – 500 nm.

Figure 2.1: Image of glass pipette puller. A glass tube is first is slid into apparatus, with the center of the tube at the red arrow tip. Then a heating unit heats the center of the tube. Once red-hot, cables on both ends of the tube pull it in the direction of the orange arrows, stretching and shrinking the tubes. This process is called a "pull" and can be repeated multiple times to achieve the desired pipette dimensions. Image provided with permission from Mark Flaming. Copyright 2022 Sutter Instrument Company.

Polymer films are created by polymerizing monomer units together to form long molecular chains that are spin coated to create films. All nanopore devices I created in polymer films were made using the track-etch method, which is described in detail in the next section. Polyethylene terephthalate (PET) is synthesized through an esterification process between ethylene glycol and terephthalic acid at elevated temperature and pressure (Figure 2.2A).[33] In the Siwy lab we purchase 12 micrometer (μm) thick PET films that we can create devices with just a single nanopore or over a billion nanopores as needed. Polycarbonate (PC) can be synthesized through a variety of routes, but the traditional method involves reacting a sodium hydroxide solution of bisphenol-A (BPA) with phosgene in dichloromethane (Figure 2.2B).[34] Like with PET, PC films are 12 μm thick and can contain a single nanopore or over a billion. Kapton is synthesized through a condensation reaction between pyromellitic dianhydride and 4,4'-oxydianiline (Figure 2.2C) in an aprotic dipolar solvent (e.g. *N*,*N*-dimethylformamide, DMF).[35,36] The Kapton membranes we purchase are also 12 μm thick, with nearly identical pore control as in PET and polycarbonate films. Polymer films are excellent materials for creating nanopores with high aspect ratios (length to radius ratio of pore).

The solid-state films we fabricate nanopores in are made through chemical vapor deposition (CVD). In CVD, chemical precursors (SiH_4 or $SiCl_2H_2$ and NH_3, typically for SiN_x) are vaporized (if not already vapors) and transported over a substrate (silicon wafer) where the precursors deposit and react to form the insulating film (SiN_x synthesis shown in Figure 2.3).[37–39] The reason for the subscript "x" in silicon nitride is because the films are made of amorphous silicon nitride and can have varying Si/N ratios. Typically the amorphous ratio is roughly 3:4 silicon to nitrogen, making Si_3N_4 another common

abbreviation for the film.[39] We believe the Si/N ratio in our films does not significantly influence our nanopore devices (as long as all the films are prepared the same), however it might influence the isoelectric point of the surface when in contact with an electrolyte solution. Films of SiO_2 are also made with CVD by simply using different precursors (replacing NH_3 with O_2, typically).[38] Films made with CVD have well controlled thicknesses (usually in the 10s of nm), which in turn allows us to create nanopores with well-defined lengths and small aspect ratios. By using films with a variety of thicknesses, we can straightforwardly investigate how pore dimensions influence transport properties.
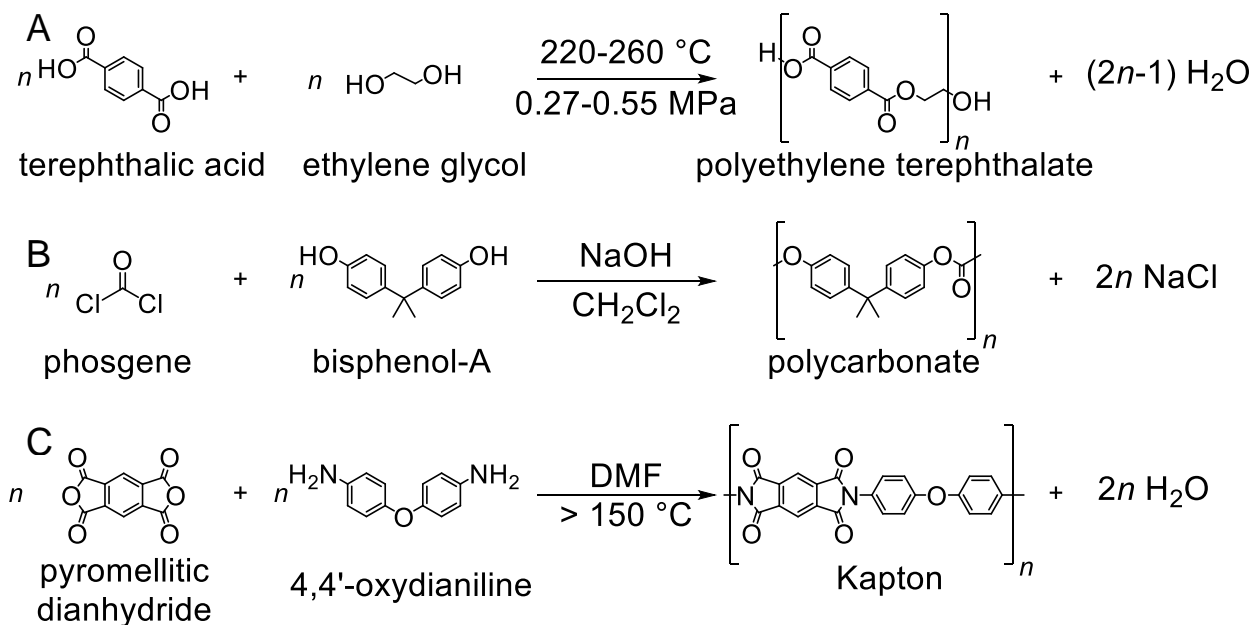
Figure 2.2: Synthetic scheme for polymers utilized as films. (A) Synthesis of PET membranes. (B) Synthesis of polycarbonate membranes. (C) Synthesis of Kapton membranes.
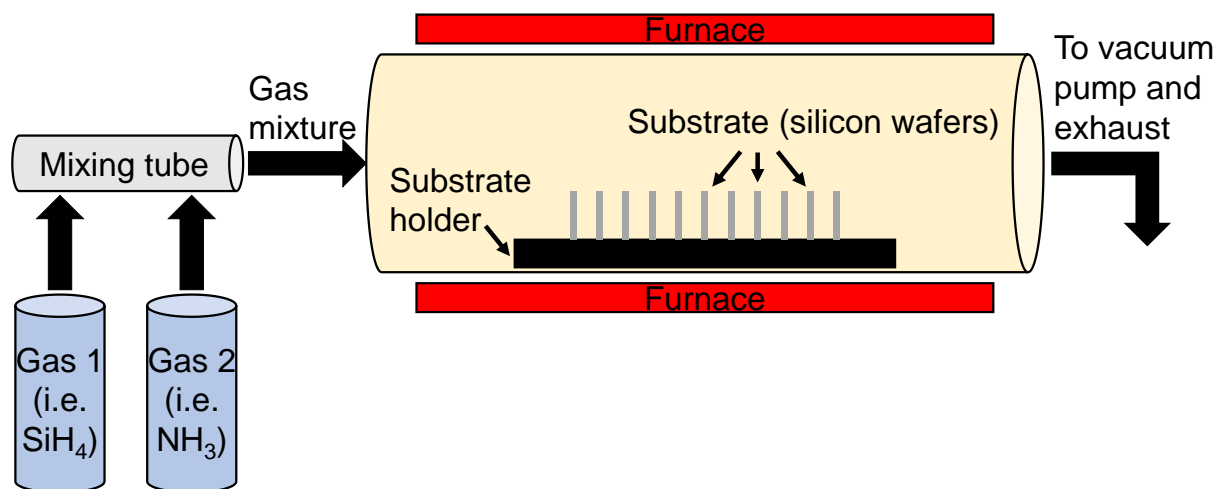

Figure 2.3: Simplified example of CVD. Precursor gasses are mixed and fed into the reactor where they adsorb to the substrate surface, diffuse on the surface, and react to form films.

Nanopore Fabrication

To expand both the nanopore field and the general understanding of interfaces, nanopore fabrication techniques advanced to achieve smaller pores and more dimensional control. Nanopores can be fabricated in two general approaches: building the pore in negative space (i.e. creating everything surrounding the pore), or controllably destroying a material to make the pore (i.e. removing material to create the pore).

The first approach (building the pore in negative space) is typically done through a common semiconductor fabrication technique called photolithography. I will only briefly detail this technique, as I did not use it for any work in this thesis. Nanopores made through photolithography utilize a sacrificial layer to create nanochannels (these are typically called nanochannels since they are often rectangular in shape and only have one dimension on the nanoscale). A few-nanometer-thick layer of sacrificial material is deposited onto a substrate using CVD. This layer can be manipulated by using masks to selectively etch portions (say, to achieve specific channel dimensions for length and width). Once the channel has appropriate length and width (remember, height is on the nm range and is controlled with CVD), a scaffold (of different material!) is built around this layer. The scaffold serves to protect the channel from debris, provide reservoirs for testing solutions, and to allow access to testing equipment, such as pellet electrodes. In the final step, the sacrificial layer is etched away using a chemical etchant, leaving a nanochannel with well-defined dimensions. A detailed technical description of this sacrificial layer process can be found in Ref. [40].

I will divide the second approach (controlled destruction to create the pore) into three categories: track-etching, drilling, and dielectric breakdown. Track-etching utilizes

18

heavy ions with ~GeV total kinetic energy that create damage tracks and wet chemicals to etch nanopores. Track-etching can be performed in both polymer and solid-state films and is the most straightforward way to fabricate films with a controlled number of pores—between 1 and billions of pores per cm^2. Drilling involves focusing ions or electrons of ~keV energy, depending on the instrument, at a thin, solid-state film. The particles will have enough energy to controllably destroy the film in a small area and create a nanopore by eroding small amounts of material. Drilling can create nanopores with different shaped openings as well as multiple nanopores, although much slower than track-etching. In dielectric breakdown, a solid-state film is placed between two electrolyte reservoirs at different (large) voltages. The high voltage drop across the film induces film breakdown and creates a nanopore. The exact mechanism of dielectric breakdown is still being studied, but the technique can successfully and repeatedly create nanopores with varying diameters. These three techniques are methods I utilized in my graduate study to fabricate nanopores. Each has their benefits and drawbacks, which I will detail below.

Track-Etch Nanopore Fabrication

The track-etch method begins by irradiating the substrate (polymer or solid-state film) with high energy particles to generate latent damage tracks. This step is commonly performed by either bombarding the film with nuclear fission fragments or using ion beams from particle accelerators.[41] The films we purchase are made using the second method at a linear accelerator (UNILAC) in the GSI accelerator center in Darmstadt, Germany. The 12 µm thick polymer films (PET, PC, or Kapton) are irradiated with heavy ions (such as U$^+$) having extremely high kinetic energies (11.4 MeV), capable of penetrating ~100 µm thick polymer material.[41,42] Since our polymer films are only 12 µm

19

thick, up to seven films can be stacked together and irradiated at the same time. A detector placed behind the films quantifies how many ions penetrated the films. The number of ions penetrating the films is equal to the number of pores in the film once etched. To control the number of ions, the ion beam can be defocused and a metal shutter can block ions such that only one ion reaches the films. In this way, films with 1 to >10^9 latent damage tracks per square centimeter can be made, producing films with the same number of pores once etched.

To create the nanopores, a single polymer film is first irradiated with an ultraviolet (UV) lamp for one hour on each side. Treating the films with UV light helps prepare them for etching by increasing the track to bulk etching ratio.[43] Next, the polymer film is placed in a conductivity cell and exposed to an etchant solution. The etchant used depends on the polymer film, with sodium hydroxide (NaOH) for PET and PC films and bleach (NaOCl) for Kapton films.[41] Depending on the desired pore geometry, etching solution is either placed on both sides (cylindrical pores) or only one side (conical pores) of the conductivity cell. A key aspect for controlling pore geometry is manipulating the ratio between the track etch rate (v_t) and the bulk etch rate (v_b). At room temperature v_t is only slightly greater than v_b. Thus, when making a conical pore, the etching solution is at room temperature and only placed on one side of the film and a neutralizing solution (formic acid) on the other side (Figure 2.4A). As the etching solution travels along the damage track, more of the path is exposed to the etchant (v_b) and the pore base grows. Once the etchant reaches the other side of the film, the solution is neutralized by the formic acid. This asymmetric etching procedure creates a conical pore.

On the other hand, cylindrical pores are created when v_t is much greater than v_b. By using elevated temperature, the ratio between v_t and v_b increases such that the damage track is completely etched before significant bulk etching occurs. In addition, etchant is placed on both sides of the film, ensuring symmetrical geometry. Thus, all parts of the pore are etched at the same rate (v_b), creating a cylindrical pore (Figure 2.4B).

Although not currently used in the Siwy lab, previous members created nanopores in track-etched solid-state films, such as SiN_x. Silicon nitride films are irradiated with energetic Bi or Xe ions and subsequently etched with hot phosphoric acid (H_3PO_4) or hydrofluoric acid (HF).[7] Manipulating the vt and vb ratio is generally employed in most track-etching systems to control pore geometry. Regardless of if etching a single cylindrical or 10^9 conical pores, the track-etching process is monitored electrochemically and will be detailed after the fabrication sections of this chapter.
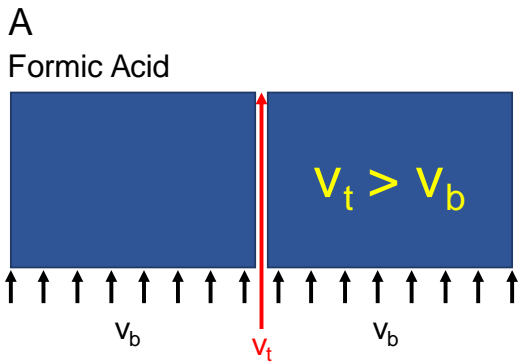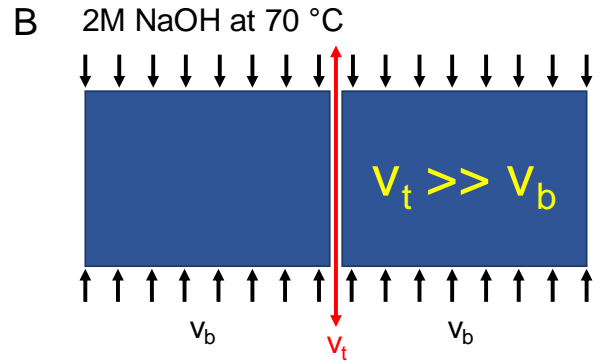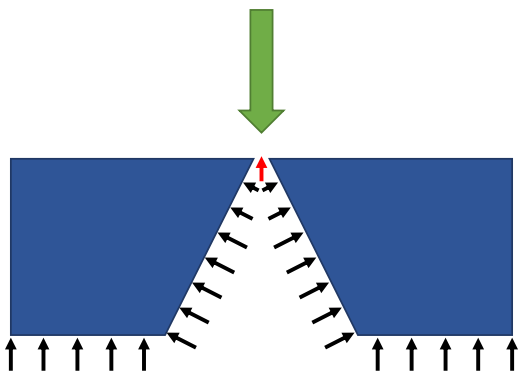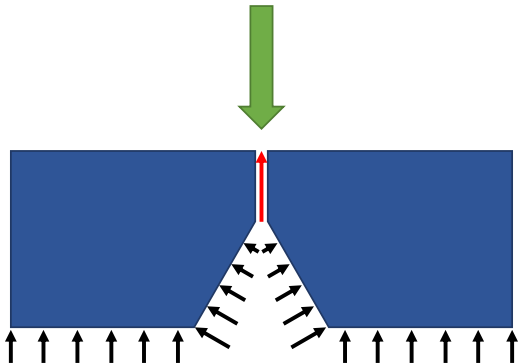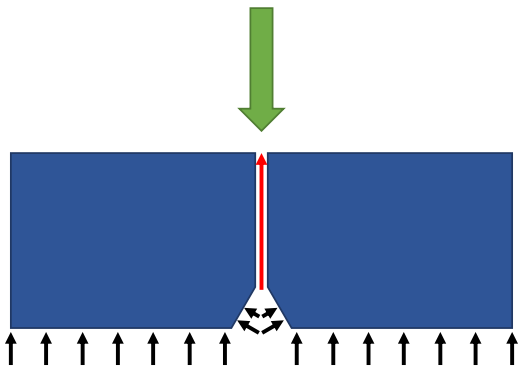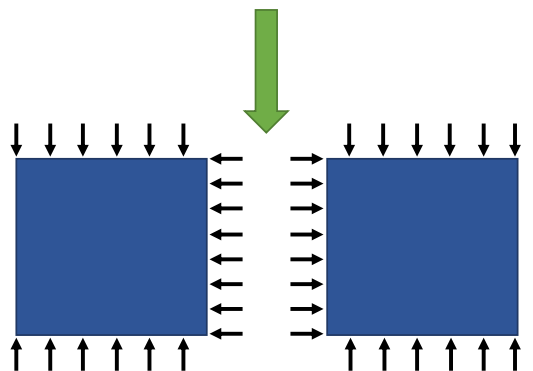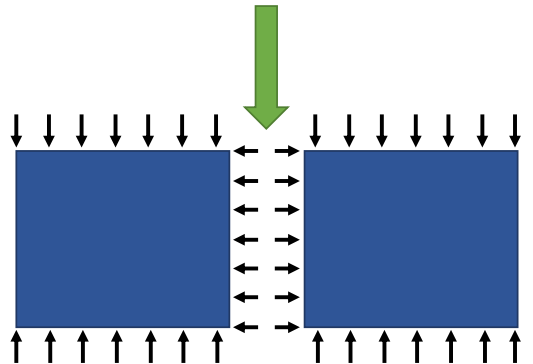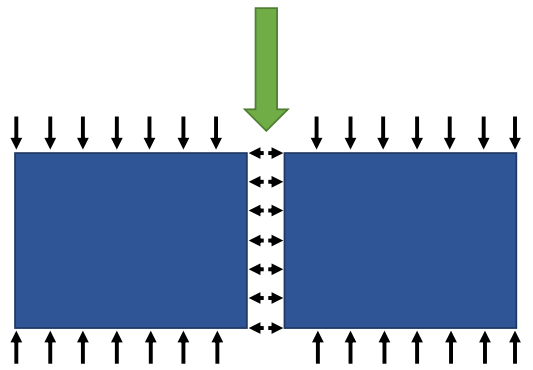
Figure 2.4: Nanopore wet etching mechanisms. (A) Conical nanopores are asymmetrically etched at room temperature. (B) Cylindrical nanopores are symmetrically etched at elevated temperature. Note: figure not drawn to scale.

Drilling Nanopore Fabrication

Drilling nanopores is achieved by using particles with ~keV energy to selectively destroy, or drill, a solid-state film. These particles are either ions or electrons. The technique utilizing ions is called Focused Ion Beam (FIB) and is usually used in conjunction with a scanning electron microscope (SEM). For nanopores drilled with electrons, a transmission electron microscope (TEM) is used. Both SEM and TEM are forms of microscopy that utilize electrons, instead of light, to visualize their target. To generate electrons shot at the sample, an electron source, likely tungsten (W) or lanthanum hexaboride (LaB_6), is heated (thermionic source) or has a large electric potential applied to it (field-emission source).[44] The generated electrons are then focused through a complex system of lenses and finally into the sample. In TEM the electron detector is placed under the target, and only electrons that pass through the target will hit the detector and create an image. For SEM, electrons that bounce off the sample form the image. Thus, pores will appear as bright spots in TEM images (Figure 2.5A) and dark spots in SEM images (Figure 2.5B). Both FIB and TEM drilling can create pores with diameters below 100 nm, down to <1 nm in TEM, but require expensive instrumentation. In addition, the device fabrication time for TEM is significantly slow, usually taking over an hour to create one nanopore (FIB is around five times quicker). Although these drilling techniques are resource-intensive, they give superb control on nanopore opening diameter and provide high quality images of drilled nanopores, easily proving their size.
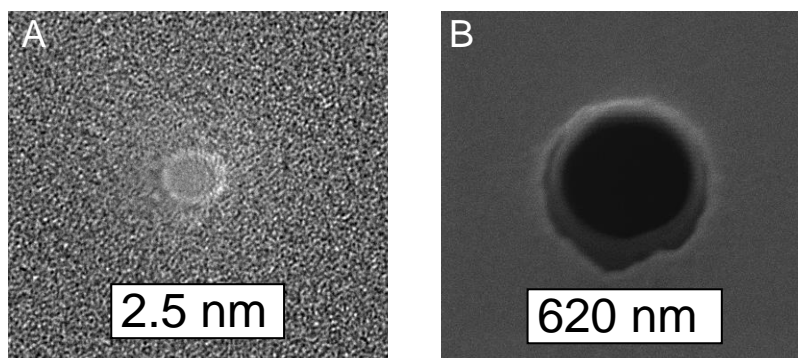
Figure 2.5: Nanopores fabricated (and imaged) in (A) TEM and (B) FIB/SEM with indicated diameters. Diameter size given in image. Image (B) courtesy of Rachel Lucas.

Focused Ion Beam drilling is performed under vacuum, typically in the same chamber as an SEM. A solid-state film is first brought into focus with the SEM and then bombarded with ions from the FIB. One advantage of SEM/FIB nanopore fabrication is that multiple devices can be placed in the imaging chamber at the same time, allowing for higher throughput than TEM drilling. Gallium is the most commonly used ion source in FIB due to its low volatility, inert chemical nature with tungsten, and low melting temperature.[45] Liquid gallium is fed through a tungsten needle and a large electric field pulls the gallium out and ionizes it to Ga^+.[46] The Ga^+ is accelerated towards the sample and enters the sample, spreading the energy through the sample, resulting in expulsion of a particle. This mechanism is called sputtering, and results in selective damage to the sample, creating a nanopore. Film thickness is not a large issue with FIB drilling, since thicker films simply need to be drilled for longer periods of time or with a larger beam current. Nanopores drilled with FIB have diameters in the 10s of nanometers but are capable of being shrunk to the single-digit nanometer scale.[47] Nanopore shrinking is a technique where you hold the pore in focus of an electron beam (from SEM or TEM) for a set amount of time. As the local area is heated from the beam, film material flows on

the surface and into the pore, shrinking the diameter.[47] When shrinking a nanopore the instrument operator must be meticulous, as focusing the beam for too long or at too high of magnitude can actually enlarge the pore. Fabricating nanopores and manipulating their dimensions with high energy particles is an art as much as it is a science.

The other drilling technique utilizes electrons, instead of ions, in a TEM to selectively destroy the solid-state film. A single solid-state film is inserted into the instrument and placed under vacuum. It takes 20–30 minutes for the vacuum to reach appropriate operating pressure. Pulling vacuum is the bottleneck for TEM drilling, since traditional TEM blades can only hold one sample. Compared to SEM/FIB drilling, where >10 samples can be placed under vacuum at the same time, TEM drilling has significantly lower throughput. Once sufficient vacuum is pulled, the electron beam is focused on a single point and held for a few minutes. The high-energy electrons are accelerated into the sample, displacing and ejecting (sputtering) atoms from the surface.[44] The electrons also heat the sample, which can shrink the pore as mentioned above. After drilling the beam is spread and an image of the pore can be captured immediately.

What TEM drilling lacks in throughput it makes up for in nanopore dimensions. Nanopores drilled in TEM are typically under 10 nm in diameter *before* shrinking. With enough practice shrinking, it is possible to fabricate a nanopore with diameter less than 1 nm in a TEM. Recalling from chapter 1, many biological nanopores have diameters less than 1 nm, making TEM drilling an ideal system for mimicking the small dimensions of biological nanopores.

Dielectric Breakdown Nanopore Fabrication

Dielectric Breakdown (DB) is a relatively new method for fabricating nanopores. While track-etching requires a linear accelerator and drilling requires expensive microscopes, DB is a benchtop technique that only requires a voltage source (to create the pore) and a picoammeter (to electrochemically monitor pore formation).[48] In dielectric breakdown, a solid-state film (SiN_x, for example) is placed between two electrolyte solutions and a large ($\geq$10 V) transmembrane potential is applied. The breakdown process is hypothesized to have four main steps, summarized in Figure 2.6A–D. When the large transmembrane potential is applied, an electric field is produced in the solid-state film, polarizing it, and charging the surface with opposite-charged ions (Figure 2.6A). Cations on the positive electrode side are pushed towards the surface and anions on the negative electrode side are pushed towards the surface. Ions at the solid-state film surface undergo redox reactions and electrons/holes can tunnel through the film through traps (defects in the membrane, white boxes in Figure 2.6B). The electric field can also induce bond breaking and produce defects. As breakdown continues, defect sites localize (Figure 2.6C), and eventually a discrete breakthrough event occurs and forms a nanopore (Figure 2.6D).[48] The entire breakdown process is tracked with ion-current measurements (Figure 2.6E) and pore formation is indicated by an increase in current (indicated with green arrow in Figure 2.6E). In the example shown in Figure 2.6E, the current increased by ~60 nA and the fabricated pore was ~12 nm. Since dielectric breakdown is a somewhat stochastic process, the etching times can vary from a few minutes to a few hours. When initially applying the voltage, there will be a large current spike due to capacitive charging (few µA) that will slowly decrease down to 10s of nA, unless a pore is formed before that point. The residual current is called leakage current and is attributed

to the defect-assisted electron tunneling, as shown in Figure 2.6B and C.[48] As shown in Figure 2.6E, a pore formed after only a few minutes. Once a pore is formed, the diameter can be widened by applying a slightly lower voltage and monitoring the current increase. Although DB is less resource intensive as drilling techniques, it does not provide an image of the pore, cannot shrink pores, and sometimes fails to create a pore after many hours. The trade-off for avoiding expensive electron microscopes comes at a price!
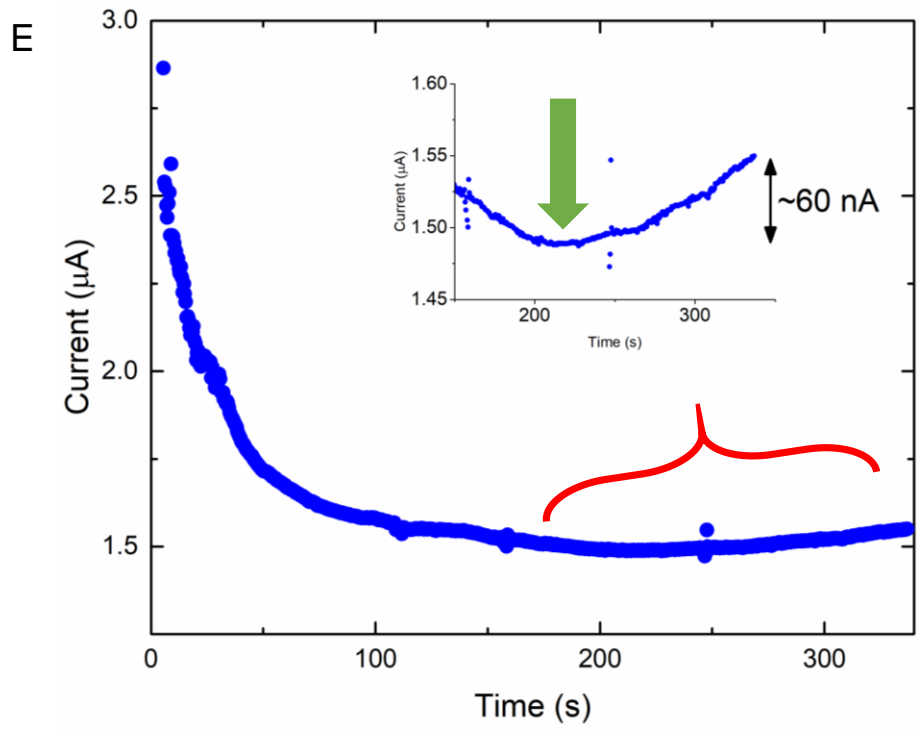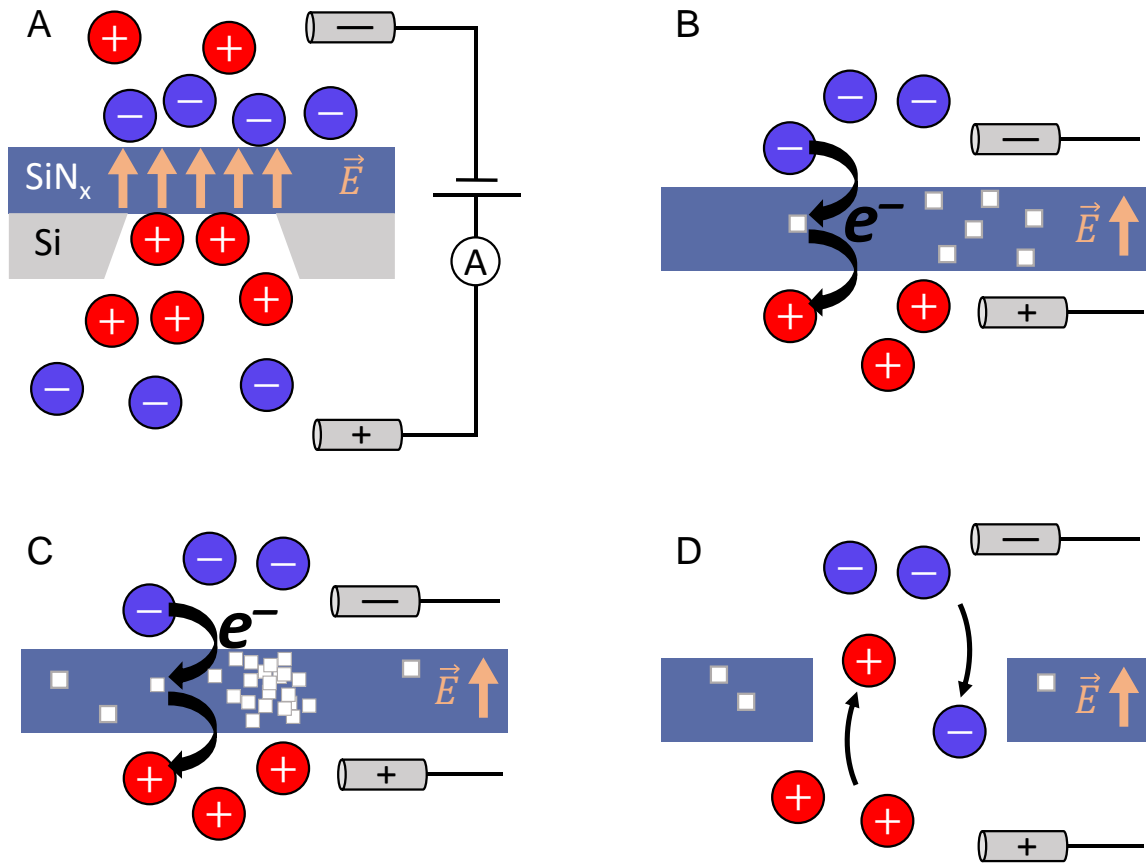
Figure 2.6: Dielectric breakdown process to fabricate nanopores. (A) A large transmembrane potential creates an electric field within the SiN$_x$ film and attracts opposite ions. (B) Ions at the SiN$_x$ surface can undergo redox reactions and electrons/holes can tunnel through the film via trap-assisted transport and produce leakage current. The large electric field and electron/hold tunneling can break bonds and generate heat, increasing the number of defect sites. (C) Induced defect sites localize along a path. (D) A distinct breakdown event occurs, and a nanopore is formed. Breakdown is classified as an irreversible current increase. (E) Current-time trace for dielectric breakdown. Inset shows the current increase due to nanopore formation. The formed nanopore diameter was 12 nm. Figure adapted with permission from Kwok, H.; Briggs, K.; Tabard-Cossa, V. Nanopore Fabrication by Controlled Dielectric Breakdown. *PLOS ONE* **2014**, *9* (3), e92880.[48] Copyright 2014 Kwok et al.

Electrochemical Monitoring of Nanopore Formation

Nanopore track-etching and dielectric breakdown are tracked electrochemically using a picoammeter. We do not electrochemically track nanopore formation with drilling techniques since we will have an image of the fabricated pore from the associated electron microscope (although we still electrochemically confirm their presence). We use a picoammeter to track nanopore formation because nanopores follow the same laws of physics as that of a metal wire, but instead of electrons flowing through a metal wire there are ions flowing through the nanopore. The geometry and dimensions of the nanopore will dictate the ion flow. In our system, the nanopore acts as a resistor since it is restricting the flow of electrolyte. Thus, we can utilize fundamental physics of resistors to model our nanopore systems.

According to Ohm's Law, when a voltage is applied across a conductive path, current will flow by a factor of the resistance. In equation terms, Ohm's law reads:

$$V = IR \rightarrow I = \frac{V}{R} \tag{2.1}$$

where V is voltage, I is current, and R is resistance. From this law, when a constant voltage is applied a system with *larger* resistance will produce *less* current than a system with a *smaller* resistance. Comparing this to a nanopore, a *larger* nanopore will be *less* restrictive (lower R) to electrolyte flow, thus producing *more* current (higher I). On the other hand, a *smaller* nanopore is *more* restrictive (higher R) to electrolyte flow, producing *less* current (lower I). If there is no pore in the film, the system resistance is extremely large and practically zero current will be measured.

We utilize Ohm's Law to help track nanopore creation during track-etching conical nanopores (cylindrical nanopores are etched based off bulk etch rate). Pore formation is monitored by applying a small voltage (1 V) across the film and measuring the produced current. At the start of the etching, no pores exist in the film, meaning the system has extremely high resistance and virtually no current is flowing. When a pore is formed, electrolyte beings to flow through the film, producing current we measure on a picoammeter. Pore breakthrough usually occurs once the current becomes finite ($\sim$0.1 – 0.2 nA, Figure 2.7). Etching can be continued as different experiments and projects require specific nanopore geometries. To halt the etching process, etchant is removed and the pore is flushed with neutralizing solution (formic acid neutralizes NaOH and potassium iodide (KI) neutralizes NaOCl).
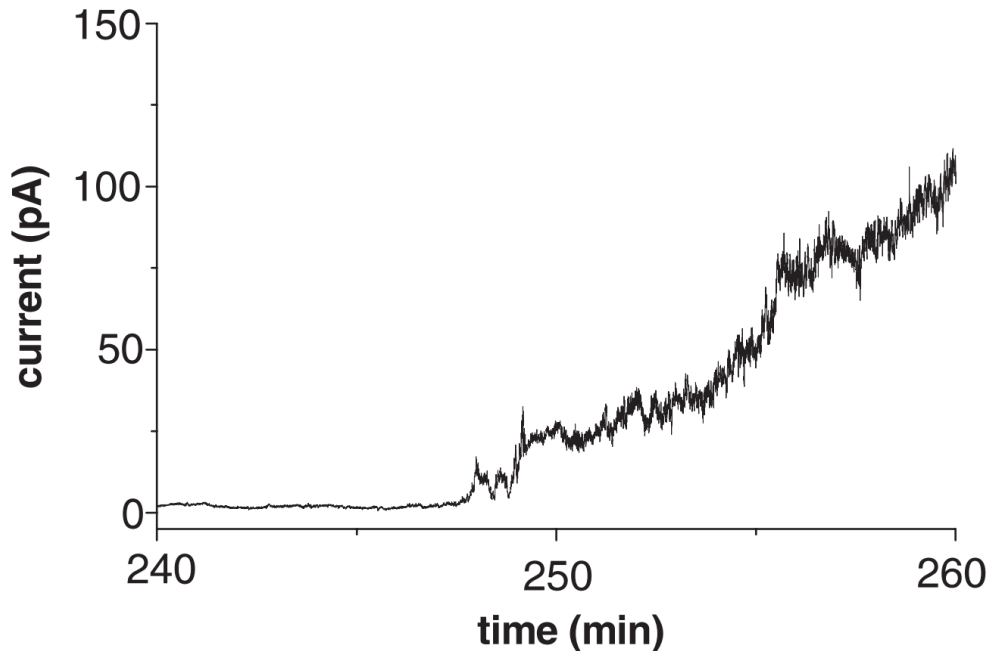
Figure 2.7: Current-time measurements for a nanopore during track-etching. Pore breakthrough occurs at ~248 minutes. Reprinted by permission from Springer Nature Customer Service Centre GmbH: Springer, Applied Physics A: Materials Science & Processing, Electro-responsive asymmetric nanopores in polyimide with stable ion-current signal, Siwy, Z., Dobrev, D., Neumann, R., Trautmann, C., Voss, K, Copyright 2003 Springer-Verlag.[49]

Measuring nanopore dimensions

After the etching solution is neutralized the pore size can be characterized. There are a few ways to determine pore size, with each method having advantages and disadvantages. The most straightforward way is to view the cross-section of a pore using a microscope. Every microscopy technique has a resolving power—the smallest resolvable distance between two features—that scales with the wavelength of source radiation.[38] Optical microscopy uses visible light photons (400 – 800 nm wavelength) and can resolve down two a few micrometers. Since our nanopores are much smaller than the resolving power of optical microscopes, it is impossible to see the pores using visible light. However, electron microscopy utilizes electrons—with wavelengths <1 Å— instead

31

of visible light photons to probe the sample surface, allowing them to resolve down to ~1 nm.[38] In a scanning electron microscope (SEM), electrons are shot at the sample and can either knock an electron out of the sample (secondary electron) or bounce off from the sample (backscattered electrons).[50] Both of these mechanisms produce signals that are collected by a detector and a computer interprets the resulting electron current to create a visible image. Since most of our research is focused on pores less than 10 nm in diameter, utilizing electron microscopy is one key technique to visualize our nanopore geometry.[50]

I previously described how SEM/FIB and TEM drilling are advantageous because the pores can be directly imaged after drilling them. However, for pores created with other techniques, imaging the pores is a slightly more sophisticated process. To view the cross-section of a nanopore in a track-etched film, the film must first be embrittled and then cleaved in half. The polymer films are embrittled by exposing them to ultraviolet (UV) light (310 – 320 nm wavelength) for 10+ hours.[51] By using UV light to embrittle the films, instead of, say, freezing the film in liquid nitrogen, the pore structure remains intact.[52] These cleaved films are then viewed under SEM. Cross-sectional SEM gives valuable insight into etching rates and pore geometry, as you can directly measure the pore diameter and length and evaluate the geometrical shape. An example of a cross-sectional SEM image for a polymer film is shown in Figure 2.8 (a cross-sectional SEM image of a SiN_x pore is in Figure 1.1C). Although this sizing method gives exquisite detail on nanopore geometry, it also destroys the sample and can only be performed on a film with 10^9 pores, making it an impractical technique if samples need to be further tested.
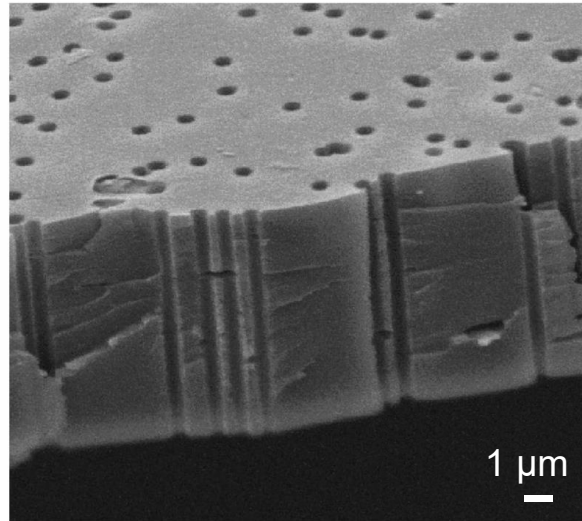
Figure 2.8: Cross-sectional SEM image of track-etched polymer pores. Reprinted from T. E. Gomez Alvarez-Arenas; P. Y. Apel; O. Orelovitch. Ultrasound Attenuation in Cylindrical Micro-Pores: Nondestructive Porometry of Ion-Track Membranes. *IEEE Transactions on Ultrasonics, Ferroelectrics, and Frequency Control* **2008**, *55* (11), 2442–2449.[53] Copyright 2008 IEEE.

A non-destructive way to size a single nanopore is using ion current measurements. In the previous section, I described how our nanopores are modeled as resistors, and we can use this to our advantage when sizing the pores. As stated in Ohm's law, voltage, current, and resistance are all related. This means that by applying a voltage and measuring the current produced, we can determine the resistance of the system, which gives insight into the nanopore size. The system includes the silver/silver chloride (Ag/AgCl) electrodes, which apply the voltage and measure ion current, the electrolyte (1 M KCl), and the nanopore (Figure 2.9). The key aspect of our experimental setup is the two reservoirs are separated only by the nanopore. Thus, it is straightforward to understand the ion transport physics since we know the ions are traveling through the nanopore.
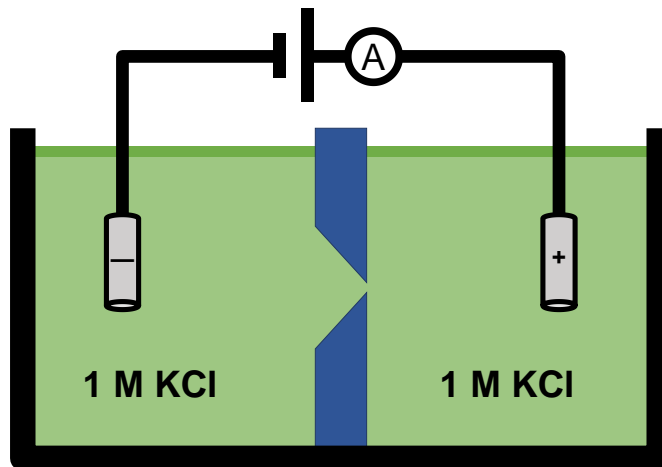
Figure 2.9: Experimental setup for polymer nanopore experiments. Two electrolyte reservoirs are separated by a film containing a single conical nanopore. The system is electronically connected to the picoammeter with Ag/AgCl electrodes.

Since all parts of the experimental setup are all in series, the measured resistance value for the system will be the sum of the resistances of each part. However, the nanopore's resistance is typically in the mega- (10^6) or giga- (10^9) ohm range, while the electrolyte and electrode resistances are together usually less than a kilo- (10^4) ohm.[54] Thus, since the nanopore's resistance dominates the system (99 to 99.999% of total resistance), we attribute all the measured resistance to the nanopore.

Ohm's law also predicts a *linear* response between applied voltage and measured current. In symmetric experimental conditions with a geometrically symmetrical (cylindrical) nanopore, we observe a linear current-voltage response (Figure 2.10C). However, asymmetric current-voltage response occurs when there is electrochemical asymmetry in the system, such as asymmetric geometry or surface charge distribution, or electrolyte concentration gradients. An asymmetric current-voltage response is called

ion-current rectification and is a very important part of nanopore research. More time will be dedicated to ion-current rectification in the theory chapter.

To calculate the nanopore diameter using ion current measurement, we first must make some assumptions. For cylindrical pores, we assume the geometry is a perfect cylinder, and we model the pore as a cylindrical resistor. Cylindrical resistors have their resistance defined as:

$$R = \frac{4L}{\sigma \pi d^2} \tag{2.2}$$

where L is the pore length (i.e. film thickness), σ is bulk conductivity (~10 S m^{-1} for 1 M KCl), and d is pore diameter (Figure 2.10A). Because the films have a known thickness (12 μm for PET and Kapton films), the nanopore length is also known (experimentally the length does decrease by the size of the diameter, however this does not strongly impact the sizing). The resistance is determined by sweeping voltage and monitoring current, which is then plotted as shown in Figure 2.10C. The voltage range for sizing is typically from -100 to 100 mV because low magnitude voltage regions produce the most linear voltage responses. Larger voltage ranges can be used for cylindrical pores, as shown in Figure 2.10C, since they will still produce a linear current-voltage response at 1 V. The slope from the current-voltage curve is equal to the pore conductance (inverse of resistance) as described by Ohm's Law. We then plug the resistance into the equation for a cylindrical resistor and can determine the pore's diameter. This model is most appropriate when using high concentrations of electrolyte, as the surface effects are sufficiently screened (described in theory chapter).[48,55]

When sizing conical pores, there are two different diameters to consider: the small tip diameter, d, and the large base diameter, D (Figure 2.10B). A simplified analytical solution for a conical resistor takes the following form:[56]

$$R = \frac{4L}{\sigma \pi d D} \qquad (2.3)$$

where d is the tip diameter and D is the base diameter; R, L, and σ are system resistance, pore length, and bulk conductivity, respectively. The derivation of this approximation is detailed in Refs. [43,56]. The base diameter (D) is calculated from the bulk etch rate (e.g., 2.13 nm per minute for PET films in 9 M NaOH at 25 °C), since the base diameter begins etching at roughly the bulk etch rate. The tip diameter is determined from the pore's resistance and using the above equation.

A Cylindrical Pore

$$R = \frac{4L}{\sigma \pi d^2}$$

B Conical Pore

$$R = \frac{4L}{\sigma \pi dD}$$

L = 12 µm

C

Cylindrical
d = 1 µm

Current (nA)
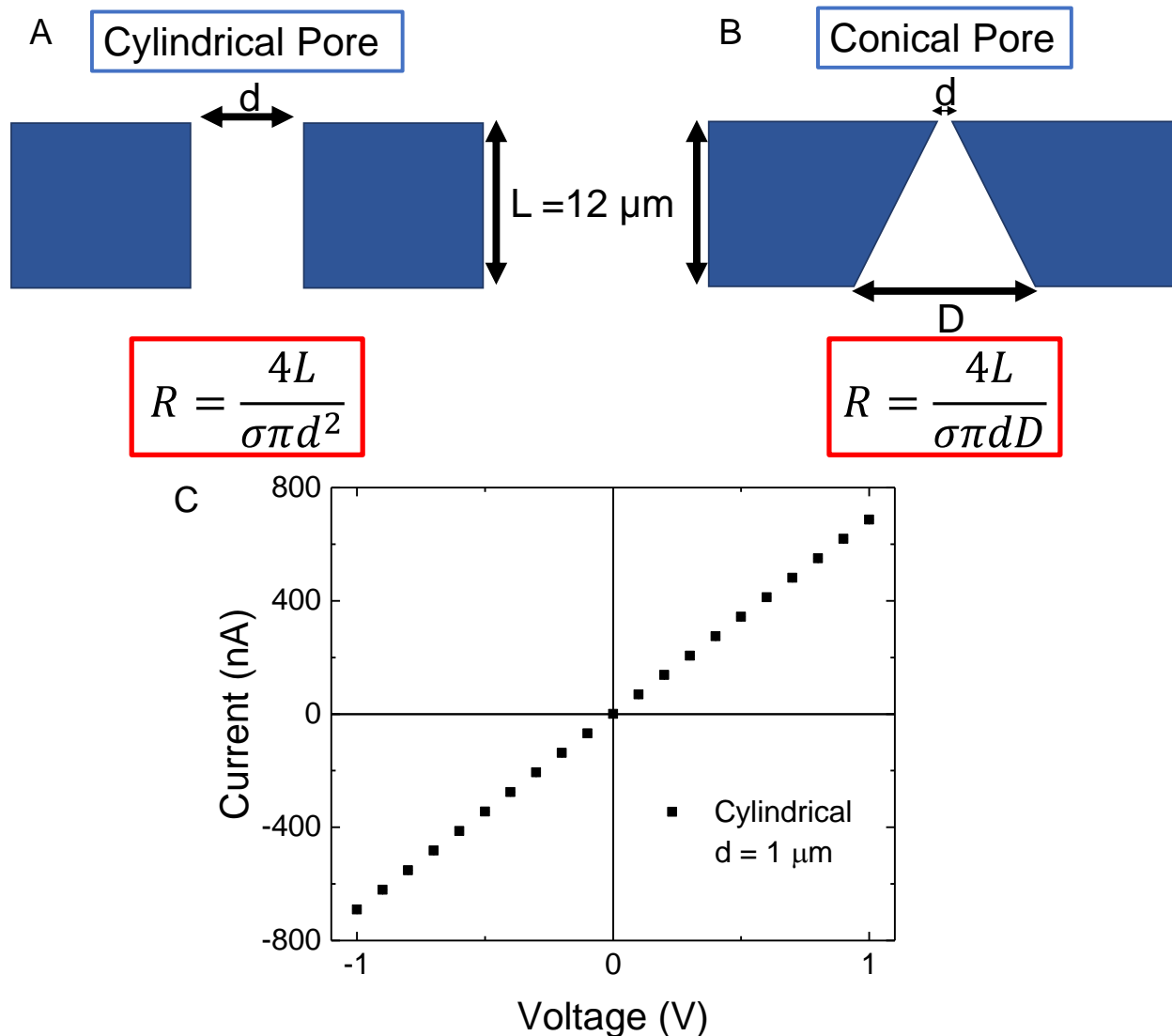
Voltage (V)

Figure 2.10: Electrochemically sizing polymer pores. (A) Cylindrical pores. (B) Conical pores. (C) Current-voltage scan for a 1 µm cylindrical pore.

The above sizing equations fit well for nanopores with high aspect ratios (*i.e.,* pores with lengths many times larger than their diameters). However, as nanopores are made in thinner and thinner films we must include an additional resistance term called access resistance. Access resistance is produced when the lines of electric field converge from the bulk to the pore mouth.[57,58] Access resistance is derived by considering the resistance

between a circular conductive disk (at the pore opening) and a half-spherical electrode at infinite distance.[57] When sizing, the access resistance term is doubled due to contributions from both ends of the pore.[58] When combined, the pore sizing resistance is as follows:

$$R_{total} = R_{channel} + 2R_{access} = \frac{4L}{\sigma \pi d^2} + 2 * \left(\frac{1}{2\sigma d}\right) \qquad (2.4)$$

where L is pore length, σ is bulk conductivity, and d is pore diameter. Sizing these pores with ion current measurements is done in the same way as longer pores, but the L term will be on the order of nanometers instead of micrometers.

Measuring pore diameter by using a conductance model listed above gives a fair approximation on the pore diameter without using expensive microscopes or destroying the sample. However, the models require a few key assumptions for pore properties, such as having only a single pore present, ignoring surface effects on pore resistance, or having a perfectly cylindrical (or conical) pore, to name a few. Based on the fabrication technique used, one or more of these assumptions might be somewhat incorrect, such as TEM-drilled pores having an hourglass shape instead of a perfect cylinder.[59] That being said, the conductance-based model has been shown to be an accurate estimate of nanopore opening diameter based on TEM imaging and DNA translocation experiments,[48,59] although it is still being actively researched to this day.

Chemical Modification of Pore Surface

As prepared pores will have surfaces like the bulk material in which they were fabricated. For example, PET pores will be terminated in carboxylic acid groups with pKa values around 4 – 5.[60] Thus, when studying a PET pore at pH 8, the surface will be negatively charged due to the deprotonated carboxylic acid groups. Depending on the scientific question a specific project is working to answer, a negatively charged surface might be sufficient. However, different experiments require different surface chemistry within the pore. Pores are susceptible to similar surface chemistry modifications as bulk materials, opening the devices up to many modification techniques. Here I will describe three techniques I used extensively during my research projects.

The first surface modification technique I learned, and one commonly used in thin-film research, is electrostatic attachment of a polyelectrolyte. Polyelectrolytes are large, highly charged polymers that have a strong electrostatic attraction to substances with the opposite charge. In electrostatic attachment, a charged polyelectrolyte is exposed to an oppositely charged surface and adsorbs to the surface.[61] The polyelectrolytes are selected such that they have enough charged groups to overcome and invert the native surface charge. In this way, we can change any negatively charged pore into a positively charged pore, or vice versa. For example, to modify our PET pores to have a positive surface charge, we expose the pores to a positively charged polyelectrolyte (e.g., poly(allylamine); process shown in Figure 2.11).
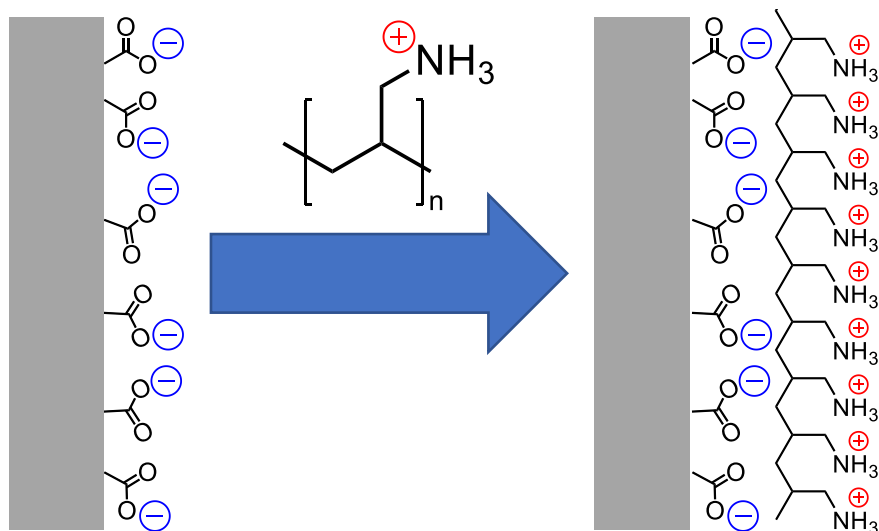
Figure 2.11: Electrostatic attachment of polyelectrolytes to pore surface. A surface terminated in negatively charged, deprotonated carboxylic acid groups is exposed to the positively charged polyelectrolyte, poly(allylamine). The surface is rendered positively charged.

Another powerful modification technique for silicon-based nanopores is silane coupling. Silane coupling creates a bond between a silicon substrate and an organic group. There are nearly endless possibilities for the organic group, which opens our silicon-based nanopore devices to many interesting solid-liquid interfaces and an equal number of fascinating scientific questions. Silane coupling agents are molecules with a silicon atom bonded to an organic group and alkoxy groups. When exposed to water, the alkoxy groups hydrolyze to silanol groups, which then coordinate with hydroxyl groups on the silicon surface.[62] Once heated, water is removed and a siloxane bond is formed, connecting the organic group to the nanopore surface (Figure 2.12).

40
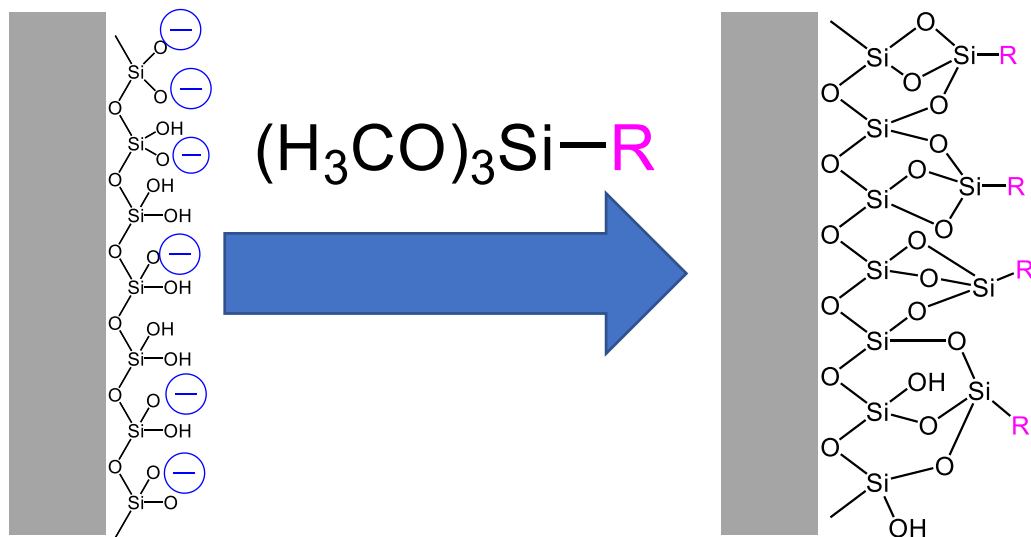
Figure 2.12: Silane coupling with pore surface. A silicon surface is covalently bonded to an organic group (purple R in figure) through a silane coupling agent. The vast diversity of R groups allows us to introduce unique molecules into our nanopore devices.

Another way to introduce various organic molecules into our nanopores is through the third method, EDC coupling. EDC coupling is a crosslinking reaction that bonds a carboxylic acid group with a primary amine, forming an amide bond.[63,64] This technique can be used on a carboxylic acid terminated pore, such as PET, to introduce any group that has a primary amine. For example, our group used EDC coupling to decorate a carboxylic acid terminated nanopore with DNA and crown ethers.[65] The EDC coupling mechanism involves first exposing the carboxylic acid surface to EDC (1-ethyl-3-(3-dimethylaminopropyl)carbodiimide)) to form an unstable intermediate *O*-acylisourea.[64] This intermediate can then be reacted with the primary amine to form an amide bond, completing the coupling. However, the *O*-acylisourea intermediate can quickly hydrolyze in aqueous solutions, meaning that the coupling process can be slow or outright fail without an activation step. To make our EDC coupling more efficient, we expose the carboxylic acid surface to EDC and an excess of *N*-hydroxysulfosuccinimide (sulfo-NHS).

41

The sulfo-NHS reacts with the *O*-acylisourea intermediate, forming a sulfo-NHS ester intermediate that is very reactive towards amine groups.[64] The sulfo-NHS activation step ensures a fast and efficient coupling reaction. The entire EDC/sulfo-NHS modification mechanism is shown in Figure 2.13.

With these modifications we can modulate a nanopore surface to have a specific surface charge, chemical functional group, wettability, or other property. Every physical and chemical aspect of a nanopore's surface strongly influences the transport through the nanopore and has direct applications to pore selectivity. In the next chapter I will describe the theory of ion transport through our nanopore devices and shed light on the importance of surface modifications.

O-acylisourea
intermediate
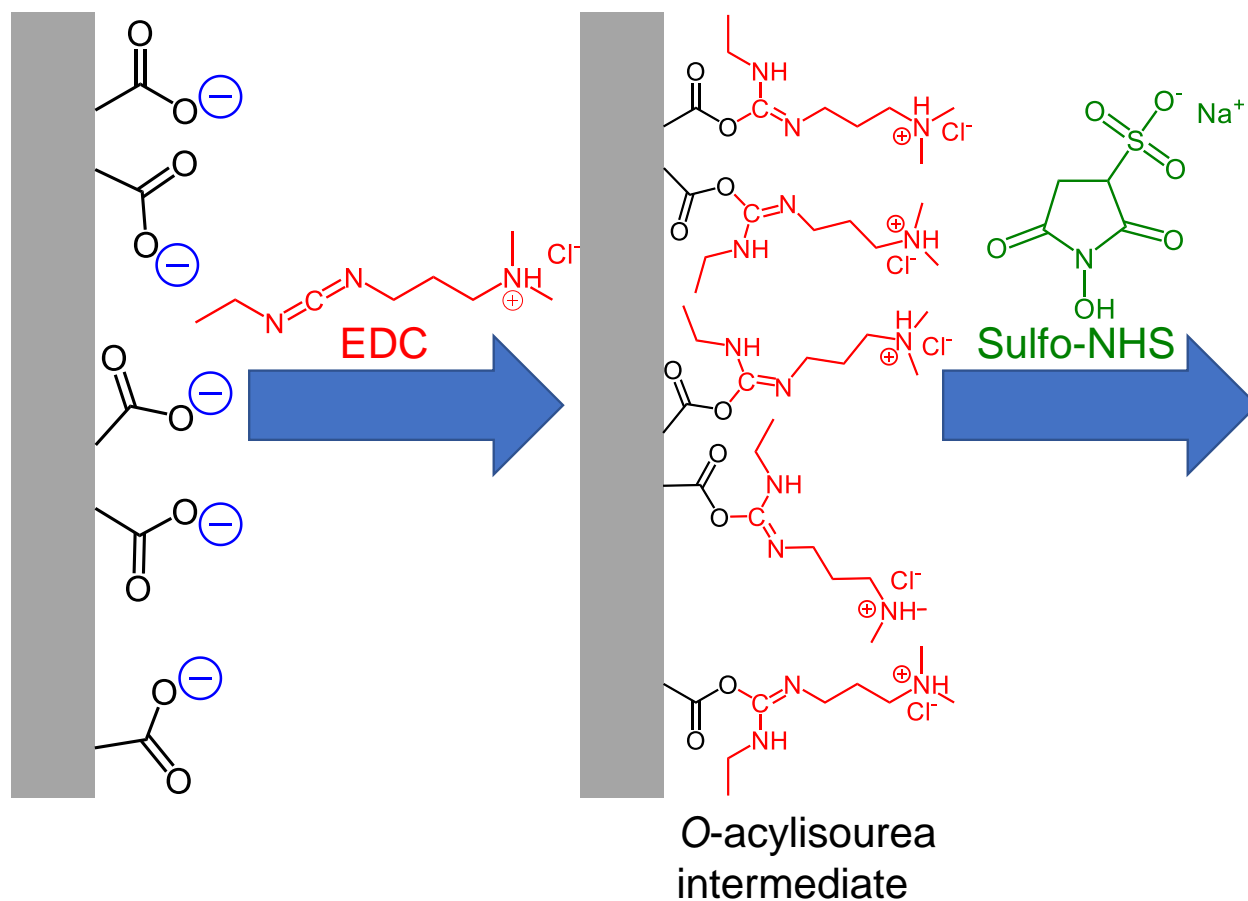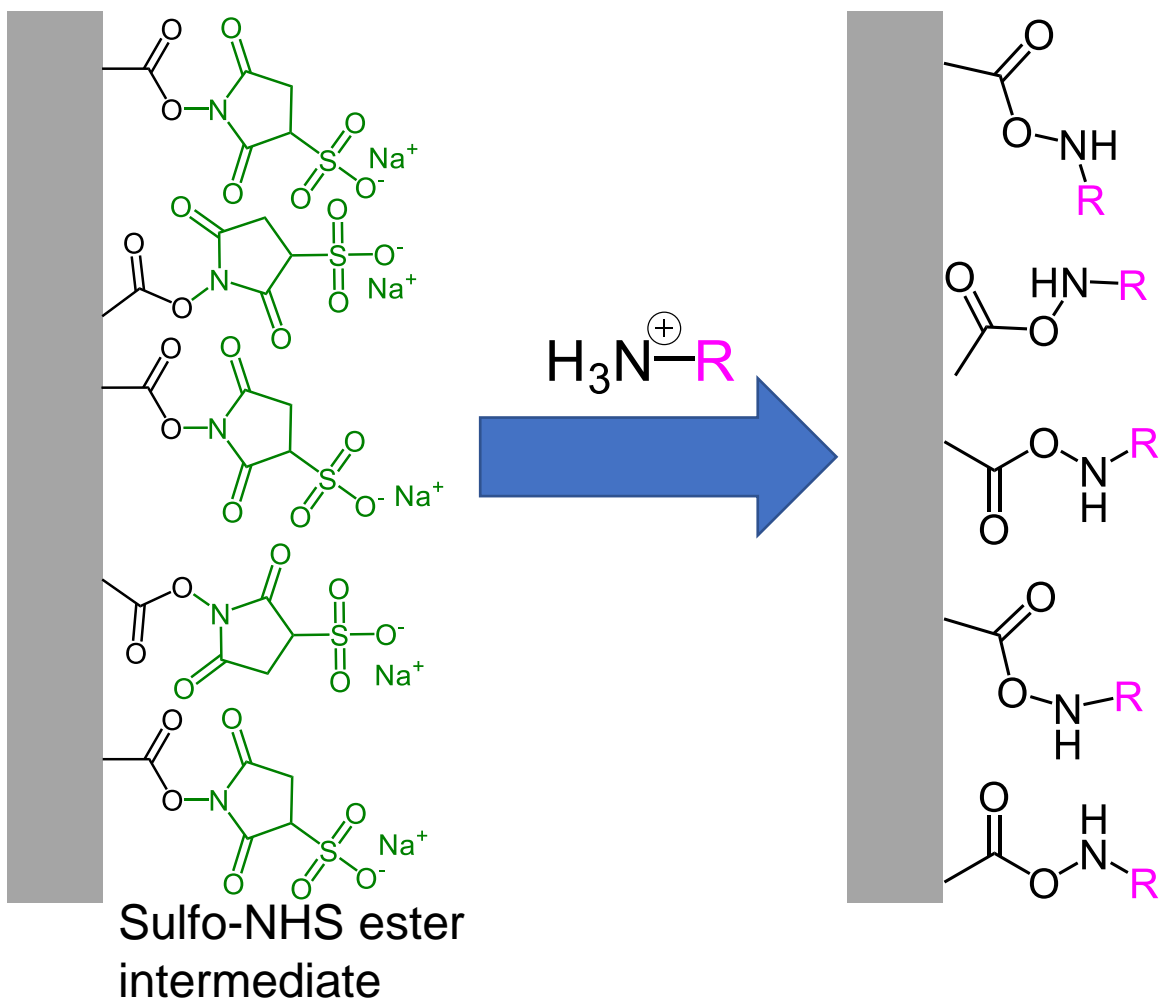
Figure 2.13: EDC coupling with sulfo-NHS activation. A carboxylic acid terminated nanopore is exposed to EDC to form an *O*-acylisourea intermediate that quickly reacts with sulfo-NHS to form a sulfo-NHS ester intermediate. The nanopore is then exposed to the desired anime-terminated group. The amine group reacts with the sulfo-NHS intermediate to create an amide bond and complete the coupling.

Chapter 3: Theory of Transport Phenomena

Charged Surfaces

Surface chemistry plays a crucial role in nearly every aspect of nanopore research. Our nanopore materials are often negatively charged when immersed in an electrolyte solution at neutral pH due to chemical functional groups at the surface. The surfaces of PET pores are covered in carboxylic acid groups with pK_a values around 4.[66] This means that if we buffer our test solutions at pH 8, the entire pore surface will be covered in deprotonated carboxylic acid groups, rendering a negatively charged surface. In bulk electrolyte solution, positive ions (cations) and negative ions (anions) are evenly distributed. However, when a negatively charged surface is immersed in an electrolyte, counterions (in this case cations) will accumulate at the interface to maintain electroneutrality – the negatively charged wall will be offset by positively charged ions. The accumulation of counterions forms what is known as the electrical double-layer (EDL), which is shown in Figure 3.1. As more research is done on the EDL, modifications to the original models are continuously discovered (one such modification is detailed in Chapter 4). For this thesis, I will describe the general description of the EDL for traditional solid-liquid interfaces.

The EDL is broken up into different sections, including the Stern (immobile) and Debye (mobile) layers.[67] The Stern layer corresponds to the immobile, first layer of ions on the surface, whereas the Debye layer is the diffuse, mobile layer of counterions and co-ions (Figure 3.1). The Stern layer is an example of one such modification to the EDL. Stern reasoned that an ion with a finite size is not able to get closer to the surface than its own ionic radius.[67] This distance is called the inner Helmholtz plane. However, the ions can also be solvated, adding another region to the EDL called the outer Helmholtz plane.

The Stern layer encompasses both the inner and outer Helmholtz planes. After the Stern layer comes the diffuse, mobile layer. The electrostatic description of the diffuse layer is described next.

The electrical potential and ion distribution in the Debye layer are well described by the Poisson-Boltzmann (PB) equation that treats ions as point charges and the solvent as a structureless dielectric medium.[67] I will start with describing an infinite charged plane, and the Poisson equation that describes the distribution of electric potential due to any charge density:

$$\nabla^2 \phi = -\frac{\rho}{\varepsilon_0 \varepsilon_r} \tag{3.1}$$

where ∇^2 is the Laplace operator, ϕ is the electric potential, ρ is the charge density, ε_0 is the permittivity of free space, and ε_r is the permittivity of the solvent (water, in our example). The charge density in an electrolyte solution is dependent on the number and charge of ions present, given by:

$$\rho = e \sum_i n_i z_i \tag{3.2}$$

where e is the charge on an electron, n_i is the ion volume density for ion i, and z_i is the charge of ion i. In bulk solution, the charge density for positive and negative ions cancels each other out since there are equal amounts, creating a neutral solution. However, the number of cations and anions are not equal in the EDL and vary based on the distance (z) from the charged wall. The ion density is determined from Boltzmann statistics and yields the Boltzmann equation:

$$n_i = n_i^\infty \exp\left(\frac{-z_i e\phi}{k_B T}\right) \tag{3.3}$$

where n_i^∞ is the bulk ion volume density ($n_i^\infty = 1000 N_A c_i$), N_A is the Avogadro constant, c_i is bulk electrolyte concentration, k_B is the Boltzmann constant, and T is temperature. Combining Eqs. 3.1, 3.2, and 3.3 yields the Poisson-Boltzmann equation, which describes the electrostatic potential due to a distribution of ions:[67]

$$\nabla^2\phi = \frac{d^2\phi}{dz^2} = -\frac{\rho}{\varepsilon_0\varepsilon_r} = -\frac{e}{\varepsilon_0\varepsilon_r}\sum_i z_i\, n_i^\infty \exp\left(\frac{-z_i e\phi(z)}{k_B T}\right) \tag{3.4}$$

The Poisson-Boltzmann equation (Eq. 3.4) can be analytically solved by assuming a small surface potential ($z_i\phi_0 < 25.7$ mV at 25 °C) and expanding the exponential:[67]

$$\nabla^2\phi = \frac{d^2\phi}{dz^2} = \kappa^2\phi(z) \tag{3.5}$$

where z is distance from the charged planar surface, and

$$\kappa = \left(\frac{e^2 \sum_i z_i^2\, n_i^\infty}{\varepsilon_0\varepsilon_r k_B T}\right)^{\frac{1}{2}} \tag{3.6}$$

This approach is called the Debye-Hückel (DH) approximation, and κ is referred to as the Debye-Hückel parameter.[67] However, the more popular term is the Debye length, λ_D, the inverse of κ. The Debye length is often considered the characteristic thickness of the Debye layer. When Eq. 3.5 is analytically solved with the boundary conditions of $\phi(z) = 0$ as $z \to \infty$ and ϕ_0 is equal to the surface potential, the solution is:[67]

$$\phi(z) = \phi_0 \exp(-\kappa z) \tag{3.7}$$

This solution shows that at a distance from the charged wall equal to one Debye length, the electrostatic potential decays by a factor of e ($\approx$2.718). This decay is seen in the potential curve of Figure 3.1. As mentioned above, the DH approximation treats ions as point charges, and the Stern modification accounts for the finite size of ions and their hydration radius. Therefore, the potential drop across the Stern layer is a linear decrease, not exponential.

We typically use 3λ_D as an approximate length for the total surface charge screening length, since at 3λ_D the surface potential has decayed by ~95%. For a symmetric electrolyte (one anion for every one cation) in water at 25 °C, the Debye length (in nanometers) is:

$$\lambda_D = \frac{0.304}{z_i\sqrt{c_i}} \tag{3.8}$$

For example, one common test solution, 0.1 M KCl, has a λ_D of 1 nm. It is important to note these length scales are very similar to the biological nanopore diameters described in Chapter 1. One main method of selectivity in nanoconfinement is utilizing the EDL to screen ions of a certain charge. Since the EDL has enhanced concentrations of counterions, if the EDL spans the entire nanopore, the entire cross-section of the pore will be filled with the enhanced counterion concentration. In this way, with small enough nanopores, we can create ion-selective transport such that only counterions can pass through the pore when electric field is applied.

The Debye-Hückel approximation assumed a small surface potential. However, in cases with high surface potential, the PB equation for a system with an infinite charged plane can only be analytically solved by assuming a symmetrical electrolyte ($z_- = z_+$).

This approach is called the Gouy-Chapman (GC) model. The solution to the PB equation (Eq. 3.4) using the GC model is:[67]

$$\tanh\left(\frac{z_i e \phi(z)}{4 k_B T}\right) = \tanh\left(\frac{z_i e \phi_0}{4 k_B T}\right)\exp(-\kappa z) \tag{3.9}$$

It is important to note that for small values of x, $\tanh(x) \approx x$, which would reduce Eq. 3.9 to Eq. 3.7, showing how the two models are related.
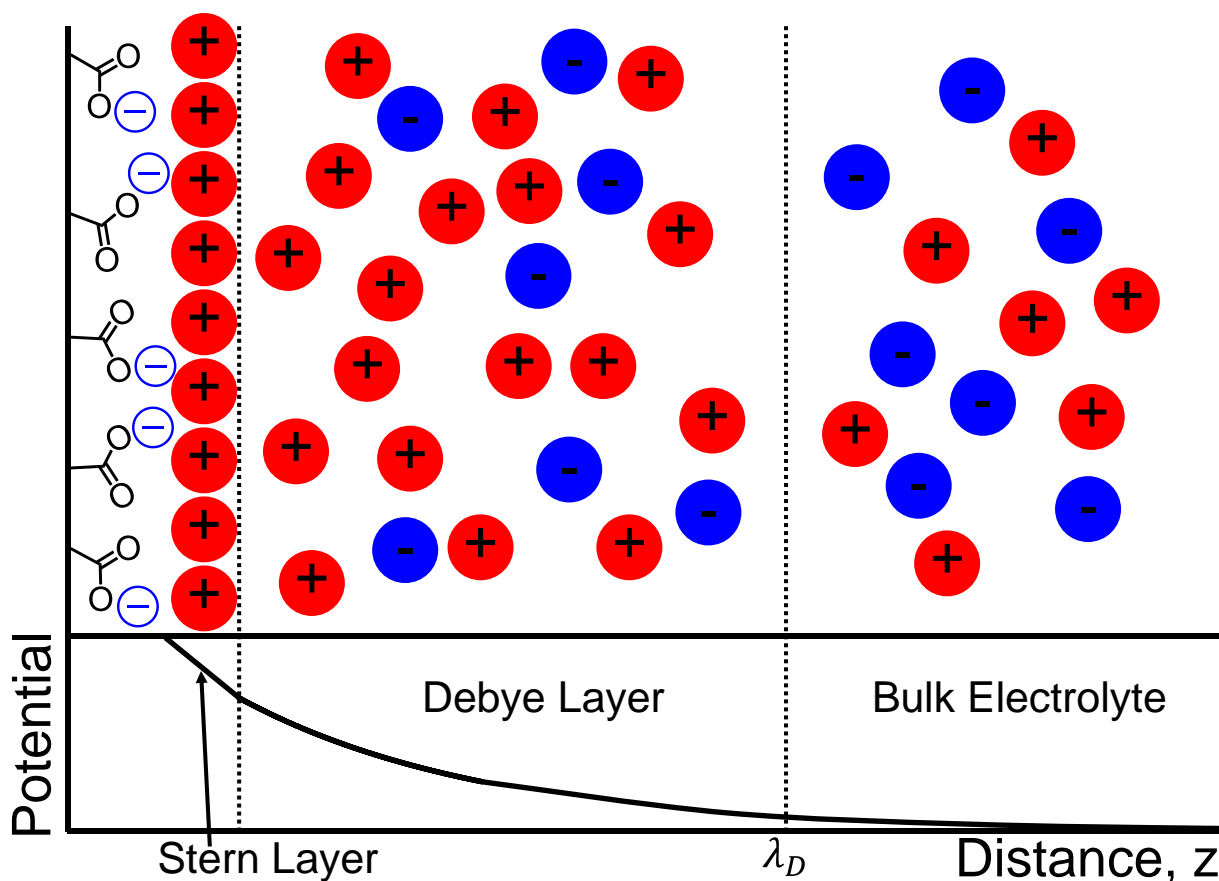
Figure 3.1. The electrical double-layer. A negatively charged surface submerged in an electrolyte solution creates an enhanced concentration of counterions (cations here) in the surrounding region. The electrostatic potential from the charged surface decays away from the surface in a linear manner in the Stern layer and then exponentially in the Debye layer. Figure adapted with permission from Probstein, R. F. Solutions of Electrolytes. In *Physicochemical Hydrodynamics: An Introduction*, 2nd ed.; Wiley: New York, 2005; pp 165–210.[68] Copyright 2005 John Wiley & Sons, Inc.

Ion Transport Phenomena

The previous discussion was for charged surfaces submerged in an electrolyte without external stimuli. However, one of the largest parts of my research is studying the consequences of the EDL, specifically how it influences ion transport within nanopores. To introduce the topic of ion transport, I will begin with an example. I previously described a situation where a nanopore has a diameter of similar length to the EDL. Here we will consider a positively charged pore. Let us also assume the diameter is small enough that *only* counterions (anions) fill the pore (Figure 3.2A). Now we have a situation where the pore is only filled with anions and only anions can enter the pore. Now comes the most interesting part: we apply an external stimulus to push another anion into the pore. What will happen? As one anion enters the pore, one anion must exit the pore to maintain charge neutrality (Figure 3.2B). Then another anion enters, and the process repeats itself. What I just described is an ion-selective nanopore: this nanopore will only allow the transport of negatively charged ions. This is example of one of the consequences of EDL overlap within our pores and how we study the system.
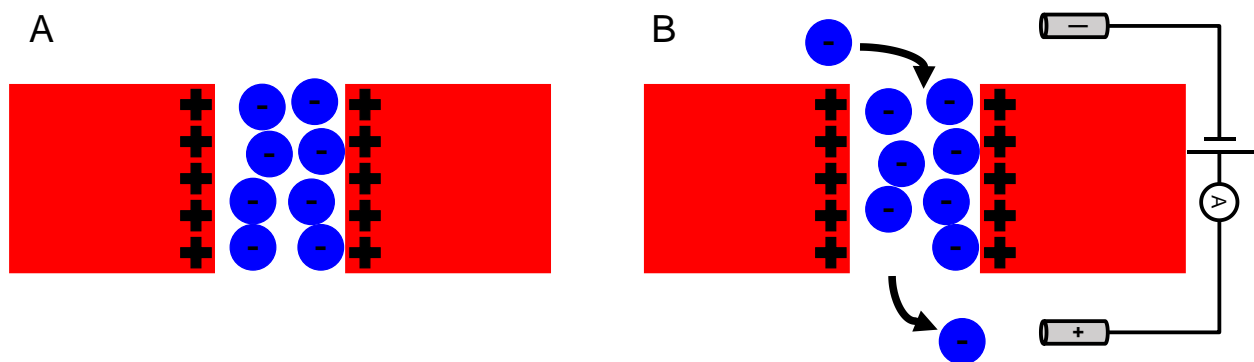
Figure 3.2. Nanopore with ideal anion selectivity. (A) A small, positively charged nanopore is completely filled with counterions. (B) When an external stimulus pushes one anion into the nanopore, one anion leaves. No cations can transport through the pore. Black arrows represent the flux for the negative ions.

When ions transport through a solution it is considered mass transfer. Mass transfer can occur from three different phenomena: diffusion, migration, and convection. Diffusion and migration occur when there is an electrochemical potential gradient in the system, and convection occurs due to an imbalance of forces in the solution. The total flux of an ion is the sum of the three individual contributions and takes the form of the Nernst-Planck (NP) equation:[67]

$$J_i = -D_i \nabla c_i - \frac{z_i F}{RT} D_i c_i \nabla \phi \pm v_c c_i \tag{3.10}$$

where J_i is the flux for ion I, D_i is the diffusion coefficient for ion I, F is the Faraday constant, R is the gas constant, and v_c is the solution velocity. The Nernst-Planck equation combines Fick's first law (molecule diffusion due to concentration gradient), and migration due to electric potential. The last component of Eq. 3.10 describes convective transport. In a charged nanopore system this term often describes electroosmosis, which can be ignored in cases with small pore diameters,[69] leaving us with the following modified NP equation:

$$J_i = -D_i \nabla c_i - \frac{z_i F}{RT} D_i c_i \nabla \phi \tag{3.11}$$

which describes the flux of ions in our nanopore system. The first term describes that an ion will move down a concentration gradient (that is, from *high* to *low* ion concentration) by a factor of its diffusion coefficient. The second term expresses how an ion will migrate due to an electric potential gradient. Upon examination, ions with identical diffusion coefficients and spatially homogeneous concentrations but different charges (i.e., $z_i = +1$, $z_j = -1$) will have equal and opposite flux under an electric potential gradient.

Let us connect the above NP equations to our nanopore with ideal anion selectivity. We first must additionally describe key parameters of the system. We assume the nanopore's surface charge is homogeneous (e.g., there are no regions of the pore with higher or lower positive charge), and the pore is separating two electrolyte reservoirs with identical salt concentrations. The pore is also sufficiently small such that we can ignore contributions from electroosmosis.[69] In this situation there is no electrolyte concentration gradient, and without an external stimulus (e.g., an electric field), the nanopore system is at equilibrium and there is no ionic flux (all terms in Eq. 3.10 are zero; $J_+ = J_- = 0$) . Upon the addition of an external stimulus (electric field), we know from the NP equations that there will be an associated mass transfer. From Eq. 3.10, we know an electric field will induce flux proportional to the ion's charge, diffusion coefficient, and concentration. One might be inclined to conclude that the positive and negative ions will simply have the opposite flux by a factor of their diffusion coefficient. However, we must remember that the nanopore is completely filled with the EDL, meaning there are *no* cations within the pore. That means $c_+ = 0$ and thus $J_+ = 0$. The nanopore is filled with anions, thus c_- is finite and J_- is finite (the sign of J_i indicates the direction). Therefore, the flux of anions through the ideal anion selective nanopore will depend on the applied electric field, anion concentration, and the diffusion coefficient of the anion.

A quick note about the electrodes in our system and their role in applying electric potential to drive ion transport. Our picoammeter measures current generated from the movement of electrons, but our experiments involve transport of ions. Thus, we need a way to convert ion movement to electron movement. This is accomplished by utilizing Ag/AgCl electrodes to apply a voltage (electric potential) across our membrane. The

Ag/AgCl electrodes consist of an Ag wire with a layer of semi-soluble AgCl on it. The associated reduction and oxidation reactions are:

$$Ag(s) + Cl^-(aq) \leftrightharpoons AgCl(s) + e^-$$
Rxn (3.1)
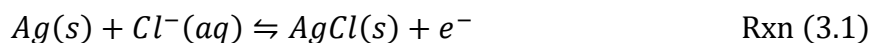
where the forward reaction shows the oxidation of Ag(0) to Ag(+1) and the reverse reaction shows the reduction of Ag(+1) to Ag(0). The e$^-$ in Rxn. 3.1 represents an electron, which will travel through the silver wire through the picoammeter towards the other electrode, generating current. During our ion transport experiments, both the forward and reverse reactions from Rxn. 3.1 are occurring, but at opposite electrodes. For example, in Figure 3.2 as an anion from the top reservoir enters the pore, it leaves behind an uncompensated positive charge in the top reservoir. To maintain electroneutrality, the reverse of Rxn. 3.1 occurs at the negative (top) electrode: an electron is consumed to release a Cl$^-$ ion into the top reservoir. In the bottom reservoir, the forward reaction occurs; when an anion leaves the pore it brings an uncompensated negative charge. To maintain electroneutrality, Rxn. 3.1 proceeds in the forward direction, consuming a negatively charged Cl$^-$ ion and sending an electron towards the other electrode. The same redox reactions occur in large nanopores as well. In this way, we couple the movement of an anion with the movement of an electron.

You may also notice that 1 M KCl is used as the standard electrolyte in our sizing and modification tracking experiments. This is done for a few reasons. First off, K$^+$ and Cl$^-$ are biologically relevant ions, being two of the most common ions in the human body. This allows our studies to closer mimic the biological nanochannels within our cells. In addition, K$^+$ and Cl$^-$ have similar diffusion coefficients (1.957 and 2.032 $\times$ 10^{-5} cm^2 s^{-1}, respectively).[70] This means that flux differences between the ions will depend on other

factors (e.g., local concentration differences due to charged surfaces). We also pick 1 M as the concentration since at this concentration, λ_d is only 0.3 nm in length, meaning that, except for our smallest of pores, the EDL can fully form and the pore is mostly filled with bulk solution. This allows us to use bulk conductivity for sizing the nanopores, using Eqs. 2.2, 2.3, and 2.4.

In nanopore systems with large diameters, we must consider electroosmosis. The transport described by Eq. 3.10 applies to the movement of charged species in a solvent. Above, we assumed the solvent is immobile (Eq. 3.11) in our small nanopores. However, in larger nanopores this is not always the case. For example, in Figure 3.3 the pore diameter is sufficiently larger than the EDL, meaning the effects of the EDL are sufficiently screened and the center of the pore is filled with bulk electrolyte solution. When an electric field is applied, the charged species in the system move according to Eq. 3.10. However, since the surface is positively charged, the excess negative ions in the EDL will drag the solvent molecules with them towards the positive electrode. The solvent movement is called electroosmosis (or electroosmotic flow, EOF, green arrows in Figure 3.3). The solvent molecules flow through our large pores following the plug flow model, which means the fluid velocity is constant across the nanopore cross-section and zero at the surface. We only consider EOF in larger pores, as the EDL can be fully formed and plug flow will occur. Overlapping EDLs in small nanopores means EOF does not significantly contribute to ion flux because the fluid velocities are very low.[69,71]

When ions in the EDL drag solvent molecules with EOF, they also bring the bulk solution from that reservoir with them. For example, consider the situation in Figure 3.3, but the top reservoir has a larger bulk electrolyte concentration (*C1*) than the bottom

reservoir (*C2*). The electric field polarity shown in Figure 3.3 creates an EOF that will draw the *C1* bulk electrolyte from the top reservoir into the nanopore. When the opposite electric field polarity is applied, the EOF's direction will flip, and the *C2* bulk electrolyte will fill the nanopore. Since *C1* > *C2*, when *C1* is the bulk electrolyte filling the nanopore there will be larger ion fluxes (J_- and J_+), and smaller ion fluxes when *C2* is filling the nanopore. The different ion fluxes create different magnitudes of current, and ion current rectification occurs, where different electric field polarities create different current magnitudes.

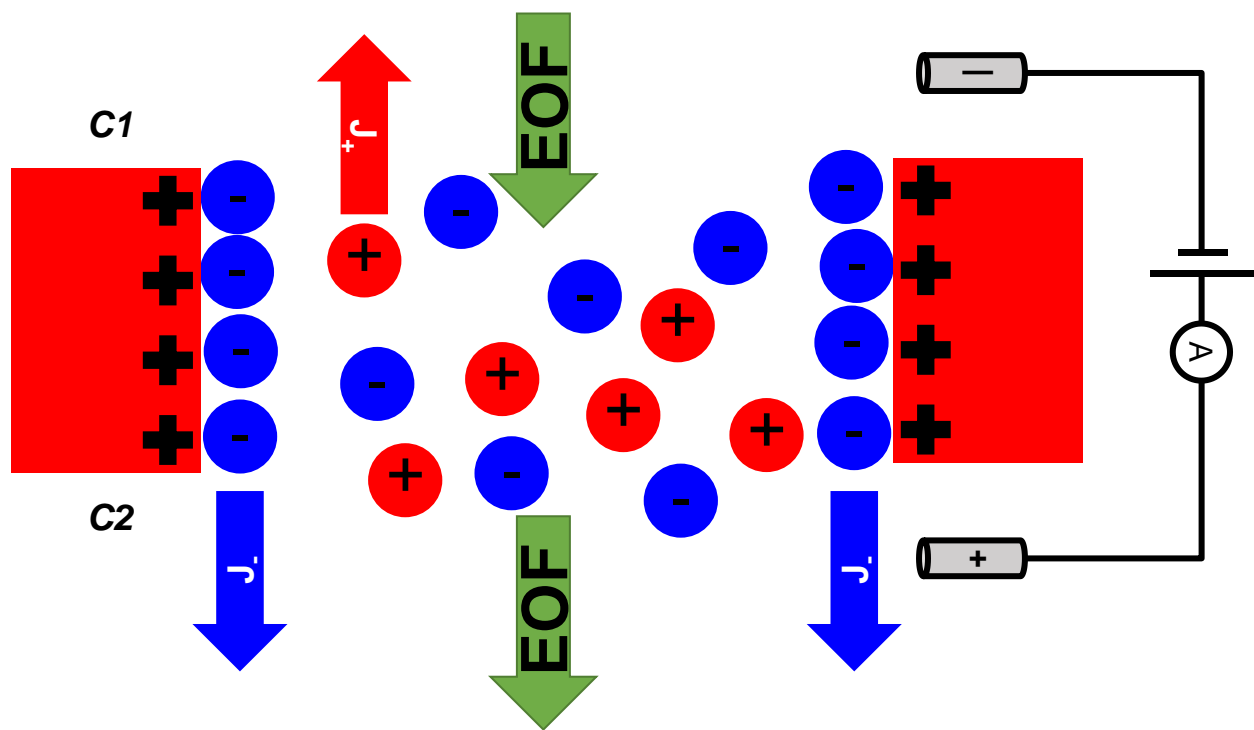Figure 3.3. Electroosmosis in large nanopores. A large, positively charged nanopore separates a top and bottom reservoir having bulk electrolyte concentrations *C1* and *C2*, respectively. When placed in an electric field, EOF will drag *C1* or *C2* into the nanopore depending on the direction of the field and the sign of the nanopore surface charge. The shown electric field will drag *C1* into the nanopore.

Ion Current Rectification Showcase: Nanofluidic Diode

Ion current rectification (ICR) is a crucial aspect in nanopore research. As previously mentioned, presence of ICR indicates electrochemical asymmetry in the nanopore system. Described in Figure 3.3, that asymmetry is due to a concentration gradient ($C1 > C2$) and charges on the pore walls. Another classic example of ICR is in a nanofluidic diode. A diode is an electrical component that allows current to flow in one direction but restricts flow in the opposite direction. Common diodes are made with semiconductor materials, such as silicon, doped such that a junction between positive (p-type, electron-deficient) and negative (n-type, electron-rich) regions exist (called a pn junction). These devices are called bipolar diodes since they are made of two opposite polarity regions. In nanofluidic diodes, we mimic the bipolar diode but utilize ions and surface charge modifications.

In a bipolar nanofluidic diode, a nanopore is modified such that half the pore is positively charged, and half negatively charged. This can be accomplished using a modification technique previously described, such as silane coupling. As previously described, the charged surfaces attract oppositely charged ions. Thus, the nanofluidic diode has two adjacent regions with excess anions (positively charged surface) and cations (negatively charged surface). The asymmetric ion distribution creates a system that will rectify ion current when an electric field is applied.[69,72,73] Shown in Figure 3.4, the device has a forward-bias ("on" state) and a reverse-bias ("off" state). The forward-bias occurs when the electric field causes the flux of both anions and cations to flow *into the pore*, whereas the reverse-bias occurs when the flux of anions and cations flows *out of the pore*. The diagrams in Figures 3.4A and 3.4B also show ionic concentration and

electric potential distribution within the nanofluidic diode. The ion concentration in the "on" state is enhanced within the pore (blue, anion, and red, cation, lines in Figure 3.4A). The electric potential distribution in the "on" state increases across the entire pore, meaning the second term in the NP equation (Eq. 3.10) is finite at all points. In the "off" state an ion depletion zone forms within the diode, creating a zone with negligible ion concentrations (depletion zone in the middle of Figure 3.4B). The electric potential in the "off" state has a sharp drop over the depletion zone and is relatively constant throughout the rest of the pore. This indicates that the second term in Eq. 3.10 will essentially be zero in the "off" state. The ion concentration and electric potential distribution in the forward and reverse biased devices result in asymmetric current flow, and thus the ICR seen in Figure 3.4C. The forward-biased device will have finite ion flux through the system, whereas the reverse-biased device will have negligible ion flux. The nanofluidic diode is an example of a nanodevice that can rectify ion current while being in symmetric electrolyte solutions.
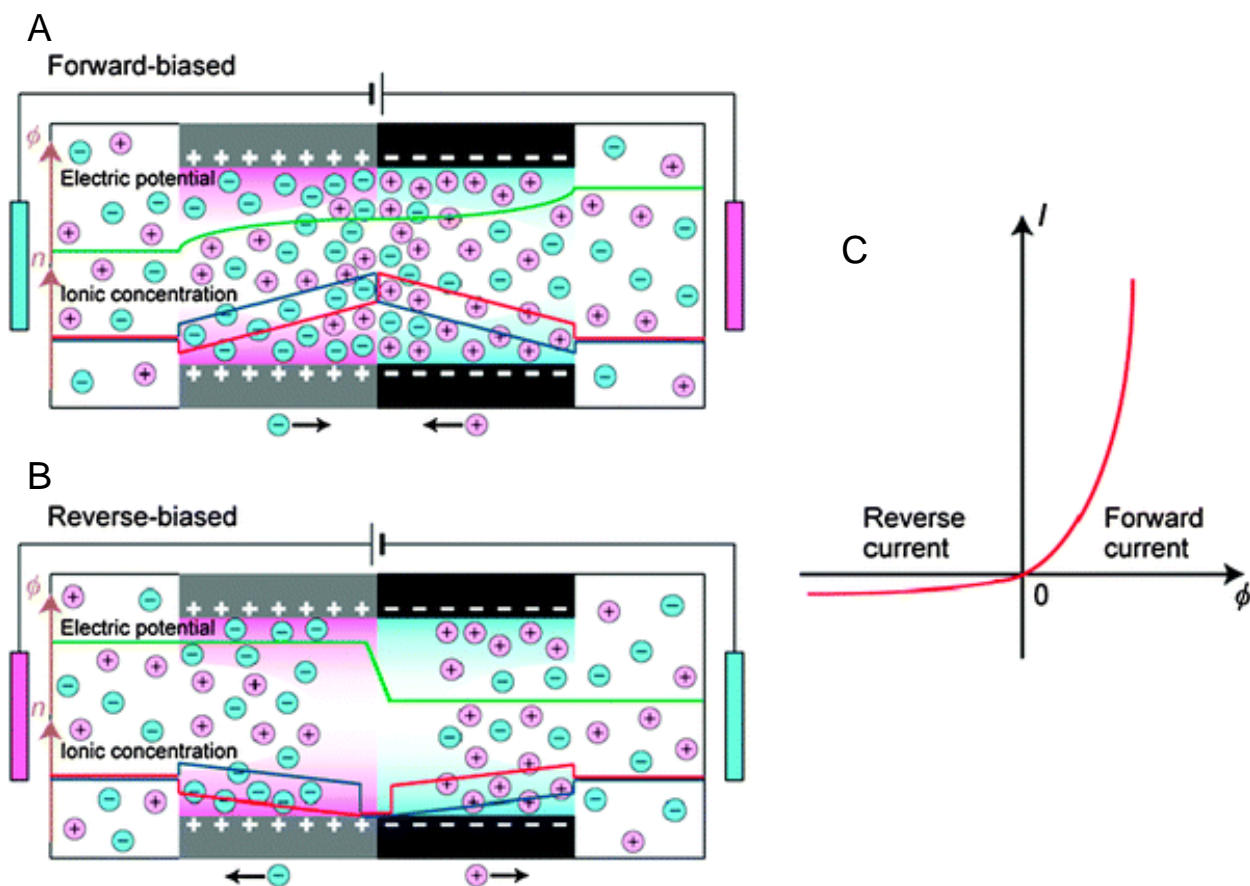
Figure 3.4. Nanofluidic diode and ion-current rectification. A nanopore is asymmetrically modified such that half the pore is positively charged, and half is negatively charged. Upon application of an external electric potential, an "on" (A) or "off" (B) state is formed based on direction of the potential. (A) The forward-biased device increases ion concentrations within the nanopore and has increasing electric potential through the entire pore length. (B) The reverse-biased device forms a depletion zone, with decreased ion concentration at the junction between the positive and negatively charged surface regions. The electric potential sharply drops through the depletion zone and remains otherwise constant throughout the rest of the pore length. (C) The asymmetric current-voltage response in a nanofluidic diode. The device can fluctuate between the "on" and "off" states by inverting the electric field direction. Figure republished with permission of The Royal Society of Chemistry, from Daiguji, H. Ion Transport in Nanofluidic Channels. *Chem. Soc. Rev.* **2010**, *39* (3), 901–911.[73] Copyright 2010 The Royal Society of Chemistry; permission conveyed through Copyright Clearance Center, Inc.

The above descriptions of charged surfaces in electrolytes and ion transport work well for traditional solid-liquid interfaces. However, assumptions made in these theories, such as treating ions as point charges and the solvent as structureless, tend to fall apart for non-traditional solid-liquid interfaces. The breakdown of these traditional descriptions and theories results in unique ion transport properties in nanopores containing these non-traditional solid-liquid interfaces, such as surface charge inversion and controllable ion transport gating. My PhD research has focused on exploring these non-traditional solid-liquid interfaces through our nanopore model system. The results from this research help build a better understanding of fundamental surface properties of these unique interfaces as well as guide next-generation chemical separation technologies, ion-selective membranes, and energy storage devices.

The following chapters describe my research projects studying non-traditional solid-liquid interfaces under nanoconfinement. I first detail my work looking at how organic solvents organize near a glass interface and what interesting ion transport properties arise. I then describe my two projects looking at hydrophobic interfaces in water. The two projects explore controllable ion transport through hydrophobic nanopores and seek to understand important physical properties of ions at the solid-liquid-gas interface. As you will see, all my projects have been interdisciplinary, with collaborations for molecular dynamics simulations and spectroscopy. I truly believe working alongside these amazing researchers has not only helped answer more in-depth, complex research questions, but also helped me grow as a researcher myself.

Chapter 4: The Electrical Double Layer Revisited

Chapter adapted from:

Polster, J. W.; Souna, A. J.; Motevaselian, M. H.; Lucas, R. A.; Tran, J. D.; Siwy, Z. S.; Aluru, N. R.; Fourkas, J. T. The Electrical-Double Layer Revisited. *Natural Sciences* **2022**, e20210099. https://doi.org/10.1002/ntls.20210099.

My first project focuses on what happens to the electrical double-layer (EDL) when we move from an aqueous system to a non-aqueous (organic) system. The EDL model is a fundamental element of our understanding of interactions in ionic solutions, and is widely used in chemical, biological, and technological contexts, particularly in the description of aqueous electrolyte solutions. As previously mentioned, the traditional explanations of EDL treat the solvent (water) as a structureless medium, with ion and electric potential distributions being a result of the native surface potential. However, recent experiments have raised questions regarding the validity of this model in polar, aprotic solvents; some observations, such as a surface potential that changes sign with increasing salt concentration, are not consistent with the EDL picture. In this project, we demonstrate in a model system, acetonitrile at a silica interface, that solvent organization dictates the ionic distributions. Ion-transport measurements in nanopores, surface-selective spectroscopy, and molecular dynamics simulations reveal that the distribution of ions in acetonitrile at a silica interface is determined by the lipid-bilayer-like organization that the interface imposes upon the liquid, which accounts for the change in sign of the potential. Our findings emphasize the importance of including solvent molecules and ions explicitly in descriptions of solid/liquid interfaces.

Introduction

The surface electrostatic potential plays an important role in processes at solid/liquid (SL) interfaces.[67,74] In water, this potential is often dominated by surface charges. For instance, silica surfaces can deprotonate in aqueous solutions, creating a negative surface potential.[74] As described in the previous chapter, local distributions of ions are frequently described by the Poisson-Boltzmann equation,[75] which treats ions as

point charges and the solvent as a homogeneous dielectric medium. The resulting model of the so-called EDL consists of a charged surface in contact with a liquid region with an enhanced concentration of counterions.[74] This model is widely applied in describing transport phenomena in nanofludics,[67,76–79] separations based on charged membranes,[80–82] electrokinetic effects,[67] energy storage devices such as supercapacitors,[83,84] sensors,[85,86] and biological phenomena such as protein aggregation[87,88] and lipid bilayer permeability.[89,90]

The continuum solvent description in the EDL model has been highly successful in modeling aqueous interfaces. Although ion-dependent effects are often observed, for monovalent salts they typically lead to minor deviations in ionic distributions and ionic transport. One key feature contributing to the success of the EDL model for water is that this liquid does not generally exhibit long-range ordering at interfaces, although short-range organization (on the order of two molecular diameters) is often observed.[91,92] Experiments further suggest that electrolytes can disrupt this interfacial organization.[93–95]

The question of whether a continuum description is appropriate for solvents that undergo strong ordering at interfaces has received only limited attention.[96,97] As an example of such a system, liquid acetonitrile exhibits a well-ordered, and effectively immobile, lipid-bilayer-like organization at silica interfaces.[98] The bilayer consists of a first sublayer of molecules in which the cyano groups accept hydrogen bonds from surface silanols, and a second, interdigitated layer of molecules that predominantly point in the opposite direction.[99–101] Simulations have revealed that this organizational motif repeats, with decreasing fidelity, for more than 2 nm from a flat silica surface.[99] In addition, the 3.92 D dipole moment of acetonitrile[102] is among the highest for any solvent, and so the

cyano groups might be expected to play a key role in determining the EDL structure. The organization of acetonitrile at a silica interface is remarkably persistent in the presence of large mole fractions of water.[103–105] If the organization also persists in the presence of ions, then the classical EDL picture would not be expected to provide an adequate description of this system. Indeed, ion transport through nanopores containing lithium perchlorate solutions in acetonitrile revealed the presence of a positive effective surface potential in silica and polymer pores, even though both systems had a negative surface potential in aqueous solutions.[106,107] We use the term "effective" to denote that the potential is a property of the SL system collectively, and can be non-zero even in the absence of any charged surface groups.

Here, a combination of electrochemical and spectroscopic experiments with molecular dynamics simulations reveals that the local solvent organization imposed by an interface can lead to a substantial effective surface potential even in the absence of surface charge. Our work provides a molecular-level understanding of electrolyte solutions in acetonitrile at a silica interface, highlighting the major role that the organization of the solvent plays in determining both the distribution of the ions and the effective surface potential. We find that this ordering is remarkably insensitive to the presence of an electrolyte, even at concentrations of 1 M and above, and creates specific, preferential locations for anions and cations over the entire range of distances at which the surface imposes organization on the liquid. As a consequence of this organization, the polarity and magnitude of the effective surface potential depend on the electrolyte concentration and the identities of the anion and cation. The layered solvent structure

modifies ionic distributions over length scales and concentrations that are substantially larger than predicted by the classical EDL picture.

Methods

Ion-current measurements

The salts, lithium perchlorate (99.99%, Sigma-Aldrich), lithium tetrafluoroborate (98%, Acros Organics), lithium hexafluorophosphate (98.0%, Alfa Aesar), and sodium perchlorate (98.0 – 102.0%, Alfa Aesar), were used as received. Acetonitrile (99.9%, Fisher Scientific) was degassed by sparging with argon, and then was dried by passage through two columns of activated alumina. The solvent and solutions were stored in a nitrogen glove box over 3 Å sieves.

Each experiment was performed in a glass pipette with a filament (World Precision Instruments, Inc.). The pipettes had an internal opening diameter of 400 ± 80 nm and were filled using MicroFil syringe needles (34 gauge/67 mm, WPI). The pipettes were used as received, and each pipette was used with only one type of solution. Electrical contact with an electrode was established via the luer lock fitting of the pipette.

Current/voltage curves were recorded in a nitrogen glove box using a Keithley 6487 picoammeter/voltage source (Keithley Instruments, Cleveland, OH) and home-made Ag/AgCl electrodes. The ground electrode was placed in the pipette and the working electrode was placed in the bulk reservoir. The voltage was swept between -2 V and +2 V in 0.1 V or 0.2 V increments. At least three scans were performed for every pair of solutions.

Vibrational sum-frequency-generation experiments

Vibrational sum-frequency-generation (VSFG) spectra were collected with a counter-propagating VSFG spectrometer that has been described in detail elsewhere.[99] All spectra were collected according to the methods described in Section 3.4. For this study, the IR pulse had an energy of 15 µJ and a bandwidth of 250 cm^{-1}. The probe pulses had an energy of 15 µJ and a bandwidth of 5 cm^{-1}. The probe pulses were delayed relative to the IR pulse by 667 fs to maximize the probe pulse's overlap with the molecular response of the methyl symmetric stretch transition.

Sample cuvettes were rinsed sequentially with acetone, methanol, and then water. The cuvettes were then oven dried, cleaned for 3 min in an oxygen plasma, and then oven dried overnight. The cuvettes were placed in the glove box while still hot. After the cuvettes had cooled, each was filled with dry acetonitrile as a reference. All sample vials and cuvettes were removed from the glove box prior to collecting spectra. Spectra of dry acetonitrile were collected within 1 h of removing the samples from the glove box, during which time the cuvettes remained tightly capped. The spectra from subsequent cuvettes of dry acetonitrile remained the same, indicating that a negligible amount of ambient water had entered the cuvettes and reached the silica surface. After reference spectra were collected, the neat acetonitrile and the series of electrolyte solutions that were removed from the glove box were added to each of the reference cuvettes, replacing the dry acetonitrile, after flushing twice with the new sample.

The spectra were obtained using the SSP polarization configuration. Normalization and calibration spectra were obtained according to a method described previously.[108] Acquisition times for low concentrations of electrolyte solutions were 1 min. For higher

concentrations, acquisition times were 2 to 4 min, depending on the signal strength. Spectra for each sample were recorded at least three times.

Simulations

Molecular dynamics (MD) simulations were performed using GROMACS[109] with a time step of 1 fs. For simulations of $LiClO_4$ in bulk acetonitrile, random configurations were initially equilibrated in the NVT ensemble by a simulated annealing procedure with the following sequential steps: melting at $T = 533$ K for 1 ns, annealing from 533 K to 298 K for 1 ns, and equilibrating at 298 K for 1 ns. The final configuration was equilibrated for 2 ns followed by a production run of 10 ns in the NPT ensemble at a pressure of 1 atm and temperature of 298 K. The temperature and pressure were kept constant using the Nosé-Hoover thermostat[110] and the Parrinello-Rahman barostat,[111] with time constants of 0.2 ps and 1 ps, respectively. Periodic boundary conditions were applied in all directions. For the short-ranged interactions, the cutoff radius was set to 1.2 nm. Both energy and pressure tail corrections[112] were applied to the standard 12-6 LJ potential for the bulk MD simulations. The long-range electrostatic interactions were calculated using the particle-mesh Ewald summation[113] with a cutoff radius of 1.2 nm and a fast Fourier transform (FFT) grid spacing of 0.12 nm. The forcefield parameters for all salts were adopted from the OPLS-AA forcefield.[114,115] The interaction parameters for acetonitrile molecules were obtained from Nikitin and Lyubartsev.[116] The bulk densities for different systems were calculated using the final 6 ns of the trajectories of the NPT production simulation. The mean bulk densities were 11.161 nm^{-3} for acetonitrile and 0.612 nm^{-3} for Li^+ and ClO_4^-.

Figure A.9 shows a schematic view of the simulation setup for the electrolyte system at a hydroxylated silica surface. The hydroxylated silica surface was created

following a procedure similar to that of Lee and Rossky.[117] The electrolyte was sandwiched between the silica substrate and a graphene sheet separated by a surface-to-surface distance of 15.24 nm in the z direction. During the simulation, only the positions of the liquid, the electrolyte, and the hydrogen atoms of the surface silanol groups were allowed to change. The system was periodic in all directions, with an extra empty space (vacuum) of length 45 nm added in the z direction. The long-range electrostatic interactions were modeled employing the Ewald algorithm adapted for a slab geometry[118] (Ewald3dc), which excludes long-ranged electrostatic contributions from the periodic image cells in the z direction. The carbon atoms in the graphene sheet were modeled as hard spheres, i.e., with zero attraction. The numbers of molecules and ions were tuned to make sure that the density of each species was within 2% of the corresponding bulk density. Atomic configurations were stored every 0.1 ps of the simulation for analysis. The equilibrium properties were averaged over a set of four, 40-ns simulations, each with different initial velocities and positions, of which the first 5 ns were discarded.

Results and discussions

The sign of the effective surface potential of silica depends on the concentration of $LiClO_4$ in acetonitrile

Surface charge is often characterized using zeta-potential measurements.[67] However, water has a strong influence on the zeta potential of silica, and acetonitrile is hygroscopic. We therefore used ion-current measurements, which can be performed in a glove box, to probe the effective surface potential of the silica/acetonitrile interface. A glass pipette tip with a 400 nm inner diameter was immersed in a solution of $LiClO_4$ in acetonitrile (Figures 4.1A,B). The Debye length in this situation[67] is significantly smaller than 400 nm. Consequently, the ion concentration in the pipette tip is determined largely

67

by the bulk concentration, rather than by local concentration modification due to the surface potential.[119] The solutions inside and outside of the pipette had electrolyte concentrations $[C_{in}] < [C_{out}]$, respectively. If the pipette is charged, then ions with the opposite sign of the surface charge (counterions) will dictate the direction of electroosmotic flow (EOF) that occurs when voltage is applied across the pipette. This means that, for one voltage polarity, the counterions will electroosmotically drag the less conductive $[C_{in}]$ into the pipette tip, and $[C_{out}]$ for the opposite voltage polarity. For example, if the pipette is negatively charged, the movement of cations will dictate EOF. Therefore, the tip is filled with $[C_{out}]$ at voltages that are positive with respect to the ground in the pipette (V) and with $[C_{in}]$, at voltages that are negative ($-V$) with respect to ground (Figure A.1). Consequently, asymmetric current/voltage (I-V) curves will be observed, with $|I(-V)| < |I(V)|$ (Figure 4.1C). If the surface charge of the pipette is positive, the pipette tip will be filled with the more conductive $[C_{out}]$ at negative voltages and the less conductive $[C_{in}]$ at positive voltages, implying that $|I(-V)| > |I(V)|$. If the effective surface potential is zero, no electroosmotic flow will occur, and the I-V curve will be linear. Representative data are shown in Figures 4.1D,E.

For characterizing the asymmetry in the I-V curves, we introduce a quantity that we call the ion-current anisotropy:

$$A(V) = \frac{I(-V) + I(V)}{I(-V) - I(V)} \tag{4.1}$$

where I($\pm$V) is the current at the indicated voltage. By construction, $A(V)$ is a linear measure of rectification. In our electrode configuration, $A(V)$ is zero in the absence of rectification, positive when the effective surface potential is positive, and negative when

the effective surface potential is negative (Figure 4.1C). To determine the I-V anisotropy as accurately as possible, we report $A(V)$ based on measurements at the voltages of the largest magnitudes used, ±2 V (Figure 4.1F). For comparison, $A(V)$ in a range of voltages between 1 and 2 V is shown in Figure A.2 for the same set of concentrations. These data are consistent with those in Figure 1F.

Representative I-V data for four gradients of $LiClO_4$ concentration are shown in Figure 4.1D,E. For the gradient with the lowest concentrations, 0.1 mM/ 1 mM, $A(2V)$ is negative (Figure 4.1F). The effective surface potential is therefore negative, as in measurements performed on aqueous solutions at silica surfaces[120] (Figure A.3). Presumably the same holds true for the neat liquid, even though acetonitrile is not a strong enough base to dissociate silanol groups in the absence of water.[121] For concentrations of 10 mM or larger, $A(2V)$ becomes positive, indicating a positive effective surface potential. Conventional EDL theory cannot account for a change in the sign of the effective surface potential with increasing electrolyte concentration.
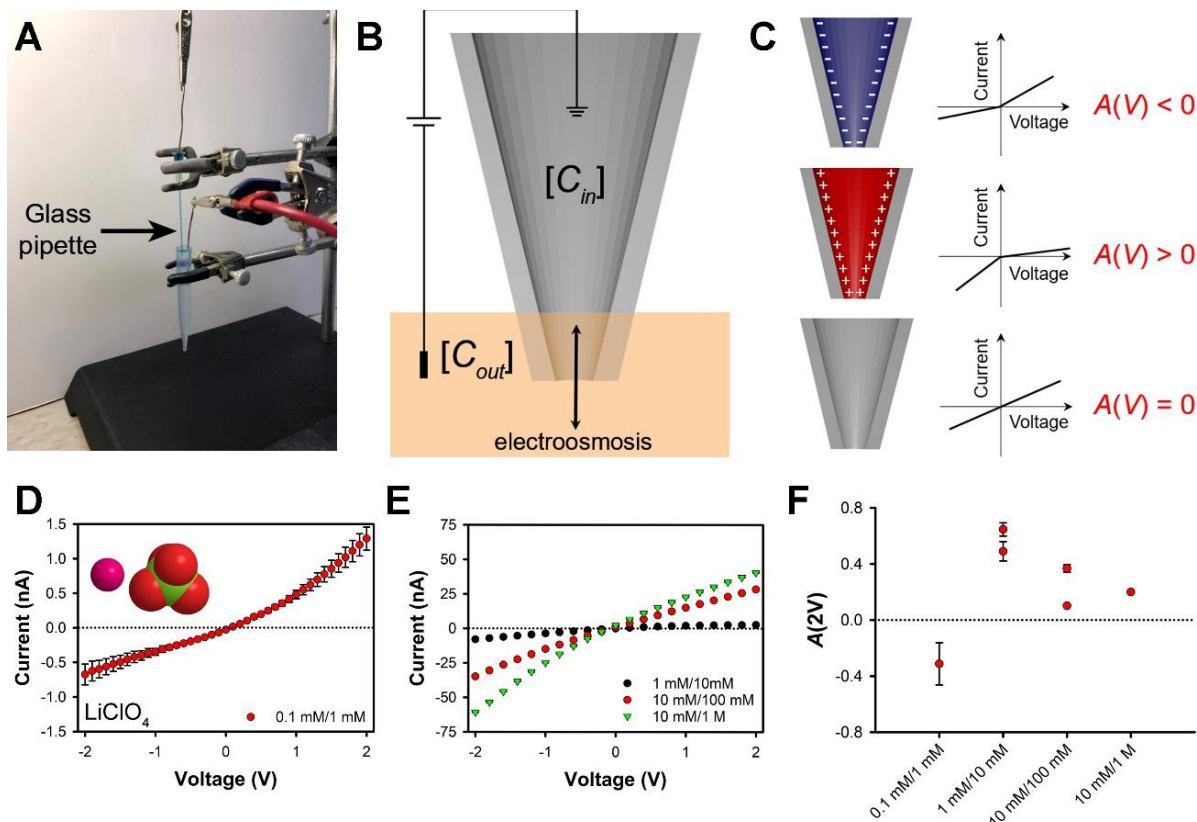
Figure 4.1: Probing the effective surface potential with ion current. (A) Experimental setup for and (B) schematic of I-V measurement with a glass pipette tip with a 400 nm inner diameter. The tip is immersed in $LiClO_4$ at concentration $[C_{out}]$ in acetonitrile. The solution inside the pipette has concentration $[C_{in}]$. The ion current is measured for various values of $[C_{out}] > [C_{in}]$. The working electrode, which is connected to the red wire, is in the liquid outside of the tip. (C) Relationship between the ion-current anisotropy, A(V), and the effective surface potential of the pipette. The signs of A(V) and the effective surface potential are the same. A(V) = 0 in the absence of an effective surface potential. I-V curves recorded at (D) low concentrations, for which A(V) is negative, and (E) higher concentrations, for which A(V) is positive. (F) The concentration dependence of A(2V).

Spectroscopic and simulation data provide insights into the microscopic nature of the effective surface potential

To probe the microscopic mechanism of effective surface potential polarity reversal, we studied the molecular organization of $LiClO_4$ solutions in acetonitrile on a flat silica substrate using vibrational sum-frequency-generation (VSFG) spectroscopy. In VSFG,[122–124] an infrared pulse that is resonant with a vibrational transition is used to create a vibrational coherence. This coherence is probed using a Raman transition, generating a signal at the sum of the infrared and probe frequencies. Within the electric dipole approximation, no VSFG signal is generated in an isotropic bulk medium.[125] VSFG is therefore exquisitely sensitive to molecules at interfaces between two isotropic or centrosymmetric media.

The pipette glass is not identical to the silica in the VSFG substrate, but the acetonitrile organization is a robust feature of a broad range of experimental and simulated, flat and curved silica interfaces.[98] Although the surface bilayer is roughly centrosymmetric, the hydrogen bonding of the cyano groups in the first sublayer shifts the methyl stretching frequency enough to be distinct from that of the molecules in the second sublayer.[99] Thus, the VSFG spectrum of the symmetric methyl stretch is a sensitive probe of the organization of acetonitrile molecules at a silica surface.

Representative VSFG spectra are shown with relative intensities in Figure 4.2A and height normalized in Figure 4.2B for neat acetonitrile and solutions of $LiClO_4$ with concentrations from 10^{-9} M to 1 M. Although the intensity decreases at high electrolyte concentrations, the readily measurable signal at the highest concentration indicates that the solvent organization is robust in the presence of this salt.

Three parameters characterize the concentration dependence of the VSFG spectra: the relative intensity (Figure 4.2C), the spectral shift relative to the neat liquid (Figure 4.2D), and the full width at half maximum (FWHM) of the peak (Figure 4.2E). The spectral intensity is slightly larger than that of the neat liquid at low concentrations, before decreasing at concentrations greater than $\sim 3 \times 10^{-6}$ M. At a concentration of 1 M, the intensity is a few percent of that of the neat liquid. The spectral shift is zero until the electrolyte concentration becomes greater than $\sim 3 \times 10^{-4}$ M, after which the shift increases monotonically. The FWHM in the solutions is greater than that in the neat liquid. The additional broadening is less than 1 cm^{-1} at low concentrations, increases at concentrations greater than $\sim 10^{-4}$ M, reaches a peak at $\sim 3 \times 10^{-1}$ M, and then decreases.

We can construct a model of this system based on the ion-current and VSFG data. In neat acetonitrile, the surface bilayer is stable,[126] and is not expected to be mobile due to the strength of the hydrogen bonds to the first sublayer[127] and the interdigitation of the second sublayer.[99–101] The exterior of the second sublayer consists primarily of cyano groups. Therefore, the effective surface potential of the neat liquid is negative (top panel of Figure 4.2F).

At concentrations of $\sim 3 \times 10^{-6}$ M and less (region I in Figure 4.2C-F), our data suggest that lithium ions partition to the exterior of the surface bilayer, causing partial neutralization of the negative effective surface potential. Adsorption of Li$^+$ could create a higher degree of alignment of molecules with methyl groups pointing towards the interface, but this phenomenon would decrease the VSFG signal. Such adsorption could also reduce the population of molecules in the second sublayer that point in the same direction as those in the first sublayer. Lineshape simulations (Figure A.4) demonstrate

72

that such ordering can reproduce the observed spectral changes. Adsorption of Li^+ on the second sublayer may also lead to a further increase in inhomogeneous broadening. Lithium ions would not be expected to cause other substantial organizational changes in the surface bilayer until these ions reach a concentration at which they can penetrate the bilayer. Indeed, as shown below, molecular dynamics simulations suggest that the influence of ions on the surface bilayer is minimal even at concentrations on the order of 1 M.

As the $LiClO_4$ concentration increases, through $\sim3 \times 10^{-4}$ M (region II), the VSFG intensity decreases, whereas the FWHM and peak position remain the same within experimental uncertainty. The effective surface potential changes sign in this concentration range (Figure 4.1F); a pipette exhibited a negative $A(2V)$ in contact with a 0.1 mM/1 mM salt gradient and a positive $A(2V)$ in contact with a 1 mM/10 mM $LiClO_4$ gradient. Thus, adsorption of Li^+ neutralizes the negative potential of the surface bilayer of acetonitrile in region II. Based on the 3.92 D dipole moment and the 1.157 Å C≡N bond length[128] of acetonitrile, the nitrogen atom has ~0.7 of an electron charge. Thus, an upper limit for the Li^+ adsorption that would lead to neutralization is ~2 cations for every 3 acetonitrile molecules. Under these circumstances, virtually every cyano group in the second sublayer is associated with a cation. In this scenario, the difference in transition frequencies between the methyl groups in the two sublayers will decline, decreasing the VSFG signal intensity. Any narrowing as a consequence of this spectral shift may be compensated by an increase in inhomogeneous broadening.

In region III, which extends up to $\sim3 \times 10^{-2}$ M, the VSFG intensity decreases precipitously. The spectrum blue shifts, and the FWHM increases substantially. The

effective surface potential becomes positive in this region, as evidenced by positive values of A(2V) (Figure 4.1F). The broadening and spectral shift are suggestive of the presence of ions in the surface bilayer. Perchlorate, which is relatively hydrophobic and has a low charge density, is expected to be the predominant species in this region. The direction of the shift is consistent with that expected from the Stark effect[129] for anions in the middle of the bilayer. Because the transition frequencies of the methyl groups in both sublayers are influenced by the increasing anion concentration within the bilayer, the difference in shifts between the two sublayers will decrease, reducing the VSFG intensity. The presence of anions in the hydrophobic region of the surface bilayer is further suggestive of partitioning of lithium ions to the surface. Given anions within the bilayer, the adsorption of Li$^+$ to the exterior of the bilayer can increase further, leading to a positive effective surface potential.

In region IV, concentrations greater than $\sim 3 \times 10^{-2}$ M, the intensity decreases further, the spectral shift increases substantially, and the FWHM reaches a maximum before decreasing again. The FWHM maximum in this concentration regime arises from the presence of two contributions (Figure 4.2B), one that is in the same position as at lower concentration and another that is blue-shifted. Both peaks contribute significantly to the spectrum at concentrations of 10^{-2} M to 10^{-1} M, but the blue-shifted peak predominates at higher concentrations. A(2V) remains positive in this concentration range (Figure 4.1F), but is smaller than its maximum value. These observations suggest that perchlorate anions continue to partition into the hydrophobic region of the bilayer in this concentration range, leading to the blue-shifted spectral feature. The blue shift saturates when the concentration of anions in the bilayer reaches its maximum, so the FWHM at

high concentration is that of methyl groups adjacent to anions. The presence of anions makes the methyl transition frequencies in the two sublayers more similar, decreasing the intensity further. There continues to be an excess of lithium ions on the outer portion of the bilayer, maintaining a partial positive effective surface potential.
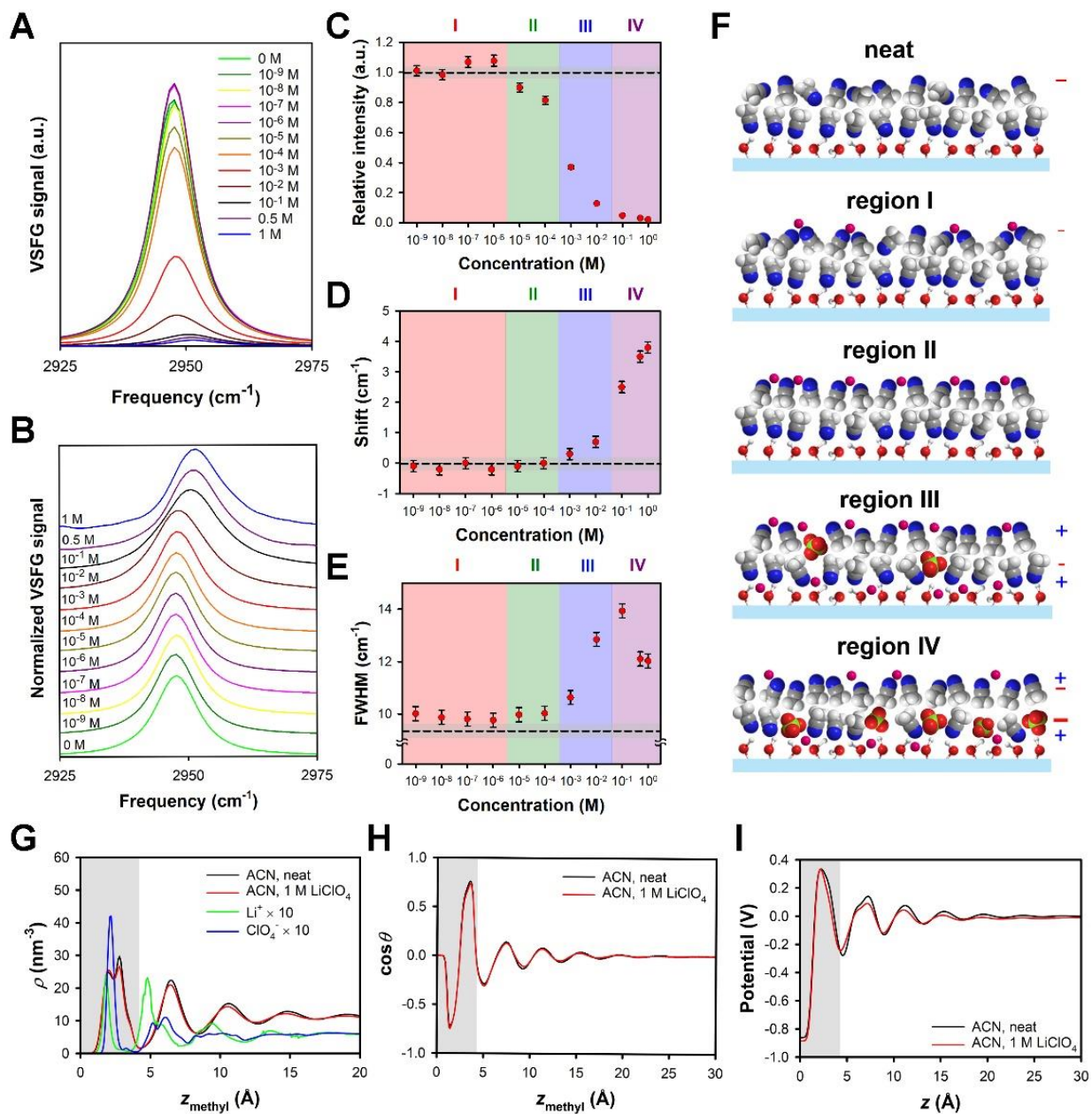
Figure 4.2: VSFG spectra and molecular dynamics simulations of LiClO$_4$ in acetonitrile at a silica surface. Representative spectra as a function of electrolyte concentration with (A) relative and (B) normalized intensities. Concentration dependence of (C) the relative intensity, (D) the spectral shift relative to the neat liquid, and (E) the FWHM. Dashed lines indicate values for the neat liquid and gray bands indicate uncertainties. (F) Schematic representations of the organization of the acetonitrile bilayer in the neat liquid and in the LiClO$_4$ solution in the concentration regions in (C)-(E). In depicting the silica surface, only O (red) and H (white) atoms in the silanol groups are shown. The molecules closest to the silica surface constitute the first sublayer. The molecules farther from the surface, which predominantly point in the opposite direction, constitute the second sublayer. This 2D depiction does not illustrate the interdigitation of these sublayers. (G) The density of

the methyl transition dipoles of acetonitrile in the neat liquid (black) and a 1 M solution of LiClO$_4$ (red) as a function of distance from the interface. The density profiles of Li$^+$ (green) and ClO$_4^-$ (blue) are also shown, and have been multiplied by 10 for ease of comparison. (H) Average molecular orientation as a function of distance of the methyl transition dipole from the interface for neat acetonitrile (black) and acetonitrile in the solution (red). A θ value of 0 indicates that the cyano group points towards the silica. (I) Electrical potential as a function of distance from the interface for neat acetonitrile and in the solution. The gray regions in (G)-(I) indicate the approximate extent of the surface bilayer.

Molecular dynamics simulations show that 1 M LiClO$_4$ has remarkably little influence on the organization of acetonitrile at a silica surface.

In the above model, solvent ordering is the driving force in determining the distribution of interfacial ions, rather than the surface charges described by the EDL theory. To investigate this behavior further, we performed MD simulations of 1 M LiClO$_4$ in acetonitrile at a silica surface, using a well-studied model of this interface.[116,117,130] Figure 4.2G shows the methyl transition dipole density distribution for neat acetonitrile (black) and a 1 M solution of LiClO$_4$ (red). The methyl transition dipole was chosen for comparison with VSFG results (the center-of-mass density distribution is shown in Figure A.5). Oscillations with a period of ~4.8 Å are indicative of the repeating lipid-bilayer-like organization of the liquid. The differences in the density profiles between the neat liquid and the solution are remarkably small, and can be attributed largely to the slightly lower concentration of acetonitrile in the solution. Due to interdigitation, the density peak closest to the surface arises from methyl groups of molecules in the second sublayer, and the second peak arises from methyl groups of molecules in the first sublayer.

The density profiles of the cations (green) and anions (blue) are also shown in Figure 4.2G. The first cation density peak is closer to the surface than the density peak of the methyl groups of the second sublayer, whereas the first anion density peak is slightly farther from the surface than this methyl density peak. In agreement with the

77

experiments and model presented above, the perchlorate density peak closest to the surface is in the hydrophobic region of the bilayer. The center of the anion peak is not in the middle of the hydrophobic region, because perchlorate can accept hydrogen bonds from surface silanol groups.

The ion density distributions reveal the source of the positive effective surface potential observed at moderate to high concentrations of $LiClO_4$. Given the interdigitation of the surface bilayer, transport parallel to the interface does not occur in this region, although the second sublayer has some mobility perpendicular to the interface.[101,126] Some Li^+ ions, and a larger number of ClO_4^- ions, partition into the bilayer. In response to this charge imbalance, there is a Li^+ density peak near the exterior of the first bilayer, at ~4.8 Å. Given their association with the immobile second sublayer, we believe that these cations do not contribute to transport parallel to the surface, and therefore create an effective positive surface charge for the immobile layer.

Figure 4.2H shows the orientational distribution of acetonitrile molecules based on the position of the methyl transition dipoles in the neat liquid (black) and the 1 M $LiClO_4$ solution (red). The presence of the electrolyte has remarkably little influence on the solvent orientation; see Figure A.6 for the corresponding plot for the center-of-mass of acetonitrile. The charge-density profile (Figure 4.2I), the electric field (Figure A.7), and the potential (Figure A.8) are similarly unaffected by the electrolyte.

A constant electric field can introduce a third-order, bulk component in VSFG spectra that does not depend upon broken inversion symmetry.[131] The Debye screening of such a field can influence the magnitude and phase of this contribution.[132–134] However, our simulations demonstrate that the local electric field in this system does not depend

significantly on electrolyte concentration, which is why we are able to interpret the VSFG data without explicitly considering any concentration dependence of this contribution.

The Debye length in a 1 M electrolyte solution is short enough that the field is not expected to project away from the interface. Performing simulations at substantially lower concentrations is challenging. However, the fact that the organization and charge density of acetonitrile are so similar between the neat liquid and the 1 M $LiClO_4$ solution strongly suggests that the same features persist throughout the entire concentration range explored here experimentally. The lack of abrupt changes in the VSFG spectra with increasing electrolyte concentration further supports this picture.

The concentration-dependent effective surface potential behavior depends on the electrolyte identity

To explore the generality of this phenomenon, we performed ion-current measurements on salts with a common cation or anion. Electrolytes that are soluble in acetonitrile typically have a large, polyatomic anion, so we investigated solutions of $LiBF_4$ and $LiPF_6$. Figure 4.3A shows $A(2V)$ for different concentrations of $LiBF_4$; the effective surface potential is negative at low concentrations and is zero at higher concentrations. Although BF_4^- is not much smaller than ClO_4^-, acetonitrile solutions of $LiClO_4$ and $LiBF_4$ behave differently at a silica surface. The likely source of this disparity is ion pairing, which commences at considerably lower concentrations of $LiBF_4$ than $LiClO_4$ in this solvent.[135]

Figure 4.3B shows $A(2V)$ data for $LiPF_6$ at different concentrations. At low concentrations, the effective surface potential is negative, becoming positive at a concentration between 10 mM and 100 mM. The behavior of $LiPF_6$ solutions is similar to that of $LiClO_4$ solutions, but the transition to a positive effective surface potential occurs

at a concentration that is an order of magnitude higher for $LiPF_6$ than for $LiClO_4$. Given the relative sizes of the anions, the energetic cost for PF_6^- to partition into the bilayer is considerably greater.

To explore the role of the cation, we performed ion-current measurements with $NaClO_4$. A(2V) for $NaClO_4$ in acetonitrile is negative at low concentrations, and becomes positive at a considerably higher concentration than for $LiClO_4$ (Figure 4.3C). The behavior of the $NaClO_4$ solutions is more similar to that $LiPF_6$ solutions than $LiClO_4$ solutions, suggesting that there is a greater energetic penalty for the larger Na^+ ions to partition to the silica surface than there is for Li^+ ions.
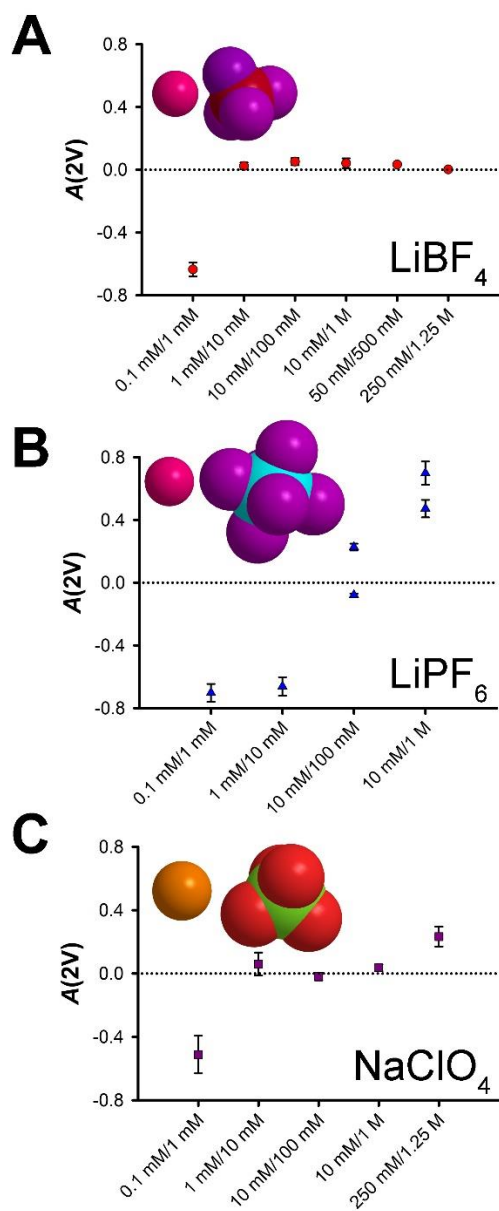
Figure 4.3: Dependence of the effective surface potential on the electrolyte. A(2V) at different concentrations of (A) LiBF$_4$, (B) LiPF$_6$, and (C) NaClO$_4$ in acetonitrile.

Conclusions

Our results stand in stark contrast to the classic EDL model, which treats the solvent as a homogeneous continuum and the ions as point charges. These approximations work well for aqueous solutions at silica surfaces, which are generally negatively charged due to deprotonation of silanol groups. This negative charge determines the distribution of ions in the interfacial solution. In contrast, we find that in the silica/liquid acetonitrile system, the interface can exhibit either a negative or a positive charge, depending on the concentration and identity of the salt. Because the silica surface remains uncharged but polar, the acetonitrile organizes itself in a manner that resembles a thermodynamically stable, supported lipid bilayer. At low electrolyte concentrations, the effective surface potential is determined by the cyano groups that point into the mobile portion of the liquid and is negative. At a high enough electrolyte concentration, it becomes thermodynamically favorable for cations to partition to the silica surface, allowing anions to move into the hydrophobic region of the bilayer. These anions reinforce the stability of the layer of cations on the exterior of the second sublayer of the solvent, leading to a positive effective surface potential. Thus, in this type of system, the notion of surface charge needs to be replaced by the effective surface potential of the silica/liquid interface.

There appears to be no definable Debye length in the silica/acetonitrile system. If any such exponential decay exists, it acts as an envelope for the oscillatory spatial distribution of ions driven by the solvent organization. More conventional behavior might also be observed at distances for which the acetonitrile organization disappears. These features are not unique to acetonitrile, and are likely recapitulated in other polar, aprotic

solvents. For instance, a positive effective surface potential has also been observed on surfaces with silanol or carboxylic acid groups for electrolytes in propylene carbonate[106,107] and acetone[107].

Our experimental and modeling results underscore the importance of solvent organization and ion identity in determining the ionic distribution, and hence the effective surface potential, in the sort of system studied here. Deviations from the EDL model due to effects such as the finite size of ions and solvent molecules, the interactions among all components of the system, and the organization of the solvent have been considered previously.[136–139] Deviations from this model arising from layering of ions have also been reported, but only at high concentrations.[140] Thus, the deviations that we have observed point towards the need for a new paradigm for understanding the organization of ions in electrolyte solutions in polar, aprotic solvents. Additional work will be required to address the role of contact ion pairs and solvent-separated ion pairs in such systems.[141,142]

Appendix A: Supplementary Materials for Chapter 4

Chapter adapted from:

Polster, J. W.; Souna, A. J.; Motevaselian, M. H.; Lucas, R. A.; Tran, J. D.; Siwy, Z. S.; Aluru, N. R.; Fourkas, J. T. The Electrical-Double Layer Revisited. *Natural Sciences* **2022**, e20210099. https://doi.org/10.1002/ntls.20210099.

Supplementary Text

Principles of ion-current measurements

Here we describe in more detail how ion-current measurements can reveal the sign of the effective surface potential. We will consider the case in which the electrolyte concentration is greater in the external solution than in the pipette, i.e. [C_{out}] > [C_{in}], which was the case for all measurements reported here. The ground electrode was located in the pipette, i.e. in the less concentrated solution. If the effective surface potential is negative and the external electrode is positive relative to the internal electrode, then cations will flow into the pipette from the more concentrated solution (Figure A.1A), electroosmotically dragging the more concentrated solution into the pipette tip. If the external electrode is negative relative to the internal electrode, then cations will flow out of the less concentrated solution in the pipette, leading to the pipette tip being filled with the less concentrated solution, and consequently to a lower current. Thus, the current under positive bias will be greater than the current under negative bias, leading to a negative ion-current anisotropy. If instead the effective surface potential is positive (Figure A.1B), the situation will be reversed, i.e. there will be more current under negative bias, when anions flow into the pipette, than under positive bias, when anions flow out of the pipette, leading the positive ion-current anisotropy.

Ion-current anisotropies at other voltages

The ion-current anisotropies reported in the main text were for voltages of ±2 V to minimize any uncertainties in the measurements. As shown in Figure A.2 for measurements made at different concentrations of LiClO$_4$, similar results are observed at lower voltages (compare with Figure 4.1F). Because the ion-current curves are generally either positively curved or negatively curved (see Figures 4.1D,E), $A(V)$ does depend on

the voltage to some extent, but the general trend in this quantity is the same regardless of the voltage.

Control experiments in aqueous solution

Given that the isoelectric point of silica is at a pH on the order of 3,[143] the surface silanol groups of silica tend to dissociate in aqueous solutions. Thus, the surface potential of the glass pipettes used for ion-current measurements is expected to be negative. As a control experiment, we measured the IV curves for 100 mM/1 M aqueous KCl solutions. A representative IV curve is shown in Figure A.3. Based on these data, A(2V) is -0.29, which confirms that the surface potential is negative.

VSFG lineshape simulations

In neat acetonitrile, the second sublayer of the surface bilayer is more disordered than the first sublayer, with a small subset of molecules having methyl groups pointing into the bulk liquid.[144] Partitioning of Li$^+$ ions to the exterior of the second bilayer should lead to a greater degree of organization in this sublayer, including causing an even larger majority of the methyl groups in this sublayer to be oriented towards the interface. This situation might be assumed to lead to an even greater degree of cancellation between the contributions from the two sublayers. In contrast, in Region I, we observe a slight increase in the intensity of the VSFG signal (Figure 4.2C), in addition to a small red shift (Figure 4.2D) and a slight amount of broadening (Figure 4.2E).

To test whether our spectroscopic observations are consistent with lithium cations leading to increased ordering in the second sublayer of the surface bilayer, we performed lineshape simulations. The spectrum $S(\bar{v})$ was assumed to be the magnitude squared of

two Lorentzian features, one corresponding to methyl groups in each of the sublayers of the surface bilayer:

$$S(\bar{v}) = \left| \frac{A_1}{(\bar{v} - \bar{v}_1) + i\Gamma} + \frac{A_2}{(\bar{v} - \bar{v}_2) + i\Gamma} \right|^2 \qquad (A.1)$$

Here, A_1 and A_2 are the amplitudes of the two components, which are assumed to be opposite in sign because the methyl groups in the two sublayers largely point in opposite directions, $\bar{v}_1$ and $\bar{v}_2$ are the center frequencies of each component, and Γ is the linewidth, which is assumed to be the same for each component.

We note that the probe spectral bandwidth used in the current study is lower than in previous VSFG work on neat acetonitrile,[99] so in our simulations we explored different separations between the two components ($\Delta\bar{v} = \bar{v}_2 - \bar{v}_1$), as well as different linewidths Γ. For the neat liquid, we retained the ratio of the absolute values of the amplitude of the peak for the second sublayer divided by that for the first sublayer measured previously, $|A_2/A_1| = 0.89$; we note that in Table 2 of a previous publication,[99] the values listed are the inverse of this ratio. We examined three values of $\Delta\bar{v}$: 2 cm^{-1}, 4 cm^{-1}, and 6 cm^{-1}. The value of Γ for each value of $\Delta\bar{v}$ was chosen such that the overall spectral line had the same full width at half maximum (FWHM) as the experimental spectrum for the neat liquid (9.46 cm^{-1}) for $|A_2/A_1| = 0.89$. The value of Γ was 7.0 cm^{-1} for $\Delta\bar{v}=$ 2 cm^{-1}, 6.6 cm^{-1} for $\Delta\bar{v}=$ 4 cm^{-1}, and 5.3 cm^{-1} for $\Delta\bar{v}=$ 6 cm^{-1}.

The results of these simulations are shown in Figure A.4. Figure A.4A shows the VSFG intensity as a function of $|A_2/A_1|$ for these three scenarios. Above $|A_2/A_1| = 0.89$, the peak intensity decreases with increasing $|A_2/A_1|$ for $\Delta\bar{v}=$ 2 cm^{-1}, increases a few percent for $\Delta\bar{v}=$ 4 cm^{-1}, and increases more substantially for $\Delta\bar{v}=$ 6 cm^{-1}. As seen in Figure A.4B, over the same range of $|A_2/A_1|$ the FWHM decrease for $\Delta\bar{v}=$ 2 cm^{-1} and 4 cm^{-1}, but

increases for $\Delta\bar{\nu}$= 6 cm^{-1}. As shown in Figure A.4C, over the same range of $|A_2/A_1|$ there is a red shift of the peak for all values of $\Delta\bar{\nu}$; however, the shift in the case $\Delta\bar{\nu}$= 6 cm^{-1} is the smallest. The simulated spectra for $\Delta\bar{\nu}$= 6 cm^{-1} exhibit all the qualitative trends observed in the experimental data for LiClO$_4$ concentrations in Region I. Thus, our data are consistent with the increase of organization of the second sublayer of the surface bilayer in the presence of low concentrations of Li$^+$, as long as the contributions from the two sublayers are separated by an amount $\Delta\bar{\nu}$ that is comparable to the widths of each contribution.

Additional results from molecular dynamics simulations

In Figures A.5 through A.9 we present additional results from molecular dynamics simulations. Figure A.5 shows the density profile as a function of the distance of the molecular center of mass from the silica interface. Figure A.6 shows the average molecular orientation as a function of the distance of the molecular center of mass from the silica interface. Figures A.7 and A.8 show the average electric field and potential as a function of distance from the silica interface (z), respectively. Due to the homogeneity in the *x-y* plane, the electric field varies only in the *z* direction and is calculated via

$$E(z) = -\frac{d\phi(z)}{dz} \tag{A.2}$$

To compute the electrical potential, $\phi(z)$, we use the Poisson equation:

$$\frac{d^2\phi(z)}{dz^2} = -\frac{\rho(z)}{\varepsilon_0} \tag{A.3}$$

with the boundary conditions

$$\left.\frac{d\phi}{dz}\right|_{z=0} = -\frac{\sigma_{c,left}}{\varepsilon_0} \tag{A.4}$$

$$\frac{d\phi}{dz}\bigg|_{z=H} = \frac{\sigma_{c,right}}{\varepsilon_0} \qquad (A.5)$$

and

$$\phi\left(\frac{H}{2}\right) = 0 \qquad (A.6)$$

where $\rho(z)$ is the charge density as a function of distance from the interface and ε_0 is the permittivity of free space, and $\sigma_{c,left}$ and $\sigma_{c,right}$ are the surface charge densities on the left and right walls, respectively. These latter quantities are equal to zero, because both the silica and graphene walls have net zero charge. We note that, due to the third boundary condition, the electrostatic potential at any point is relative with respect to the mid-point of the channel.

Supplementary Figures
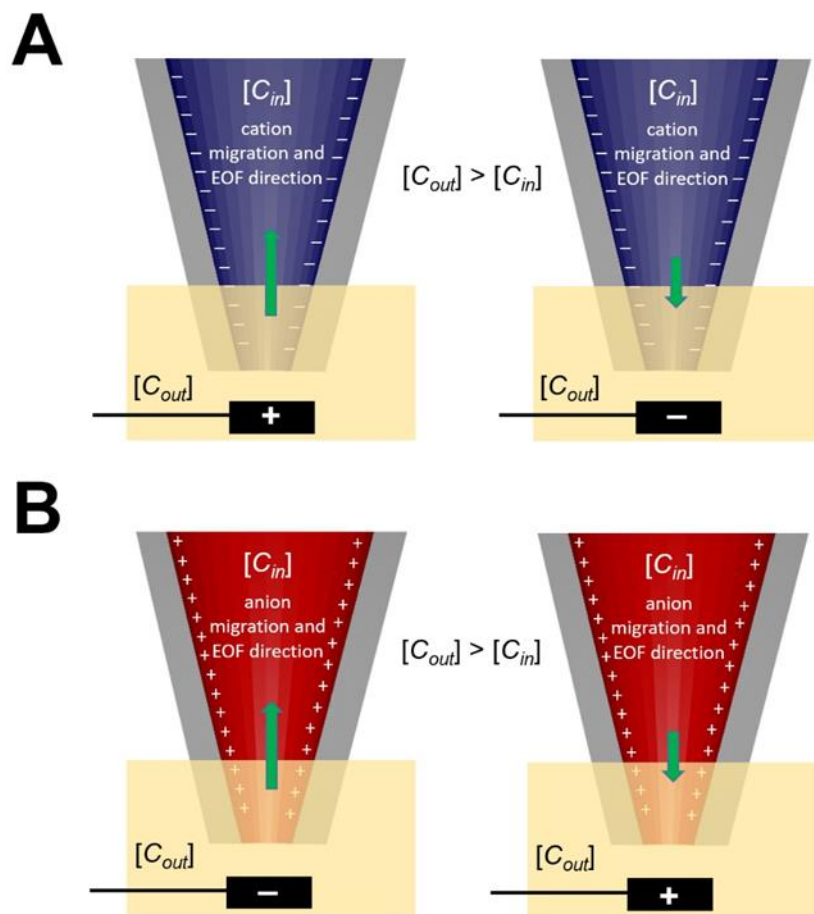
Figure A.1: Schematic physical picture of the factors determining the ion-current anisotropy when the electrolyte concentration in the reservoir, $[C_{out}]$, is greater than the electrolyte concentration in the pipette, $[C_{in}]$. (A) The pipette is negatively charged. Under a positive bias (scheme on the left), cations are sourced from the more concentrated solution that fills the pipette tip through electroosmosis. Under a negative bias (scheme on the right), cations are sourced from the pipette, such that the pipette tip becomes filled with the less concentrated solution, leading to lower current. Accordingly, $I(V) > I(-V)$, such that $A(V)$ is negative. (B) If the pipette is positively charged, then under negative bias (positive bias) anions fill the pipette tip with more concentrated (less concentrated) solution. Accordingly, $I(V) < I(-V)$, such that $A(V)$ is positive.
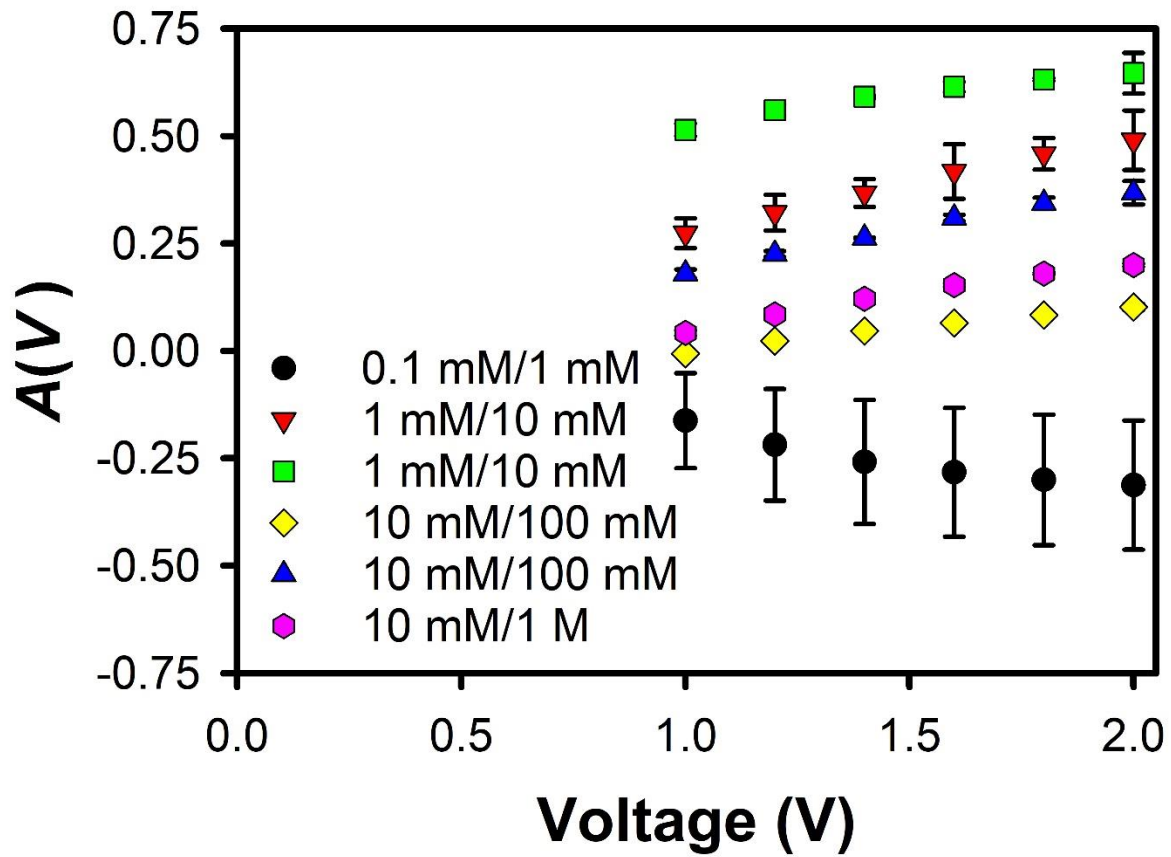
Figure A.2: Dependence of the ion-current anisotropy on the voltage for different values of [C_{in}]/[C_{out}] of LiClO$_4$. The two sets of data for 1 mM/10 mM and 10 mM/100 mM are for two different pipettes.
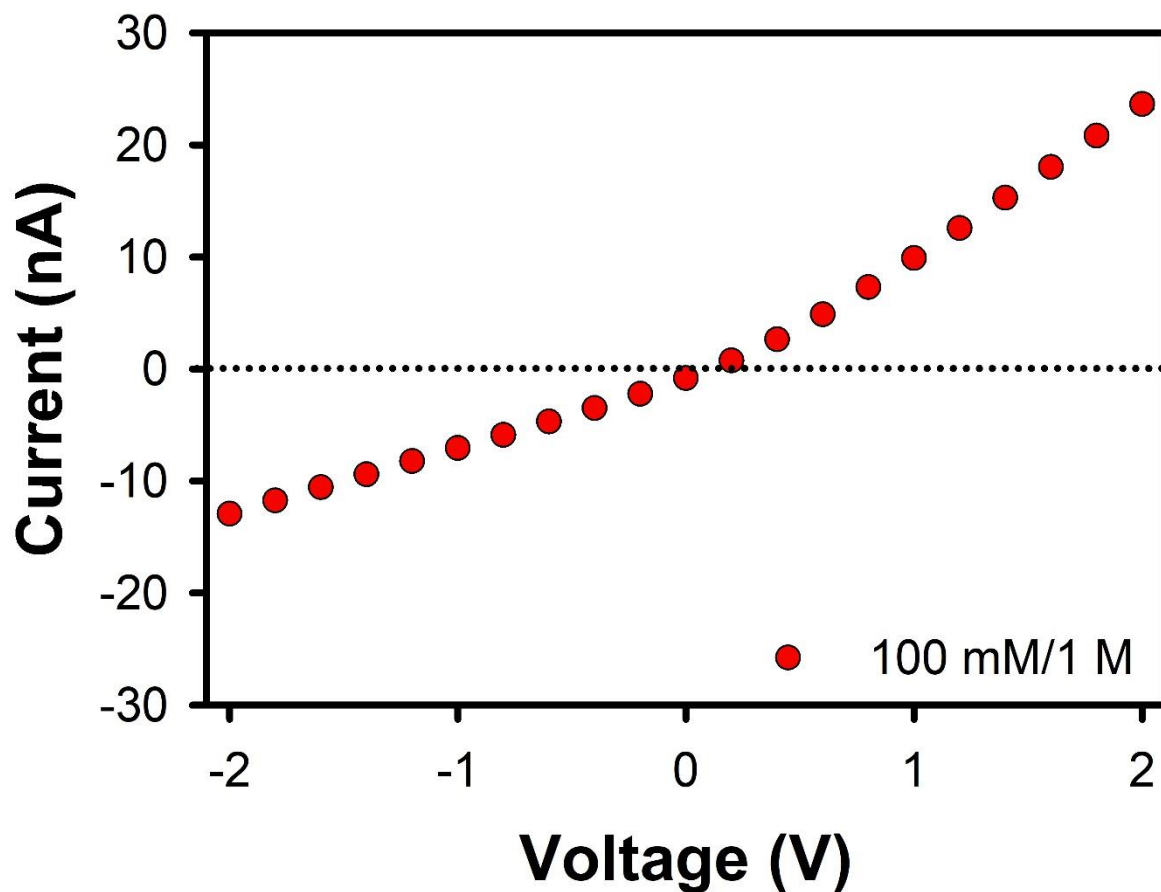
Figure A.3: IV curve for 100 mM/ 1 M KCl in water in the same type of glass pipette used for the acetonitrile experiments. A(2V) is -0.29, indicating a negative surface potential on the inner surface of the pipette.
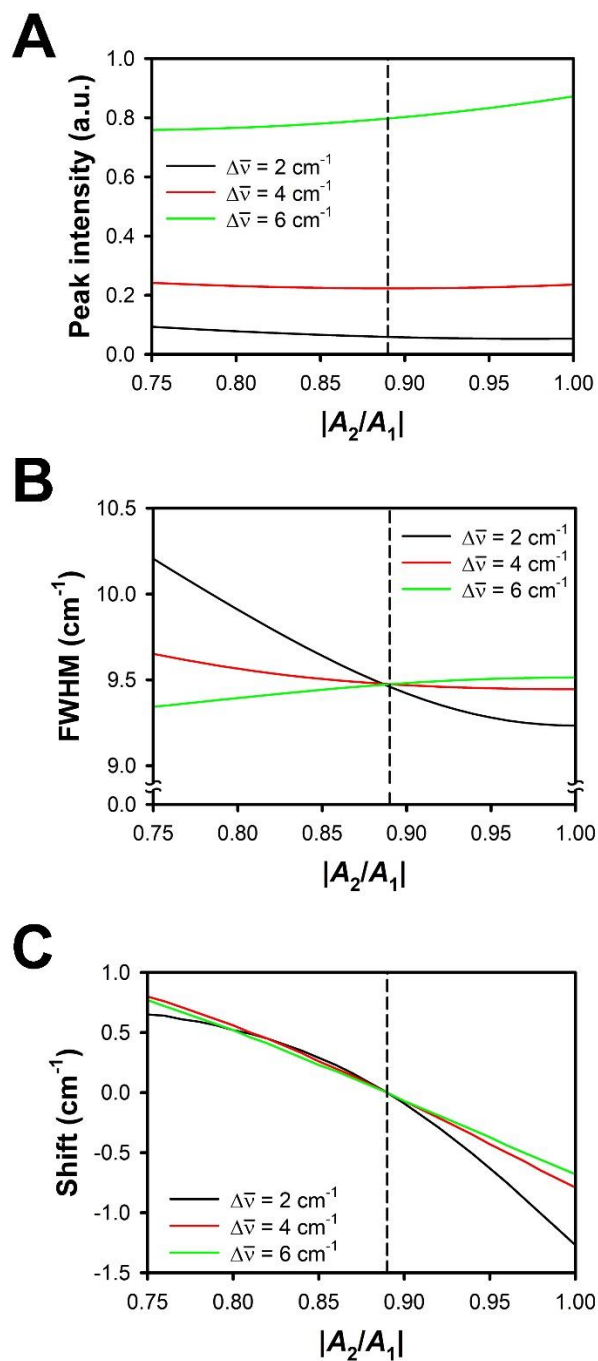
Figure A.4: Simulations of the VSFG line shape as a function of the absolute value of the amplitude of the signal contribution for methyl groups in the second sublayer divided by that of the first sublayer for different spectral shifts $\Delta\bar{\nu}$ between the two contributions. The plots are for (A) the maximum intensity of the VSFG peak; (B) the full width at half maximum of the VSFG peak; and (C) the shift of the peak relative to the position of the contribution of the second sublayer. The dashed vertical lines indicate the value of $|A_2/A_1|$ for the neat liquid.
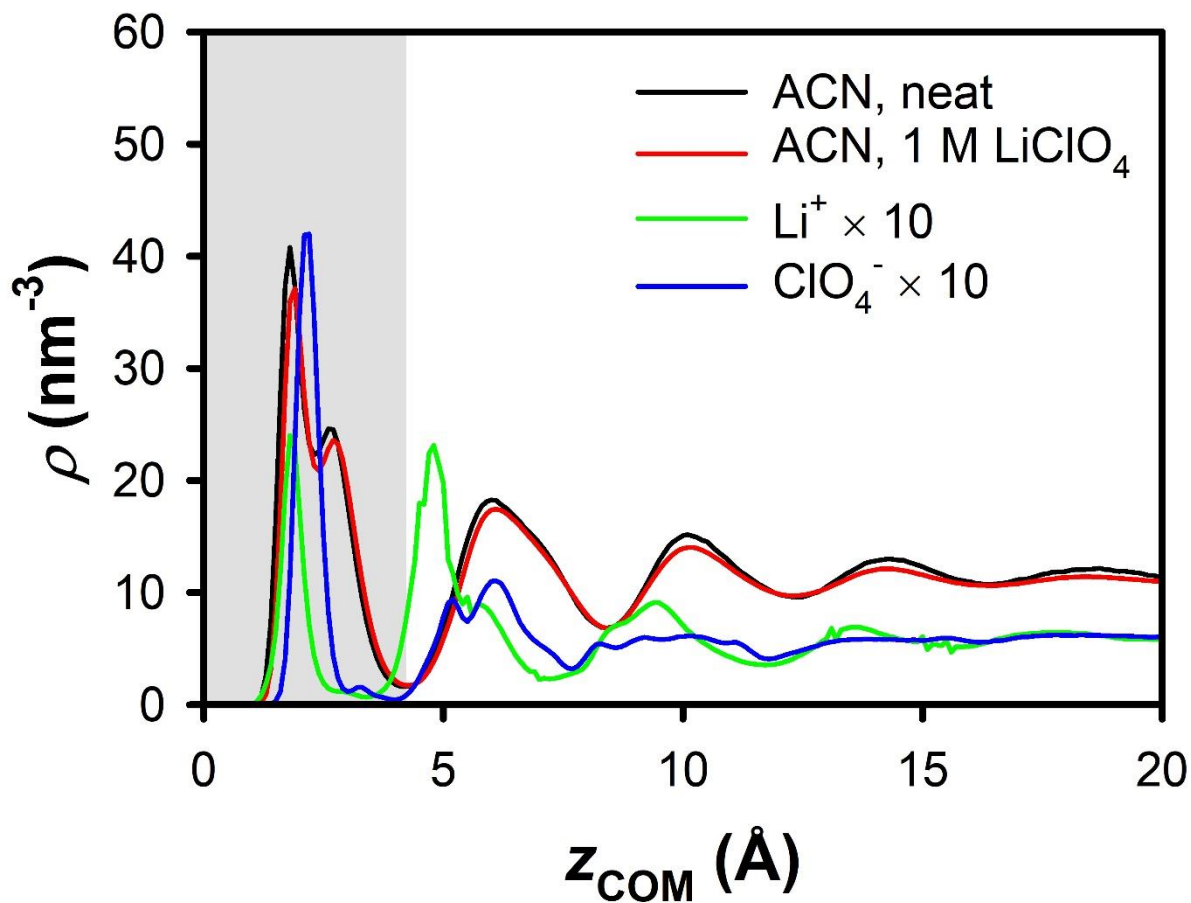
Figure A.5: Center-of-mass density profiles with respect to distance from a silica interface for neat acetonitrile (black) and 1 M LiClO$_4$ in acetonitrile (red, acetonitrile; green, Li$^+$ × 10; blue, ClO$_4^-$ × 10). The grey region indicates the approximate extent of the surface bilayer.
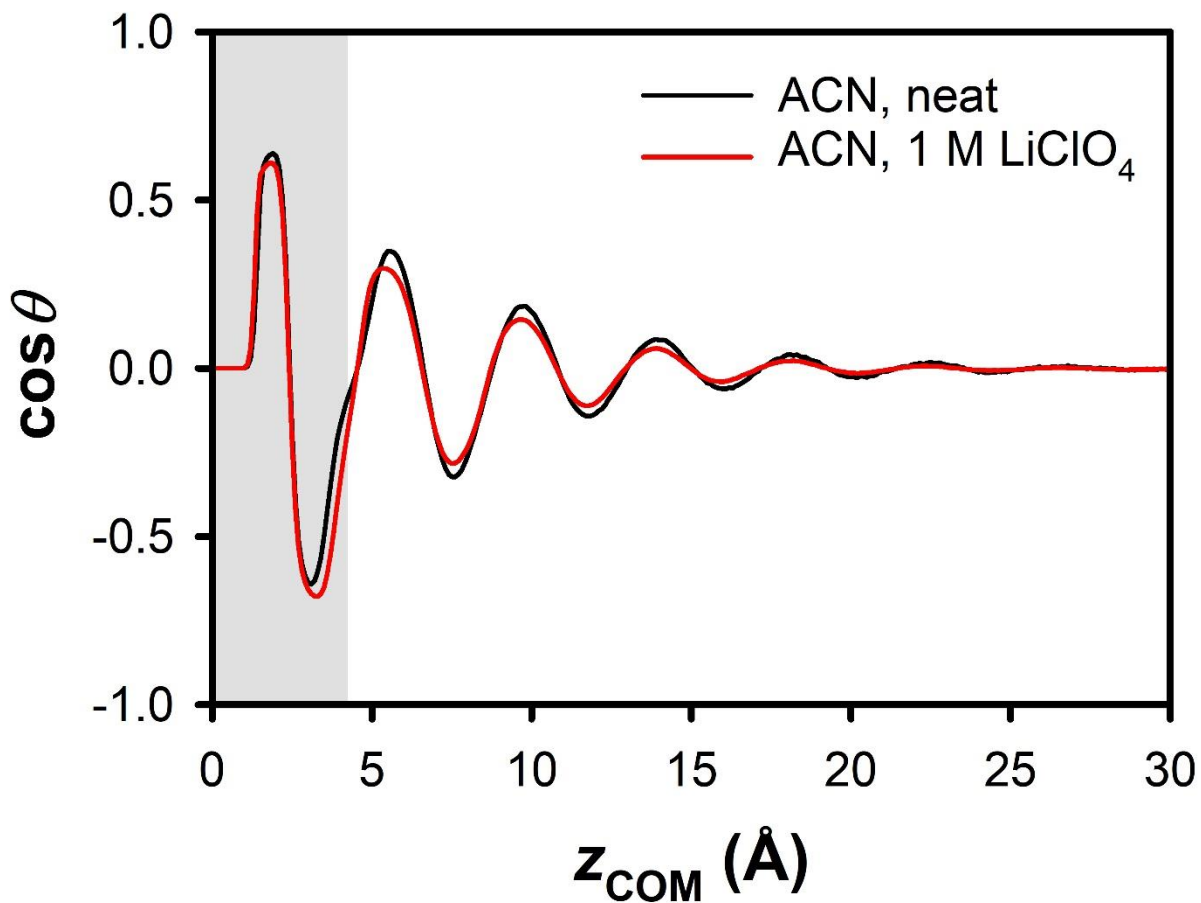
Figure A.6: Average molecular orientation as a function of the distance of the center of mass from a silica interface for neat acetonitrile (black) and acetonitrile in a 1 M LiClO$_4$ solution (red). The grey region indicates the approximate extent of the surface bilayer.
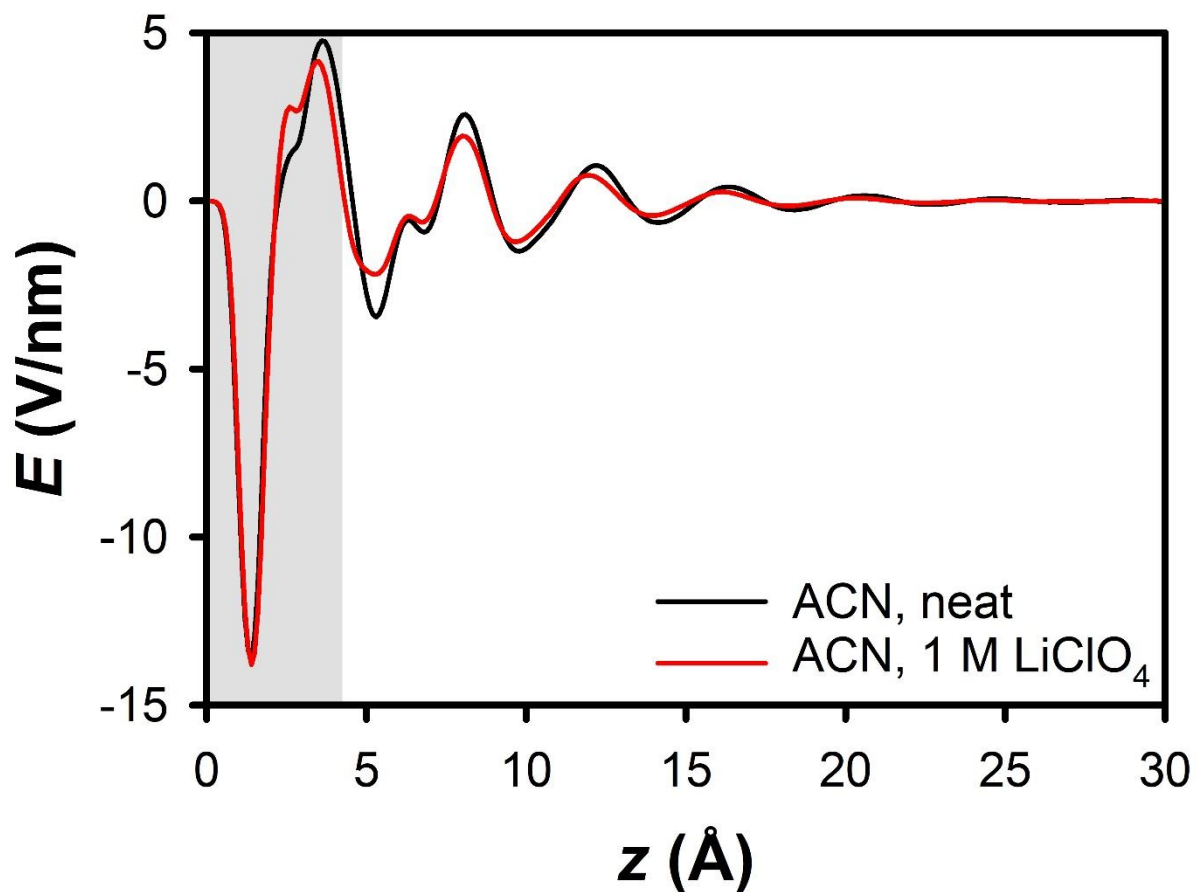
Figure A.7: Electric field as a function of distance from a silica interface for neat acetonitrile (black) and acetonitrile in a 1 M LiClO$_4$ solution (red). The grey region indicates the approximate extent of the surface bilayer.
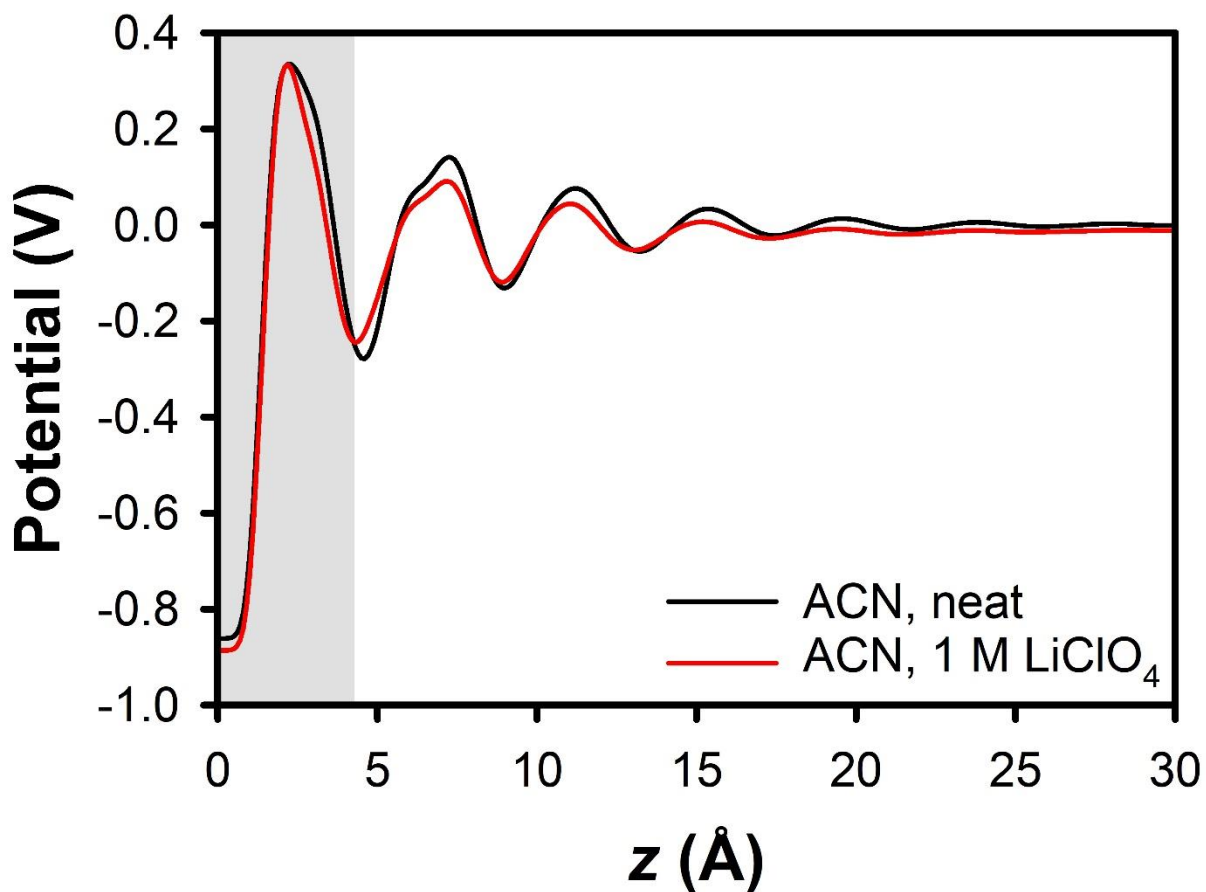
Figure A.8: Electrical potential as a function of distance from a silica interface for neat acetonitrile (black) and acetonitrile in a 1 M LiClO$_4$ solution (red). The grey region indicates the approximate extent of the surface bilayer.
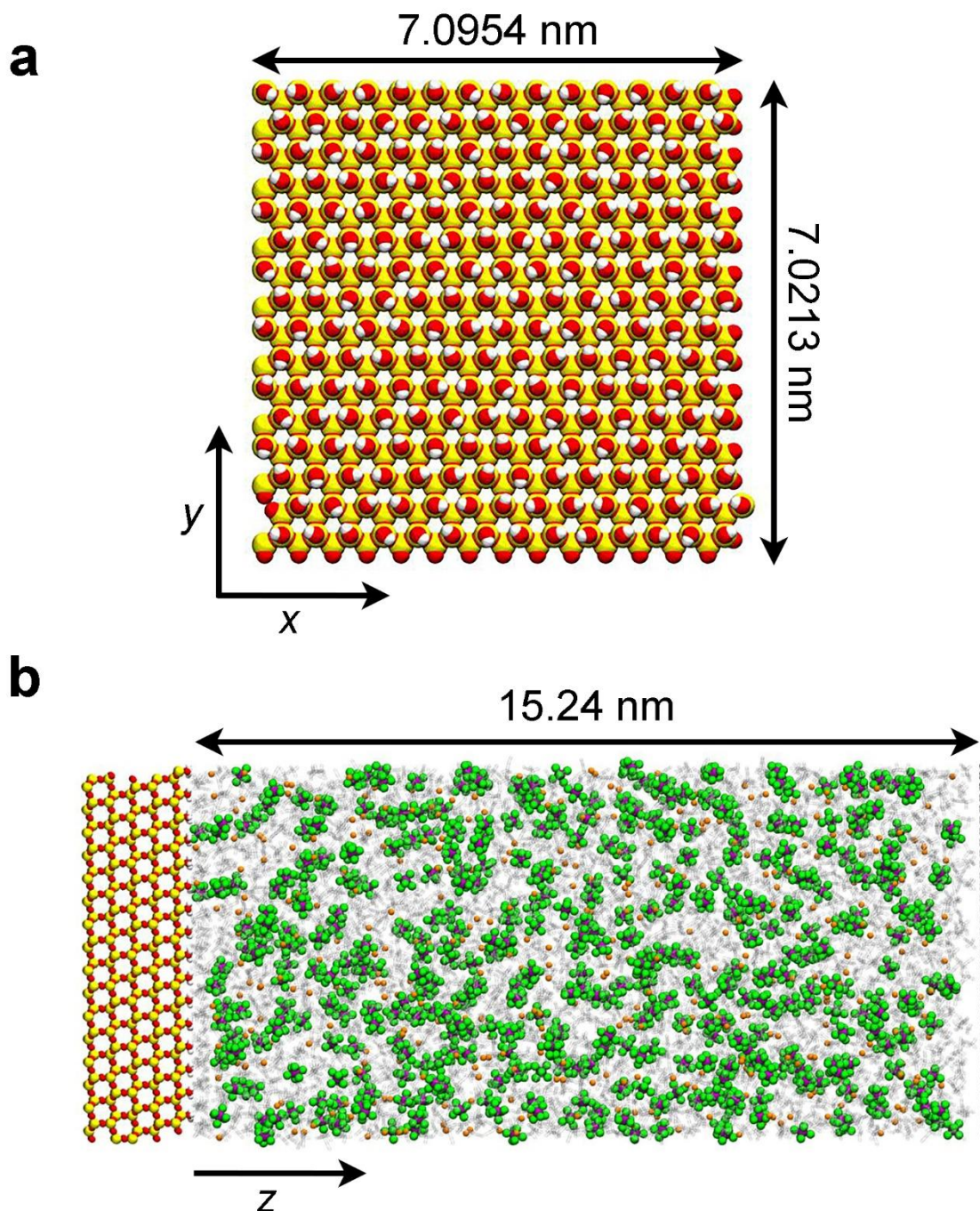
Figure A.9: Setup for molecular dynamics simulations of interfacial acetonitrile. (a) Top view of the hydroxylated silica surface. (b) The confined system consists of a silica substrate (silicon, yellow; oxygen, red; and hydrogen, white), a graphene sheet (carbon, grey), acetonitrile (ghost representation), and ions, Li^+ (purple) and ClO_4^- (green and red). The zero for the z axis is set to the location of the oxygen atoms of the silanol (SiOH) groups on the surface.

Chapter 5: Gating of Hydrophobic Nanopores with Large Anions

Chapter adapted from:

Polster, J. W.; Acar, E. T.; Aydin, F.; Zhan, C.; Pham, T. A.; Siwy, Z. S. Gating of Hydrophobic Nanopores with Large Anions. *ACS Nano* **2020**, *14* (4), 4306–4315. https://doi.org/10.1021/acsnano.9b09777**.**

Copyright 2020 American Chemical Society

For my next two chapters we will be returning to water-based experiments, as we will focus more on chemically modifying the nanopore to achieve desired transport properties. The next two projects look at nanopores rendered hydrophobic through chemical attachment of fluorinated alkyl groups. Although one might have not heard the term before, fluorinated alkyl molecules are found in many households as Teflon, a non-stick coating. Pans treated with Teflon are rendered hydrophobic, giving them their non-stick properties. If you have a non-stick pan, try putting a drop of water on it and observe the shape the water forms. You will see the water "bead up". This is because the water-water interactions are more favorable than the water-pan interactions. The water will naturally want to interact more with itself than with the pan surface, hence the beading up shape. We can measure the contact angle (*i.e.*, the interior angle of the water droplet) of this droplet and see it is greater than 90°. Hydrophobic surfaces are characterized by having a contact angle >90°. On the other hand, if you were to put a drop of water on a glass surface, you will see the water spread out. This is because the water-glass interactions are more favorable than water-water interactions. The favorable interactions cause the water to spread across the surface and maximize the number of water-glass interactions. The contact angle for a water droplet on glass, or any hydrophilic surface, will be <90°. In this way, a surface's hydrophobicity can be assessed by measuring the contact angle it makes with water.

Hydrophobic and hydrophilic properties are easy to observe at the macroscopic level, but many questions remain about what consequences arise from putting these surfaces under nanoconfinement. Interestingly, theoretical calculations estimate that when two hydrophobic surfaces are ~100 nm apart, phase separation will occur, as the

confined water vapor becomes the most thermodynamically stable state.[145–147] This makes nanopores a great system to investigate nanoconfined hydrophobic surfaces. Understanding ion transport in nanoporous materials is critical to a wide variety of energy and environmental technologies, ranging from ion-selective membranes, drug delivery, and biosensing, to ion batteries and supercapacitors. While nanoscale transport is often described by continuum models that rely on a point charge description for ions and a homogeneous dielectric medium for the solvent, in this chapter we show that transport of aqueous solutions at a hydrophobic interface can be highly dependent on the size and hydration strength of the solvated ions. Specifically, measurements of ion current through single silicon nitride nanopores that contain a hydrophobic-hydrophilic junction show that transport properties are dependent not only on applied voltage but also the type of anion. We find that in Cl^--contained solutions the nanopores only conducted ionic current above a negative voltage threshold. On the other hand, introduction of large polarizable anions, such as Br^- and I^-, facilitated the pore wetting, making the pore conductive at all examined voltages. Molecular dynamics simulations revealed that the large anions, Br^- and I^-, have a weaker solvation shell compared to that of Cl^-, and consequently were prone to migrate from the aqueous solution to the hydrophobic surface, leading to the anion accumulation responsible for pore wetting. The results are essential for designing nanoporous systems that are selective to ions of the same charge, for realization of ion-induced wetting in hydrophobic pores, as well as for fundamental understanding on the role of ion hydration shell on the properties of solid/liquid interfaces.

Introduction

Hydrophobic interactions play an important role in many biological processes, such as protein folding and regulating transport in biological cells.[148–153] Interfaces between a hydrophobic surface and an aqueous solution were often found to exhibit many similar properties to those of the water/vapor interface,[154–159] which is amenable to a variety of spectroscopic approaches that have been employed to determine the distribution of water and ions at the interfaces.[160–162] For instance, several existing experiments and modeling[159,163–165] revealed that water density at hydrophobic surfaces was lower compared to the bulk value, and that the interfacial region is dominated by large polarizable ions including iodide and bromide. On the other hand, small ions with large hydration energies, such as multivalent ions, tended to remain in the bulk solutions, or exhibit weak accumulation at the interface, as observed for chloride.[163,166–169]

The remaining unresolved question considers possible consequences of the enhanced concentration of polarizable ions on transport behavior of nanoscale systems such as hydrophobic nanopores and nanochannels. Hydrophobic nanopores have attracted a great deal of research interest due to their applications in designing valves for on-demand delivery of ions and molecules, separation processes, as well as model systems to understand wetting/dewetting transitions at the nanoscale.[170–174] If one could gate hydrophobic nanopores with different ions, such channels would provide the basis for ion-specific responsive systems with applications in ionic circuitry and sensing.

Previous results suggested that achieving ionic gating in hydrophobic nanopores should be possible. Specifically, continuum modeling that took into account solvation energies of ions predicted that iodide ions would adsorb to a hydrophobic surface and

render it negatively charged.[175] Yet, so far ionic transport through hydrophobic nanopores has been mostly studied in physiological salts, such as aqueous solutions of KCl and NaCl. In these salts, hydrophobic nanopores act like valves because they are filled with water vapor, which, in the absence of external stimulus, prevents them from transporting ions or molecules.[150,170,172,176] Transport of water and all dissolved species in it can be, however, induced by applying a pressure difference[172,177–179] or transmembrane potential.[172,176,180–182] Ion current passing through a nanopore is the main observable informing on the nanopore wetting status: when the pore is filled with water vapor the current is nearly zero, while wetting of the pore is observed as finite current. Using electric field is advantageous because, in contrast to a system gated by pressure difference, applying voltage does not require mechanical strengthening of the membrane and thus many experiments can be performed with one nanopore without its breaking. Wetting hydrophobic nanopores using an electric field has recently been explained *via* voltage-induced alignment of water dipoles that in turn allows ions to pass through the pore and produce finite ion current.[183]

In this work we show that ionic transport through hydrophobic nanopores can be gated by a combination of electric field and large polarizable anions. To this end, we designed nanopores containing a hydrophobic entrance on one side, and a hydrophilic, highly charged entrance on the other side. Such an asymmetric hydrophobic/hydrophilic junction has been shown to lower hydrophobic interactions,[184–186] allowing us to induce the wetting of nanopores for voltages below 2 V, while probing pore gating with different ion types. Our ion current measurements suggested that large polarizable anions, such as bromide and iodide, favorably adsorb to the hydrophobic interfaces and, in turn,

promote the voltage-induced wetting process. We show that the wetting process enhances nanopore conductance by at least an order of magnitude in KI and KBr solutions as compared to KCl at the same concentration. On the other hand, we find that effects of selected cations on the voltage-induced wetting process were much weaker than the influence of anions. Our experimental findings were supported by first-principles calculations and molecular dynamics simulations;[187] specifically, the simulations revealed that larger anions yield weaker and less defined hydration shells and are more prone to accumulate at a hydrophobic surface where water concentration is diminished.

Methods

Materials

The following reagents were purchased from the indicated company and used as received: potassium chloride (KCl, 99.8%, Fisher Scientific), potassium bromide (KBr, Infrared Grade, Fisher Scientific), potassium iodide (KI, $\geq$99%, Fisher Scientific), sodium chloride (NaCl, $\geq$99%, Fisher Scientific), lithium chloride (LiCl, 99%, EMD Chemicals), tris(hydroxymethyl)aminomethane (Tris, 99.9%, Sigma-Aldrich), poly(allylamine hydrochloride) (PAH, MW ~17,500, Sigma-Aldrich), poly-L-glutamic acid sodium salt (PGA, MW ~93,600, Pilot Chemicals), 1H,1H,2H,2H-perfluorooctyltrichlorosilane (hydrophobic silane, 97%, Alfa Aesar), hydrogen peroxide (H_2O_2, 30% w/w, Sigma-Aldrich), sulfuric acid (H_2SO_4, 95-98%, VWR). All solutions were made in Milli-Q water (18.2 MΩ). Low-stress silicon nitride membranes (SiN_x, 50 x 50 μm, 30 ± 2 nm thick) were purchased from Norcada and cleaned with piranha solution (3:1, H_2SO_4:H_2O_2) at 100 °C for 30 min prior to pore fabrication.

Nanopore fabrication

30 nm thick silicon nitride films (50 x 50 µm^2 window) were subjected to the dielectric breakdown process to fabricate single nanopores.[48] Dielectric breakdown was performed in a homemade polydimethylsiloxane conductivity cell. Larger pores (opening diameter > 20 nm) underwent dielectric breakdown with the top half exposed to a strongly basic solution of 1 M KCl (pH 13.1) and the bottom half exposed to a strongly acidic solution of 1 M KCl (pH 1.6). In order to prepare smaller pores (opening diameter < 20 nm), both sides were exposed to the pH 1.6 solution. Dielectric breakdown was performed by applying 11.2 V (larger pores) or 12 V (smaller pores) with two Ag/AgCl pellet electrodes. Pore formation was observed as an increase of the current recorded during the dielectric breakdown process by ~20 – 1200 nA above the base current. Effective pore diameter was estimated using the pore resistance from an I-V curve in 1 M KCl at pH 8, and assuming a cylindrical geometry of the pore. The total resistance of the pore system is a sum of the access resistance and geometrical pore resistance,[57] thus the opening diameter (D) can be calculated using the following equation:[188]

$$D = \frac{G}{2\sigma}\left[1 + \sqrt{1 + \frac{16\sigma L}{\pi G}}\right] \qquad (5.1)$$

where σ is the solution conductivity, L is pore length (30 nm), and G is the pore conductance determined by the slope of the I-V curve. We consider the calculated value of D as an effective pore diameter.

Nanopore surface modification with poly(allylamine hydrochloride) (PAH) and hydrophobic silanes

Once fabricated, the pores were first modified with a positive polyelectrolyte (PAH), followed by modification with hydrophobic silanes. In the first step, a nanopore was placed in a conductivity cell; one side of the membrane was exposed to ~7 mM solution of PAH in pH 6 water for 30 minutes; the other side of the conductivity cell contained water. Successful PAH modification was assessed by a decrease of transmembrane current and presence of ion current rectification. After a thorough drying of the chip, the same pore was subsequently subjected to the modification with 1H,1H,2H,2H-perfluoro-octyltrichlorosilane performed from the opposite side of the membrane, previously in contact with water. The modification was performed from a 0.2% silane solution in toluene for five minutes, followed by washing the whole pore in ethanol and heating it at 120 °C for 30 minutes. Successful silane modification showed a large decrease in the nanopore conductance in KCl. In order to estimate the thickness of the silane layer, two nanopores were modified with silanes from both sides and submerged in ethanol overnight. They were subsequently characterized in a 1:1 mixture of 1 M KCl and ethanol. In the presence of ethanol, the nanopores were wet and their I-V curves informed on the effective pore size and the silane layer thickness. The calculations were performed assuming a homogeneous thickness of the layer on the pore wall and membrane surface.[189] Once wetted, the nanopores were also characterized in 1 M aqueous KCl, and the thickness was estimated again. Example recordings of current-voltage curves before and after silanization are included in Figure B.14. Based on all recordings the silane layer is estimated to be ~5 nm thick.

Additional pore modification with polyglutamic acid (PGA)

After PAH and silane modification, a few pores were modified with an additional polyelectrolyte to yield a negatively charged surface at one pore entrance, while the other entrance remained hydrophobic. For these select pores, the bottom of the chip containing PAH was exposed to ~0.35 mM solution of PGA in pH 8 water for 30 minutes while the other side of the membranes was in contact with water.

Electrochemical measurements

Current-voltage curves were recorded with an Axopatch 200B and Digidata 1322A (Molecular Devices Inc.) from -2 V to +2 V using 200 mV steps and a sampling frequency of 10 kHz. Current at each voltage step was recorded for 100 s, and reported values are averages and standard deviations of the time series excluding first and last ~5 s for each voltage. A few measurements of current-voltage curves were performed with Keithley 6487 picoammeter/voltage source (Keithley Instruments, Cleveland, OH); average and standard deviations were calculated based on three subsequent voltage scans. Pellet Ag/AgCl electrodes were used in all current experiments, with the ground electrode placed at the side of the nanopore modified with silanes. All salt solutions were prepared with 10 mM tris buffer and adjusted to pH 8.

Contact angle measurements

Contact angle measurements were performed using a homemade imaging setup at room temperature. A micropipette tip was filled with 2 μL of solution and dispensed on the SiN_x membrane. Images were captured on a VRI Phantom v7.3 camera outfitted with an Infinity Photo-Optical Model K2 DistaMax Long-Distance Microscope. Contact angle values were calculated using the ImageJ Contact Angle plugin by M. Brugnara.

First-principles and classical simulations

For the simulations of ions in bulk liquid water, all solutions were modeled by periodic cubic cells consisting of 63 water molecules and a single solvated ion, with the excess charge compensated by a uniform background charge. The size of the cells was chosen to yield the experimental density of liquid water under ambient conditions. Our first-principles simulations were carried out using Born-Oppenheimer MD with the Qbox code,[190] with the interatomic force derived from density functional theory (DFT) and the Perdew, Burke, and Ernzerhof (PBE) approximation for the exchange-correlation energy functional.[191] The interaction between valence electrons and ionic cores was represented by norm-conserving pseudopotentials,[192] and the electronic wave functions were expanded in a plane-wave basis set truncated at a cutoff energy of 85 Ry. All hydrogen atoms were replaced with deuterium to maximize the allowable time step, which was chosen to be 10 atomic units. The equilibration runs were carried out at an elevated temperature of T = 400 K in order to recover the experimental water structure and diffusion, while also providing a good description of the ion solvation at room temperature.[187,193–195] For the analysis of structural properties, the statistics were collected over 45 ps microcanonical simulations after an equilibration run of 15 ps.

Classical MD simulations of the hydrophobic interfaces were carried out using the LAMMPS simulation package.[196] The simulation systems consist of an aqueous solution (KBr, KCl or KI) confined between two parallel Si (111) surfaces that are functionalized with flexible silane molecules. The lateral dimensions of the simulation cell are about 3 nm x 3 nm, and the separation distance between the two surfaces is approximately 7.8 nm from the tips of silane groups after the structures are equilibrated. The confined region

was solvated by TIP3P water molecules, and the ions were added to obtain an experimental concentration of 1 M. We employed OPLS-AA force fields for the description of ions and CF_n groups of silane molecules.[197,198] The systems were first energy minimized and then equilibrated for 1 ns under NPT ensemble by using a Berendsen barostat.[199] The production simulations were run for 30 ns under the NVT ensemble, where a Nosé-Hoover thermostat[110,200] was used to maintain the temperature at 298.15 K. The hydrogen bonds of water molecules were constrained by using the SHAKE algorithm,[201] and the long-range electrostatic interactions were computed using the particle-particle particle-mesh method.[202]

Results and discussions

Asymmetrically modified nanopores displayed ion-size-dependent hydrophobic gating

All nanopores were prepared in 30 nm thick silicon nitride films by the dielectric breakdown process.[48,188] Pore diameter was tuned *via* controlling the magnitude of the breakthrough current measured when the dielectric breakdown process was stopped. Nanopores prepared by this technique are known to exhibit various characteristics of current-voltage curves suggesting that their shape might not be cylindrical.[203] In order to estimate the effective pore opening diameter and to allow comparison between independently prepared nanopores, the nanopores were sized based on their conductance measured in 1 M KCl and using a cylindrical pore model with access resistance. Results presented in this manuscript were obtained from nanopores with effective opening diameters between 10 nm and 140 nm.

The membranes were rendered hydrophobic by silanization reaction with 1H,1H,2H,2H-perfluoro-octyltrichlorosilane.[204] Silicon nitride surfaces subjected to the modification exhibited a contact angle in water of ~120° (Figure 5.1A,B); a silicon nitride surface before functionalization had a contact angle of 60° (Table B.T1). Two nanopores (25 and 50 nm diameter) were silanized symmetrically from both sides, resulting in the silanes' attachment to the entire pore wall and membrane surface. Figure 5.1C and Figure B.1 show recordings for the 50 nm diameter nanopore before and after the silanization reaction. The pore exhibited nearly no ion current in KCl, KBr, and KI, which is consistent with the strong hydrophobic character of the pore walls (Figure 5.1D); the increase of the current in KI is not significant and remains within the noise. Recordings for the 25 nm nanopore are shown in Figure B.2, which was additionally probed in NaCl and LiCl (not

shown). The 25 nm pore conducted finite current only in KBr, indicating that these silanized nanopores were too resistive to achieve voltage or ion induced hydrophobic gating (Figure 5.1D, Figure B.2). This conclusion was supported by experiments in KCl with 5 additional silanized nanopores, which conducted just few tens of pA at 2 V for both voltage polarities.
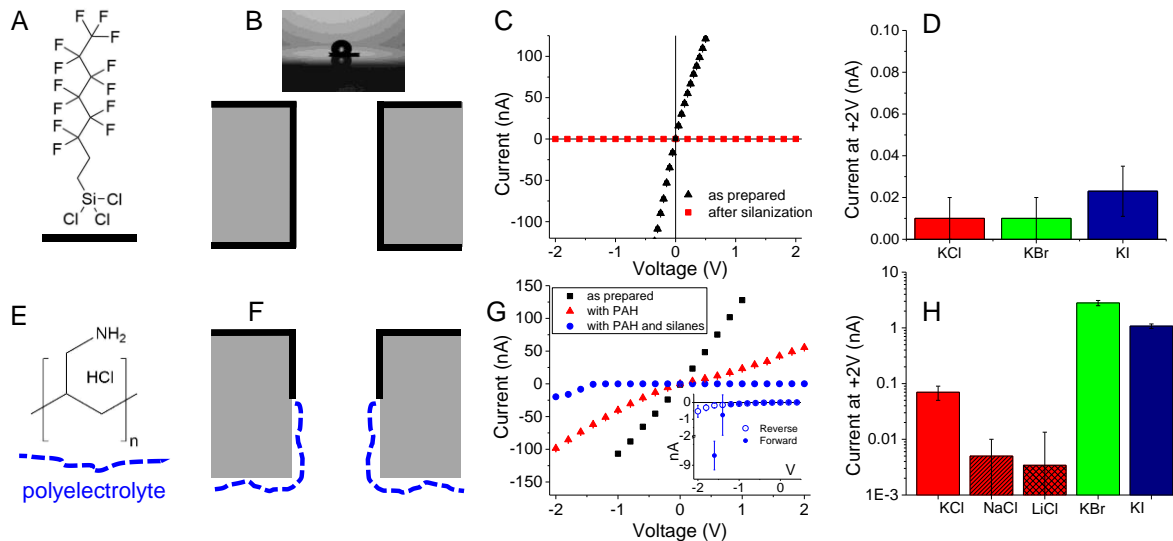
Figure 5.1: Preparation of hydrophobic nanopores. (A) Chemical structure of silanes used to render the silicon nitride surface hydrophobic. (B) Scheme of a nanopore subjected to symmetric silanization together with a contact angle measurement performed on a flat, silane-modified silicon nitride surface. (C) Current-voltage curves of a 50 nm diameter nanopore before and after silanization, recorded in 1 M KCl. (D) Current magnitude at +2 V recorded in 1 M KCl, KBr, and KI for the same nanopore as shown in (C). (E) Polyelectrolyte poly (allylamine hydrochloride) (PAH) used to render one pore entrance positively charged. (F) Scheme of a nanopore subjected to PAH and silanization modifications. (G) Current-voltage curves for a 25 nm diameter nanopore before and after chemical modifications. Forward scans are shown in the main panel; the inset contains a reverse scan (open symbols) and zoomed in part of the forward scan (filled symbols) in 1 M KCl. Note that in the inset, for clarity, voltage range only from -2 V to +0.4 V is shown, and the y-axis scale contains a break. (H) Summary of ion current at +2 V for the same nanopore in different salts; recordings after the PAH and silane modifications are shown. Error bars shown in panels (C), (D), (G) and (H) are standard deviations found based on ion current signals recorded at each voltage for 100 s (see Materials and Methods section). The exception is one recording in (G) shown as red triangles that was performed without time resolution using a picoammeter; average value and standard deviation at each voltage were found based on three consecutive current-voltage curves. In (C) and some recordings in (G) (shown as black and red data points) the error bars are smaller than data points.

112

In the design of hydrophobic nanopores, which would be closed for ionic transport at low voltages but would conduct ions at higher voltages, we were inspired by earlier simulations and experiments that indicated charge placement near hydrophobic groups could lower hydrophobic interactions.[184,185] The nanopores were therefore equipped with a junction between a hydrophobic pore entrance and a hydrophilic, highly charged entrance. To this end, a single-nanopore chip was first exposed from one side to a solution of positively charged polyelectrolyte, poly(allylamine hydrochloride) (PAH) (Figure 5.1E).[205] Due to the negative surface charges of silicon nitride, PAH was expected to electrostatically attach to the membrane surface and part of the pore walls, creating a junction between positively charged PAH and negatively charged unmodified silicon nitride. As shown before, such junctions induce ion current rectification,[69,79,206,207] thus recording asymmetric current-voltage curves indicated successful modification with PAH (Figure 5.1G). In the next step, the unmodified side of the membrane was subjected to silanization modification and was rendered hydrophobic, completing the proposed hydrophobic/hydrophilic junction (Figure 5.1F). Ionic transport properties of a hybrid nanopore containing such hydrophobic/hydrophilic junction in 1 M KCl are shown in Figure 5.1G. The nanopore showed nearly no conductance at all positive voltages but opened for ionic transport at negative voltages where hysteresis was observed. During the first forward scan, when voltage was changed from -2 V to +2 V with 200 mV steps, the pore started in the open – conductive state at high negative voltages and closed for ionic transport at -1.2 V, when the measured current decreased to few tens of pA. The pore remained closed for the rest of the scan. The transition from a conductive state to a non-conductive state corresponds to a dewetting process *i.e.,* formation of a vapor region

113

within the pore. For the reverse scan, when the voltage was changed from +2 V to -2 V, the pore opened for ionic transport only at -1.6 V (see the inset to Figure 5.1G); this transition corresponds to filling the pore with condensed water. Existence of the hysteresis such that voltage needed to open the pore for ionic transport (-1.6 V) was higher than the voltage magnitude (-1.2 V) at which the pore underwent dewetting (nearly zero conductance) is consistent with earlier observations with hydrophobic nanopores.[208] Note that the pore opened for ionic transport in KCl only for negative voltages thus when anions were sourced from the side with positively charged PAH and moved towards the silanized side of the membrane.

The same nanopore was also examined in 1 M NaCl and LiCl, as well as KBr and KI to probe the influence of cations and anions on the voltage-dependence of ion current and nanopore wetting. Figure 5.1H summarizes the results and shows ion currents at +2 V, the condition most sensitive to the wetting transition. In our electrode configuration, hydrophobic nanopores exhibit negligible conductance in KCl at positive voltages. Thus, finite values of positive currents could indicate diminished hydrophobic interactions and pore wetting. The recordings in Figure 5.1H clearly display a large current increase in bromide and iodide solutions, while no significant increase for currents in sodium and lithium solutions was observed. The series of experiments suggested that the presence of large polarizable ions in the solution indeed influenced the solid/liquid interface and promoted the process of nanopore wetting. Figure B.4 shows ion currents for all salts at -2 V; due to finite conductance of this nanopore in KCl, the wetting effect of Br$^-$ and I$^-$ was less visible compared to the recordings at +2 V. Similar to ion currents at +2 V, however,

the conductance of this nanopore at -2 V was still the highest in KBr and KI among all salts.

The nanopore shown in Figure 5.1G,H was 25 nm in diameter, thus as the next step we probed how the opening size influenced the pore's ability to respond to the presence of different ions. Figure 5.2 summarizes ion current recorded for four different pores with openings between 12 nm and 140 nm. At +2 V in KCl, all nanopores were in their low conductance state such that the value of ion current remained below 100 pA independent of the pore opening size. This finding is in agreement with earlier experiments reporting low ion currents through hydrophobic nanopores with opening of ~140 nm.[172] All nanopores exhibited significantly higher currents in KBr or KI compared to the recordings in KCl, providing evidence that the large anions facilitated the pores' wetting. We hypothesize that when a pore is wet, a continuous column of electrolyte is created along the pore length, connecting the two reservoirs on both sides of the membrane. It is important to note, however, that the current in KI/KBr shows only a weak dependence on the pore opening diameter, suggesting that the electrolyte does not fill the entire cross-section of the pores. Moreover, the continuous column of electrolyte might not be created along the pore axis, but rather multiple columns of water with possible tortuosity can be present in wider pores. The set of intertwined electrolyte columns would exhibit high ionic resistance and explain the lack of clear dependence of current on the pore diameter, seen in Figure 5.2.
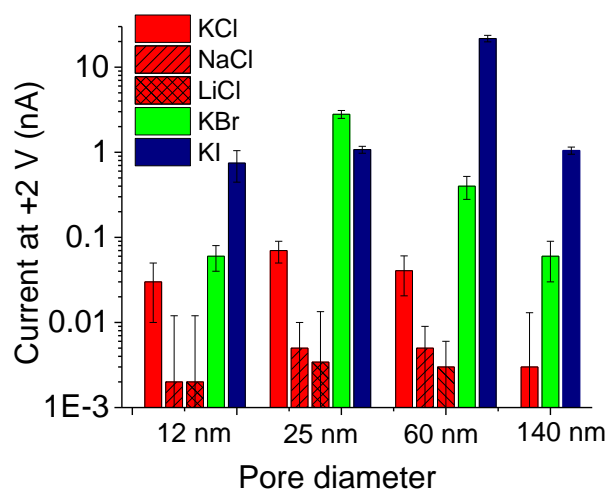
Figure 5.2: Ionic gating as a function of nanopore diameter. Ionic transport characteristics of nanopores containing a hydrophobic/hydrophilic junction in different 1 M salt solutions. Note that the 140 nm pore was first modified with silanes followed by PAH, thus in reverse order than done for other pores. The error bars are standard deviations found based on ion current signals in time for each device. One sample was tested for each pore diameter.

The change in ion current behavior in KI compared to KCl is even more striking when we compare the characteristics of ion current signals in time. Figure 5.3 shows ion current recordings in 1 M KCl and 1 M KI for two independently prepared nanopores at different voltages. The pores shown are examples of two types of hydrophobic gating observed in KCl. In the first type of gating, fluctuations of ion current in time were observed for voltages above a certain threshold – the signal would switch between a current value close to 0 nA and a finite current value (Figure 5.3A); four out of twelve nanopores prepared for this project exhibited this behavior. The number of current instabilities increased with the increase of negative voltage. In the second type of behavior shown (n = 4), ion current also became finite at a threshold negative voltage, but the ion current signals did not exhibit switching behavior (Figure 5.3C).

Figure 5.3A shows recordings in KCl for the reverse scan of the 25 nm nanopore shown in Figure 5.1G that exhibited the first type of gating. When the same pore was exposed to 1 M KI, current fluctuations ceased in the second scan followed by stable current signals for all voltages examined (Figure 5.3B, Figure B.5). The ion current recordings in KI also indicated that the presence of the large anions alone, without external voltage, was not sufficient to induce nanopore wetting; indeed, contact angle of a hydrophobic surface remained at a constant value of ~105° for all salts (Table B.T1). The nanopore opens in KI only when an external electric field is applied.
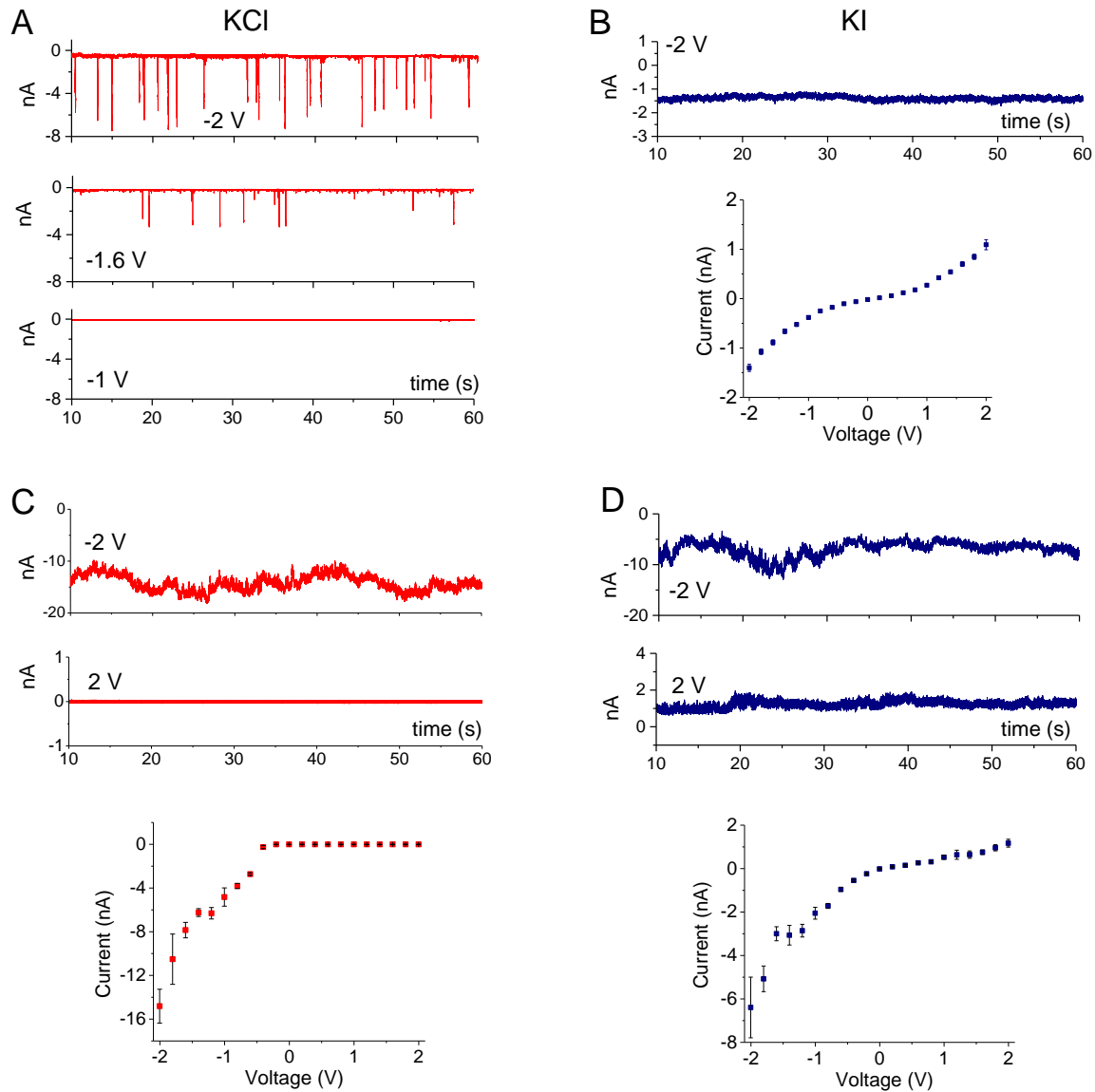
Figure 5.3: Types of hydrophobic gating. Ion current signals in two nanopores containing a hydrophobic/hydrophilic junction. (A) and (B) Recordings for a 25 nm diameter pore in 1 M KCl and 1 M KI, respectively. (C) and (D) Recordings in 1 M KCl and 1 M KI for a 12 nm diameter pore, respectively. Recordings in KCl and KI are presented in red and navy, respectively.

The second type of voltage response in KCl involved a sudden pore opening without significant current fluctuations. Figure 5.3C provides recordings for a 12 nm diameter pore showing this response. A sudden pore opening in the reverse scan without ion current instabilities was observed at -0.6 V (see current-voltage curve in Figure 5.3C), and no on-off current switching occurred for higher voltages. When exposed to KI, the nanopore exhibited similar behavior for negative voltages but opened for transport at positive voltages (Figure 5.3D).

The ion current recordings in Figure 5.3 revealed fluctuations whose amplitude significantly exceeds variations in ion current observed with as prepared nanopores (Figures B.1, B.3). In order to probe if the current fluctuations were caused by trapped air bubbles, the entire conductivity cell, containing the nanopore and electrolyte solution (1 M KCl), was placed in a vacuum desiccator for 30 minutes. Figure B.6 shows examples of ion current recordings before and after removal of air bubbles. Presence of ion current bursts in both experiments suggests that the ion current instabilities are intrinsic to hydrophobic nanopores.[150,183] We believe the current instabilities arise, because the pore is not entirely filled with electrolyte, thus even when the pore is conductive, the continuous electrolyte column (or multiple columns, see above) has a radius that is locally smaller than the geometrical pore opening.[150,183] When voltage is applied, the flow of ions can lead to instabilities in the effective radius of the electrolyte paths, observed as ion current fluctuations.

When analyzing the magnitude of ion current at negative voltages for both nanopores shown in Figure 5.3 we realized that at -2 V the pores conduct higher currents in KCl than at KI. In Figure 5.3A the current bursts at -2 V reach an amplitude of even -7

119

nA while in KI the current is only -1.5 nA. The reasoning for this is less clear but it was observed for multiple devices. Possible explanations stem from the fact that large anions are predicted to adsorb to the silanized pore walls, making the walls effectively negatively charged. This alteration in surface charge distribution could impact measured current.

It should also be noted that three out of 12 pores we prepared did not open for current in KCl for positive or negative voltages; two of the three pores conducted current in KI or/and KBr, which led to finite ion current for both voltage polarities, and one pore was not conductive in any salt. In addition, one nanopore was not successfully modified with hydrophobic silanes, as suggested by the pore's high conductance in KCl for all voltages.

Control experiments were also performed with an unmodified silicon nitride nanopore in KCl, KBr, and KI. These measurements provided evidence that the ion current dependence on voltage and anion type occurred due to the chemical modifications we performed and was not intrinsic to silicon nitride nanopores. Figure B.7 shows current-voltage curves for an as prepared silicon nitride nanopore. As expected, all recordings are linear with similar current magnitudes, in agreement with comparable bulk conductivity of the salts.

The experiments suggested that large polarizable anions enhanced wetting of nanopores containing a junction between a hydrophobic zone and a hydrophilic, positively charged zone. We realized, however, that the anion's effect on ion transport could have two origins: (i) affinity of large anions towards a hydrophobic surface, as mentioned above; or/and (ii) enhanced concentration of anions at the pore entrance containing PAH. The locally enhanced ion concentration could promote wetting, because previous

120

experiments from our group indicated that wetting of hydrophobic nanopores is enhanced in high ionic strength solutions.[171] In order to elucidate which of these phenomena dominates, we prepared a nanopore with one entrance containing a negatively charged polyelectrolyte while the other entrance remained hydrophobic. This system was created by subjecting a nanopore, as schematically shown in Figure 5.1F, to a solution of polyglutamic acid (PGA). Polyglutamic acid was expected to electrostatically attach to PAH and switch the surface charge from positive to negative. In a control experiment, we confirmed that the attachment of PGA to PAH indeed occurred, as evidenced by a current decrease and inversion of rectification (Figure B.8). Figure B.9 shows data for a nanopore that was originally 12 nm in diameter and subjected to modification with PAH, silanes, and PGA. This pore exhibited negligible conductance in KCl, NaCl, LiCl, and KBr but opened for ion transport in KI. These experiments provide evidence that the propensity of anions to concentrate at a hydrophobic surface determines the nanopore wetting. It is important to note that the nanopore with PGA was not conductive in KBr, even though hydrophobic nanopores containing positively charged polymer on one side would be open for ionic transport in both KBr and KI. This observation suggested that the effect of pre-concentrating anions at pore entrance might also play a role in the pore wetting.

Our experimental observations on anion-induced wetting of nanopores is consistent with a wide literature on ion-dependent surface tension.[167,209] Surface tension of water/air interface is known to increase with the addition of inorganic salts such as KCl, or KI, however, heavier, more polarizable halides, such as I^-, increase surface tension to a smaller extend than Cl^-. The lower surface tension in I^- salts was explained by

accumulation of the anions at the interface. Our hydrophobic nanopores can indeed be wetted in the presence of larger anions and are closed for ionic transport in KCl.

It is also well known that surface tension increases linearly with concentration for a majority of inorganic salts.[210] Consequently, our hydrophobic nanopores are expected to be wetted in less concentrated solutions due to their decreased surface tension. Our earlier results in KCl with nanopores containing a hydrophobic/hydrophilic junction as mentioned above revealed an opposite trend: the nanopores were more prone to become conductive in more concentrated solutions.[171] Pre-concentrating of anions by PAH, capable of promoting nanopore wetting, also contradicts the intuition gathered from previous work on surface tension. One nanopore we prepared for this project was probed in 1 M and 100 mM KCl and a similar trend was observed – the nanopore remained mostly closed in 100 mM KCl (Figure B.10). The influence of salt concentration on hydrophobic gating will be probed by us in the future. We believe an explanation of this behavior needs to include the neighboring polar groups as well as application of electric field.

Simulations revealed large, polarizable anions had more flexible solvation shells and accumulated near hydrophobic surfaces

In order to complement and provide insights into our experimental findings, we carried out first-principles molecular dynamics (MD) simulations of chloride, bromide, and iodide ions in bulk water. These simulations provided detailed understanding on the nature of ion hydration, which can be related to the wetting behavior observed in the experiments. Here, our examination of ion solvation structures was based on the calculated radial distribution functions (RDFs) between the hydrogen atoms in water and the anions, $g_{XH}(r)$, where X = Cl$^-$, Br$^-$, or I$^-$. As shown in Figure 5.4A, the position of the

$g_{XH}(r)$ first maximum, r_X, follows the order $r_{I^-} > r_{Br^-} > r_{Cl^-}$, yielding values of 2.54, 2.35, and 2.17 Å for I⁻, Br⁻, and Cl⁻, respectively. This ordering indicates an increase in the size of the first solvation shell from Cl⁻ to I⁻ and reflects the ion radius increase among the three anions. More importantly, the calculated RDFs indicate that Cl⁻ yields a significantly stronger solvation shell compared to Br⁻ and I⁻, as supported by a shorter average ion-hydrogen r_X distance as well as a higher intensity in the $g_{XH}(r)$ first maximum. This analysis also reveals that I⁻ exhibits the weakest solvation shell among the three anions.

Additional information on the difference in the solvation structures among the ions can be obtained by examining the probability distributions of the ion-hydrogen coordination numbers (n_{XH}). For instance, as shown in Figure 5.4B, we find that larger ions, such as I⁻, exhibit a much broader n_{XH} distribution compared to that of Cl⁻. The broad distributions imply that the solvation shells of Br⁻ and I⁻ are rather flexible and are characterized by more frequent exchanges of water molecules between the first and second ion solvation shells. Collectively, our simulations support the interpretation of weaker and more flexible solvation shells of Br⁻ and I⁻ compared to that of Cl⁻, implying that these larger anions are more prone to migrate to hydrophobic surfaces where the water concentration is diminished.
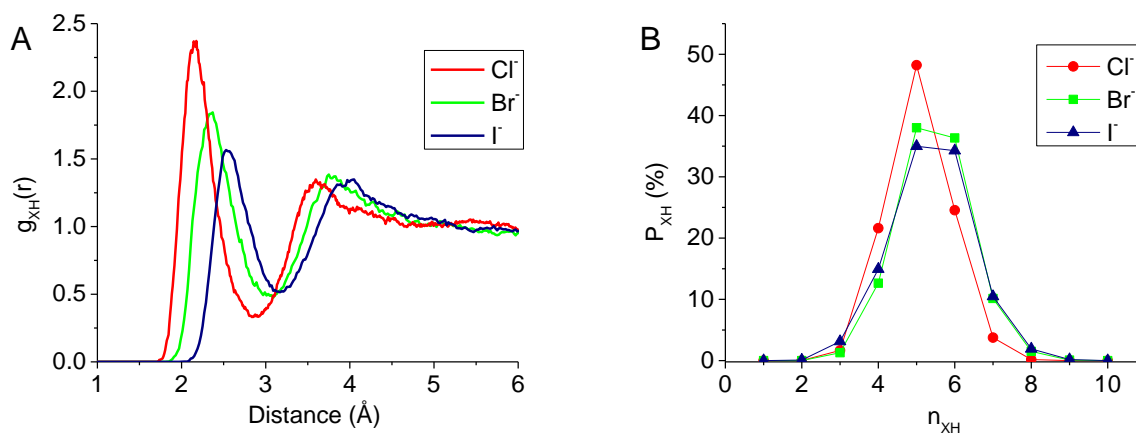
Figure 5.4: Solvation shell of anions in bulk liquid water. (A) The calculated ion-water hydrogen radial distribution functions for chloride (Cl⁻), bromide (Br⁻), and iodide (I⁻) in bulk water; (B) Histograms of the water hydrogen coordination number in the first shell around the anions. The first minima in the corresponding $g_{XH}(r)$ were used as distance cutoffs for determination of the first solvation shells. The results indicate that large anions yield a weaker and more flexible solvation shell.

To support this initial assessment, we directly probed adsorption behavior of the anions on a hydrophobic surface. To this end, we carried out MD simulations of KBr, KCl, and KI solutions at the interface with a silicon surface functionalized with flexible silane molecules, where a high surface coverage of 100% was used to represent high hydrophobicity conditions in experiments (Figure 5.5A,B). In addition, given the complexity of the system, classical simulations were utilized instead of first-principles simulations that require significant computational resource. Here, our simulations were carried out using the TIP3P water model and OPLS-AA force fields[197] were employed for the description of ions and surface silane molecules. We emphasize that these force fields have been parametrized to recover the experimental hydration energy and solvation structure of the ions in liquid water.[197] In addition, we note that ion surface affinity is largely determined by ion-silane, ion-ion, and ion-water interactions rather than the interactions of ions with the substrate, as aqueous solutions are separated from the silica surface by

almost 16 Å (see Figure B.11). This distance is larger than the cut-off distance of the OPLS force-field employed in our MD simulations, therefore the substrate has only a minor effect on the behavior of ions at the interface.

The calculated density of ions as a function of the distance from the surface is shown in Figure 5.5C-E. The results indicate that anions with larger ionic radius exhibit stronger adsorption at the interface. In particular, we found that Br^- and I^- are favorably adsorbed at the interface, as indicated by a peak located at a distance of about 6 Å and 5 Å from the surface, respectively, with the strongest enhancement in interfacial density obtained for I^-. This contrasts with the smaller Cl^- ion, whose distribution reveals depleted density at the interface (Figure 5.5C). Such an adsorption ordering of the anions can be straightforwardly related to the strength of their solvation assessed in Figure 5.4. Specifically, larger ions, such as I^-, yield a weak solvation shell, and therefore can be easily desolvated and adsorbed at the hydrophobic interface. In contrast, the smaller ions have a much stronger solvation environment and prefer to remain solvated, preventing them from approaching the interface. The results are in agreement with earlier studies showing that large anions increase surface tension of water/air interface to a weaker degree compared to smaller anions.[209] Collectively, our simulations indicate that large ions, such as I^-, exhibit a stronger affinity toward hydrophobic surfaces, and further support the conclusion that the ions can induce nanopore wetting. We emphasize that our conclusions remain valid for the surface with a lower coverage of silanes (50%), as well as graphene, which can also be considered a model of a hydrophobic system (see Figure B.12).[211,212] We also note that, the affinity of I^- toward the interface is weaker for the surface with a 50% coverage of silanes due to the decreased hydrophobicity of the

surface. As a result, our simulations suggest that the details of the ion distribution are strongly dependent on the chemical characteristics of the surface.

We also used the electronic continuum correction (ECC) to investigate the effect of polarizability on the behaviors of ions at the interface, where we confirmed that the trend in the surface affinity among the three ions remains the same. Interestingly, we found that the use of the ECC approximation increases surface affinity of all the anions; for instance, interfacial density of chloride was found to be significantly larger than the bulk density in the ECC simulations (Figure B.13). This is likely to be a consequence of the discontinuity in the electronic relative permittivity at the interface between the solutions and silane molecules, which has also been found to be responsible for an overestimation of ionic surface affinity in simulations of the water/vapor interface with the ECC approximation.[213] We note that ECC approximation is known to be more suitable for systems that are electronically homogeneous, such as water/oil interface, and is less applicable for those with a discontinuity in the electronic relative permittivity.

The distribution of ions in Figure 5.5 also shows that an enhanced concentration of I$^-$ at the surface leads to formation of a neighboring region with enhanced concentration of potassium ions, an effect shown before.[175] The two peaks corresponding to anions at the surface and cations resemble properties of an electrical double-layer with a distinction that in the case presented here, the ionic distributions are governed by hydrophobic properties of the surface and solvation shell of ions in a solution, instead of charges on the surface.[67]
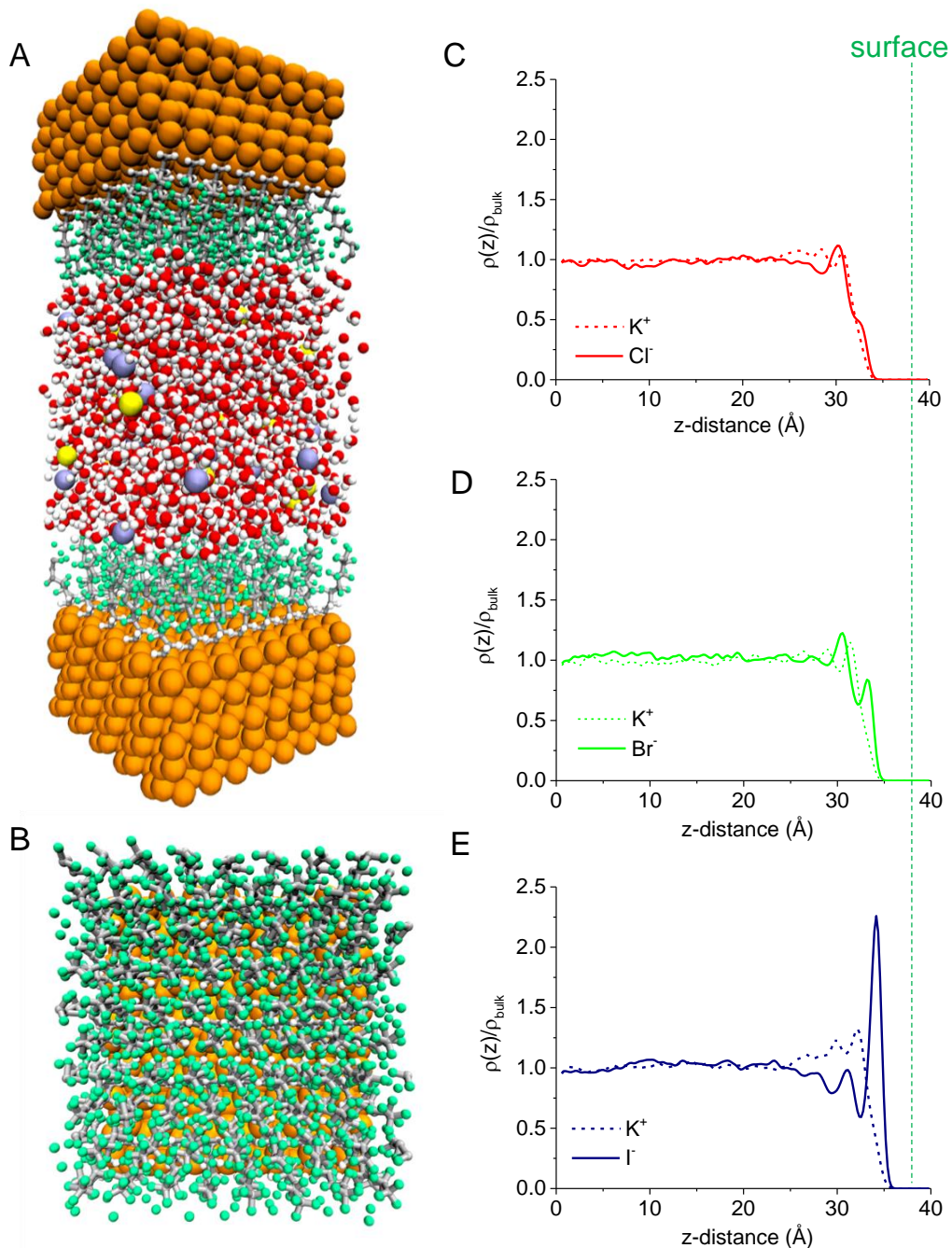
Figure 5.5: Modeling of ion adsorption at a hydrophobic interface. (A) Side and (B) top view of the atomistic structure of the system composed of silicon surfaces (orange) functionalized with silane molecules (white, silver, and green atoms correspond to hydrogen, carbon, and fluorine, respectively), water (white and red atoms correspond to hydrogen and oxygen, respectively), and ions (yellow cations and blue anions). (C-E) Ion distribution along the direction perpendicular to the surface. The solid and dashed lines show the distributions for the anions and cations for the solutions considered in this work, respectively.

Conclusions

In this chapter we examined single nanopores containing a junction between a hydrophobic region, and hydrophilic, highly charged region. The presence of the junction made the system responsive not only to applied voltage but also the type of ions present in the solution. Our experiments and modeling provided evidence that bromide and iodide ions, due to their weaker solvation shell, had a tendency to accumulate at hydrophobic surfaces and promoted nanopore wetting.

Earlier continuum modeling showed that iodide ions could indeed accumulate at a hydrophobic surface, which was captured by so-called hydrophobic solvation energy related with the ion volume.[175] Our results provide a detailed physical mechanism, which describes effects governing location of ions near a hydrophobic interface. It is the strength of the ion solvation shell that determines whether an ion will have an enhanced or diminished density at a hydrophobic surface. In the confined geometry of a nanopore, which does not *de facto* contain a bulk phase, small ions with strong hydration shells might not even enter the pore. On the other hand, large polarizable ions will accumulate next to hydrophobic walls and induce ionic transport through the nanopore. The importance of ion solvation for ionic distributions near a hydrophobic surface is in strong contrast with a charged surface, where charged chemical groups play a dominant role in modulating local ionic concentrations.[67]

The results presented here will be of great interest in preparing ion-responsive systems based on hydrophobic pores. We also imagine it should be possible to prepare a valve-like membrane, which becomes open for ionic and molecular transport when a threshold voltage or/and gating ion is added. Our future studies will focus on

understanding the role of ionic concentration in the hydrophobic gating and introducing electric fields into modeling of hydrophobic interfaces. The experiments and modeling will also be extended to more types of anions and cations. It will be especially important to understand the role of cation and anion affinity to a hydrophobic surface when it is connected to a highly charged zone, as done in the system shown here. It is possible that the adsorption of large ions at a hydrophobic surface is influenced by the presence and polarity of the nearby charges. These experiments will involve probing different salts individually as well as in mixtures.

Appendix B: Supplementary Materials for Chapter 5

Chapter adapted from:
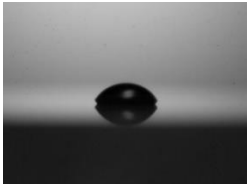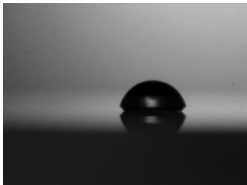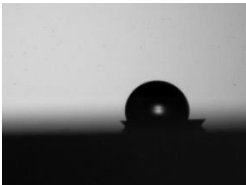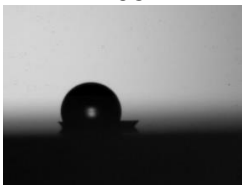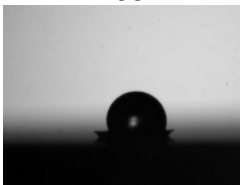
Polster, J. W.; Acar, E. T.; Aydin, F.; Zhan, C.; Pham, T. A.; Siwy, Z. S. Gating of Hydrophobic Nanopores with Large Anions. *ACS Nano* **2020**, *14* (4), 4306–4315. https://doi.org/10.1021/acsnano.9b09777**.**

Supplementary Table

Table B.T1: Contact angle, θ, measured in water and various salt solutions on untreated SiN$_x$ chips, chips modified with poly(allylamine hydrochloride) (PAH), and hydrophobic silanes.

	θ in H$_2$O (deg)	θ in 1 M KCl (deg)	θ in 1 M KBr (deg)	θ in 1 M KI (deg)
Clean SiN$_x$	60	-[a]	-	-
PAH-modified SiN$_x$	75	-	-	-
Silane-modified SiN$_x$	120	105	105	105

-[a] data was not collected

Supplementary Figures
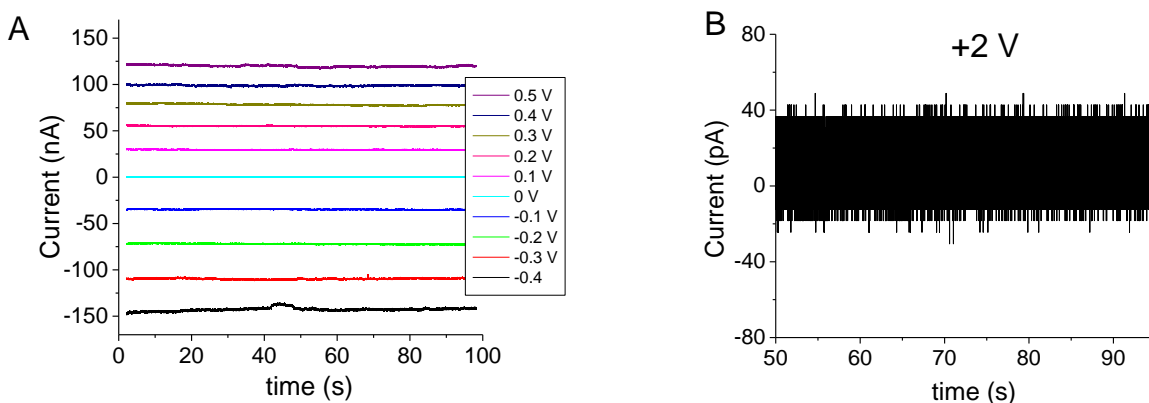
Figure B.1: (A) Recordings of ion current for an as prepared nanopore shown in Figure 5.1C. (B) Part of ion current recording at +2 V for the same nanopore after silanization. These measurements were performed using ion current amplifier (Axopatch 200B).
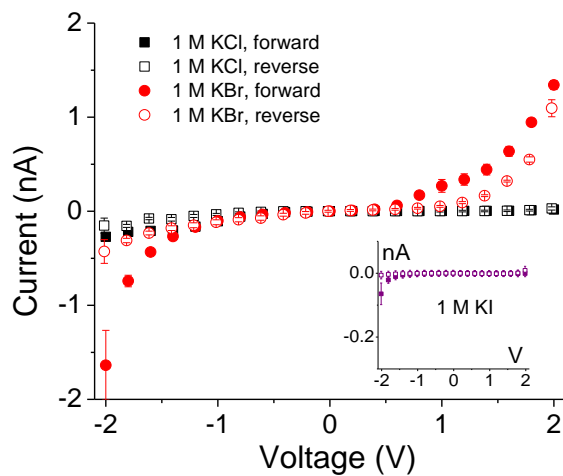
Figure B.2: Recordings for a 25 nm nanopore that was modified with hydrophobic silanes from both sides. This pore opened up for ionic transport in the presence of KBr but not KI (see the inset). The error bars are standard deviations of ion current recordings for each voltage.
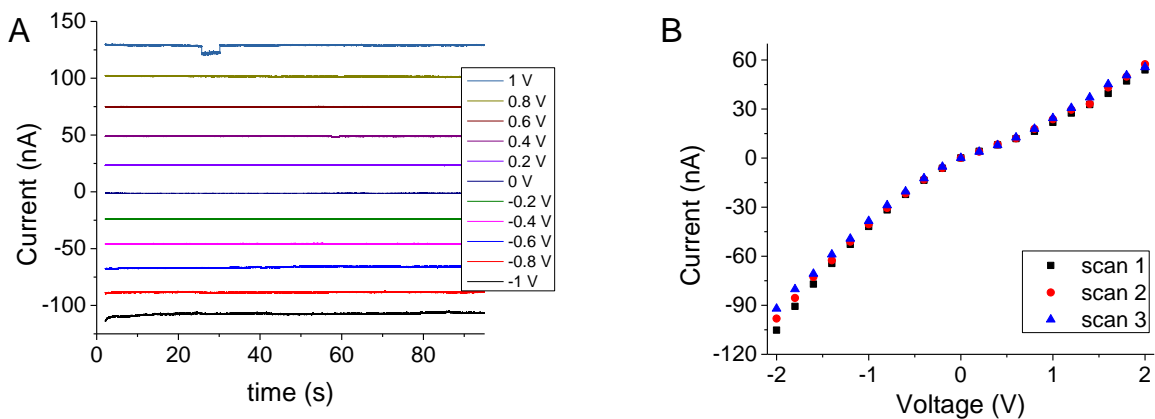
Figure B.3: (A) Recordings of ion current in 1 M KCl for an as prepared nanopore shown in Figure 5.1G. These measurements were performed using ion current amplifier (Axopatch 200B). (B) Current-voltage curves in 1 M KCl of a nanopore shown in Figure 5.1G after the attachment of PAH. This set of data was recorded with a picoammeter (Keithley 6487) without time resolution. Three subsequent scans that overlap on top of each other indicate the nanopore stability.
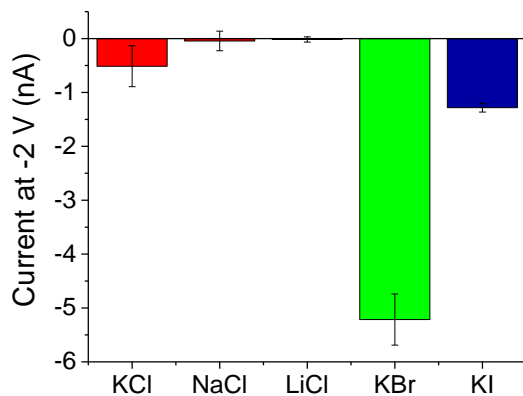
Figure B.4: Ion current recordings at -2 V for the nanopore shown in Figure 5.1H. Average values and standard deviations of the recordings in the reverse bias are shown.
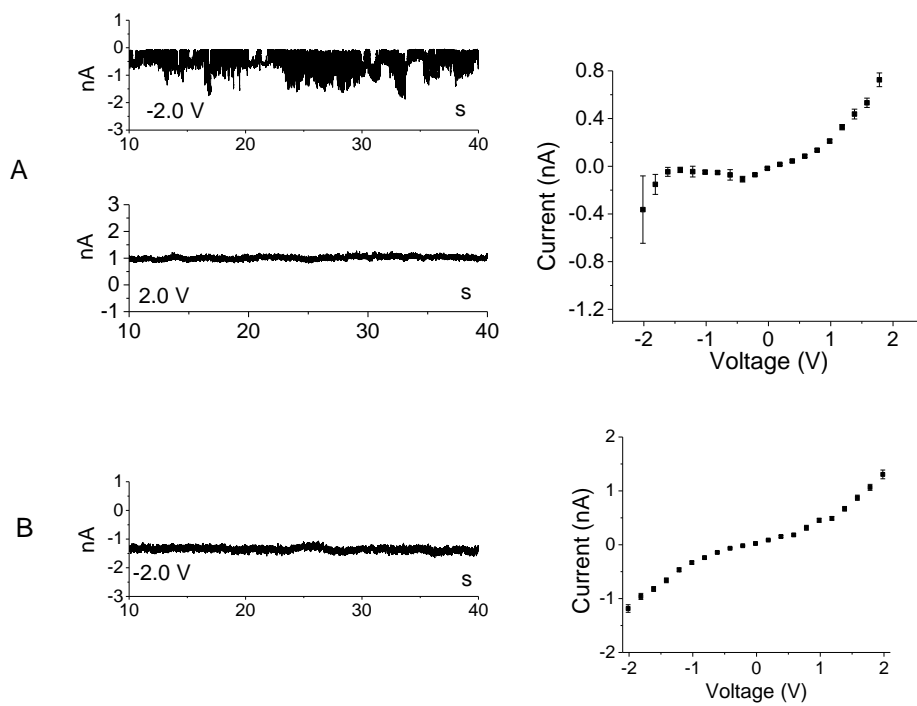
Figure B.5: Recordings for a 25 nm nanopore modified with the positively charged polyelectrolyte, PAH, and hydrophobic silanes in 1 M KI. This is the same pore as shown in Figure 5.1F,G. (A) The first forward scan (the voltage was changed from -2 V to +2 V) after changing KCl to KI. Note the instabilities of ion current at -2 V. (B) The first reverse scan taken immediately after the scan shown in (A). In both panels examples of ion current signal in time are shown together with current-voltage curves.
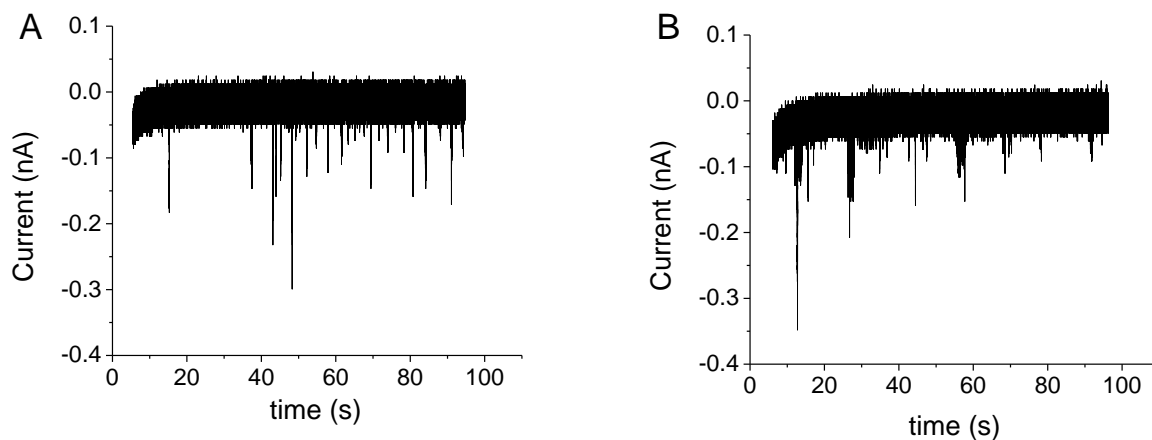
Figure B.6: Recordings of ion current in time through a 12 nm diameter nanopore containing a hydrophobic/hydrophilic junction (A) before, and (B) after 30-minute-long incubation in a vacuum desiccator. Placing the whole conductivity cell with the nanopore membrane in a vacuum desiccator was expected to remove trapped air bubbles. The recordings were performed in 1 M KCl, -2 V.
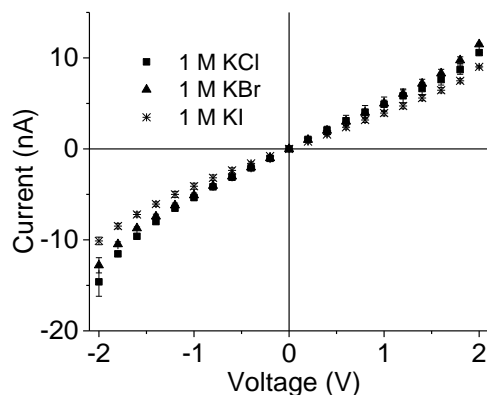
Figure B.7: Control experiments with an unmodified silicon nitride nanopore in 1 M KCl, 1 M KBr and 1 M KI. This pore had an opening diameter of 5 nm.
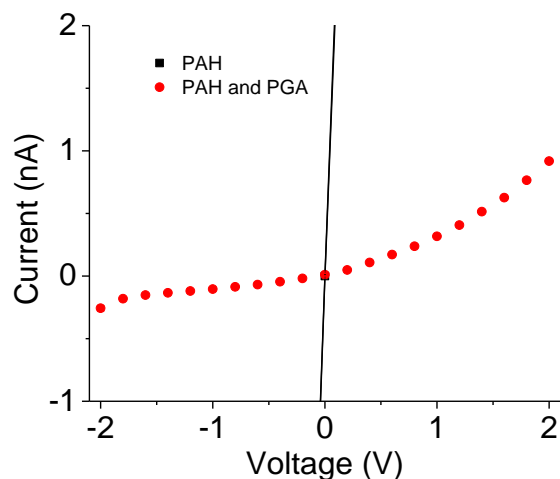
Figure B.8: Current-voltage curves in 1 M KCl for a 22 nm diameter nanopore modified first with PAH and subsequently with polyglutamic acid (PGA). Note that after PGA modification, positive currents were larger than negative currents. This pore was very stable, and the error bars are smaller than the data points.
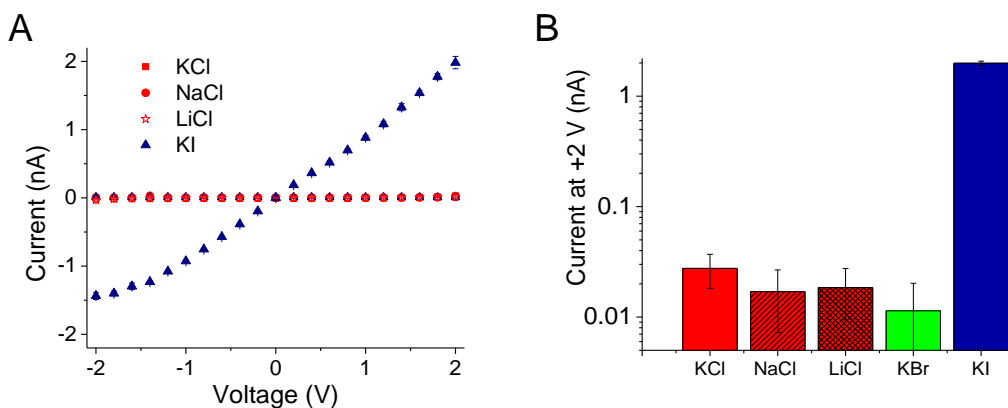
Figure B.9: Ion current recordings for a nanopore that was originally 12 nm in diameter and subjected to poly(allylamine hydrochloride), hydrophobic silanes, and polyglutamic acid modifications. Recordings in 1 M KCl, 1 M NaCl, 1 M LiCl, and 1 M KI are shown. (A) Current-voltage curves and (B) magnitude of ion current at +2 V for all salts. Panel (B) also contains recordings in KBr. The error bars are standard deviations of ion current recordings for each voltage.
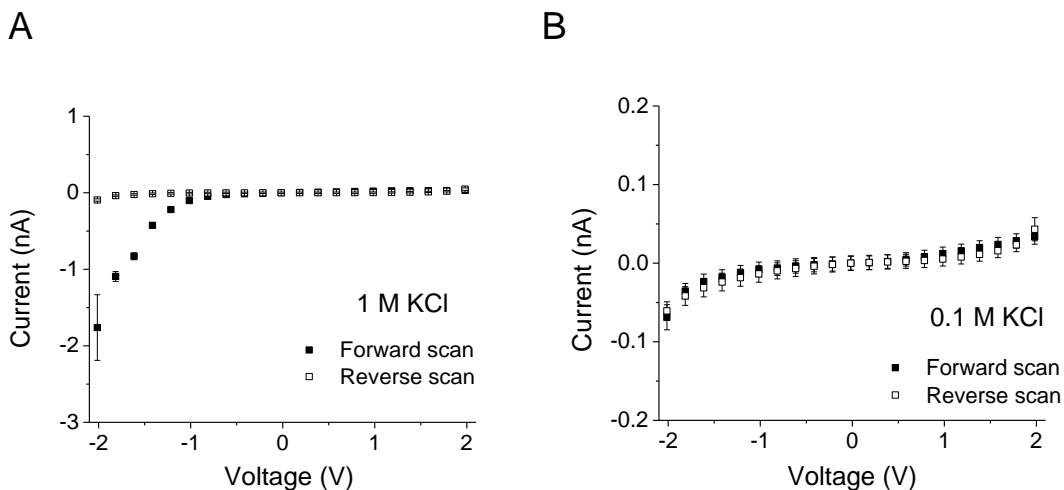
Figure B.10: Ion current recordings for a 100 nm diameter nanopore in (A) 1 M and (B) 100 mM KCl. The pore was subjected to PAH and hydrophobic silanization modifications.
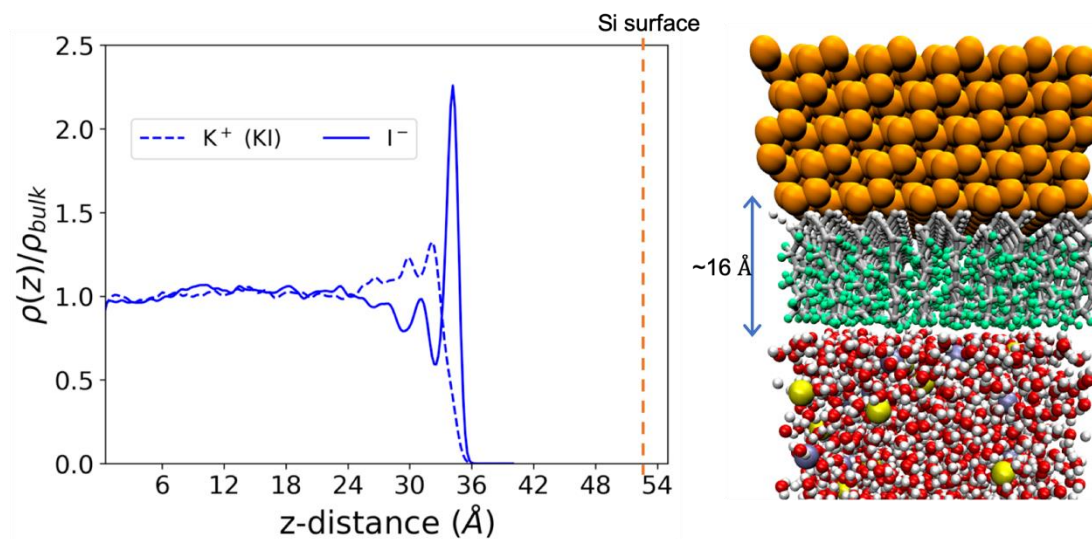
Figure B.11: (Left panel) Ion distribution along the direction perpendicular to the surface. (Right panel) An illustration demonstrating the separation between the silicon surface and aqueous solution composed of water and ions; the separation is due to the presence of silanes.
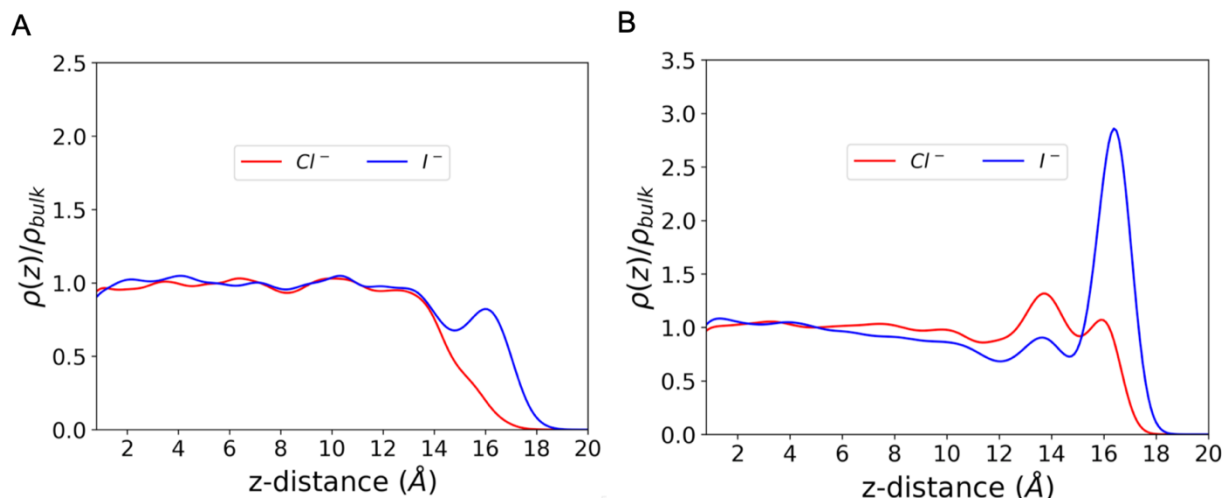
Figure B.12: Anion distributions in KCl and KI solutions along the direction perpendicular to the surface. (A) The Si(111) surfaces functionalized with silane groups at 50% surface coverage. (B) Graphene surfaces with no functional groups. The force field and simulation protocols are the same for graphene and functionalized surfaces. The simulation box is reduced to half in the direction perpendicular to the surface for the 50% surface coverage and graphene surfaces.
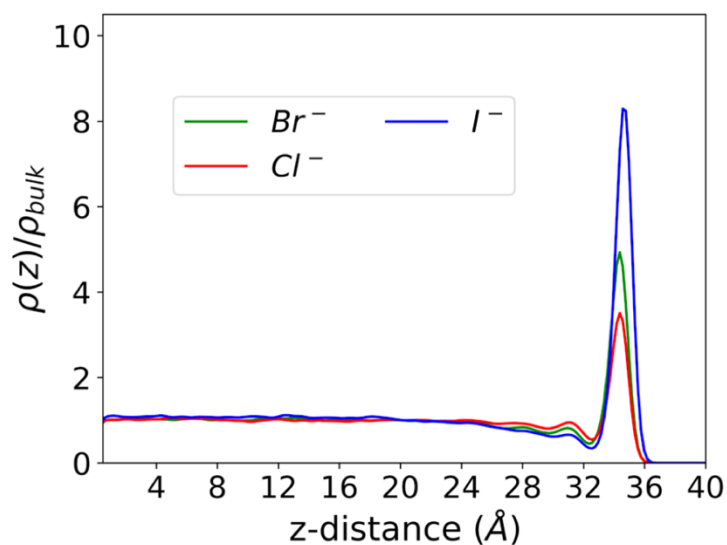
Figure B.13: The distribution of Cl^-, Br^-, and I^- anions along the direction perpendicular to the surface, as obtained from the MD simulations with the electronic continuum correction (ECC) approximation.

138
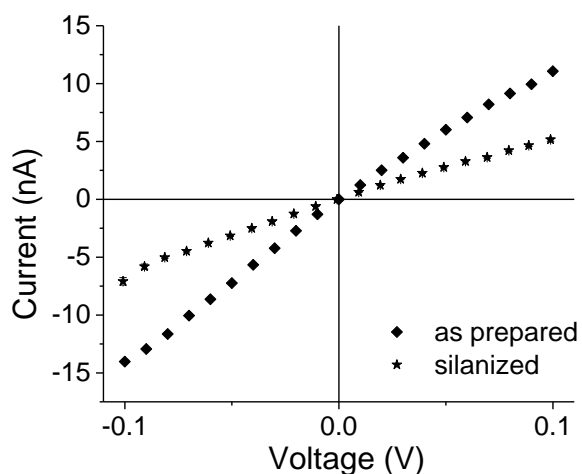
Figure B.14: Current-voltage curves of a nanopore before and after symmetric silanization in 1 M KCl aqueous solution. This pore was prior open for ionic transport by submerging it in ethanol and measuring current-voltages curves in 1 M KCl solution prepared in 50% water and 50% ethanol. The opening diameter of an as prepared nanopore was 27 nm. Symmetric silanization decreased the pore opening to 18 nm indicating the thickness of the silane layer is ~5 nm. The diameter of the silanized nanopore was calculated assuming the modification also led to increased pore length, as described in Ref. [189]. Note, the sizing of the pore before and after modification is based on voltage range between -0.1 V and +0.1 V where the current-voltage curves are most linear.

Chapter 6: Rectified and Salt Concentration Dependent Wetting of Hydrophobic Nanopores

Modeling figures and discussion used with permission from Fikret Aydin

Theoretical figures and discussion used with permission from Pedro de Souza

The previous chapter details ion transport results for nanopores containing a hydrophobic/hydrophilic junction and modeling results for a nanoconfined hydrophobic interface. The work shines light on the missing components of an EDL description for a hydrophobic surface. The classic EDL description treats ions of the same charge identically, and does not differentiate between large, polarizable ions, and small, hard ions. However, our work has shown that this description cannot be used to describe hydrophobic surfaces, and the difference in distribution between iodide and chloride ions has stark consequences when used in nanoconfined systems. The enhanced iodide density near hydrophobic surfaces was shown to drive ion transport through a nanopore containing a hydrophobic/hydrophilic junction. The ion transport was also gated by the electric field polarity, with negative fields more easily wetting nanopore devices. These conclusions point to the importance of local ion concentration on wetting hydrophobic nanopores. What remains missing, however, is how bulk ion concentration can influence gating in hydrophobic nanopores. What is especially interesting is bulk surface tension trends predict that *larger* electrolyte concentrations have higher surface tension, and thus would be more difficult to wet a hydrophobic nanopore. In this chapter, we explore the role of electrolyte concentration on wetting behaviors in our hydrophobic/hydrophilic nanopore system. Herein we show a hydrophobic nanopore system whose wetting and ability to transport water and ions is rectified and can be controlled with salt concentration. The nanopore we examine contains a similar hydrophobic/hydrophilic junction as the device in the previous chapter. The nanopore devices are closed for transport at low salt concentrations and exhibit finite current only when the concentration reaches a threshold value that is dependent on the pore's opening diameter, voltage polarity and magnitude,

and type of electrolyte. The smallest nanopore studied for this project had a 4 nm diameter and did not open for ionic transport in any concentration of KCl or KI examined. A 12 nm nanopore was closed for all KCl solutions but conducted current in KI at concentrations above 100 mM for negative voltages and opened for both voltage polarities above 500 mM KI. Nanopores with a hydrophobic/hydrophilic junction can thus function as water and ionic diodes, such that one can identify a range of salt concentrations where the pores transport water and ions for only one voltage polarity. Molecular dynamics simulations in conjunction with continuum electrowetting models provided a multi-scale explanation of the observed phenomena and linked the salt concentration dependence of wetting with an electrowetting model. Results presented in this chapter are crucial for designing next-generation chemical and ionic separation devices, as well as understanding fundamental properties of hydrophobic interfaces under nanoconfinement.

Introduction

Hydrophobic interactions under nano-constriction, such as in nanopores, have shown to control transport of water and all dissolved species.[74,152,204,214] If a pore wall is lined with hydrophobic groups, in the absence of any external stimuli, such as pressure or voltage difference, the pore will be filled with water vapor even if in contact with a salt solution.[150,170,172,204] As the voltage or pressure is gradually increased, the solution will enter the pore only once a threshold stimulus magnitude is reached.[170,177,180,215] A hydrophobic nanopore is therefore an ideal valve that stops all transport, including diffusion, in the absence of stimuli or presence of sub-threshold magnitude stimulus. Importantly, a hydrophobic nanopore in a wetted state can undergo reversible dewetting once a pressure difference or voltage is decreased or switched off entirely.[150,170,215]

The possibility of controlling transport in hydrophobic nanopores by electric field is especially exciting. Applying an electric field does not necessitate mechanical strengthening of the pore membrane. Consequently, hydrophobic gating can be achieved even in thin, fragile systems including channels in a cell membrane.[152,215] In addition, the transmembrane current magnitude is a direct indication of the pore's wetted or dewetted state and allows one to probe the nanoscale wetting - dewetting transitions occurring within the pore.[170,172] A dewetted state is observed as negligible current; finite current can only be measured if there is a continuous column of electrolyte along the whole pore length, indicating wetting. Switching between the closed (nearly zero current) and open (finite current) states of a pore is called hydrophobic gating. Wetting of hydrophobic nanopores with electric field was explained to occur through alignment of water dipoles that in turns leads to lowering the interfacial surface tension and finally wetting.[176,183] Electrostriction was another effect shown to be important in wetting hydrophobic nanopores.[180,216] Hydrophobic gating with voltage has been demonstrated for biological channels[152] as well as synthetic polymer[170] and solid state nanopores.[172,217]

Recent work demonstrated that hydrophobic gating can also be controlled by placing charged chemical groups in the vicinity of the pore's hydrophobic zone. In one study, a few charged amino acids present in a model protein nanopore derived from the 5-HT$_3$ receptor made the pore's hydrophobic gating asymmetric with respect to voltage polarity.[215] When the external voltage had the same polarity as the intrinsic potential difference induced by the charged amino acids, the pore wetting occurred at lower electric field magnitudes compared to the opposite voltage polarity. Another nanopore system where hydrophobic interactions and gating were modulated by the presence of charged

143

groups was created in silicon nitride films.[217] One entrance of the silicon nitride pore contained highly hydrophobic groups, while the other opening was modified with a positively charged polyelectrolyte. In 1 M KCl, the nanopore was nearly completely closed for positive voltages, but opened up for transport at sufficiently high magnitudes of negative voltages.[217] Voltage polarity dependent wetting was also seen in conically shaped polyethylene terephthalate nanopores after modifying their carboxylated surface with long hydrocarbon chains.[171] The position and density of the hydrophobic modifications were not, however, controlled, and the polymer walls remained overall hydrophilic, with contact angle below 90 degrees.

The prospect of tuning transport properties of hydrophobic nanopores by placement of surface charges brought another interesting opportunity to control hydrophobic gating with ion concentrations. As the salt concentration decreases, the local electric field that originates from the pore's surface charges is finite over larger distances from the surface. Consequently, one could hypothesize that less concentrated solutions could promote wetting, since surface-effects are encompassing more of the pore's cross-sectional area. The dependence of liquid-vapor interfacial tension on salt concentration would also suggest that a smaller external stimulus is required to wet a hydrophobic nanopore in contact with a less concentrated solution compared to the same pore in contact with a more concentrated solution.[177,218] Interestingly, the conical nanopore system modified with hydrophobic hydrocarbon chains was more likely to wet in higher salt concentrations.[171] Since the modified polymer walls exhibited contact angle below 90 degrees, the observed salt dependence could not be only attributed to hydrophobic interactions.

144

In this chapter we examine the role of bulk ion concentration on wetting of silicon nitride nanopores containing a hydrophobic/hydrophilic junction. Nanopores with opening diameters between 4 and ~20 nm were fabricated by electron-beam drilling in a transmission electron microscope (TEM).[189,219] One entrance of the pore was modified with fluorinated alkyl chains while the other opening was modified with amines. The pores were examined in a wide range of concentrations of two salts, KCl and KI. We found that the wetting transition was promoted by an increase in electrolyte concentration. The dependence of the dewetted – wetted transition on ionic concentration was especially clear in solutions of KI. The experimental results are explained by molecular dynamics (MD) simulations that revealed voltage-polarity and salt concentration dependent water and ionic concentrations at the hydrophobic/hydrophilic junction. Accumulation of ions in both the hydrophobic and the hydrophilic zones of the nanopore was found to promote wetting. A continuum theory was subsequently applied and utilized ionic concentrations obtained from MD simulations. A physical model of a hydrophobic system was built that provides analytical equations to predict nanopore wetting as a function of applied voltage and salt concentration.

Methods

Materials

The following reagents were purchased from the specified company and used as received: potassium chloride (KCl, 99.8%, Fisher Scientific), potassium iodide (KI, ≥99%, Fisher Scientific), tris(hydroxymethyl)aminomethane (Tris, 99.9%, Sigma-Aldrich), (3-aminopropyl)trimethoxysilane (APTMS, 97%, Sigma-Aldrich), 1*H*,1*H*,2*H*,2*H*-perfluorooctyltrichlorosilane (hydrophobic silane, 97%, Alfa Aesar), hydrogen peroxide

(H_2O_2, 30% w/w, Sigma-Aldrich), sulfuric acid (H_2SO_4, 95-98%, VWR). Milli-Q water (18.2 MΩ) was used for all solutions. Nanopores were drilled in low-stress silicon nitride films (SiN_x, 50 x 50 μm window, 30 ± 2 nm thick, Norcada).

Nanopore fabrication and modification

Single nanopores were drilled in silicon nitride films using a 200 kV electron beam in a JEOL 2100F TEM.[189,219] Nanopores were fabricated by focusing the electron beam on a single spot for ~5 minutes. The silicon nitride films containing the drilled nanopore were then cleaned in piranha solution (3:1, H_2SO_4:H_2O_2) at 120 °C for 60 mins. Once cleaned, nanopores were asymmetrically modified with hydrophilic (bottom) and hydrophobic (top) silanes. First, the film was placed in a homemade polydimethylsiloxane (PDMS) conductivity cell and the bottom of the cell was filled with a 1% solution of APTMS in ethanol while the top contained pure ethanol (Figure C.1a).[220] The film was exposed to the APTMS solution for 30 minutes before being rinsed with copious amounts of pure ethanol and subsequently heated at 70 °C for 60 minutes. Asymmetric modification with APTMS was confirmed by a decrease in transmembrane current and appearance of ion current rectification.[217] The film was dried and any residual salt was removed by submerging first in Milli-Q water followed by ethanol and finally toluene before letting the film air dry. Once dry, the top of the film was exposed to a 0.2% solution of 1*H*,1*H*,2*H*,2*H*-perfluorooctyltrichlorosilane in toluene for 5 minutes while the bottom was in contact with pure toluene (Figure C.1b). The film was then rinsed in ethanol and heated at 120 °C for 30 minutes.[217] Hydrophobic silane modification was confirmed by closed state of the pores at low voltages in KCl solutions.

To estimate the thickness of the modification we analyzed current-voltage curves of all nanopores before and after the APTMS modification, thus in conditions when the pore could be assumed entirely wet. The values we received ranged from ~2 nm for the smallest pores (4 nm) to 5 nm for the largest pore (19 nm x 7 nm). The smaller thickness of the attached silane layer in the smaller pore can stem from the hindered access of the reagents to the nanopore.

Electrochemical measurements

Ion-current measurements were performed with a patch-clamp amplifier Axopatch 200B and Digidata 1322A (Molecular Devices, Inc.). Transmembrane voltage was swept from -2 to +2 V in 200 mV steps with a sampling frequency of 10 kHz. Each voltage was held for 50-100 seconds, with reported values as averages and standard deviations of the time series for the forward sweep, omitting the first and last 5-10 seconds of each step. To calculate pore opening probability (POP), the total time the pore conducted current was divided by the examined scan time (35 or 85 seconds, depending on the total scan time).[215] Threshold current for pore conductance was defined as 6 times the standard deviation of the current at 0 V. Current-time sweeps were analyzed with the event detection program in Clampfit. All events were inspected, with errors and false positives removed by hand. Discretization of the current-time curves was performed by assigning a 1 or 0 to current values based on the threshold current described above.

Pellet Ag/AgCl electrodes (A-M Systems) were utilized for all electrochemical measurements, with the working and ground electrodes on the hydrophilic (bottom) and hydrophobic (top) sides of the film, respectively. Stock salt solutions (1 and 2 M) were

prepared with 10 mM Tris buffer and adjusted to pH 8 before diluting to desired concentration.

Contact angle measurements

Contact angle measurements were performed at room temperature with a homemade imaging setup. Two samples were investigated: unmodified and hydrophobically modified SiN_x membranes. Contact angle measurements were performed with 2 µL drops of the indicated solution, and contact angles for the two membranes were measured for each solution used in the ion transport experiments. Membranes were washed with Milli-Q water between each measurement. Images were captured on a Nikon D5200 camera outfitted with an Infinity Photo-Optical Model K2 DistaMax Long-Distance Microscope. Contact angle values were calculated using the ImageJ Contact Angle plugin by M. Brugnara. In addition, water contact angle measurements of SiN_x membranes that were first modified with APTMS and subsequently modified with three different concentrations of the hydrophobic silane were collected. These contact angle experiments for double layered SiN_x membranes were performed on a Kruss DSA30.

Molecular dynamics simulations

Classical molecular dynamics (MD) simulations were carried out using the LAMMPS simulation package.[221] Our simulation models consist of a slit pore made of graphene layers and a chloride or iodide aqueous solution with potassium used as the counter ion. The pores size is 1.5 nm, which is defined as the distance between the center-of-mass of adjacent graphene layers, and the lateral dimension of the pore is 3.1 nm x 3.3 nm. To mimic the hydrophobic/hydrophilic junction in the experimental system,

half of the pore is made hydrophobic by changing the depth of the potential well of Lennard-Jones interactions, and the other half is made hydrophilic by adding a positive charge of 0.012e to each carbon atom. In this way, ion/water-surface chemistry interactions are implicitly captured in the MD simulations. Similar modifications were applied in the previous studies. For example, carbon nanotubes were made more hydrophilic by changing the LJ parameters of CNT.[222] The atoms of the slit pore structure are kept rigid, and their positions are constrained to prevent rigid-body translation of the pore structure during the simulations. We note that the slit opening and length of the pore modeled is an order of magnitude smaller than the pores probed experimentally. This is done to make the modeling tractable and amenable to probing different conditions. We expected these smaller pores to wet in the simulations, as their reduced length was previously shown to facilitate wetting.[223] Thus, the smaller slit pore could qualitatively describe physical phenomena occurring in a pore containing a hydrophobic/hydrophilic junction that we studied experimentally.

The system was solvated by TIP3P water molecules,[224] where hydrogen-oxygen bonds were constrained using the SHAKE algorithm. The ions described by OPLS-AA force fields[197] were added to obtain a concentration of either 0.1 M or 1 M. The long-range electrostatic interactions were solved using particle particle-mesh method.[197] The systems were first energy minimized and then equilibrated under the NPT ensemble by the Berendsen barostat.[199] The production runs spanning 16 ns were performed under the NVT ensemble by the Nosé-Hoover thermostat[110] maintaining the temperature at 298.15 K.

Results and Discussion

Voltage-gating of nanopores with a hydrophobic/hydrophilic junction

Nanopores used in this manuscript were prepared by electron beam drilling in a transmission electron microscope,[189,219] and their diameters were measured immediately after fabrication. The nanopores were subsequently subjected to a two-step chemical modification that introduced a junction between a hydrophilic zone and a hydrophobic zone (Figure 6.1a). Our earlier work showed that nanopores containing such a junction exhibited hydrophobic gating and could open for ionic transport with applied voltage.[217] Nanopores with a hydrophobic/hydrophilic junction were used here to understand the role of ionic concentration and type of salt on the voltage-induced wetting and hydrophobic gating.
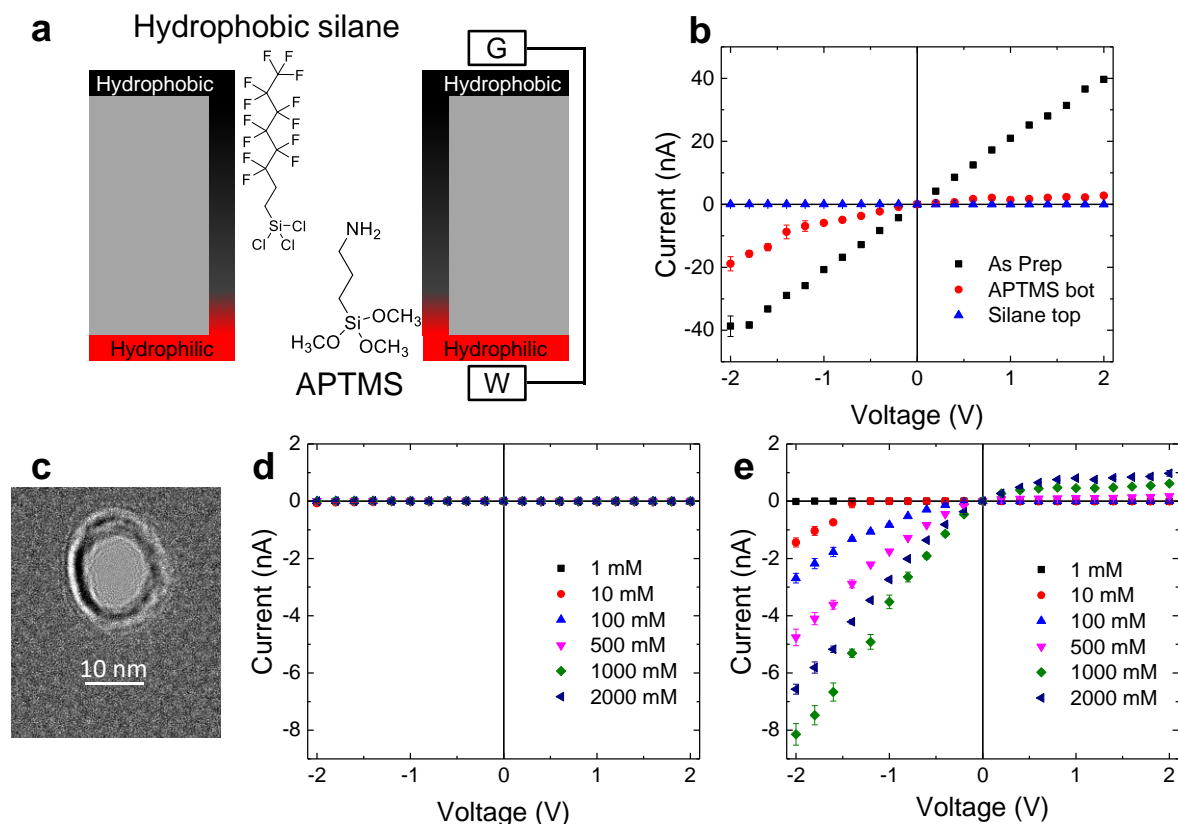
Figure 6.1: Preparation and performance of a nanopore with a hydrophobic/hydrophilic junction. (a) Nanopore scheme, with electrode (W = working; G = ground) placement as indicated. Nanopores were subjected to two asymmetric modifications, creating a junction between hydrophobic (perfluorooctyl) and hydrophilic (aminopropyl) silanes. Note that the transition between these two zones is expected to be gradual and located close to one pore opening. The junction location was estimated based on contact angle measurements of planar surfaces modified with gradually decreasing concentration of the hydrophobic silane. (b) Current-voltage curves in 1 M KCl for a 12 nm diameter nanopore as prepared (black squares), after APTMS modification (red circles), and after modification with hydrophobic silanes (blue triangles); the pore was prepared in a 30 nm thick SiN$_x$ chip. (c) TEM image of the 12 nm diameter nanopore as drilled. (d, e) Current-voltage curves in a range of KCl (d) and KI (e) concentrations for the 12 nm pore after the two chemical modifications. The current-voltage curves in panels (b), (d), and (e) were obtained by averaging ion current signals recorded at each voltage for 50 or 100 s. Error bars were calculated by standard deviations of ion current signals during recording.

151

To introduce the hydrophobic/hydrophilic junction in a nanopore, a silicon nitride chip with a drilled nanopore was first subjected to asymmetric modification with an amino silane (APTMS, shown in Figure 6.1a). To this end, one side of the membrane was in contact with the silane solution, while the other side was in contact with the solvent. This procedure is expected to modify only part of the pore walls since we created two boundary conditions with one pore entrance in contact with the bulk APTMS concentration, and the other with zero APTMS concentration (Figure C.1a). Assuming a cylindrical shape of the pore, the profile of the silane concentration in the pore is linear,[225] suggesting that there might be a density gradient of the attached amines along the pore length. Limiting the amination to only a fraction of the walls was, however, assured by the choice of incubation time and APTMS concentration. Previous work on modifications with a similar silane, (3-aminopropyl)triethoxysilane (APTES), showed that for the same incubation time we used (30 min), ten times lower silane concentration led to minimal modification.[226] We therefore expect that at least 20% of the pore walls will have minimal amine coverage. Presence of a junction between modified and unmodified zones of the pore walls was confirmed by recording rectified current-voltage curves in 1 M KCl at pH 8. The positively charged amino groups and the negatively charged, unmodified silanol groups create asymmetric surface charge distribution within the nanopore, leading to ion current rectification such that current values for negative voltages were greater than for positive voltages (Figure 6.1b).[79]

The second and final modification step was aimed at the attachment of hydrophobic groups to the opposite side of the membrane. To this end, 1*H*,1*H*,2*H*,2*H*-perfluorooctyltrichlorosilane was placed in contact with the pore opening that in the

152

amination step was only exposed to the solvent (Figure C.1b). Successful attachment of this silane was confirmed by measuring a contact angle of 110 degrees for the modified chip.[217] Attachment of the hydrophobic silanes is also evidenced by current-voltage recordings, because the hydrophobic silane modification would leave the pore in its dewetted state and the resulting ion current in 1 M KCl would be nearly zero for all voltages (Figure 6.1b). In order to probe the depth of the 1H,1H,2H,2H-perfluorooctyltrichlorosilane attachment, we modeled the conditions of the modification on a series of planar SiN$_x$ surfaces. Note that in this modification, the side of the membrane that was not modified with amines in the prior modification was now in contact with the hydrophobic silane, while the fully aminated end would be in contact with a much lower concentration of the hydrophobic silane (Figure C.1b). Therefore, we modified a series of SiN$_x$ chips first with APTMS at the same bulk concentration as used before (1%), followed by modification with 1H,1H,2H,2H-perfluorooctyltrichlorosilane at the original bulk concentration, and concentrations diminished to 25% and 10% of the bulk. Water contact angle measurements of the chips were then performed. The results indicated that even the lowest concentration considered led to a contact angle of 110 degrees, which is comparable to the surface modified with the maximum concentration. We concluded that the hydrophobic silane could attach to the aminated surface, and the hydrophobic modification extends through most of the pore wall. Consequently, the hydrophobic/hydrophilic junction is expected to be present close to one pore opening (Figure 6.1a).

Such hydrophilic/hydrophobic nanopores were subsequently tested for their ion transport properties in a wide range of KCl and KI concentrations between 1 and 2000

mM. Ion currents were recorded in the voltage range between -2 and +2 V. Time series of ion current at each voltage were averaged to obtain current-voltage curves. Figure 6.1d,e summarizes current-voltage curves for the 12 nm diameter nanopore shown in Figure 6.1c. In KCl this pore remained predominantly closed for all concentrations and voltages and underwent gradual opening in a voltage-dependent manner only when subjected to increasing concentrations of KI. The non-conductive state observed in ion-current measurements of KCl indicates that the pore was not entirely filled with liquid water, and thus closed.[170,215,217] Based on previous work,[150,152,170,183,215,217] we believe that when the pore was closed, a zone of water vapor existed in its cross-section, preventing transport of liquid water and ions. On the other hand, recording finite ion current was only possible if there was a continuous column of water along the entire pore length. In 1 mM KI no measurable current was observed for any voltage polarity, suggesting the pore was at least partly dewetted. At 10 mM KI, the pore began opening for ion transport and conducted finite current for negative voltages equal and larger in magnitude than -1.4 V. For 100 mM KI, the pore conducted finite ion current for all negative voltages but remained closed at positive voltages. Only when the KI concentration was increased to 500 mM did the pore become conductive for both positive and negative voltages. Note that for negative voltages, currents recorded in 1 M KI are larger than currents in 2 M KI. We believe this effect could stem from a stronger screening of charges in the higher concentration that weakens the enhancement of ionic concentrations within the pore and is responsible for the nonlinear current increase with negative voltage.[77,79,227–229] The current for positive voltages, on the other hand, follows the expected dependence on salt concentration, with 2 M KI producing the largest current.

The difference in the concentration dependence of ion current for negative and positive voltages can be understood through the rectifying properties of this pore. In rectifying nanopores, the voltage polarity that produces lower currents, positive voltages in our case, leads to a depletion zone of ions in the pore.[69,227] However, with the increase of salt concentration, the surface charges are more screened and more ions reside in the pore, thus preventing the depletion zone from completely developing in higher salt concentration solutions. The resulting current-voltage response follows bulk solution conductivity trends.

The differences in ion transport properties for KCl and KI solutions are unique to nanopores that were subjected to two asymmetric modifications, first with APTMS, followed by modification with 1H,1H,2H,2H-perfluorooctyltrichlorosilane, as described above. As prepared nanopores[217] as well as nanopores entirely modified with APTMS (Figure C.2) were open for ionic transport in both KCl and KI, and produced nearly identical, linear current-voltage curves in the two salts. These results agree with the salts' nearly identical bulk conductivities. Moreover, nanopores that were modified symmetrically with the hydrophobic silane did not open for transport with external voltage either in KCl or KI.[217] The clearly distinct transport properties of the asymmetrically modified nanopores provide additional evidence for the existence of a junction between aminated and hydrophobic zones of the pore walls.

The more conductive nature of hydrophobic nanopores in KI versus KCl aqueous solutions agrees with our earlier molecular dynamics results that revealed accumulation of large, polarizable ions, such as iodide, on the hydrophobic pore walls.[217] The accumulation of iodide on hydrophobic surfaces was postulated to facilitate pore wetting

but it cannot, however, explain the concentration dependence of the pore wetting, reported here. As shown in Figure 6.1, the nanopores were more likely to open for ionic transport in higher salt concentrations than at lower salt concentrations. As surface tension of a water-air interface exhibits a weak increase with the increase of salt concentration,[218] an analysis based on surface tension alone would actually predict only a weak and possibly opposite effect of ionic strength on pore wetting to what we are reporting here.[218] In addition, the contact angle of the hydrophobic surface probed here did not show an obvious dependence on the salt concentration of either KCl or KI (Table C.T1).

Analysis of ion current time series and hydrophobic gating

To visualize the voltage-induced wetting of nanopores and to facilitate comparison of recordings at different salt concentrations, we carefully analyzed the ion current time series. Nanopores studied here had opening diameters below 20 nm and were found to exhibit spontaneous switching between non-conductive and conductive states, even at a constant voltage (see example in Figure 6.2). We changed the raw current recordings into a dichotomous, two-state signal consisting of level 0, the closed state with no current, and level 1, the open state with finite current.[215] A nanopore was considered conductive/open for ionic transport if the ion current signal was larger than 6 times the standard deviation of the current signal at 0 V. At each voltage we determined the fraction of the recording a nanopore spent in its conductive, {1}, state, and this fraction became our measure of the pore opening probability (POP).[215] This analysis allowed us to find the dependence of pore wetting on ionic concentration, applied voltage, and pore diameter.
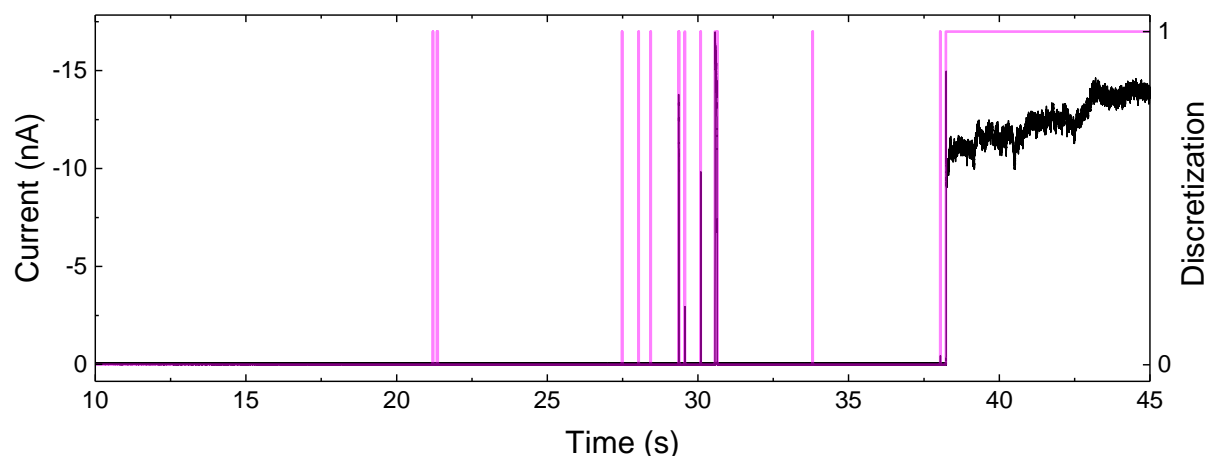
Figure 6.2: Recording of ion current time series for the pore shown in Figure 6.3d for 500 mM KI at -2 V. The experimental data displayed in black is discretized into {0, 1} states indicating closed and open states of the pore, shown in magenta. The pore opening probability for this voltage was 0.2.

Note that before the nanopore in Figure 6.2 reached a long-lasting open state at the end of the recording, there were brief bursts of finite current separated by seconds-long periods with zero current. The long duration of the closed state suggests that the air bubbles created in the nanoscopic system can be very stable, in agreement with previous results,[230] as discussed in the modeling section below. The opening of the nanopore at ~38 s indicates formation of a long open state, but as shown in Figure C.3, the subsequent sweep at −1.8 V started with the pore in a closed state again. These recordings demonstrate that the time scale of the hydrophobic gating spans many orders of magnitude, and more studies are needed to understand the origin of the short and long wetted and dewetted states. As described below, such gating exists right at the threshold voltage and concentration values. This is likely due to hydrophobic hysteresis,[172,208,217] where both states are metastable.

Figure 6.3 summarizes the pore opening probability of four nanopores with different opening diameters, all below 20 nm, as a function of salt concentration and voltage. The smallest nanopore we examined was 4 nm in diameter and did not open for ionic transport in either KCl or KI for any examined concentrations, as shown in Figure 6.3a. We suspect that the voltage range of -2 to +2 V was insufficient to induce wetting.[170,172,215] Another pore had a 6 nm diameter and remained closed in KCl but opened for ionic transport only in 2000 mM KI, the largest examined concentration, at negative voltages (Figure 6.3b). A POP analysis for the 12 nm diameter pore shown in Figure 6.1 confirmed its closed state for nearly all concentrations of KCl, and gradual opening with the increase of KI concentration (Figure 6.3c). Note: the 12 nm nanopore conducted finite current for both positive and negative voltages when the KI concentration reached 500 mM. Finally, the nanopore in Figure 6.3d was not circular and measured 19 x 7 nm. The oblong shape of this pore resulted from a slight drift of the e-beam in the TEM while drilling. In KCl, this pore remained mostly closed, except for 500 mM and 2000 mM at high negative voltages. In KI on the other hand, the pore was closed for all voltages at concentrations ≤ 100 mM and started to conduct current at negative voltages for KI concentrations ≥ 500 mM. As the concentration increased from 500 to 2000 mM, the pore transported ion current for a wider range of negative voltages, qualitatively following the same trend as the pores in Figure 6.3b,c. Higher KI concentrations lowered the threshold voltages required to open the pore, decreasing from -1.4 V for 500 mM to -0.8 V for 2000 mM. The 19 x 7 nm oblong nanopore did not open for ion transport at positive voltages, most likely due to one of its axes measuring below 10 nm. Note: the sub-10 nm pores in Figure 6.3a,b indeed did not conduct current at positive voltages for either electrolyte.

The presence of the larger axis, however, made the pores conductive in lower magnitudes of negative voltages, compared to sub-10 nm circular nanopores. Thus, transport properties of oblong nanopores are determined by both axes.

Similar to the existence of a pore diameter and voltage threshold, there also seems to be a concentration threshold at which a pore begins to open. For nanopores with an opening above 10 nm (Figure 6.3c,d), the threshold concentration was between 10 and 500 mM. Abrupt current spikes, seen in Figures 6.2, 6.4d, were observed for intermediate concentrations and voltages, where the pore underwent intermittent wetting and dewetting. These conditions yielded pore opening probabilities in the 25-75% range.
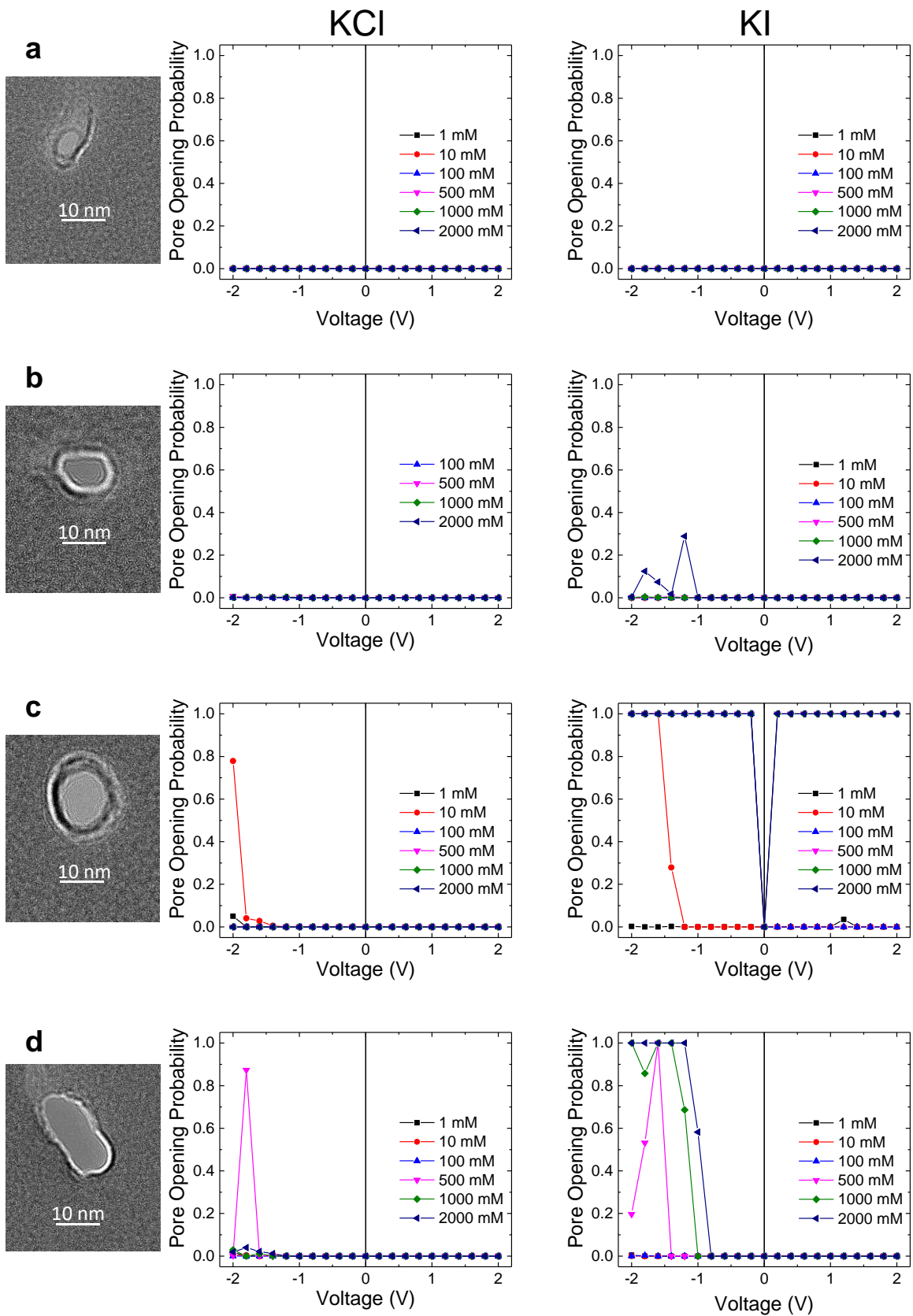
Figure 6.3: Pore opening probability for nanopores in a wide range of KCl and KI concentrations. (a-e) TEM images of as prepared pores are shown on the left. The middle and right-hand side panels show data for KCl and KI, respectively.

The ability to control gating with ionic concentrations is especially evident when examining the dichotomous current-time graphs recorded for the same voltage but different salt concentrations (Figure 6.4). All current-time graphs in Figure 6.4 were recorded at -2 V in KI for the nanopore shown in Figures 6.2, 6.3d. For 1-100 mM, the current never reached past the threshold required to be conductive (Figure 6.4a-c). At 500 mM (Figure 6.4d), there were a few short bursts of current followed by a continuous opening towards the end of the sweep. Finally, recordings at 1000 mM and 2000 mM KI (Figure 6.4e,f) revealed continuous conductance of the oblong nanopore (Figure 6.3d). These six sweeps show that the salt concentration plays an important role in the pore wetting, with intermediate concentrations displaying unstable conductance.
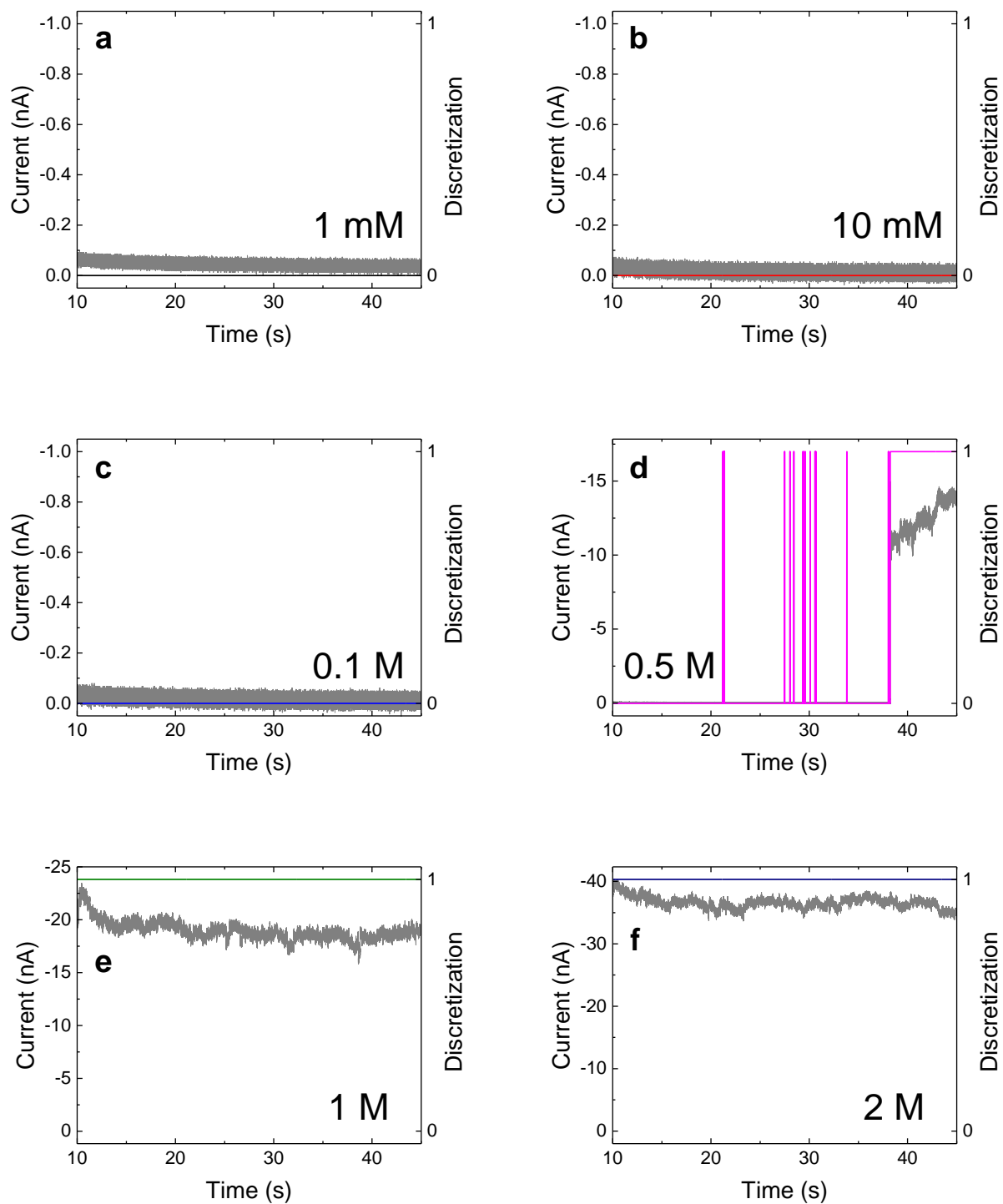
Figure 6.4: Time resolved recordings of ion current for the nanopore shown in Figure 6.3d at -2 V for six different KI concentrations, as indicated in panels (a-f).

Another striking feature of the recordings shown in Figures 6.1, 6.3 is the ability for nanopores with a hydrophobic/hydrophilic junction to function as a diode for water and all dissolved ions, such that transport is allowed mostly at negative voltages. A similar asymmetric voltage response was observed earlier only in KCl with nanopores that were few tens of nanometers in diameter and contained such a hydrophobic/hydrophilic junction.[217] The voltage polarity (negative) that promoted pore opening was determined by the migration direction of counterions (anions) in the positively charged hydrophilic zone. Pores would conduct ionic transport for the voltage polarity that sourced counterions from the reservoir in contact with the hydrophilic zone. In the system presented here, for negative voltages that facilitate wetting, anions are indeed sourced from the pore entrance decorated with APTMS and transported towards the hydrophobic entrance. In addition, the hydrophobic/hydrophilic nanopores shown here are conductive only after a threshold voltage and threshold concentration of KCl or KI was reached. The two stimuli – voltage and electrolyte concentration – work synergistically. As the salt concentration increased, the pores exhibited lower threshold wetting voltages for negative polarity and were more likely to open at positive voltages. All these observations provide strong evidence that salt concentration and pore opening probability are directly related.

The possibility of controlling the wetting-dewetting transition in nanopores with salt concentration, ion type, and applied voltage is modeled below by molecular dynamics simulations as well as using a mechanistic approach involving the existence of air bubbles and electrowetting. The molecular dynamics approach provides an atomistic insight into pore wetting and dewetting at different experimental conditions, while the continuum model, *infra vide*, considers the energy associated with the ionic adsorption and charging.

The model predicts that wetting is indeed facilitated by the increase of ionic concentration that leads to adsorption of ions to the surface and lowering of the effective solid-liquid interfacial tension.

Molecular dynamics simulations of nanopores with a hydrophobic/hydrophilic junction

Molecular dynamics simulations of a model system were carried out to provide insights into the mechanism for how ion concentration and applied potentials promote wetting of nanopores with a hydrophobic/hydrophilic junction. We considered a 1.5 nm wide and 3.1 nm long slit pore made of hydrophobic graphene layers. Half remained uncharged and hydrophobic, and the other were assigned net positive charge (Figure 6.5a). This model system allowed us to probe the importance of the junction between two zones with dissimilar chemical properties without considering its exact position in the pore. To explore the effect of applied voltages, electric fields with different magnitudes and polarities were applied across the model nanopore. We considered electric fields of 0.005 and 0.008 V/Å, as they are comparable to experimental conditions. We note that 0.005 V/Å is equivalent to a 1.4 V potential across a 30 nm thick film, which was often insufficient to lead to pore wetting (Figure 6.3). On the other hand, 0.008 V/Å represents the maximum voltage employed experimentally (2 V). Herein, the two electric fields will be called low and high, respectively. The simulations were performed in 1 M and 0.1 M solutions of KI and KCl.

We first considered the hydrophobic region of the model nanopore that determines when the transport of ions can occur. Our simulations showed that the nanopore was not wetted at the low electric field, regardless of the ion type, electric field polarity, or salt

concentration. On the other hand, at the high electric field (0.008 V/Å) and 1 M KI, the pore was filled with water and became conductive only at negative potentials; the same nanopore remained closed at 1 M KCl (Figure C.4, Figure 6.5b top panel). The salt dependence could be explained by the weaker solvation shell of iodide ions that enable their accumulation on the hydrophobic surface, as reported by us before,[217] as well as their accumulation near the water-vacuum interface (Table C.T2). The simulations also reproduced experimentally observed dependence of the nanopore wetting on salt concentration. At the high electric field, when the KI concentration was lowered to 0.1 M, the nanopore did not open for ionic transport in either salt (Figure 6.5c top panel, Figure C.4). Overall, these observations are consistent with experimental findings shown in Figures 6.1, 6.3. Furthermore, the analysis provides a more detailed understanding of the wetting process; for example, the simulations indicate that the hydrophobic region is first filled with water molecules, followed by the influx of ions that occurs within a timescale of a fraction of ns (Figure 6.5a middle panel, and Figure 6.5b top panel). Similar behavior has been observed for biological hydrophobic pores.[183]

To further understand the effect of ion concentration on nanopore wetting, we also calculated the number of water molecules and ions in the hydrophilic region of the pore (Figure 6.5b,c, lower panels, Figures C.5, C.6). As expected, the hydrophilic zone is filled with water in all conditions (Figure C.6), confirming that the transport properties of the nanopore are dominated by the state of the hydrophobic zone. The modeling also confirmed anion selectivity of this region, especially pronounced in 0.1 M KCl and KI as well as in all 1 M conditions when the pore was not wet. The anion selectivity decreased in 1 M KI when the pore wetted, as evidenced by the nearly identical number of potassium

and iodide ions only after ~8 ns at -0.008 V/Å (Figure 6.5b, lower panel). These results allowed us to conclude that concentrations of ions in the hydrophobic and hydrophilic region are coupled, and the pore wetting is facilitated by increased ionic concentrations in both regions of the nanopore.
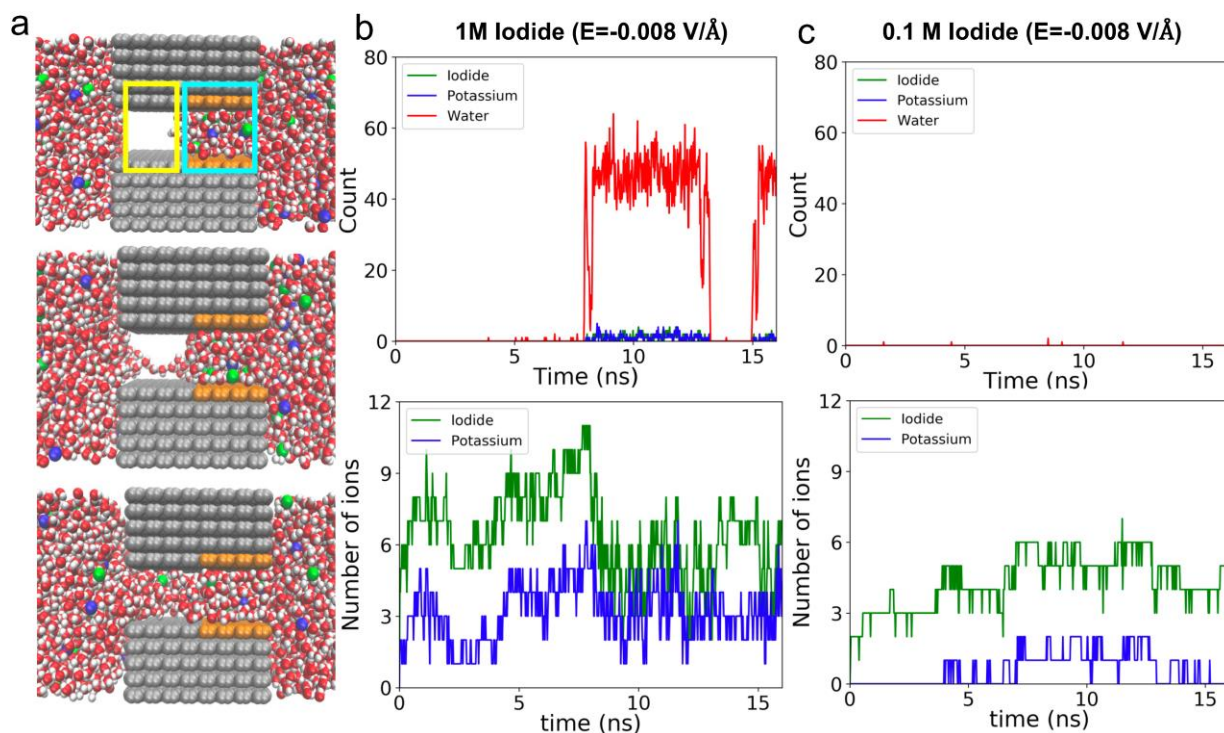
Figure 6.5: Molecular dynamic simulation results for a hydrophobic/hydrophilic nanopore model. (a) Simulation snapshots showing different stages of pore wetting in 1 M KI salt solution and at a negative electric field of 0.008 V/Å. Areas encircled by yellow and cyan lines correspond to hydrophobic and hydrophilic regions of the pore, respectively. (b, c) Number of water molecules, potassium, and iodide ions in the hydrophobic (top panels) and hydrophilic (bottom panels) regions of the pore as a function of time for (b) 1 M KI and E = -0.008 V/Å and (c) 0.1 M KI and E = -0.008 V/Å.

Finally, we also investigated the stages of pore wetting by examining snapshots from the simulations (Figure 6.5a). First, a short string of water molecules was instantaneously formed from the bulk solution. This was followed by connecting two such strings of water molecules that were initiated from both sides of the hydrophobic region. The connected string of water molecules was found to grow with time to finally fill up the entire hydrophobic region of the pore. We also looked at the molecular details of the inverse process of dewetting observed in Figure 6.5b at ~13 ns. The region filled with water was found to shrink with time and eventually strings of water molecules were completely disconnected so that the pore became fully dewetted (Figure C.7).

In summary, the molecular dynamics simulations revealed voltage and concentration-controlled wetting of a nanopore with a hydrophobic/hydrophilic junction. The large number of ions present in the hydrophilic region at high bulk concentrations likely causes disruption of the hydrogen bond network and facilitates pore wetting by enabling formation of water strings from the bulk solution. The simulations also suggest that formation of the water strings is further facilitated by the weaker solvation shell of iodide ions, as the water-water interactions are destabilized due to the accumulation of the iodide ions at the hydrophobic surface. These results provide explanation for the experimentally observed anion-dependent wetting of the pores.

The modeling also confirmed that the hydrophobic/hydrophilic junction is crucial for breaking symmetry of the system and the diode-like behavior of these pores. In an entirely hydrophobic pore, ionic concentrations are not expected to be dependent on the pore axial position.[217] Thus, the diode-like behavior and controllable gating is dependent

on the presence of a hydrophobic/hydrophilic junction. The importance of contrasting hydrophobic/hydrophilic properties of two pore entrances for electric field induced wetting was already suggested by earlier studies with a protein nanopore derived from the 5-HT$_3$ receptor.[215] The biological structure contained charges near one opening, which did not induce as such a striking rectifying behavior as in the nanopores presented here but was sufficient to result in voltage polarity dependent wetting. For the next step, we developed a continuum model to provide an analytical formula describing the influence of ionic concentrations and voltage on wetting.

Description of nanopore wetting using an electrowetting model

The position dependent ionic concentrations found through MD modeling shown here and in Ref. [217] were subsequently used to provide a continuum model of the wetting process as well as analytical equations that predict wetting conditions. To qualitatively explain the dependence of nanopore wettability on salt concentration and voltage, we applied a continuum model of wettability including ionic surface adsorption, as described in Ref. [231] based on the thermodynamic analysis of double layer charging.[232] Here, we compute the energy associated with the ionic adsorption and charging to determine the change in effective solid-liquid interfacial tension.

While the interfacial tension is central in determining the wettability for macroscopic bubbles, bubbles at the nanoscale, such as those one might expect to exist encompassing and within the nanopores in our study, exhibit much more complex nanoscale physics,[230] including contact line pinning, dynamic equilibrium, and surface heterogeneities. Therefore, we do not expect this model to give quantitatively exact

predictions of the bubble dynamics, but rather we use this model as a guide to understand the possible physics at play in the hydrophobic/hydrophilic system.

Our wettability model is based on the approach presented in Ref. [231] that we extended to include the polarization of the membrane domain that is coupled to the double layers in the solution domains. Here, we solve for the electrostatic potential in the membrane and in the double layers at the membrane interfaces as first described in Ref. [233], then use that profile to compute the effective surface energy. The formulation assumes anion adsorption on the hydrophobic side of the membrane that varies as a function of the local anion concentration, while the surface charge on the hydrophilic side is assumed to be positive and constant. Note: the adsorption component allows us to take into account the differences in local concentrations of chloride and iodide ions at the hydrophobic surface/liquid interface, revealed by MD.[217] To avoid the geometric complexity of the pore and its opening within the membrane, we focus our model on the wettability further away from the pore, where we can safely assume that the potential varies only in the normal direction to the membrane surface. Such an assumption would be relevant for regions near the contact line for large bubbles (large relative to the pore length scale) existing far from the pore entrance. Even though such a simplified geometry misses the detailed potential profile near the pore mouth and bubble interfaces, as well as the profile around the bubble corners,[234] it provides an intuitive model to capture the role of ionic concentrations and voltage in wetting. A schematic of the continuum model is included in Figure 6.6a. Details of the theoretical basis and solution of the continuum model are presented in Appendix C.

The key parameters of the model include the anionic adsorption equilibrium constant, K, the thickness of the membrane, L, the Debye length, λ_D, the salt concentration, c_0, the applied electric potential difference V_{app}, the number density of surface sites for anion adsorption, N, and the membrane and solution permittivities, ϵ_m and ϵ_w, respectively. As the anionic adsorption equilibrium constant decreases or the ionic concentration increases, the adsorption of ions to the surface is enhanced, leading to the increase in surface charge density. The higher surface adsorption gives two contributions that make wetting more favorable: (i) the electrostatic energy stored in the diffuse double layers and (ii) the energy of surface anion adsorption. As the applied voltage across the membrane increases, charge is stored across the polarizable membrane, providing a favorable contribution to wetting. Figure 6.6b shows the change in the effective surface energy as a function of the ionic concentration for different anion adsorption equilibrium constants and different applied voltages. The full set of nonlinear formulas for solid-liquid interfacial energy, $\Delta\gamma_{sl}$, is shown in Appendix C.

While the full theory requires the solution of a coupled set of nonlinear equations, we can also derive analytical, explicit solutions to the energy for the double layer assuming small surface potentials and a weakly polarizable membrane. The small surface potential relative to the thermal voltage leads to a constant capacitance in the double layers. The weakly polarizable membrane assumption, applicable due to the large thickness of the membrane relative to the Debye length and the membrane's low dielectric constant relative to the solution, allows us to decouple the contributions to the energy from the membrane and the independent double layers. The various contributions from

the diffuse double layers, ionic adsorption on the hydrophobic side, and the membrane polarization can be assumed to act in an additive manner.

For small surface potentials and weakly polarizable membranes, the contribution from the diffuse double layers to the solid-liquid interfacial energy, $\Delta\gamma_{sl}$, is:

$$\Delta\gamma_{sl,dl} = -\frac{\epsilon_w}{2\lambda_D}\zeta^2 = -\frac{N^2 e^2 c_0^2 \lambda_D}{2\epsilon_w K^2} \tag{6.1}$$

the contribution from the ionic adsorption is:

$$\Delta\gamma_{sl,ads} = -\frac{N\, k_B T\, c_0}{K} \tag{6.2}$$

and the contribution from the membrane to the surface energy is:

$$\Delta\gamma_{sl,m} = -\frac{\epsilon_m}{2L}V_{app}^2 \tag{6.3}$$

where e is the elementary charge, and ζ is the surface potential of the hydrophobic surface. Overall, since we assume a constant surface charge on the hydrophilic side of the membrane, and that the hydrophilic side remains wetted even when the hydrophobic side is dewetted, the change in the surface energy of the hydrophobic side due to the charge on the hydrophilic side is typically negligible in the model.

The Eqs. 6.1 and 6.3 displayed above are direct analogues to the Lipmann equation of electrowetting, where the effective interfacial tension varies with the square of the applied potential. Clearly, there is a direct connection between the polarization across the membrane, as studied here, to the classical electrowetting problem, where the wettability of a droplet on an electrode surface is manipulated by an applied electrode potential.[235] The experimental findings, in the context of the continuum model, suggest

that the electrowetting phenomenon can be extended to membrane systems to control the wettability of the pores.

Based on these simplified formulas, we can directly observe that a decrease in the adsorption equilibrium constant, K, an increase in the ionic concentration, c_0, and an increase in the applied electrode potential, V_{app}, all lead to more wetting of the hydrophobic interface. The observed differences between the iodide and chloride salts may be explained by a difference in the adsorption equilibrium constant at the interfaces, as evidenced by differences in the extent of ionic adsorption of the different ions in MD simulations. Based on the model, iodide ions have a smaller equilibrium constant than chloride ions, leading to more adsorption and a greater change in the solid-liquid surface energy for iodide. The trend is fully supported by the nonlinear results in Figure 6.6b. While the model predictions exhibit a weak dependence on the applied voltage polarity, the model itself does not capture the local concentration changes within the pore, since the concentration within the pore is assumed to be voltage-independent. Qualitatively, if we take the concentration changes into account, the model predictions are consistent with the experimental voltage polarity dependence. Since negative voltages in our experimental setup increase local ionic concentrations within the pore, this voltage polarity is more likely to cause wetting of the hydrophobic interface and, in turn, pore wetting.

While the full nonlinear theoretical predictions are qualitatively in agreement with the experimental results, the model cannot yet predict the results in a quantitative manner. It is because large wettability changes ($\Delta\gamma_{sl} < $ -10 mJ/m^2) would require (i) large surface charge density and (ii) large applied electrode potential. For example, in the absence of

applied voltage, the equilibrium constant must be $K = 0.3$ M in order for $\Delta \gamma_{sl} = -10$ mJ/m^2 at $c_0 = 1$ M. Benchmarking our theoretical model to our MD simulations, we find that the continuum model ($K = 0.3$ M) corresponds to an adsorbed anion density of 1.1 nm^{-2} at c_0 = 1 M. In molecular simulations of potassium iodide near a hydrophobic interface,[217] the adsorbed anion density for classical MD simulations is only 0.2 nm^{-2} at $c_0 = 1$ M. Using molecular dynamics with electronic continuum correction (ECC) method to capture the anion polarizability more accurately, the adsorbed density in simulations is 0.54 nm^{-2} at $c_0 = 1$ M.[217] The continuum model would suggest that in order for the ionic concentration to significantly alter the wettability, the surface charge of the membrane would necessarily be larger than the MD and ECC predictions (shown with stars in Figure 6.6c). Nevertheless, in the model, both the increase in concentration and an increase in the applied electrode potential lead qualitatively to a decrease in the solid-liquid interfacial tension of the hydrophobic side, in agreement with the experiments.

In order to bring the continuum theoretical predictions closer to the experimentally observed wettability changes, one could include more microscopic details for the bubble, electrolyte, and bipolar membrane system. For example, the bubble and membrane geometry, the non-ideal thermodynamics of the electrical double layer, and the bubble's nonequilibrium deformation could all play a key role in the observed wettability changes. While we have assumed a large blocking bubble that encompasses the pore entrance, the blocking bubbles in the experiments could be as small as the pore size, resulting in more complex electrowetting behavior *within* the pore rather than at the hydrophobic side of the membrane. A more realistic model may require consideration of the contact line pinning at surface heterogeneities, either within or outside the pore, and the effect of ionic

charges and electric fields near the pinned contact line, dependent on the precise geometry of the pore/membrane.

For the purposes of our study, we do not extend the continuum theoretical analysis beyond the simple case of the equilibrium wettability of a large blocking bubble in an ideal electrolyte, since this limit gives useful trends and physical interpretations without added complexity. Instead, we capture the limit of a small blocking bubble pinned within the pore through the nonequilibrium MD simulation framework, where the applied electric field and concentration changes act to dislodge the bubble, opening the pore to ionic currents as observed in the experiments.
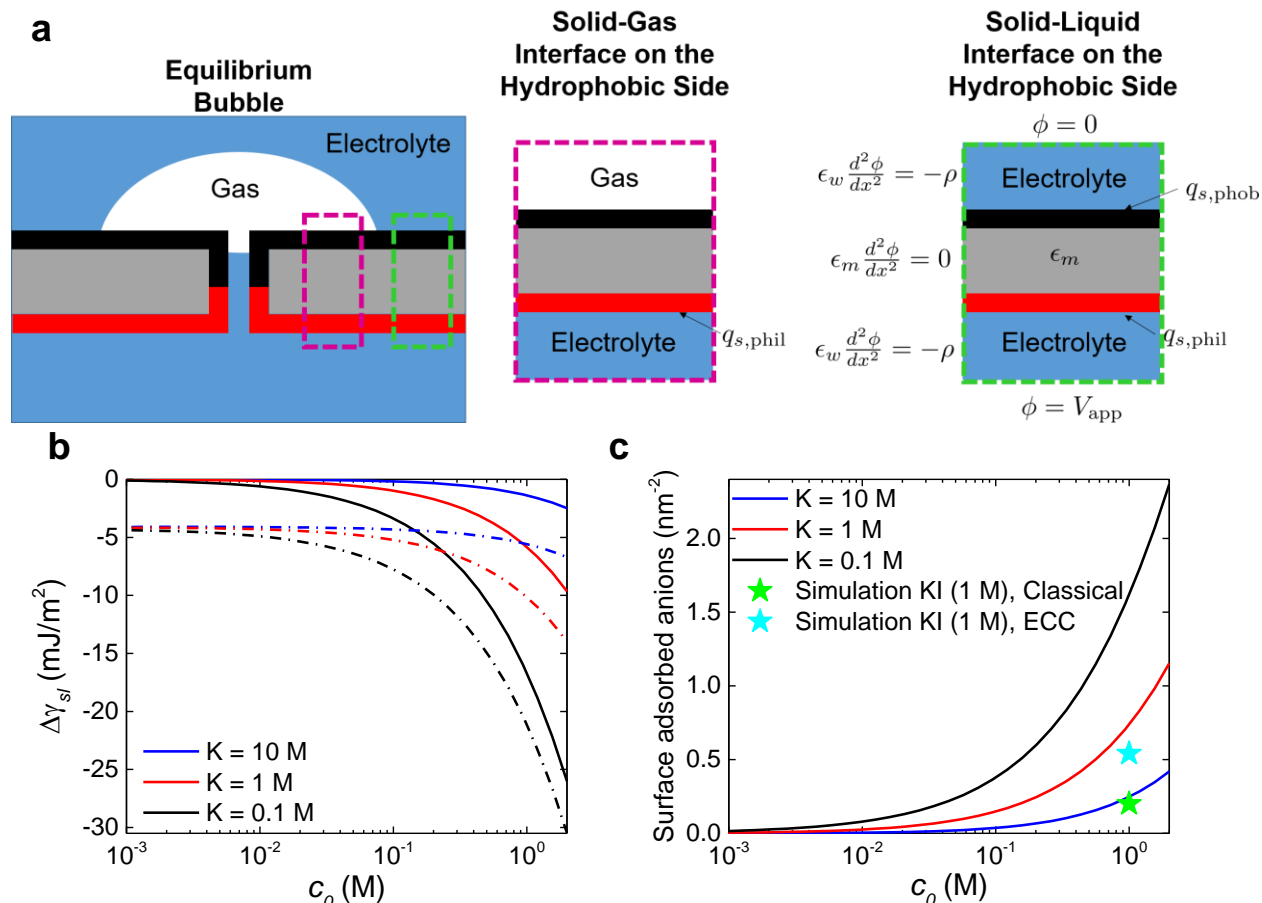
Figure 6.6: Continuum model of wettability. (a) The schematic of the continuum model, where the electrostatic potential is solved for as a function of the applied potential and the bulk ionic concentration. (b) The change in the effective solid-liquid interfacial energy, $\Delta\gamma_{sl}$, as a function of the ionic concentration for varying anionic adsorption equilibrium constant, K, and applied electrode potentials, V_{app}. The solid lines correspond to an applied voltage of 0, and the dashed dotted lines correspond to an applied voltage of +2 V. The change in interfacial energy is not strongly dependent on the sign of the applied voltage, since local concentration polarization within the pore domain is not captured by the model. (c) The surface charge density of the hydrophobic side as a function of the salt concentration for varying anionic adsorption equilibrium constant, K. Because the membrane is only weakly polarizable, the surface charge density is only a weak function of the applied potential (not shown). Here, the stars are shown for two different simulations of KI solutions at 1 M to indicate the expected value of adsorption coefficient. Fixed parameters: $N = 5 \text{ nm}^{-2}$, $\epsilon_m = 7\epsilon_0$, $\epsilon_w = 80\epsilon_0$, $L = 30$ nm, $T = 300$ K, $q_{s,phil} = 0.06 \text{ e nm}^{-2}$.

Conclusions

This chapter presents an asymmetric hydrophobic nanopore whose transport properties can be gated not only by voltage and type of ion, but also salt concentration. The key to gated transport is the presence of a hydrophobic/hydrophilic junction within the nanopore. Our experimental results clearly indicate that a higher salt concentration facilitates wetting of such asymmetric nanopores. We also show that the effect of salt concentration is linked with voltage dependence of wetting, such that the nanopores are more likely to conduct ion current for the voltage polarity that increases ionic concentrations within the pore. As a result of the voltage-dependent wetting, such an asymmetric system functions as a diode for water and all dissolved ions. The mechanism of voltage and salt-concentration induced gating was described using the tools of molecular dynamics as well as a continuum approach of electrowetting. Molecular dynamics simulations predicted local ionic concentrations inside the pore and confirmed accumulation of large iodide ions in the hydrophobic region of the pore that facilitated pore wetting. Simulations also revealed that pore wetting was initiated by short strings of water molecules connecting in the center of the pore. The ionic concentrations obtained from molecular dynamics were subsequently used to build a continuum model that described salt concentration dependence of wetting using the framework of electrowetting mechanism. Hydrophobic nanopores gated by salt concentration and voltage could become the basis for switches that control transport of water and all species dissolved in it. Such systems could find applications, for example, in drug-delivery systems and ionic circuits.

Appendix C: Supplementary Materials for Chapter 6

Modeling tables and figures used with permission from Fikret Aydin

Theoretical discussion used with permission from Pedro de Souza

Supplementary Text

Theoretical derivation of continuum electrowetting model

Defining model equations

As sketched in Figure 6.6a, the electrowetting model is based on computing the electrostatic potential profiles in the electrical double layers at the membrane electrolyte interfaces and in the membrane domain. In regions of the membrane where the hydrophobic side is dewetted (where a gas bubble is in contact with the hydrophobic side), the double layer is only present on the hydrophilic region to screen the surface charge of the hydrophilic side. On the other hand, in regions where the hydrophobic side is in contact with electrolyte solution, the double layers are present on both sides. Furthermore, when electrolyte is in contact with both sides of the membrane, the applied electrostatic field can polarize the membrane domain, impacting the electrostatic energy of the interface.

Here, in the electrolyte domains that are in contact with solid surfaces, we solve Poisson's equation:

$$\epsilon_w \frac{d^2\phi}{dx^2} = -\rho = \sum_i z_i F c_i \quad \begin{cases} x < -L, & \text{if hydrophobic side dewetted} \\ x < -L \text{ and } x > 0, & \text{if hydrophobic side wetted} \end{cases} \quad (C.1)$$

Here, ϵ_w is the dielectric constant of water, ϕ is the electrostatic potential, x is the spatial coordinate normal to the membrane surfaces, ρ is the volumetric charge density, z_i is the valency of ion i, F is the Faraday constant, c_i is the concentration of the species i, and L is the thickness of the membrane. In the membrane domains, we solve Laplace's equation (assuming the membrane is an ideal dielectric medium with constant membrane dielectric constant, ϵ_m).

$$\frac{d^2\phi}{dx^2} = 0, \quad -L \leq x \leq 0 \tag{C.2}$$

In each domain, we have assumed that the field only varies in the normal direction, valid far away from the bubble contact line and from the pore mouth opening.

Next, we outline the strategy to solve for the electrostatic and chemical energy in the double layers and membrane domain in order to predict the effective changes in the solid-liquid interfacial tension, $\Delta\gamma_{sl}$.

Following Ref. [233], we assume that the double layers are in equilibrium with the bulk solutions of fixed concentration, with ideal thermodynamics. On the hydrophilic side, the concentrations follow a Boltzmann distribution:

$$c_i = c_{i0} \exp\left(-\frac{z_i F(\phi - V_{\text{app}})}{RT}\right), \quad x < -L \tag{C.3}$$

and on the hydrophobic side, they follow a similar Boltzmann distribution with the bulk solution when the hydrophobic side is wetted:

$$c_i = c_{i0} \exp\left(-\frac{z_i F\phi}{RT}\right), \quad x > 0 \tag{C.4}$$

Here, c_{i0} is the bulk concentration of species i (equal to the bulk salt concentration, c_0, for the symmetric 1:1 solutions investigate here), R is the gas constant, and T is the absolute temperature. Such a double layer equilibrium assumption is only valid far from the pore opening, where the double layers are unperturbed by the applied currents. Realistically, the concentrations can be significantly perturbed from their bulk values near and within the pore mouth, but we neglect such effects in order to reduce the complexity of the model.

At the membrane interfaces, we enforce boundary conditions based on the amount of adsorbed surface charge. When the hydrophobic side is dewetted, the only boundary condition is:

$$\epsilon_w \frac{d\phi_w}{dx}(x = -L) = q_{s,\text{phil}} \qquad (C.5)$$

Since the field is not considered within the membrane domain when the hydrophobic side is dewetted. When the hydrophobic side is wetted, the boundary conditions at each interface are given by:

$$-\epsilon_m \frac{d\phi_m}{dx}(x = -L) + \epsilon_w \frac{d\phi_w}{dx}(x = -L) = q_{s,\text{phil}} \qquad (C.6)$$

$$\epsilon_m \frac{d\phi_m}{dx}(x = 0) - \epsilon_w \frac{d\phi_w}{dx}(x = 0) = q_{s,\text{phob}} \qquad (C.7)$$

The w subscript means that the electric field is evaluated on the electrolyte side of the interface, while the m subscript means that the electric field is evaluated on the membrane side of the interface. The surface charge per unit area on the hydrophilic side is $q_{s,\text{phil}}$, while that on the hydrophobic side is $q_{s,\text{phob}}$. Far away, the potential must match the applied potential in the bulk:

$$\phi(-\infty) = V_{\text{app}} \qquad (C.8)$$

$$\phi(\infty) = 0 \qquad (C.9)$$

While we assume the amount of surface charge is fixed on the hydrophilic side, we assume that the amount of surface charge on the hydrophobic side is dependent on the

local concentration of anion (either iodide or chloride) that adsorbs to the hydrophobic interface—a charge regulation boundary condition:

$$q_{s,\text{phob}} = -e\,N\,\alpha = -\frac{eNc_0 \exp\left[\frac{F\phi(x=0)}{RT}\right]}{c_0 \exp\left[\frac{F\phi(x=0)}{RT}\right] + K} \qquad (C.10)$$

In the above formula, e is the elementary charge, N is the number density of surface sites where anions can adsorb, α is the fraction of surface sites on which anions are adsorbed, and K is the equilibrium constant of anionic adsorption. At large concentrations of anions relative to the equilibrium constant, the surface charge saturates to a constant set by the number of surface sites:

$$q_{s,\text{phob}} = -e\,N \qquad (C.11)$$

For small potentials and adsorbed charge fractions, the surface charge is approximated by:

$$q_{s,\text{phob}} = -\frac{eNc_0}{K} \qquad (C.12)$$

We will return to the approximate values of the surface charge when approximating the contribution to the energy of the double layer in linear response.

While the system of differential equations is nonlinear and difficult to solve exactly, we can perform one analytical integration to derive algebraic equations relating the potential at the membrane interfaces to the surface charge densities (again following Ref. [233]):

$$\left(q_{s,phil} - Q\right)^2 = 4\epsilon_W RT c_0 \left(cosh\left(\frac{F\phi(x=0)}{RT}\right) - 1\right) \qquad (C.13)$$

$$\left(q_{s,\text{phob}} + Q\right)^2 = 4\epsilon_W RTc_0 \left(\cosh\left(\frac{F\left(\phi(x=-L) - V_{\text{app}}\right)}{RT}\right) - 1\right) \qquad (C.14)$$

$$Q = \frac{\epsilon_m}{L}\left(\phi(x=-L) - \phi(x=0)\right) \qquad (C.15)$$

These three Eqs. (C.13, C.14, and C.15) with an additional substitution from equation C.10 can be solved simultaneously for the three unknowns: $\phi(x=0), \phi(x=-L),$ and Q. The variable Q signifies the extent of polarization of the membrane domain and controls the coupling between the different sides of the membrane domain. When the hydrophobic side is dewetted, Q=0. As we will see in the following subsection, we can express the free energy of the double layers and membrane domain in terms of these unknowns, so we can reduce the complexity of the problem down to solving these three algebraic equations.

Defining the surface energy changes

So far, we have outlined the complete set of equations that can be systematically solved as a function of the membrane/electrolyte parameters to find the electrostatic potential at the membrane interfaces and the fraction of sites with adsorbed anions on the hydrophobic side. Now, we need to synthesize the information from the electrostatic model into a calculation of the free energy change due to anion adsorption, membrane polarization, and the free energy stored in the electrical double layers, where we will follow Ref. [231] with modifications to account for membrane polarization. From these free energy contributions, we can then make a prediction for the shift in the solid-liquid surface energy.

First, the chemical energy due to anion adsorption is given by:

182

$$F_{\mathrm{ads}} = Nk_B T \ln(1 - \alpha) \qquad (C.16)$$

where k_B is the Boltzmann constant. The free energy of the double layer on the hydrophobic side is:

$$F_{dl,\mathrm{phob}} = -16RTc_0\lambda_D \sinh^2\left(\frac{F\,\phi(x=0)}{4RT}\right) \qquad (C.17)$$

and the free energy on the hydrophilic side is:

$$F_{dl,\mathrm{phil}} = -16RTc_0\lambda_D \sinh^2\left(\frac{F\left(\phi(x=-L) - V_{\mathrm{app}}\right)}{4RT}\right) \qquad (C.18)$$

In the above equations, the parameter λ_D is the Debye length. The free energy of the membrane domain is:

$$F_{\mathrm{m}} = -\frac{\epsilon_m}{2L}\left(\phi(x=0) - \phi(x=-L)\right)^2 \qquad (C.19)$$

Now, we can synthesize the different free energy contributions of the double layer to predict the change in the apparent solid-liquid surface energy. Here, we assume that $\gamma_{sl}^{\mathrm{base}}$ is the solid-liquid surface tension of the hydrophobic side in the absence of applied voltage or anion adsorption. We calculate the shift in the apparent solid liquid surface tension on the hydrophobic side when there is nonzero membrane polarization and anion adsorption, $\Delta\gamma_{sl}$:

$$\gamma_{sl,\mathrm{phob}} = \gamma_{sl}^{\mathrm{base}} + \Delta\gamma_{sl} \qquad (C.20)$$

The quantity $\Delta\gamma_{sl}$ can be further decomposed into contributions from (i) the ionic adsorption, $\Delta\gamma_{sl,\mathrm{ads}}$ (ii) the double layers, $\Delta\gamma_{sl,\mathrm{dl}}$, and (iii) the membrane polarization $\Delta\gamma_{sl,\mathrm{m}}$.

From the definitions of the free energy, the ionic adsorption contribution is:

$$\Delta\gamma_{sl,\text{ads}} = F_{\text{ads}} \qquad (C.21)$$

The contribution from the double layers is:

$$\Delta\gamma_{sl,dl} = F_{dl,\text{phob}}^{\text{wetted}} + F_{dl,\text{phil}}^{\text{wetted}} - F_{dl,\text{phil}}^{\text{dewetted}} \qquad (C.22)$$

where we have set the reference free energy of the hydrophilic side to the free energy of the hydrophilic side with the hydrophobic side in the dewetted state. The contribution from the membrane polarization is:

$$\Delta\gamma_{sl,\text{m}} = F_{\text{m}} \qquad (C.23)$$

In generating Figure 6.6b–c, these contributions are computed numerically from the nonlinear equations and summed together to give $\Delta\gamma_{sl}$.

Approximating the contributions to solid-liquid interfacial energy

As explained in the previous chapter, we can generate useful formulas by assuming small potentials, low surface adsorption, and a weakly polarizable membrane. While these formulas do not accurately describe the full nonlinear solutions, they display the same qualitative trends, and allow for quick computations.

First, for anionic adsorption, starting from equation C.16, the chemical energy due to adsorption for small values of α is:

$$\Delta\gamma_{sl,ads} = -Nk_BT\alpha = -\frac{N\,k_BT\,c_0}{K} \qquad (C.24)$$

For the membrane domains, if there are only small perturbations in potential due to the double layers, then the membrane polarization is mainly attributable to the applied voltage:

$$\Delta \gamma_{sl,m} = -\frac{\epsilon_m}{2L} V_{\text{app}}^2 \qquad (C.25)$$

Finally, the double layer contribution from the hydrophilic side of the membrane will be zero under the simplifying assumptions, since due to the low polarizability of the membrane and the constant surface charge of the hydrophilic side, the double layer contribution from the hydrophilic side is identical whether the hydrophobic side is wetted or dewetted. The only contribution from the double layer will come from the hydrophobic side. There, the surface potential can be approximated as:

$$\phi(x = 0) = \zeta \approx \frac{-Nec_0\lambda_D}{K\epsilon_w} \qquad (C.26)$$

And assuming small potentials, the double layer contribution can be approximated from the expanded form of equation C.17 as:

$$\Delta \gamma_{sl,dl} = -\frac{\epsilon_w}{2\lambda_D} \zeta^2 = -\frac{N^2 e^2 c_0^2 \lambda_D}{2\epsilon_w K^2} \qquad (C.27)$$

Supplementary Tables

Table C.T1: Contact angle measurements on a flat silicon nitride surface before and after modification with 1H,1H,2H,2H-perfluorooctyltrichlorosilane. We estimate 10% error based on image processing for all angles.

Salt	Concentration (mM)	Clean SiN$_x$ contact angle (deg)	Hydrophobically modified SiN$_x$ contact angle (deg)
H$_2$O	-	62	110
KCl	1	72	120
	10	55	110
	100	68	111
	500	65	117
	1000	75	110
	2000	74	114
KI	1	67	117
	10	60	113
	100	61	103
	500	67	103
	1000	65	110
	2000	63	113

Table C.T2: Average number of ions near the water-vacuum interface in the pore before the pore is open. Results from molecular dynamics simulations.

	Negative E (1 M)	Positive E (1 M)
Chloride	0.64 ± 0.76	0.50 ± 0.64
Iodide	1.83 ± 1.19	1.29 ± 0.98

Supplementary Figures
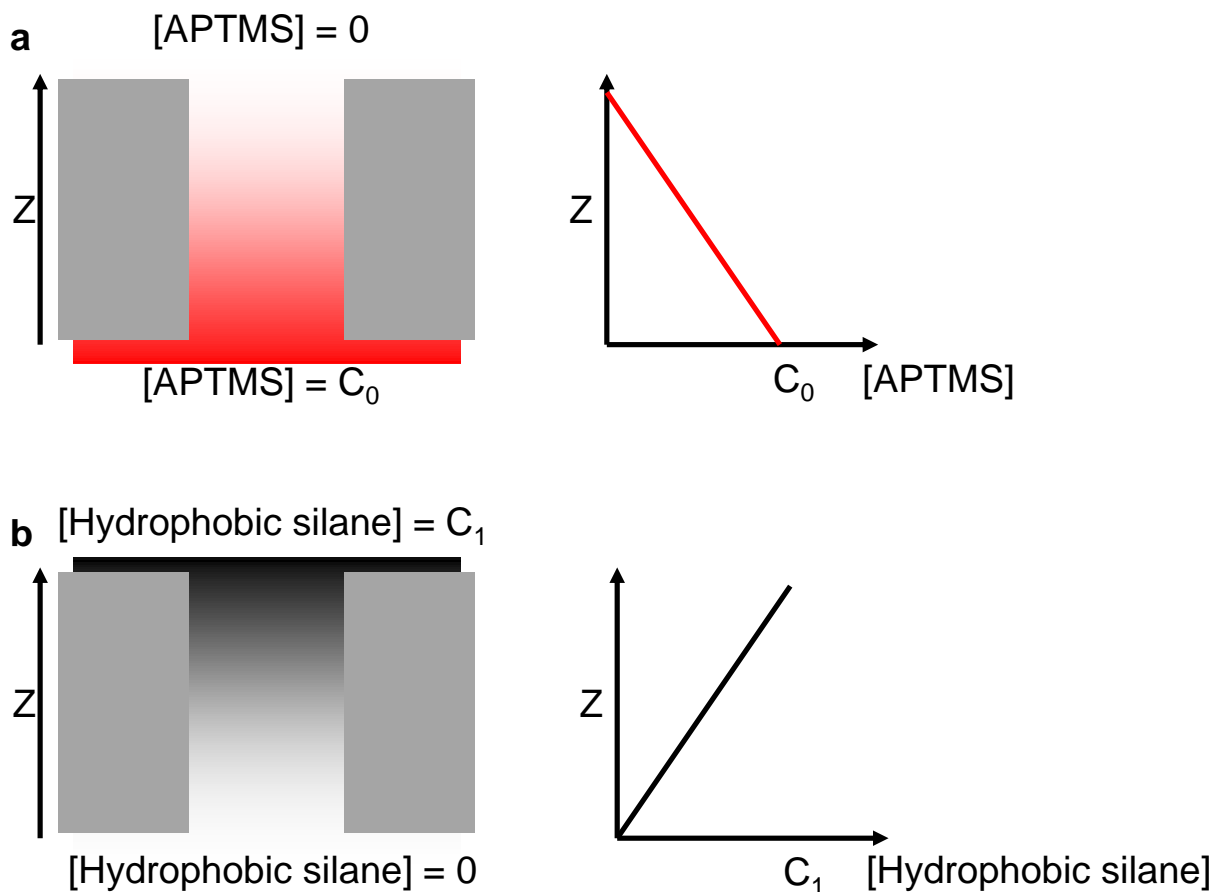
Figure C.1: Schemes of two asymmetric modifications used to prepare nanopores with a hydrophobic/hydrophilic junction. The two modifications were performed asymmetrically such that only one side of the pore was in contact with the silane solution, and the other one with a solvent. The shape of the pores is assumed cylindrical, consequently the concentration profiles of the two silanes in the pore are linear.[225] (a) The modification with APTMS was done first, with the APTMS solution placed at the bottom of the chip. (b) The second modification using 1*H*,1*H*,2*H*,2*H*-perfluorooctyltrichlorosilane was performed with the hydrophobic silane solution placed on top of the chip.
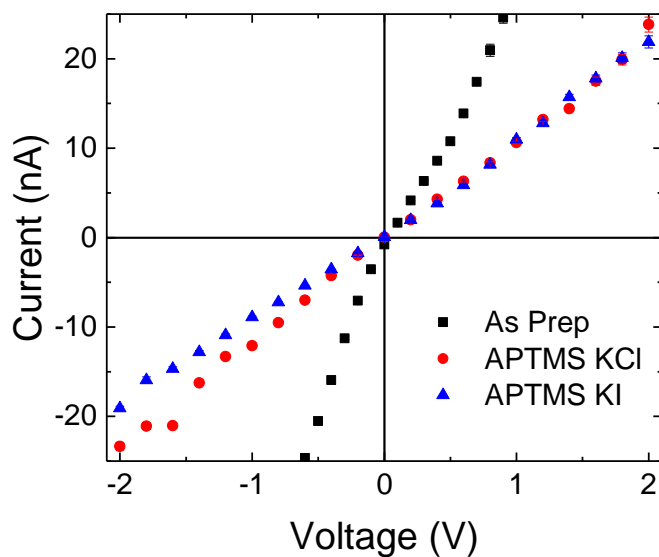
Figure C.2: Current-voltage curves of a 14 nm diameter pore as prepared (1 M KCl, black squares), and after symmetric modification with APTMS (1 M KCl in red circles, 1 M KI in blue triangles). The current-voltage curves were obtained by averaging ion current time series recorded at each voltage for 50 s. The error bars are standard deviations of current, also calculated from the time series data. The recordings allowed us to estimate the thickness of the attached APTMS to 3 nm.[189]
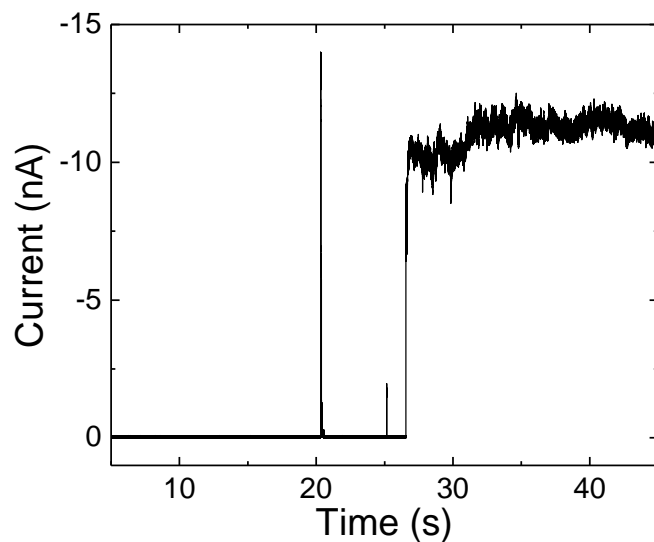
Figure C.3: Recording of ion current time series for the pore shown in Figure 6.3d for 500 mM KI at -1.8 V. This time series was recorded directly after the data in Figure 6.2 in Chapter 6. The pore opening probability for this voltage was 0.53.
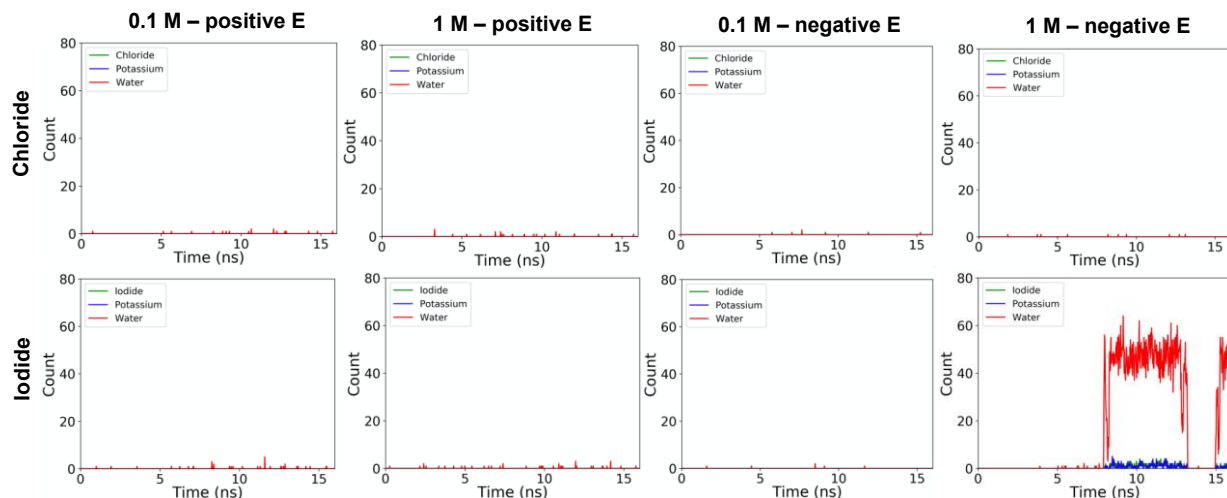
Figure C.4: Number of water molecules and ions inside the hydrophobic region of the pore as a function of time at different conditions (low and high concentration, ion type, different polarities of electric fields). The magnitude of electric field is of 0.008 V/Å at all conditions. The length of the hydrophobic region chosen for this analysis is 0.6 nm.
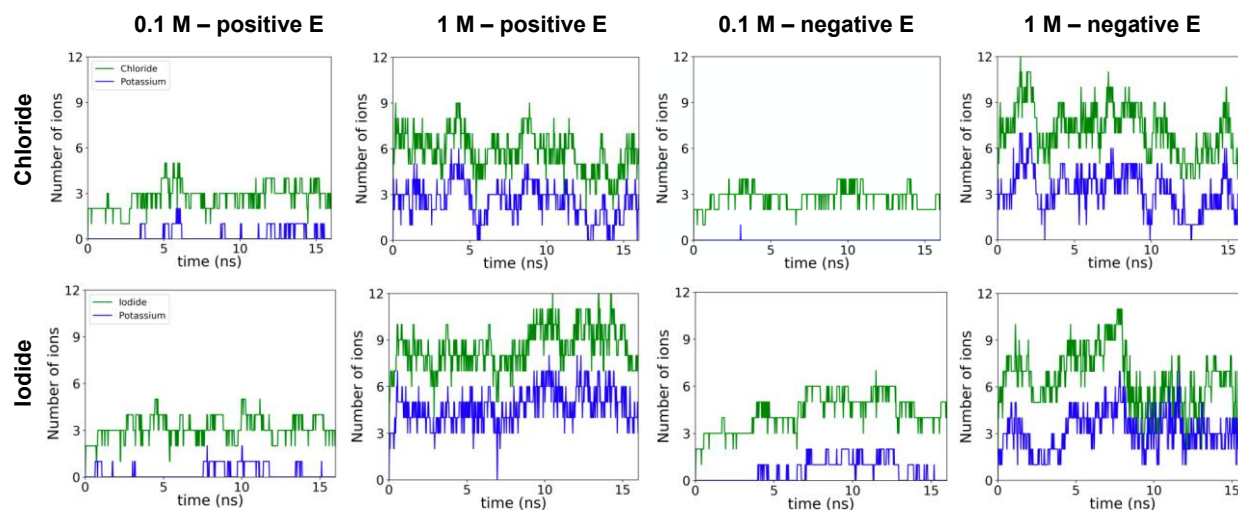
Figure C.5: Number of ions inside the hydrophilic region of the pore as a function of time at different conditions (low and high concentration, ion type, different polarities of electric fields). The magnitude of electric field is of 0.008 V/Å at all conditions. The length of the hydrophilic region chosen for this analysis is 1.5 nm.

189
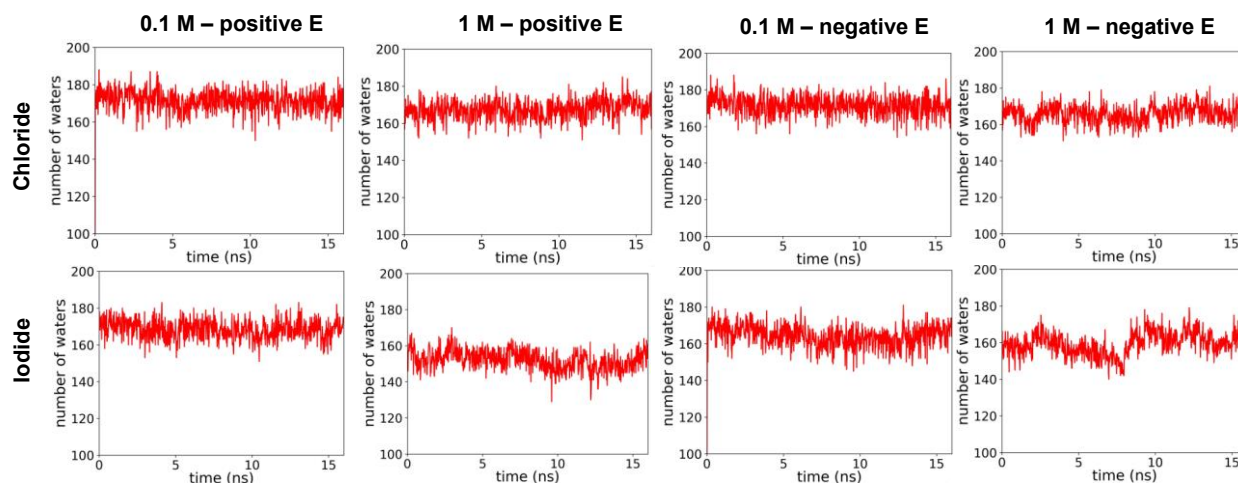
Figure C.6: Number of water molecules inside the hydrophilic region of the pore as a function of time at different conditions (low and high concentration, ion type, different polarities of electric fields). The magnitude of electric field is of 0.008 V/Å at all conditions. The length of the hydrophilic region chosen for this analysis is 1.5 nm.

Figure C.7: Simulation snapshots showing different stages of pore dewetting in 1 M KI salt solution at a negative electric field of 0.008 V/Å.

References

(1)   de Groot, B. L.; Grubmüller, H. Water Permeation Across Biological Membranes: Mechanism and Dynamics of Aquaporin-1 and GlpF. *Science* **2001**, *294* (5550), 2353. https://doi.org/10.1126/science.1066115.

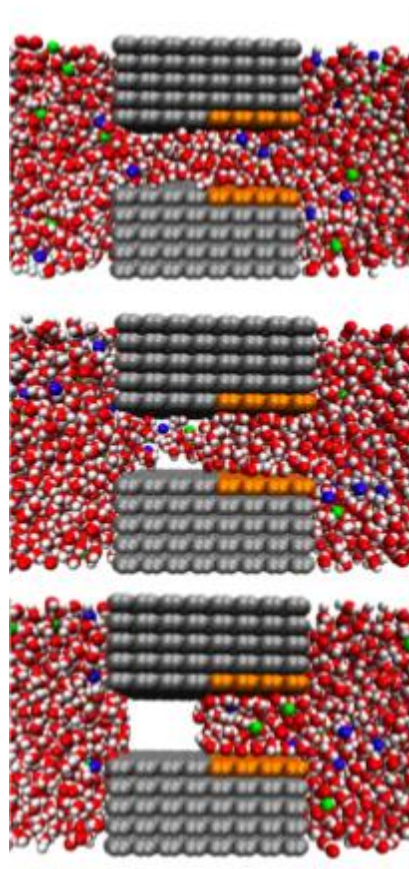(2)   Sui, H.; Han, B.-G.; Lee, J. K.; Walian, P.; Jap, B. K. Structural Basis of Water-Specific Transport through the AQP1 Water Channel. *Nature* **2001**, *414* (6866), 872–878. https://doi.org/10.1038/414872a.

(3)   Kuang, Q.; Purhonen, P.; Hebert, H. Structure of Potassium Channels. *Cell. Mol. Life Sci.* **2015**, *72*, 3677–3693. https://doi.org/10.1007/s00018-015-1948-5.

(4)   Doyle, D. A.; Cabral, J. M.; Pfuetzner, R. A.; Kuo, A.; Gulbis, J. M.; Cohen, S. L.; Chait, B. T.; MacKinnon, R. The Structure of the Potassium Channel: Molecular Basis of K^+ Conduction and Selectivity. *Science* **1998**, *280* (5360), 69. https://doi.org/10.1126/science.280.5360.69.

(5)   Naranjo, D.; Moldenhauer, H.; Pincuntureo, M.; Díaz-Franulic, I. Pore Size Matters for Potassium Channel Conductance. *J. Gen. Physiol.* **2016**, *148* (4), 277–291. https://doi.org/10.1085/jgp.201611625.

(6)   Perry, D.; Momotenko, D.; Lazenby, R. A.; Kang, M.; Unwin, P. R. Characterization of Nanopipettes. *Anal. Chem.* **2016**, *88* (10), 5523–5530. https://doi.org/10.1021/acs.analchem.6b01095.

(7)   Vlassiouk, I.; Apel, P. Y.; Dmitriev, S. N.; Healy, K.; Siwy, Z. S. Versatile Ultrathin Nanoporous Silicon Nitride Membranes. *Proc. Natl. Acad. Sci.* **2009**, *106* (50), 21039–21044. https://doi.org/10.1073/pnas.0911450106.

(8)   Alberts, B.; Johnson, A.; Lewis, J.; Martin, R.; Keith, R.; Peter, W. *Molecular Biology of the Cell*, 4th ed.; Garland Science: New York, 2002.

(9)   de Lera Ruiz, M.; Kraus, R. L. Voltage-Gated Sodium Channels: Structure, Function, Pharmacology, and Clinical Indications. *J. Med. Chem.* **2015**, *58* (18), 7093–7118. https://doi.org/10.1021/jm501981g.

(10)   Lirk, P.; Picardi, S.; Hollmann, M. W. Local Anaesthetics: 10 Essentials. *Eur. J. Anaesthesiol. EJA* **2014**, *31* (11).

(11)   Goetz, T.; Arslan, A.; Wisden, W.; Wulff, P. GABAA Receptors: Structure and Function in the Basal Ganglia. In *Progress in Brain Research*; Tepper, J. M., Abercrombie, E. D., Bolam, J. P., Eds.; Elsevier, 2007; Vol. 160, pp 21–41. https://doi.org/10.1016/S0079-6123(06)60003-4.

(12)   Olsen, R. W.; DeLorey, T. M. GABA Receptor Physiology and Pharmacology. In *Basic neurochemistry: molecular, cellular, and medical aspects*; Siegel, G. J., Agranoff, B., Albers, R. W., Fisher, S., Uhler, M., Eds.; Lippincott Williams & Wilkins: Philadelphia, 1999.

(13)   Ranade, S. S.; Syeda, R.; Patapoutian, A. Mechanically Activated Ion Channels. *Neuron* **2015**, *87* (6), 1162–1179. https://doi.org/10.1016/j.neuron.2015.08.032.

(14)   Beurg, M.; Fettiplace, R.; Nam, J.-H.; Ricci, A. J. Localization of Inner Hair Cell Mechanotransducer Channels Using High-Speed Calcium Imaging. *Nat. Neurosci.* **2009**, *12* (5), 553–558. https://doi.org/10.1038/nn.2295.

(15)   Hudspeth, A. J. Integrating the Active Process of Hair Cells with Cochlear Function. *Nat. Rev. Neurosci.* **2014**, *15* (9), 600–614. https://doi.org/10.1038/nrn3786.

(16)   Gore, R. W. Process for Producing Porous Products. US3953566A, April 27, 1976.

(17)   Salditt, F.; Hansen, W. L. Porous Adhesive Tape. US4112177A, September 5, 1978.

(18)   Čerović, L. S.; Milonjić, S. K.; Bahloul-Hourlier, D.; Doucey, B. Surface Properties of Silicon Nitride Powders. *Colloids Surf. Physicochem. Eng. Asp.* **2002**, *197* (1), 147–156. https://doi.org/10.1016/S0927-7757(01)00863-9.

(19)   Firnkes, M.; Pedone, D.; Knezevic, J.; Döblinger, M.; Rant, U. Electrically Facilitated Translocations of Proteins through Silicon Nitride Nanopores: Conjoint and Competitive Action of Diffusion, Electrophoresis, and Electroosmosis. *Nano Lett.* **2010**, *10* (6), 2162–2167. https://doi.org/10.1021/nl100861c.

(20)   Hoogerheide, D. P.; Garaj, S.; Golovchenko, J. A. Probing Surface Charge Fluctuations with Solid-State Nanopores. *Phys. Rev. Lett.* **2009**, *102* (25), 256804. https://doi.org/10.1103/PhysRevLett.102.256804.

(21)   Mikolajick, T.; Kühnhold, R.; Schnupp, R.; Ryssel, H. The Influence of Surface Oxidation on the PH-Sensing Properties of Silicon Nitride. *Sens. Actuators B Chem.* **1999**, *58* (1), 450–455. https://doi.org/10.1016/S0925-4005(99)00125-2.

(22)   Mezzasalma, S.; Baldovino, D. Characterization of Silicon Nitride Surface in Water and Acid Environment: A General Approach to the Colloidal Suspensions. *J. Colloid Interface Sci.* **1996**, *180* (2), 413–420. https://doi.org/10.1006/jcis.1996.0320.

(23)   Bousse, L.; Mostarshed, S. The Zeta Potential of Silicon Nitride Thin Films. *J. Electroanal. Chem. Interfacial Electrochem.* **1991**, *302* (1), 269–274. https://doi.org/10.1016/0022-0728(91)85046-R.

(24)   Bousse, L.; Hafeman, D.; Tran, N. Time-Dependence of the Chemical Response of Silicon Nitride Surfaces. *Sens. Actuators B Chem.* **1990**, *1* (1), 361–367. https://doi.org/10.1016/0925-4005(90)80231-N.

(25)   Bergström, L.; Bostedt, E. Surface Chemistry of Silicon Nitride Powders: Electrokinetic Behaviour and ESCA Studies. *Colloids Surf.* **1990**, *49*, 183–197. https://doi.org/10.1016/0166-6622(90)80101-9.

(26)   Harame, D. L.; Bousse, L. J.; Shott, J. D.; Meindl, J. D. Ion-Sensing Devices with Silicon Nitride and Borosilicate Glass Insulators. *IEEE Trans. Electron Devices* **1987**, *34* (8), 1700–1707. https://doi.org/10.1109/T-ED.1987.23140.

(27)   Tunuguntla, R. H.; Henley, R. Y.; Yao, Y.-C.; Pham, T. A.; Wanunu, M.; Noy, A. Enhanced Water Permeability and Tunable Ion Selectivity in Subnanometer Carbon Nanotube Porins. *Science* **2017**, *357* (6353), 792–796. https://doi.org/10.1126/science.aan2438.

(28)   Feng, J.; Graf, M.; Liu, K.; Ovchinnikov, D.; Dumcenco, D.; Heiranian, M.; Nandigana, V.; Aluru, N. R.; Kis, A.; Radenovic, A. Single-Layer MoS2 Nanopores as Nanopower Generators. *Nature* **2016**, *536* (7615), 197–200. https://doi.org/10.1038/nature18593.

(29)   Fischbein, M. D.; Drndić, M. Electron Beam Nanosculpting of Suspended Graphene Sheets. *Appl. Phys. Lett.* **2008**, *93* (11), 113107. https://doi.org/10.1063/1.2980518.

(30)   Merchant, C. A.; Healy, K.; Wanunu, M.; Ray, V.; Peterman, N.; Bartel, J.; Fischbein, M. D.; Venta, K.; Luo, Z.; Johnson, A. T. C.; Drndić, M. DNA

Translocation through Graphene Nanopores. *Nano Lett.* **2010**, *10* (8), 2915–2921. https://doi.org/10.1021/nl101046t.

(31)   Faucher, S.; Aluru, N.; Bazant, M. Z.; Blankschtein, D.; Brozena, A. H.; Cumings, J.; Pedro de Souza, J.; Elimelech, M.; Epsztein, R.; Fourkas, J. T.; Rajan, A. G.; Kulik, H. J.; Levy, A.; Majumdar, A.; Martin, C.; McEldrew, M.; Misra, R. P.; Noy, A.; Pham, T. A.; Reed, M.; Schwegler, E.; Siwy, Z.; Wang, Y.; Strano, M. Critical Knowledge Gaps in Mass Transport through Single-Digit Nanopores: A Review and Perspective. *J. Phys. Chem. C* **2019**, *123* (35), 21309–21326. https://doi.org/10.1021/acs.jpcc.9b02178.

(32)   Purves, R. D. The Mechanics of Pulling a Glass Micropipette. *Biophys. J.* **1980**, *29* (3), 523–529. https://doi.org/10.1016/S0006-3495(80)85150-2.

(33)   Gubbels, E.; Heitz, T.; Yamamoto, M.; Chilekar, V.; Zarbakhsh, S.; Gepraegs, M.; Köpnick, H.; Schmidt, M.; Brügging, W.; Rüter, J.; Kaminsky, W. Polyesters. In *Ullmann's Encyclopedia of Industrial Chemistry*; American Cancer Society, 2018; pp 1–30. https://doi.org/10.1002/14356007.a21_227.pub2.

(34)   Singh, A. Polycarbonate Synthesis. In *Encyclopedia of Polymeric Nanomaterials*; Kobayashi, S., Müllen, K., Eds.; Springer Berlin Heidelberg: Berlin, Heidelberg, 2014; pp 1–5. https://doi.org/10.1007/978-3-642-36199-9_419-1.

(35)   de Abajo, J.; de la Campa, J. G. Processable Aromatic Polyimides. In *Progress in Polyimide Chemistry I*; Kricheldorf, H. R., Ed.; Springer Berlin Heidelberg: Berlin, Heidelberg, 1999; pp 23–59. https://doi.org/10.1007/3-540-49815-X_2.

(36)   Meador, M. A. B.; Vivod, S. L. Polyimide Synthesis. In *Encyclopedia of Polymeric Nanomaterials*; Kobayashi, S., Müllen, K., Eds.; Springer Berlin Heidelberg: Berlin, Heidelberg, 2014; pp 1–11. https://doi.org/10.1007/978-3-642-36199-9_275-1.

(37)   Kaloyeros, A. E.; Jové, F. A.; Goff, J.; Arkles, B. Review—Silicon Nitride and Silicon Nitride-Rich Thin Film Technologies: Trends in Deposition Techniques and Related Applications. *ECS J. Solid State Sci. Technol.* **2017**, *6* (10), P691. https://doi.org/10.1149/2.0011710jss.

(38)   West, A. R. *Solid State Chemistry and Its Applications*, Second edition, student edition.; John Wiley & Sons, Inc: Chichester, West Sussex, 2014.

(39)   Chapter 6 - Thin Films on Silicon. In *Handbook of Silicon Based MEMS Materials and Technologies (Second Edition)*; Tilli, M., Motooka, T., Airaksinen, V.-M., Franssila, S., Paulasto-Kröckel, M., Lindroos, V., Eds.; William Andrew Publishing: Boston, 2015; pp 124–205. https://doi.org/10.1016/B978-0-323-29965-7.00006-3.

(40)   Duan, C.; Karnik, R.; Lu, M.-C.; Majumdar, A. Evaporation-Induced Cavitation in Nanofluidic Channels. *Proc. Natl. Acad. Sci.* **2012**, *109* (10), 3688. https://doi.org/10.1073/pnas.1014075109.

(41)   Kaya, D.; Keçeci, K. Review—Track-Etched Nanoporous Polymer Membranes as Sensors: A Review. *J. Electrochem. Soc.* **2020**, *167* (3), 037543. https://doi.org/10.1149/1945-7111/ab67a7.

(42)   Howorka, S.; Siwy, Z. Nanopore Analytics: Sensing of Single Molecules. *Chem. Soc. Rev.* **2009**, *38* (8), 2360–2384. https://doi.org/10.1039/B813796J.

(43) DeSorbo, W. Ultraviolet Effects and Aging Effects on Etching Characteristics of Fission Tracks in Polycarbonate Film. *Nucl. Tracks* **1979**, *3* (1), 13–32. https://doi.org/10.1016/0191-278X(79)90026-X.

(44) Williams, D. B.; Carter, C. B. *Transmission Electron Microscopy: A Textbook for Materials Science*, 2. ed.; Springer: New York, 2009.

(45) Das, K.; Freund, J. B.; Johnson, H. T. Mechanisms of Material Removal and Mass Transport in Focused Ion Beam Nanopore Formation. *J. Appl. Phys.* **2015**, *117* (8), 085304. https://doi.org/10.1063/1.4913449.

(46) Giannuzzi, L. A.; Stevie, F. A. A Review of Focused Ion Beam Milling Techniques for TEM Specimen Preparation. *Micron* **1999**, *30* (3), 197–204. https://doi.org/10.1016/S0968-4328(99)00005-0.

(47) Prabhu, A. S.; Freedman, K. J.; Robertson, J. W. F.; Nikolov, Z.; Kasianowicz, J. J.; Kim, M. J. SEM-Induced Shrinking of Solid-State Nanopores for Single Molecule Detection. *Nanotechnology* **2011**, *22* (42), 425302. https://doi.org/10.1088/0957-4484/22/42/425302.

(48) Kwok, H.; Briggs, K.; Tabard-Cossa, V. Nanopore Fabrication by Controlled Dielectric Breakdown. *PLOS ONE* **2014**, *9* (3), e92880. https://doi.org/10.1371/journal.pone.0092880.

(49) Siwy, Z.; Dobrev, D.; Neumann, R.; Trautmann, C.; Voss, K. Electro-Responsive Asymmetric Nanopores in Polyimide with Stable Ion-Current Signal. *Appl. Phys. A* **2003**, *76* (5), 781–785. https://doi.org/10.1007/s00339-002-1982-7.

(50) Vernon-Parry, K. D. Scanning Electron Microscopy: An Introduction. *III-Vs Rev.* **2000**, *13* (4), 40–44. https://doi.org/10.1016/S0961-1290(00)80006-X.

(51) Orelovitch, O. L.; Apel, P. Y.; Sartowska, B. Preparation of Porous Polymer Samples for SEM: Combination of Photo Oxidation Degradation with a Freeze Fracture Technique. *Mater. Chem. Phys.* **2003**, *81* (2), 349–351. https://doi.org/10.1016/S0254-0584(03)00019-1.

(52) Apel, P. Y.; Blonskaya, I. V.; Dmitriev, S. N.; Orelovitch, O. L.; Presz, A.; Sartowska, B. A. Fabrication of Nanopores in Polymer Foils with Surfactant-Controlled Longitudinal Profiles. *Nanotechnology* **2007**, *18* (30), 305302. https://doi.org/10.1088/0957-4484/18/30/305302.

(53) T. E. Gomez Alvarez-Arenas; P. Y. Apel; O. Orelovitch. Ultrasound Attenuation in Cylindrical Micro-Pores: Nondestructive Porometry of Ion-Track Membranes. *IEEE Trans. Ultrason. Ferroelectr. Freq. Control* **2008**, *55* (11), 2442–2449. https://doi.org/10.1109/TUFFC.951.

(54) Kalman, E. B. Controlling Ionic Transport for Device Design in Synthetic Nanopores, University of California Irvine, 2010.

(55) Liebes, Y.; Drozdov, M.; Avital, Y. Y.; Kauffmann, Y.; Rapaport, H.; Kaplan, W. D.; Ashkenasy, N. Reconstructing Solid State Nanopore Shape from Electrical Measurements. *Appl. Phys. Lett.* **2010**, *97* (22), 223105. https://doi.org/10.1063/1.3521411.

(56) Romano, J. D.; Price, R. H. The Conical Resistor Conundrum: A Potential Solution. *Am. J. Phys.* **1996**, *64* (9), 1150–1153. https://doi.org/10.1119/1.18335.

(57) Hall, J. E. Access Resistance of a Small Circular Pore. *J. Gen. Physiol.* **1975**, *66* (4), 531. https://doi.org/10.1085/jgp.66.4.531.

(58) Vodyanoy, I.; Bezrukov, S. M. Sizing of an Ion Pore by Access Resistance Measurements. *Biophys. J.* **1992**, *62* (1), 10–11. https://doi.org/10.1016/S0006-3495(92)81762-9.

(59) Kowalczyk, S. W.; Grosberg, A. Y.; Rabin, Y.; Dekker, C. Modeling the Conductance and DNA Blockade of Solid-State Nanopores. *Nanotechnology* **2011**, *22* (31), 315101. https://doi.org/10.1088/0957-4484/22/31/315101.

(60) Wade, L. G. *Organic Chemistry*, 8th ed.; Pearson: Boston, 2013.

(61) Decher Gero. Fuzzy Nanoassemblies: Toward Layered Polymeric Multicomposites. *Science* **1997**, *277* (5330), 1232–1237. https://doi.org/10.1126/science.277.5330.1232.

(62) Pape, P. G. 29 - Adhesion Promoters: Silane Coupling Agents. In *Applied Plastics Engineering Handbook*; Kutz, M., Ed.; William Andrew Publishing: Oxford, 2011; pp 503–517. https://doi.org/10.1016/B978-1-4377-3514-7.10029-7.

(63) Fischer, M. J. E. Amine Coupling Through EDC/NHS: A Practical Approach. In *Surface Plasmon Resonance: Methods and Protocols*; Mol, N. J., Fischer, M. J. E., Eds.; Humana Press: Totowa, NJ, 2010; pp 55–73. https://doi.org/10.1007/978-1-60761-670-2_3.

(64) Hermanson, G. T. *Bioconjugate Techniques*, Third edition.; Elsevier/AP: London ; Waltham, MA, 2013.

(65) Acar, E. T.; Buchsbaum, S. F.; Combs, C.; Fornasiero, F.; Siwy, Z. S. Biomimetic Potassium-Selective Nanopores. *Sci. Adv.* **2019**, *5* (2), eaav2568. https://doi.org/10.1126/sciadv.aav2568.

(66) Pérez-Mitta, G.; Toimil-Molares, M. E.; Trautmann, C.; Marmisollé, W. A.; Azzaroni, O. Molecular Design of Solid-State Nanopores: Fundamental Concepts and Applications. *Adv. Mater.* **2019**, *31* (37), 1901483. https://doi.org/10.1002/adma.201901483.

(67) Schoch, R. B.; Han, J.; Renaud, P. Transport Phenomena in Nanofluidics. *Rev. Mod. Phys.* **2008**, *80* (3), 839–883. https://doi.org/10.1103/RevModPhys.80.839.

(68) Probstein, R. F. *Physicochemical Hydrodynamics: An Introduction*; Wiley: New York, 2005.

(69) Vlassiouk, I.; Smirnov, S.; Siwy, Z. Nanofluidic Ionic Diodes. Comparison of Analytical and Numerical Solutions. *ACS Nano* **2008**, *2* (8), 1589–1602. https://doi.org/10.1021/nn800306u.

(70) *CRC Handbook of Chemistry and Physics*, 102nd Edition (Internet Version 2021).; Rumble, J. R., Ed.; CRC Press/Taylor & Francis: Boca Raton, FL, 2021.

(71) Xue, J. M.; Zou, X. Q.; Xie, Y. B.; Wang, Y. G. Molecular Dynamics Simulations on the Ionic Current through Charged Nanopores. *J. Phys. Appl. Phys.* **2009**, *42* (10), 105308. https://doi.org/10.1088/0022-3727/42/10/105308.

(72) Vlassiouk, I.; Siwy, Z. S. Nanofluidic Diode. *Nano Lett.* **2007**, *7* (3), 552–556. https://doi.org/10.1021/nl062924b.

(73) Daiguji, H. Ion Transport in Nanofluidic Channels. *Chem. Soc. Rev.* **2010**, *39* (3), 901–911. https://doi.org/10.1039/B820556F.

(74) Israelachvili, J. N. *Intermolecular and Surface Forces*, 3rd ed.; Academic Press: Burlington, MA, 2011.

(75) Honig, B.; Nicholls, A. Classical Electrostatics in Biology and Chemistry. *Science* **1995**, *268* (5214), 1144–1149. https://doi.org/10.1126/science.7761829.

(76) Vlassiouk, I.; Smirnov, S.; Siwy, Z. Ionic Selectivity of Single Nanochannels. *Nano Lett.* **2008**, *8* (7), 1978–1985. https://doi.org/10.1021/nl800949k.

(77) White, H. S.; Bund, A. Ion Current Rectification at Nanopores in Glass Membranes. *Langmuir ACS J. Surf. Colloids* **2008**, *24* (5), 2212–2218. https://doi.org/10.1021/la702955k.

(78) Cervera, J.; Schiedt, B.; Ramírez, P. A Poisson/Nernst-Planck Model for Ionic Transport through Synthetic Conical Nanopores. *Europhys. Lett.* **2005**, *71* (1), 35–41. https://doi.org/10.1209/epl/i2005-10054-x.

(79) Siwy, Z. S.; Howorka, S. Engineered Voltage-Responsive Nanopores. *Chem. Soc. Rev.* **2010**, *39* (3), 1115–1132. https://doi.org/10.1039/B909105J.

(80) Baker, R. W. *Membrane Technology and Applications*, 3rd ed.; John Wiley & Sons: Chichester, West Sussex ; Hoboken, 2012.

(81) Sata, T. *Ion Exchange Membranes: Preparation, Characterization, Modification and Application*; Royal Society of Chemistry: Cambridge, 2004.

(82) Mehta, A.; Zydney, A. L. Permeability and Selectivity Analysis for Ultrafiltration Membranes. *J. Membr. Sci.* **2005**, *249* (1), 245–249. https://doi.org/10.1016/j.memsci.2004.09.040.

(83) Poonam; Sharma, K.; Arora, A.; Tripathi, S. K. Review of Supercapacitors: Materials and Devices. *J. Energy Storage* **2019**, *21*, 801–825. https://doi.org/10.1016/j.est.2019.01.010.

(84) Bu, F.; Zhou, W.; Xu, Y.; Du, Y.; Guan, C.; Huang, W. Recent Developments of Advanced Micro-Supercapacitors: Design, Fabrication and Applications. *Npj Flex. Electron.* **2020**, *4* (1), 31. https://doi.org/10.1038/s41528-020-00093-6.

(85) Munje, R. D.; Muthukumar, S.; Panneer Selvam, A.; Prasad, S. Flexible Nanoporous Tunable Electrical Double Layer Biosensors for Sweat Diagnostics. *Sci. Rep.* **2015**, *5* (1), 14586. https://doi.org/10.1038/srep14586.

(86) Smeets, R. M. M.; Keyser, U. F.; Krapf, D.; Wu, M.-Y.; Dekker, N. H.; Dekker, C. Salt Dependence of Ion Transport and DNA Translocation through Solid-State Nanopores. *Nano Lett.* **2006**, *6* (1), 89–95. https://doi.org/10.1021/nl052107w.

(87) Roberts, D.; Keeling, R.; Tracka, M.; van der Walle, C. F.; Uddin, S.; Warwicker, J.; Curtis, R. The Role of Electrostatics in Protein–Protein Interactions of a Monoclonal Antibody. *Mol. Pharm.* **2014**, *11* (7), 2475–2489. https://doi.org/10.1021/mp5002334.

(88) Zhang, J.; Liu, X. Y. Effect of Protein–Protein Interactions on Protein Aggregation Kinetics. *J. Chem. Phys.* **2003**, *119* (20), 10972–10976. https://doi.org/10.1063/1.1622380.

(89) Macdonald, R. C.; Bangham, A. D. Comparison of Double Layer Potentials in Lipid Monolayers and Lipid Bilayer Membranes. *J. Membr. Biol.* **1972**, *7* (1), 29–53. https://doi.org/10.1007/BF01867908.

(90) Sinha, S.; Sachar, H. S.; Das, S. Effect of Plasma Membrane Semipermeability in Making the Membrane Electric Double Layer Capacitances Significant. *Langmuir* **2018**, *34* (4), 1760–1766. https://doi.org/10.1021/acs.langmuir.7b02939.

(91) Fenter, P.; Lee, S. S. Hydration Layer Structure at Solid–Water Interfaces. *MRS Bull.* **2014**, *39* (12), 1056–1061. https://doi.org/10.1557/mrs.2014.252.

(92) Joseph, S.; Aluru, N. R. Hierarchical Multiscale Simulation of Electrokinetic Transport in Silica Nanochannels at the Point of Zero Charge. *Langmuir* **2006**, *22* (21), 9041–9051. https://doi.org/10.1021/la0610147.

(93) Tuladhar, A.; Dewan, S.; Pezzotti, S.; Brigiano, F. S.; Creazzo, F.; Gaigeot, M.-P.; Borguet, E. Ions Tune Interfacial Water Structure and Modulate Hydrophobic Interactions at Silica Surfaces. *J. Am. Chem. Soc.* **2020**, *142* (15), 6991–7000. https://doi.org/10.1021/jacs.9b13273.

(94) Rehl, B.; Gibbs, J. M. Role of Ions on the Surface-Bound Water Structure at the Silica/Water Interface: Identifying the Spectral Signature of Stability. *J. Phys. Chem. Lett.* **2021**, *12* (11), 2854–2864. https://doi.org/10.1021/acs.jpclett.0c03565.

(95) Yang, Z.; Li, Q.; Chou, K. C. Structures of Water Molecules at the Interfaces of Aqueous Salt Solutions and Silica: Cation Effects. *J. Phys. Chem. C* **2009**, *113* (19), 8201–8205. https://doi.org/10.1021/jp811517p.

(96) Trasatti, S. Relative and Absolute Electrochemical Quantities. Components of the Potential Difference across the Electrode/Solution Interface. *J. Chem. Soc. Faraday Trans. 1 Phys. Chem. Condens. Phases* **1974**, *70* (0), 1752–1768. https://doi.org/10.1039/F19747001752.

(97) Habib, M. A. Solvent Dipoles at the Electrode-Solution Interface. In *Modern Aspects of Electrochemistry: No. 12*; Bockris, J. O., Conway, B. E., Eds.; Springer US: Boston, MA, 1977; pp 131–182. https://doi.org/10.1007/978-1-4615-7452-1_3.

(98) Berne, B. J.; Fourkas, J. T.; Walker, R. A.; Weeks, J. D. Nitriles at Silica Interfaces Resemble Supported Lipid Bilayers. *Acc. Chem. Res.* **2016**, *49* (9), 1605–1613. https://doi.org/10.1021/acs.accounts.6b00169.

(99) Ding, F.; Hu, Z.; Zhong, Q.; Manfred, K.; Gattass, R. R.; Brindza, M. R.; Fourkas, J. T.; Walker, R. A.; Weeks, J. D. Interfacial Organization of Acetonitrile: Simulation and Experiment. *J. Phys. Chem. C* **2010**, *114* (41), 17651–17659. https://doi.org/10.1021/jp104597z.

(100) Morales, C. M.; Thompson, W. H. Simulations of Infrared Spectra of Nanoconfined Liquids: Acetonitrile Confined in Nanoscale, Hydrophilic Silica Pores. *J. Phys. Chem. A* **2009**, *113* (10), 1922–1933. https://doi.org/10.1021/jp8072969.

(101) Cheng, L.; Morrone, J. A.; Berne, B. J. Structure and Dynamics of Acetonitrile Confined in a Silica Nanopore. *J. Phys. Chem. C* **2012**, *116* (17), 9582–9593. https://doi.org/10.1021/jp301007k.

(102) Alston Steiner, P.; Gordy, W. Precision Measurement of Dipole Moments and Other Spectral Constants of Normal and Deuterated Methyl Fluoride and Methyl Cyanide. *J. Mol. Spectrosc.* **1966**, *21* (1), 291–301. https://doi.org/10.1016/0022-2852(66)90152-4.

(103) Melnikov, S. M.; Höltzel, A.; Seidel-Morgenstern, A.; Tallarek, U. Composition, Structure, and Mobility of Water−Acetonitrile Mixtures in a Silica Nanopore Studied by Molecular Dynamics Simulations. *Anal. Chem.* **2011**, *83* (7), 2569–2575. https://doi.org/10.1021/ac102847m.

(104) Mountain, R. D. Molecular Dynamics Simulation of Water–Acetonitrile Mixtures in a Silica Slit. *J. Phys. Chem. C* **2013**, *117* (8), 3923–3929. https://doi.org/10.1021/jp3083562.

(105) Rivera, C. A.; Bender, J. S.; Manfred, K.; Fourkas, J. T. Persistence of Acetonitrile Bilayers at the Interface of Acetonitrile/Water Mixtures with Silica. *J. Phys. Chem. A* **2013**, *117* (46), 12060–12066. https://doi.org/10.1021/jp4045572.

(106) Plett, T.; Shi, W.; Zeng, Y.; Mann, W.; Vlassiouk, I.; Baker, L. A.; Siwy, Z. S. Rectification of Nanopores in Aprotic Solvents – Transport Properties of Nanopores with Surface Dipoles. *Nanoscale* **2015**, *7* (45), 19080–19091. https://doi.org/10.1039/C5NR06340J.

(107) Lucas, R. A.; Lin, C.-Y.; Siwy, Z. S. Electrokinetic Phenomena in Organic Solvents. *J. Phys. Chem. B* **2019**, *123* (28), 6123–6131. https://doi.org/10.1021/acs.jpcb.9b04969.

(108) Souna, A. J.; Bender, J. S.; Fourkas, J. T. How Clean Is the Solvent You Use to Clean Your Optics? A Vibrational Sum-Frequency-Generation Study. *Appl. Opt.* **2017**, *56* (13), 3875–3878. https://doi.org/10.1364/AO.56.003875.

(109) Abraham, M. J.; Murtola, T.; Schulz, R.; Páll, S.; Smith, J. C.; Hess, B.; Lindahl, E. GROMACS: High Performance Molecular Simulations through Multi-Level Parallelism from Laptops to Supercomputers. *SoftwareX* **2015**, *1–2*, 19–25. https://doi.org/10.1016/j.softx.2015.06.001.

(110) Nosé, S. A Unified Formulation of the Constant Temperature Molecular Dynamics Methods. *J. Chem. Phys.* **1984**, *81* (1), 511–519. https://doi.org/10.1063/1.447334.

(111) Parrinello, M.; Rahman, A. Polymorphic Transitions in Single Crystals: A New Molecular Dynamics Method. *J. Appl. Phys.* **1981**, *52* (12), 7182–7190. https://doi.org/10.1063/1.328693.

(112) Chialvo, A. A.; Cummings, P. T. Molecular-Based Modeling of Water and Aqueous Solutions at Supercritical Conditions. In *Advances in Chemical Physics*; John Wiley & Sons, Ltd, 1999; pp 115–205. https://doi.org/10.1002/9780470141687.ch3.

(113) Essmann, U.; Perera, L.; Berkowitz, M. L.; Darden, T.; Lee, H.; Pedersen, L. G. A Smooth Particle Mesh Ewald Method. *J. Chem. Phys.* **1995**, *103* (19), 8577–8593. https://doi.org/10.1063/1.470117.

(114) Sambasivarao, S. V.; Acevedo, O. Development of OPLS-AA Force Field Parameters for 68 Unique Ionic Liquids. *J. Chem. Theory Comput.* **2009**, *5* (4), 1038–1050. https://doi.org/10.1021/ct900009a.

(115) Doherty, B.; Zhong, X.; Gathiaka, S.; Li, B.; Acevedo, O. Revisiting OPLS Force Field Parameters for Ionic Liquid Simulations. *J. Chem. Theory Comput.* **2017**, *13* (12), 6131–6145. https://doi.org/10.1021/acs.jctc.7b00520.

(116) Nikitin, A. M.; Lyubartsev, A. P. New Six-Site Acetonitrile Model for Simulations of Liquid Acetonitrile and Its Aqueous Mixtures. *J. Comput. Chem.* **2007**, *28* (12), 2020–2026. https://doi.org/10.1002/jcc.20721.

(117) Lee, S. H.; Rossky, P. J. A Comparison of the Structure and Dynamics of Liquid Water at Hydrophobic and Hydrophilic Surfaces—a Molecular Dynamics Simulation Study. *J. Chem. Phys.* **1994**, *100* (4), 3334–3345. https://doi.org/10.1063/1.466425.

(118) Yeh, I.-C.; Berkowitz, M. L. Ewald Summation for Systems with Slab Geometry. *J. Chem. Phys.* **1999**, *111* (7), 3155–3162. https://doi.org/10.1063/1.479595.

(119) Qiu, Y.; Lucas, R. A.; Siwy, Z. S. Viscosity and Conductivity Tunable Diode-like Behavior for Meso- and Micropores. *J. Phys. Chem. Lett.* **2017**, *8* (16), 3846–3852. https://doi.org/10.1021/acs.jpclett.7b01804.

(120) Wei, C.; Bard, A. J.; Feldberg, S. W. Current Rectification at Quartz Nanopipet Electrodes. *Anal. Chem.* **1997**, *69* (22), 4627–4633. https://doi.org/10.1021/ac970551g.

(121) Belaya, M.; Levadny, V.; Pink, D. A. Electric Double Layer near Soft Permeable Interfaces. 1. Local Electrostatic. *Langmuir* **1994**, *10* (6), 2010–2014. https://doi.org/10.1021/la00018a061.

(122) Buck, M.; Himmelhaus, M. Vibrational Spectroscopy of Interfaces by Infrared–Visible Sum Frequency Generation. *J. Vac. Sci. Technol. A* **2001**, *19* (6), 2717–2736. https://doi.org/10.1116/1.1414120.

(123) Richmond, G. L. Molecular Bonding and Interactions at Aqueous Surfaces as Probed by Vibrational Sum Frequency Spectroscopy. *Chem. Rev.* **2002**, *102* (8), 2693–2724. https://doi.org/10.1021/cr0006876.

(124) Vidal, F.; Tadjeddine, A. Sum-Frequency Generation Spectroscopy of Interfaces. *Rep. Prog. Phys.* **2005**, *68* (5), 1095–1127. https://doi.org/10.1088/0034-4885/68/5/r03.

(125) Butcher, P. N.; Cotter, D. *The Elements of Nonlinear Optics*; Cambridge University Press: Cambridge; New York, 1990.

(126) Loughnane, B. J.; Farrer, R. A.; Scodinu, A.; Fourkas, J. T. Dynamics of a Wetting Liquid in Nanopores: An Optical Kerr Effect Study of the Dynamics of Acetonitrile Confined in Sol-Gel Glasses. *J. Chem. Phys.* **1999**, *111* (11), 5116–5123. https://doi.org/10.1063/1.479768.

(127) Le Questel, J.-Y.; Berthelot, M.; Laurence, C. Hydrogen-Bond Acceptor Properties of Nitriles: A Combined Crystallographic and Ab Initio Theoretical Investigation. *J. Phys. Org. Chem.* **2000**, *13* (6), 347–358. https://doi.org/10.1002/1099-1395(200006)13:6<347::AID-POC251>3.0.CO;2-E.

(128) Herzberg, G. *Molecular Spectra and Molecular Structure. Vol.3: Electronic Spectra and Electronic Structure of Polyatomic Molecules*; Van Nostrand Reinhold, 1966.

(129) Andrews, S. S.; Boxer, S. G. Vibrational Stark Effects of Nitriles I. Methods and Experimental Results. *J. Phys. Chem. A* **2000**, *104* (51), 11853–11863. https://doi.org/10.1021/jp002242r.

(130) Hu, Z.; Weeks, J. D. Acetonitrile on Silica Surfaces and at Its Liquid−Vapor Interface: Structural Correlations and Collective Dynamics. *J. Phys. Chem. C* **2010**, *114* (22), 10202–10211. https://doi.org/10.1021/jp100350y.

(131) Gragson, D. E.; McCarty, B. M.; Richmond, G. L. Ordering of Interfacial Water Molecules at the Charged Air/Water Interface Observed by Vibrational Sum Frequency Generation. *J. Am. Chem. Soc.* **1997**, *119* (26), 6144–6152. https://doi.org/10.1021/ja962277y.

(132) Gonella, G.; Lütgebaucks, C.; de Beer, A. G. F.; Roke, S. Second Harmonic and Sum-Frequency Generation from Aqueous Interfaces Is Modulated by

Interference. *J. Phys. Chem. C* **2016**, *120* (17), 9165–9173. https://doi.org/10.1021/acs.jpcc.5b12453.

(133) Jena, K. C.; Covert, P. A.; Hore, D. K. The Effect of Salt on the Water Structure at a Charged Solid Surface: Differentiating Second- and Third-Order Nonlinear Contributions. *J. Phys. Chem. Lett.* **2011**, *2* (9), 1056–1061. https://doi.org/10.1021/jz200251h.

(134) Ohno, P. E.; Wang, H.; Geiger, F. M. Second-Order Spectral Lineshapes from Charged Interfaces. *Nat. Commun.* **2017**, *8* (1), 1032. https://doi.org/10.1038/s41467-017-01088-0.

(135) Seo, D. M.; Borodin, O.; Balogh, D.; O'Connell, M.; Ly, Q.; Han, S.-D.; Passerini, S.; Henderson, W. A. Electrolyte Solvation and Ionic Association III. Acetonitrile-Lithium Salt Mixtures–Transport Properties. *J. Electrochem. Soc.* **2013**, *160* (8), A1061–A1070. https://doi.org/10.1149/2.018308jes.

(136) Abrashkin, A.; Andelman, D.; Orland, H. Dipolar Poisson-Boltzmann Equation: Ions and Dipoles Close to Charge Interfaces. *Phys. Rev. Lett.* **2007**, *99* (7), 077801. https://doi.org/10.1103/PhysRevLett.99.077801.

(137) Vangara, R.; van Swol, F.; Petsev, D. N. Ionic Solvation and Solvent-Solvent Interaction Effects on the Charge and Potential Distributions in Electric Double Layers. *J. Chem. Phys.* **2017**, *147* (21), 214704. https://doi.org/10.1063/1.5005060.

(138) Henderson, D.; Jiang, D.; Jin, Z.; Wu, J. Application of Density Functional Theory To Study the Double Layer of an Electrolyte with an Explicit Dimer Model for the Solvent. *J. Phys. Chem. B* **2012**, *116* (36), 11356–11361. https://doi.org/10.1021/jp305400z.

(139) Fleharty, M. E.; van Swol, F.; Petsev, D. N. Solvent Role in the Formation of Electric Double Layers with Surface Charge Regulation: A Bystander or a Key Participant? *Phys. Rev. Lett.* **2016**, *116* (4), 048301. https://doi.org/10.1103/PhysRevLett.116.048301.

(140) Gupta, A.; Govind Rajan, A.; Carter, E. A.; Stone, H. A. Ionic Layering and Overcharging in Electrical Double Layers in a Poisson-Boltzmann Model. *Phys. Rev. Lett.* **2020**, *125* (18), 188004. https://doi.org/10.1103/PhysRevLett.125.188004.

(141) Ma, E.; Geiger, F. M. Divalent Ion Specific Outcomes on Stern Layer Structure and Total Surface Potential at the Silica:Water Interface. *J. Phys. Chem. A* **2021**, *125* (46), 10079–10088. https://doi.org/10.1021/acs.jpca.1c08143.

(142) Ma, E.; Ohno, P. E.; Kim, J.; Liu, Y.; Lozier, E. H.; Miller, T. F.; Wang, H.-F.; Geiger, F. M. A New Imaginary Term in the Second-Order Nonlinear Susceptibility from Charged Interfaces. *J. Phys. Chem. Lett.* **2021**, *12* (24), 5649–5659. https://doi.org/10.1021/acs.jpclett.1c01103.

(143) Kosmulski, M. PH-Dependent Surface Charging and Points of Zero Charge. IV. Update and New Approach. *J. Colloid Interface Sci.* **2009**, *337* (2), 439–448. https://doi.org/10.1016/j.jcis.2009.04.072.

(144) Rivera, C. A.; Souna, A. J.; Bender, John. S.; Manfred, K.; Fourkas, J. T. Reorientation-Induced Spectral Diffusion in Vibrational Sum-Frequency-Generation Spectroscopy. *J. Phys. Chem. B* **2013**, *117* (49), 15875–15885. https://doi.org/10.1021/jp408877a.

(145) Lum, K.; Chandler, D. Phase Diagram and Free Energies of Vapor Films and Tubes for a Confined Fluid. *Int. J. Thermophys.* **1998**, *19* (3), 845–855. https://doi.org/10.1023/A:1022643006849.

(146) Lum, K.; Luzar, A. Pathway to Surface-Induced Phase Transition of a Confined Fluid. *Phys. Rev. E* **1997**, *56* (6), R6283–R6286. https://doi.org/10.1103/PhysRevE.56.R6283.

(147) Luzar, A. Activation Barrier Scaling for the Spontaneous Evaporation of Confined Water. *J. Phys. Chem. B* **2004**, *108* (51), 19859–19866. https://doi.org/10.1021/jp0470703.

(148) Anishkin, A.; Akitake, B.; Kamaraju, K.; Chiang, C.-S.; Sukharev, S. Hydration Properties of Mechanosensitive Channel Pores Define the Energetics of Gating. *J. Phys. Condens. Matter* **2010**, *22* (45), 454120. https://doi.org/10.1088/0953-8984/22/45/454120.

(149) Anishkin, A.; Sukharev, S. Water Dynamics and Dewetting Transitions in the Small Mechanosensitive Channel MscS. *Biophys. J.* **2004**, *86* (5), 2883–2895. https://doi.org/10.1016/S0006-3495(04)74340-4.

(150) Beckstein, O.; Sansom, M. S. P. Liquid–Vapor Oscillations of Water in Hydrophobic Nanopores. *Proc. Natl. Acad. Sci.* **2003**, *100* (12), 7063. https://doi.org/10.1073/pnas.1136844100.

(151) Beckstein, O.; Sansom, M. S. P. A Hydrophobic Gate in an Ion Channel: The Closed State of the Nicotinic Acetylcholine Receptor. *Phys. Biol.* **2006**, *3* (2), 147–159. https://doi.org/10.1088/1478-3975/3/2/007.

(152) Aryal, P.; Sansom, M. S. P.; Tucker, S. J. Hydrophobic Gating in Ion Channels. *Underst. Funct. Mech. Ion Channels* **2015**, *427* (1), 121–130. https://doi.org/10.1016/j.jmb.2014.07.030.

(153) Yonkunas, M.; Kurnikova, M. The Hydrophobic Effect Contributes to the Closed State of a Simplified Ion Channel through a Conserved Hydrophobic Patch at the Pore-Helix Crossing. *Front. Pharmacol.* **2015**, *6*, 284. https://doi.org/10.3389/fphar.2015.00284.

(154) Willard, A. P.; Chandler, D. The Molecular Structure of the Interface between Water and a Hydrophobic Substrate Is Liquid-Vapor Like. *J. Chem. Phys.* **2014**, *141* (18), 18C519. https://doi.org/10.1063/1.4897249.

(155) Stillinger, F. H. Structure in Aqueous Solutions of Nonpolar Solutes from the Standpoint of Scaled-Particle Theory. In *The Physical Chemistry of Aqueous System: A Symposium in Honor of Henry S. Frank on His Seventieth Birthday*; Kay, R. L., Ed.; Springer US: Boston, MA, 1973; pp 43–60. https://doi.org/10.1007/978-1-4613-4511-4_3.

(156) Chandler, D. Interfaces and the Driving Force of Hydrophobic Assembly. *Nature* **2005**, *437* (7059), 640–647. https://doi.org/10.1038/nature04162.

(157) Remsing, R. C.; Rodgers, J. M.; Weeks, J. D. Deconstructing Classical Water Models at Interfaces and in Bulk. *J. Stat. Phys.* **2011**, *145* (2), 313–334. https://doi.org/10.1007/s10955-011-0299-3.

(158) Patel, A. J.; Varilly, P.; Chandler, D. Fluctuations of Water near Extended Hydrophobic and Hydrophilic Surfaces. *J. Phys. Chem. B* **2010**, *114* (4), 1632–1637. https://doi.org/10.1021/jp909048f.

(159) Patel, A. J.; Varilly, P.; Jamadagni, S. N.; Hagan, M. F.; Chandler, D.; Garde, S. Sitting at the Edge: How Biomolecules Use Hydrophobicity to Tune Their Interactions and Function. *J. Phys. Chem. B* **2012**, *116* (8), 2498–2503. https://doi.org/10.1021/jp2107523.

(160) Brown, M. A.; D'Auria, R.; Kuo, I.-F. W.; Krisch, M. J.; Starr, D. E.; Bluhm, H.; Tobias, D. J.; Hemminger, J. C. Ion Spatial Distributions at the Liquid–Vapor Interface of Aqueous Potassium Fluoride Solutions. *Phys. Chem. Chem. Phys.* **2008**, *10* (32), 4778–4784. https://doi.org/10.1039/B807041E.

(161) Liu, D.; Ma, G.; Levering, L. M.; Allen, H. C. Vibrational Spectroscopy of Aqueous Sodium Halide Solutions and Air−Liquid Interfaces: Observation of Increased Interfacial Depth. *J. Phys. Chem. B* **2004**, *108* (7), 2252–2260. https://doi.org/10.1021/jp036169r.

(162) Petersen, P. B.; Saykally, R. J. Probing the Interfacial Structure of Aqueous Electrolytes with Femtosecond Second Harmonic Generation Spectroscopy. *J. Phys. Chem. B* **2006**, *110* (29), 14060–14073. https://doi.org/10.1021/jp0601825.

(163) Jungwirth, P.; Tobias, D. J. Molecular Structure of Salt Solutions: A New View of the Interface with Implications for Heterogeneous Atmospheric Chemistry. *J. Phys. Chem. B* **2001**, *105* (43), 10468–10472. https://doi.org/10.1021/jp012750g.

(164) Dang, L. X.; Chang, T.-M. Molecular Mechanism of Ion Binding to the Liquid/Vapor Interface of Water. *J. Phys. Chem. B* **2002**, *106* (2), 235–238. https://doi.org/10.1021/jp011853w.

(165) Dang, L. X. Computational Study of Ion Binding to the Liquid Interface of Water. *J. Phys. Chem. B* **2002**, *106* (40), 10388–10394. https://doi.org/10.1021/jp021871t.

(166) Tian, C.; Byrnes, S. J.; Han, H.-L.; Shen, Y. R. Surface Propensities of Atmospherically Relevant Ions in Salt Solutions Revealed by Phase-Sensitive Sum Frequency Vibrational Spectroscopy. *J. Phys. Chem. Lett.* **2011**, *2* (15), 1946–1949. https://doi.org/10.1021/jz200791c.

(167) Petersen, P. B.; Saykally, R. J. On the Nature of Ions at the Liquid Water Surface. *Annu. Rev. Phys. Chem.* **2006**, *57* (1), 333–364. https://doi.org/10.1146/annurev.physchem.57.032905.104609.

(168) Ghosal, S.; Hemminger, J. C.; Bluhm, H.; Mun, B. S.; Hebenstreit, E. L. D.; Ketteler, G.; Ogletree, D. F.; Requejo, F. G.; Salmeron, M. Electron Spectroscopy of Aqueous Solution Interfaces Reveals Surface Enhancement of Halides. *Science* **2005**, *307* (5709), 563–566. https://doi.org/10.1126/science.1106525.

(169) Vrbka, L.; Mucha, M.; Minofar, B.; Jungwirth, P.; Brown, E. C.; Tobias, D. J. Propensity of Soft Ions for the Air/Water Interface. *Curr. Opin. Colloid Interface Sci.* **2004**, *9* (1), 67–73. https://doi.org/10.1016/j.cocis.2004.05.028.

(170) Powell, M. R.; Cleary, L.; Davenport, M.; Shea, K. J.; Siwy, Z. S. Electric-Field-Induced Wetting and Dewetting in Single Hydrophobic Nanopores. *Nat. Nanotechnol.* **2011**, *6* (12), 798–802. https://doi.org/10.1038/nnano.2011.189.

(171) Innes, L.; Gutierrez, D.; Mann, W.; Buchsbaum, S. F.; Siwy, Z. S. Presence of Electrolyte Promotes Wetting and Hydrophobic Gating in Nanopores with Residual Surface Charges. *The Analyst* **2015**, *140* (14), 4804–4812. https://doi.org/10.1039/c4an02244k.

(172) Smirnov, S. N.; Vlassiouk, I. V.; Lavrik, N. V. Voltage-Gated Hydrophobic Nanopores. *ACS Nano* **2011**, *5* (9), 7453–7461. https://doi.org/10.1021/nn202392d.

(173) Setny, P.; Baron, R.; Michael Kekenes-Huskey, P.; McCammon, J. A.; Dzubiella, J. Solvent Fluctuations in Hydrophobic Cavity–Ligand Binding Kinetics. *Proc. Natl. Acad. Sci.* **2013**, *110* (4), 1197. https://doi.org/10.1073/pnas.1221231110.

(174) Hulteen, J. C.; Jirage, K. B.; Martin, C. R. Introducing Chemical Transport Selectivity into Gold Nanotubule Membranes. *J. Am. Chem. Soc.* **1998**, *120* (26), 6603–6604. https://doi.org/10.1021/ja980045o.

(175) Huang, D. M.; Cottin-Bizonne, C.; Ybert, C.; Bocquet, L. Ion-Specific Anomalous Electrokinetic Effects in Hydrophobic Nanochannels. *Phys Rev Lett* **2007**, *98* (17), 177801. https://doi.org/10.1103/PhysRevLett.98.177801.

(176) Bratko, D.; Daub, C. D.; Leung, K.; Luzar, A. Effect of Field Direction on Electrowetting in a Nanopore. *J. Am. Chem. Soc.* **2007**, *129* (9), 2504–2510. https://doi.org/10.1021/ja0659370.

(177) Michelin-Jamois, M.; Picard, C.; Vigier, G.; Charlaix, E. Giant Osmotic Pressure in the Forced Wetting of Hydrophobic Nanopores. *Phys. Rev. Lett.* **2015**, *115* (3), 036101. https://doi.org/10.1103/PhysRevLett.115.036101.

(178) Fadeev, A. Y.; Eroshenko, V. A. Study of Penetration of Water into Hydrophobized Porous Silicas. *J. Colloid Interface Sci.* **1997**, *187* (2), 275–282. https://doi.org/10.1006/jcis.1996.4495.

(179) Lefevre, B.; Saugey, A.; Barrat, J. L.; Bocquet, L.; Charlaix, E.; Gobin, P. F.; Vigier, G. Intrusion and Extrusion of Water in Hydrophobic Mesopores. *J. Chem. Phys.* **2004**, *120* (10), 4927–4938. https://doi.org/10.1063/1.1643728.

(180) Dzubiella, J.; Hansen, J.-P. Electric-Field-Controlled Water and Ion Permeation of a Hydrophobic Nanopore. *J. Chem. Phys.* **2005**, *122* (23), 234706. https://doi.org/10.1063/1.1927514.

(181) Toney, M. F.; Howard, J. N.; Richer, J.; Borges, G. L.; Gordon, J. G.; Melroy, O. R.; Wiesler, D. G.; Yee, D.; Sorensen, L. B. Voltage-Dependent Ordering of Water Molecules at an Electrode–Electrolyte Interface. *Nature* **1994**, *368* (6470), 444–446. https://doi.org/10.1038/368444a0.

(182) Shafiei, M.; von Domaros, M.; Bratko, D.; Luzar, A. Anisotropic Structure and Dynamics of Water under Static Electric Fields. *J. Chem. Phys.* **2019**, *150* (7), 074505. https://doi.org/10.1063/1.5079393.

(183) Trick, J. L.; Song, C.; Wallace, E. J.; Sansom, M. S. P. Voltage Gating of a Biomimetic Nanopore: Electrowetting of a Hydrophobic Barrier. *ACS Nano* **2017**, *11* (2), 1840–1847. https://doi.org/10.1021/acsnano.6b07865.

(184) Giovambattista, N.; Debenedetti, P. G.; Rossky, P. J. Hydration Behavior under Confinement by Nanoscale Surfaces with Patterned Hydrophobicity and Hydrophilicity. *J. Phys. Chem. C* **2007**, *111* (3), 1323–1332. https://doi.org/10.1021/jp065419b.

(185) Ma, C. D.; Wang, C.; Acevedo-Vélez, C.; Gellman, S. H.; Abbott, N. L. Modulation of Hydrophobic Interactions by Proximally Immobilized Ions. *Nature* **2015**, *517* (7534), 347–350. https://doi.org/10.1038/nature14018.

(186) Cheng, Y.-K.; Rossky, P. J. Surface Topography Dependence of Biomolecular Hydrophobic Hydration. *Nature* **1998**, *392* (6677), 696–699. https://doi.org/10.1038/33653.

(187) Pham, T. A.; Mortuza, S. M. G.; Wood, B. C.; Lau, E. Y.; Ogitsu, T.; Buchsbaum, S. F.; Siwy, Z. S.; Fornasiero, F.; Schwegler, E. Salt Solutions in Carbon Nanotubes: The Role of Cation−π Interactions. *J. Phys. Chem. C* **2016**, *120* (13), 7332–7338. https://doi.org/10.1021/acs.jpcc.5b12245.

(188) Acar, E. T.; Hinkle, P.; Siwy, Z. S. Concentration-Polarization-Induced Precipitation and Ionic Current Oscillations with Tunable Frequency. *J. Phys. Chem. C* **2018**, *122* (6), 3648–3654. https://doi.org/10.1021/acs.jpcc.7b12265.

(189) Lin, K.; Lin, C.-Y.; Polster, J. W.; Chen, Y.; Siwy, Z. S. Charge Inversion and Calcium Gating in Mixtures of Ions in Nanopores. *J. Am. Chem. Soc.* **2020**, *142* (6), 2925–2934. https://doi.org/10.1021/jacs.9b11537.

(190) F. Gygi. Architecture of Qbox: A Scalable First-Principles Molecular Dynamics Code. *IBM J. Res. Dev.* **2008**, *52* (1.2), 137–144. https://doi.org/10.1147/rd.521.0137.

(191) Perdew, J. P.; Burke, K.; Ernzerhof, M. Generalized Gradient Approximation Made Simple. *Phys. Rev. Lett.* **1996**, *77* (18), 3865–3868. https://doi.org/10.1103/PhysRevLett.77.3865.

(192) Schlipf, M.; Gygi, F. Optimization Algorithm for the Generation of ONCV Pseudopotentials. *Comput. Phys. Commun.* **2015**, *196*, 36–44. https://doi.org/10.1016/j.cpc.2015.05.011.

(193) Pham, T. A.; Ogitsu, T.; Lau, E. Y.; Schwegler, E. Structure and Dynamics of Aqueous Solutions from PBE-Based First-Principles Molecular Dynamics Simulations. *J. Chem. Phys.* **2016**, *145* (15), 154501. https://doi.org/10.1063/1.4964865.

(194) Grossman, J. C.; Schwegler, E.; Draeger, E. W.; Gygi, F.; Galli, G. Towards an Assessment of the Accuracy of Density Functional Theory for First Principles Simulations of Water. *J. Chem. Phys.* **2004**, *120* (1), 300–311. https://doi.org/10.1063/1.1630560.

(195) Schwegler, E.; Grossman, J. C.; Gygi, F.; Galli, G. Towards an Assessment of the Accuracy of Density Functional Theory for First Principles Simulations of Water. II. *J. Chem. Phys.* **2004**, *121* (11), 5400–5409. https://doi.org/10.1063/1.1782074.

(196) Plimpton, S. Fast Parallel Algorithms for Short-Range Molecular Dynamics. *J. Comput. Phys.* **1995**, *117* (1), 1–19. https://doi.org/10.1006/jcph.1995.1039.

(197) Jorgensen, W. L.; Maxwell, D. S.; Tirado-Rives, J. Development and Testing of the OPLS All-Atom Force Field on Conformational Energetics and Properties of Organic Liquids. *J. Am. Chem. Soc.* **1996**, *118* (45), 11225–11236. https://doi.org/10.1021/ja9621760.

(198) Watkins, E. K.; Jorgensen, W. L. Perfluoroalkanes: Conformational Analysis and Liquid-State Properties from Ab Initio and Monte Carlo Calculations. *J. Phys. Chem. A* **2001**, *105* (16), 4118–4125. https://doi.org/10.1021/jp004071w.

(199) Berendsen, H. J. C.; Postma, J. P. M.; van Gunsteren, W. F.; DiNola, A.; Haak, J. R. Molecular Dynamics with Coupling to an External Bath. *J. Chem. Phys.* **1984**, *81* (8), 3684–3690. https://doi.org/10.1063/1.448118.

(200) Hoover, W. G. Canonical Dynamics: Equilibrium Phase-Space Distributions. *Phys. Rev. A* **1985**, *31* (3), 1695–1697. https://doi.org/10.1103/PhysRevA.31.1695.

(201) Ryckaert, J.-P.; Ciccotti, G.; Berendsen, H. J. C. Numerical Integration of the Cartesian Equations of Motion of a System with Constraints: Molecular Dynamics of n-Alkanes. *J. Comput. Phys.* **1977**, *23* (3), 327–341. https://doi.org/10.1016/0021-9991(77)90098-5.

(202) Hockney, R. W.; Eastwood, J. W. *Computer Simulation Using Particles*, Special student ed.; A. Hilger: Bristol [England] ; Philadelphia, 1988.

(203) Arcadia, C. E.; Reyes, C. C.; Rosenstein, J. K. In Situ Nanopore Fabrication and Single-Molecule Sensing with Microscale Liquid Contacts. *ACS Nano* **2017**, *11* (5), 4907–4915. https://doi.org/10.1021/acsnano.7b01519.

(204) Smirnov, S.; Vlassiouk, I.; Takmakov, P.; Rios, F. Water Confinement in Hydrophobic Nanopores. Pressure-Induced Wetting and Drying. *ACS Nano* **2010**, *4* (9), 5069–5075. https://doi.org/10.1021/nn101080k.

(205) Agazzi, M. L.; Herrera, S. E.; Cortez, M. L.; Marmisollé, W. A.; Bilderling, C. von; Pietrasanta, L. I.; Azzaroni, O. Continuous Assembly of Supramolecular Polyamine–Phosphate Networks on Surfaces: Preparation and Permeability Properties of Nanofilms. *Soft Matter* **2019**, *15* (7), 1640–1650. https://doi.org/10.1039/C8SM02387E.

(206) Vlassiouk, I.; Kozel, T. R.; Siwy, Z. S. Biosensing with Nanofluidic Diodes. *J. Am. Chem. Soc.* **2009**, *131* (23), 8211–8220. https://doi.org/10.1021/ja901120f.

(207) Nguyen, G.; Vlassiouk, I.; Siwy, Z. S. Comparison of Bipolar and Unipolar Ionic Diodes. *Nanotechnology* **2010**, *21* (26), 265301. https://doi.org/10.1088/0957-4484/21/26/265301.

(208) Tinti, A.; Giacomello, A.; Grosu, Y.; Casciola, C. M. Intrusion and Extrusion of Water in Hydrophobic Nanopores. *Proc. Natl. Acad. Sci.* **2017**, *114* (48), E10266. https://doi.org/10.1073/pnas.1714796114.

(209) Jungwirth, P.; Tobias, D. J. Ions at the Air/Water Interface. *J. Phys. Chem. B* **2002**, *106* (25), 6361–6373. https://doi.org/10.1021/jp020242g.

(210) Chattoraj, D. K.; Birdi, K. S. Adsorption at Liquid Interfaces and the Gibbs Equation. In *Adsorption and the Gibbs Surface Excess*; Chattoraj, D. K., Birdi, K. S., Eds.; Springer US: Boston, MA, 1984; pp 39–82. https://doi.org/10.1007/978-1-4615-8333-2_3.

(211) McCaffrey, D. L.; Nguyen, S. C.; Cox, S. J.; Weller, H.; Alivisatos, A. P.; Geissler, P. L.; Saykally, R. J. Mechanism of Ion Adsorption to Aqueous Interfaces: Graphene/Water vs. Air/Water. *Proc. Natl. Acad. Sci.* **2017**, *114* (51), 13369. https://doi.org/10.1073/pnas.1702760114.

(212) Sala, J.; Guàrdia, E.; Martí, J. Specific Ion Effects in Aqueous Eletrolyte Solutions Confined within Graphene Sheets at the Nanometric Scale. *Phys. Chem. Chem. Phys.* **2012**, *14* (30), 10799–10808. https://doi.org/10.1039/C2CP40537G.

(213) Vazdar, M.; Pluhařová, E.; Mason, P. E.; Vácha, R.; Jungwirth, P. Ions at Hydrophobic Aqueous Interfaces: Molecular Dynamics with Effective Polarization. *J. Phys. Chem. Lett.* **2012**, *3* (15), 2087–2091. https://doi.org/10.1021/jz300805b.

(214) Vlassiouk, I.; Park, C.-D.; Vail, S. A.; Gust, D.; Smirnov, S. Control of Nanopore Wetting by a Photochromic Spiropyran: A Light-Controlled Valve and Electrical Switch. *Nano Lett.* **2006**, *6* (5), 1013–1017. https://doi.org/10.1021/nl060313d.

(215) Klesse, G.; Tucker, S. J.; Sansom, M. S. P. Electric Field Induced Wetting of a Hydrophobic Gate in a Model Nanopore Based on the 5-HT3 Receptor Channel. *ACS Nano* **2020**, *14* (8), 10480–10491. https://doi.org/10.1021/acsnano.0c04387.

(216) Dzubiella, J.; Allen, R. J.; Hansen, J.-P. Electric Field-Controlled Water Permeation Coupled to Ion Transport through a Nanopore. *J. Chem. Phys.* **2004**, *120* (11), 5001–5004. https://doi.org/10.1063/1.1665656.

(217) Polster, J. W.; Acar, E. T.; Aydin, F.; Zhan, C.; Pham, T. A.; Siwy, Z. S. Gating of Hydrophobic Nanopores with Large Anions. *ACS Nano* **2020**, *14* (4), 4306–4315. https://doi.org/10.1021/acsnano.9b09777.

(218) Ali, K.; Shah, A.-H. A.; Bilal, S.; Shah, A.-H. A. Surface Tensions and Thermodynamic Parameters of Surface Formation of Aqueous Salt Solutions: III. Aqueous Solution of KCl, KBr and KI. *Colloids Surf. Physicochem. Eng. Asp.* **2009**, *337* (1), 194–199. https://doi.org/10.1016/j.colsurfa.2008.12.023.

(219) Storm, A. J.; Chen, J. H.; Ling, X. S.; Zandbergen, H. W.; Dekker, C. Fabrication of Solid-State Nanopores with Single-Nanometre Precision. *Nat. Mater.* **2003**, *2* (8), 537–540. https://doi.org/10.1038/nmat941.

(220) Lucas, R. A.; Lin, C.-Y.; Baker, L. A.; Siwy, Z. S. Ionic Amplifying Circuits Inspired by Electronics and Biology. *Nat. Commun.* **2020**, *11* (1), 1568. https://doi.org/10.1038/s41467-020-15398-3.

(221) Thompson, A. P.; Aktulga, H. M.; Berger, R.; Bolintineanu, D. S.; Brown, W. M.; Crozier, P. S.; in 't Veld, P. J.; Kohlmeyer, A.; Moore, S. G.; Nguyen, T. D.; Shan, R.; Stevens, M. J.; Tranchida, J.; Trott, C.; Plimpton, S. J. LAMMPS - a Flexible Simulation Tool for Particle-Based Materials Modeling at the Atomic, Meso, and Continuum Scales. *Comput. Phys. Commun.* **2022**, *271*, 108171. https://doi.org/10.1016/j.cpc.2021.108171.

(222) Joseph, S.; Aluru, N. R. Why Are Carbon Nanotubes Fast Transporters of Water? *Nano Lett.* **2008**, *8* (2), 452–458. https://doi.org/10.1021/nl072385q.

(223) Trick, J. L.; Wallace, E. J.; Bayley, H.; Sansom, Mark. S. P. Designing a Hydrophobic Barrier within Biomimetic Nanopores. *ACS Nano* **2014**, *8* (11), 11268–11279. https://doi.org/10.1021/nn503930p.

(224) Jorgensen, W. L.; Chandrasekhar, J.; Madura, J. D.; Impey, R. W.; Klein, M. L. Comparison of Simple Potential Functions for Simulating Liquid Water. *J. Chem. Phys.* **1983**, *79* (2), 926–935. https://doi.org/10.1063/1.445869.

(225) Berg, H. C. *Random Walks in Biology*, Expanded ed.; Princeton University Press: Princeton, N.J, 1993.

(226) Saengdee, P.; Promptmas, C.; Thanapitak, S.; Srisuwan, A.; Pankiew, A.; Thornyanadacha, N.; Chaisriratanakul, W.; Chaowicharat, E.; Jeamsaksiri, W. Optimization of 3-Aminopropyltriethoxysilane Functionalization on Silicon Nitride Surface for Biomolecule Immobilization. *Talanta* **2020**, *207*, 120305. https://doi.org/10.1016/j.talanta.2019.120305.

(227) Cervera, J.; Schiedt, B.; Neumann, R.; Mafé, S.; Ramírez, P. Ionic Conduction, Rectification, and Selectivity in Single Conical Nanopores. *J. Chem. Phys.* **2006**, *124* (10), 104706. https://doi.org/10.1063/1.2179797.

(228) Powell, M. R.; Vlassiouk, I.; Martens, C.; Siwy, Z. S. Nonequilibrium 1/f Noise in Rectifying Nanopores. *Phys. Rev. Lett.* **2009**, *103* (24), 248104. https://doi.org/10.1103/PhysRevLett.103.248104.

(229) Karnik, R.; Duan, C.; Castelino, K.; Daiguji, H.; Majumdar, A. Rectification of Ionic Current in a Nanofluidic Diode. *Nano Lett.* **2007**, *7* (3), 547–551. https://doi.org/10.1021/nl062806o.

(230) Lohse, D.; Zhang, X. Surface Nanobubbles and Nanodroplets. *Rev. Mod. Phys.* **2015**, *87* (3), 981–1035. https://doi.org/10.1103/RevModPhys.87.981.

(231) Virga, E.; Spruijt, E.; de Vos, W. M.; Biesheuvel, P. M. Wettability of Amphoteric Surfaces: The Effect of PH and Ionic Strength on Surface Ionization and Wetting. *Langmuir* **2018**, *34* (50), 15174–15180. https://doi.org/10.1021/acs.langmuir.8b02875.

(232) Chan, D. Y. C.; Mitchell, D. J. The Free Energy of an Electrical Double Layer. *J. Colloid Interface Sci.* **1983**, *95* (1), 193–197. https://doi.org/10.1016/0021-9797(83)90087-5.

(233) Genet, S.; Costalat, R.; Burger, J. A Few Comments on Electrostatic Interactions in Cell Physiology. *Acta Biotheor.* **2000**, *48* (3), 273–287. https://doi.org/10.1023/A:1010229531210.

(234) Das, A. K.; Das, P. K. Bubble Evolution and Necking at a Submerged Orifice for the Complete Range of Orifice Tilt. *AIChE J.* **2013**, *59* (2), 630–642. https://doi.org/10.1002/aic.13828.

(235) Mugele, F.; Baret, J.-C. Electrowetting: From Basics to Applications. *J. Phys. Condens. Matter* **2005**, *17* (28), R705–R774. https://doi.org/10.1088/0953-8984/17/28/r01.

Figures

Figure 1.1A (left):
Figure from de Groot, B. L.; Grubmüller, H. Water Permeation Across Biological Membranes: Mechanism and Dynamics of Aquaporin-1 and GlpF. *Science* **2001**, *294* (5550), 2353. Reprinted with permission from AAAS.

Figure 1.1A (right):
Figure from Doyle, D. A.; Cabral, J. M.; Pfuetzner, R. A.; Kuo, A.; Gulbis, J. M.; Cohen, S. L.; Chait, B. T.; MacKinnon, R. The Structure of the Potassium Channel: Molecular Basis of K^+ Conduction and Selectivity. *Science* **1998**, *280* (5360), 69. Reprinted with permission from AAAS.

Figure 1.1B:
Adapted with permission from Perry, D.; Momotenko, D.; Lazenby, R. A.; Kang, M.; Unwin, P. R. Characterization of Nanopipettes. Anal. Chem. 2016, 88 (10), 5523–5530. https://doi.org/10.1021/acs.analchem.6b01095. Copyright 2016 American Chemical Society.

Figure 1.1C:
Adapted from Vlassiouk, I.; Apel, P. Y.; Dmitriev, S. N.; Healy, K.; Siwy, Z. S. Versatile Ultrathin Nanoporous Silicon Nitride Membranes. *PNAS* **2009**, *106* (50), 21039–21044. https://doi.org/10.1073/pnas.0911450106.

Figure 2.1:
Image provided with permission from Mark Flaming. Copyright 2022 Sutter Instrument Company.

Figure 2.6:
Adapted with permission from Kwok, H.; Briggs, K.; Tabard-Cossa, V. Nanopore Fabrication by Controlled Dielectric Breakdown. *PLOS ONE* **2014**, *9* (3), e92880. https://doi.org/10.1371/journal.pone.0092880. Copyright 2014 Kwok *et al*.

Figure 2.7:
Reprinted by permission from Springer Nature Customer Service Centre GmbH: Springer, Applied Physics A: Materials Science & Processing, Electro-responsive asymmetric nanopores in polyimide with stable ion-current signal, Siwy, Z., Dobrev, D., Neumann, R., Trautmann, C., Voss, K, Copyright 2003 Springer-Verlag.

Figure 2.8:
Reprinted from T. E. Gomez Alvarez-Arenas; P. Y. Apel; O. Orelovitch. Ultrasound Attenuation in Cylindrical Micro-Pores: Nondestructive Porometry of Ion-Track Membranes. *IEEE Transactions on Ultrasonics, Ferroelectrics, and Frequency Control* **2008**, *55* (11), 2442–2449. https://doi.org/10.1109/TUFFC.951. Copyright 2008 IEEE.

Figure 3.1:
Adapted with permission from Probstein, R. F. Solutions of Electrolytes. In *Physicochemical Hydrodynamics: An Introduction*, 2nd ed.; Wiley: New York, 2005; pp 165–210. https://doi.org/10.1002/0471725137.ch6. Copyright 2005 John Wiley & Sons, Inc.

Figure 3.4:
Republished with permission of The Royal Society of Chemistry, from Daiguji, H. Ion Transport in Nanofluidic Channels. *Chem. Soc. Rev.* **2010**, *39* (3), 901–911. https://doi.org/10.1039/B820556F. Copyright 2010 The Royal Society of Chemistry.

Figures in Chapter 4 and Appendix A:
Reprinted from Polster, J. W.; Souna, A. J.; Motevaselian, M. H.; Lucas, R. A.; Tran, J. D.; Siwy, Z. S.; Aluru, N. R.; Fourkas, J. T. The Electrical-Double Layer Revisited. *Natural Sciences* **2022**, e20210099. https://doi.org/10.1002/ntls.20210099. Copyright 2022 Wiley-VCH GmbH.

Figures in Chapter 5 and Appendix B:
Reprinted with permission from Polster, J. W.; Acar, E. T.; Aydin, F.; Zhan, C.; Pham, T. A.; Siwy, Z. S. Gating of Hydrophobic Nanopores with Large Anions. *ACS Nano* **2020**, *14* (4), 4306–4315. https://doi.org/10.1021/acsnano.9b09777. Copyright 2020 American Chemical Society.

Figures in Chapter 6 and Appendix C:
Modeling and theoretical text, figures, and tables reprinted with permission from Fikret Aydin and Pedro de Souza.